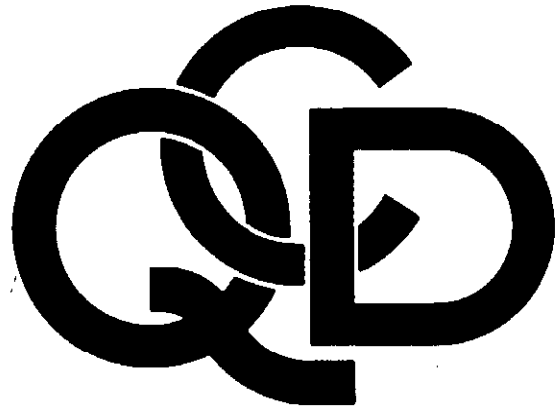


# **Handbook of Perturbative QCD**

**Version 1.0: April 1993**



## **CTEQ Collaboration**

Raymond Brock, John C. Collins, Joey Huston, Stephen Kuhlmann, Sanjib Mishra, Jorge G. Morfin,  
Fredrick Olness, Joseph Owens, Jon Pumplin, Jian-Wei Qiu, John Smith, Davison E. Soper,  
Wu-Ki Tung, Hendrik Weerts, James Whitmore, Chien-Peng Yuan

George Sterman, *Editor*

# **Handbook of Perturbative QCD**

**Version 1.0: April 1993**

**CTEQ Collaboration**

Raymond Brock<sup>2</sup>, John C. Collins<sup>3</sup>, Joey Huston<sup>2</sup>, Stephen Kuhlmann<sup>4</sup>,  
Sanjib Mishra<sup>5</sup>, Jorge G. Morfin<sup>6</sup>, Fredrick Olness<sup>8</sup>, Joseph Owens<sup>7</sup>,  
Jon Pumplin<sup>2</sup>, Jian-Wei Qiu<sup>9</sup>, John Smith<sup>1</sup>, Davison E. Soper<sup>10</sup>,  
Wu-Ki Tung<sup>2</sup>, Hendrik Weerts<sup>2</sup>, James Whitmore<sup>3</sup>, Chien-Peng Yuan<sup>2</sup>

George Sterman<sup>1</sup>, *Editor*

<sup>1</sup>Institute for Theoretical Physics,  
State University of New York at Stony Brook,  
Stony Brook, NY 11794-3840

<sup>2</sup>Department of Physics & Astronomy, Michigan State University,  
East Lansing, MI 48824-1116

<sup>3</sup>Department of Physics, Pennsylvania State University,  
University Park, PA 16802

<sup>4</sup>Argonne National Laboratory,  
Argonne, IL 60439-4815

<sup>5</sup>Department of Physics, Harvard University,  
Cambridge, MA 02138

<sup>6</sup>Fermi National Accelerator Laboratory,  
P.O. Box 500, Batavia, IL 60510

<sup>7</sup>Department of Physics, Florida State University,  
Tallahassee, FL 32306

<sup>8</sup>Department of Physics, Southern Methodist University,  
Dallas, TX 75275

<sup>9</sup>Department of Physics, Iowa State University,  
Ames, IA 50011

<sup>10</sup>Institute of Theoretical Science, University of Oregon,  
Eugene, OR 97403

CTEQ Collaboration, 1993.

## TABLE OF CONTENTS

1. Prerequisites
  - 1.1 Lagrangian. 1.2 Feynman Rules and Green Functions. 1.3 From Green Functions to Experiment. 1.4 Asymptotic Freedom. 1.5 Quark Masses. 1.6 Infrared Safety.
2. The Parton Model: Fundamental Cross Sections
  - 2.1 Overview. 2.2 Lepton-Hadron Cross Sections. 2.3  $e^+e^-$  Annihilation. 2.4 Drell-Yan Production. 2.5  $O(\alpha\alpha_s)$  Processes. 2.6 The Parton Model and Experiment.
3. Perturbative QCD: Fundamental Theorems
  - 3.1 Infrared Safety in  $e^+e^-$  Annihilation. 3.2 Factorization Theorems in Deeply Inelastic Scattering. 3.3 Other Factorization Theorems. 3.4 Operator Definitions of Parton Distribution and Fragmentation Functions.
4.  $e^+e^-$  Annihilation
  - 4.1 Total Cross Section. 4.2  $e^+e^-$  Total Cross Section at One Loop. 4.3 Energy-Energy Correlation. 4.4 Jets. 4.5 Calculations.
5. Deeply Inelastic Scattering
  - 5.1 Use of Perturbative Corrections in DIS. 5.2 One-Loop Corrections in DIS. 5.3 Two-Loop Corrections. 5.4 Computation of One-Loop DIS Correction. 5.5 Review of DIS Experiments. 5.6 Experimental Status of Parton Distributions. 5.7 Status of DIS Sum Rules.
6. Hadron-Hadron Cross Sections
  - 6.1 Hard-Scattering Corrections in the Drell-Yan Cross Section. 6.2 Drell-Yan at Two Loops. 6.3 Drell-Yan Cross Sections: Experimental Review. 6.4 Direct Photons: Theory. 6.5 Direct Photon Production: Experiment.
7. QCD-induced Hard Hadron-Hadron Cross Sections
  - 7.1 Jet Production in Hadron Collisions. 7.2 Jets in Hadron-Hadron Collisions: Experiment. 7.3 QCD Corrections: Heavy Quarks.
8. Global Analysis of Parton Distributions
  - 8.1 Evolution of Parton Distributions. 8.2 Global Analysis. 8.3 Survey of Recent Parton Distributions.

## Appendices

- A. Color Matrix Identities and Invariants.
- B. Cut Diagram Notation.
- C. Dimensional Regularization.
- D. Kinematics.

## PREFACE TO VERSION 1

The study of the strong interactions was transformed over twenty years ago with the advent of accelerators in the multi-GeV energy range. The famous SLAC experiments of the nineteen sixties and seventies were the first to show the point-like substructure of hadrons. Before long, quantum chromodynamics emerged as the favored candidate theory, apparently uniquely capable of describing a force that is at once weak at short distances and strong at large distances. By the early eighties, three-jet events in electron-positron annihilation experiments and high- $p_T$  jet events at hadron colliders afforded remarkably tangible justification for a perturbative picture of short-distance cross sections. Many of us remember vividly the rapid transformation of Quantum Chromodynamics (QCD) from a promising but controversial candidate theory to a full-fledged part of the standard model, taken perhaps too confidently for granted. (In this transformation, the achievements of lattice-based numerical studies also played an important role.) At LEP, SLC, HERA and the Tevatron, multi-jet events, the exotica of yesterday, have become today's background, as high-energy physics eagerly awaits the appearance of the top quark.

Looking toward the superconducting supercollider, QCD will be tomorrow's radiative correction to every cross section, be it heavy quark or Higgs production, the manifestations of possible (super)symmetries beyond the standard model, nonperturbative baryon number violation, or whatever unexpected phenomena may surprise us at forty TeV.

There is much more to QCD at the SSC, and at the current highest energies, than this, however. Unlike its older sibling, quantum electrodynamics, QCD has yet to undergo an unequivocal " $g - 2$ " test, which validates its position as a fundamental law of nature beyond a reasonable doubt. (Note this is not the same as demonstrating that it is a self-consistent theory in the mathematical sense.) The rapid change of the QCD coupling between nucleon scales and high energy has much to do with this. The most natural description of QCD at short distances is perturbative, but this description fails for phenomena that are sensitive to the behavior of the theory at long times, long distances and low energies. A theoretical advance of the seventies and eighties, so far supported by experiment, was to recognize that many observable quantities are short-distance dominated, and are insensitive to the long-distance behavior that produces the physical hadrons. A

theoretical challenge for the nineties is to understand how nonperturbative, long-distance scales, where the strong interactions truly become strong, mesh with perturbative behavior. The two coexist in every experimental quantity at every energy. Current experiments at LEP and the Tevatron show an exciting convergence toward quantitative perturbative predictions, in a range where nonperturbative corrections remain sensible. The SSC can confront these methods with experiment over an unprecedented range of scales.

This work is meant to be a sourcebook on perturbative QCD, accessible and useful to experts and novices, experimentalists and theorists alike. In it, we have collected discussions of the basic ideas and applications of the theory. While we have no intention of replacing more scholarly presentations of field-theoretic techniques and experimental reviews, we have included in the first two sections and in the appendices considerable introductory material on the basic concepts of QCD, its perturbative treatment, and on the parton model, out of which it grew. In the third section, we summarize the basic theorems upon which the perturbative treatment rests. We hope that sophisticated readers will find useful the discussions, applications and experimental reviews of specific processes and techniques in the sections that follow. For the simplest processes, we have exhibited theoretical predictions explicitly. Given the complexity of many recent results, this is not always possible, and we have relied in this case on references to the literature and, as is increasingly becoming relevant, to specialized computer programs.

This work is the product of the CTEQ collaboration as a whole, and we have not attempted to enforce on ourselves an artificial uniformity of presentation and style. We hope and believe, however, that readers will find below a coordinated and fundamentally unified text. We would also like to think of this as an evolving document, communicable in electronic as well as "hard copy" forms. In this, initial version, only the most basic results and processes are treated in detail. Directions abound for expansion and emendation, particularly toward the perturbative-nonperturbative junction: resummation techniques, "small- $x$ " evolution, Monte Carlo simulations of event structure, QCD coherence, elastic scattering, and so on. Suggestions in this regard, and toward the improvement and, where necessary, correction, of the existing text, are solicited from our colleagues in the high energy community.

We wish to thank the Texas National Research Laboratory Commission for support of the CTEQ Collaboration, and of the recent CTEQ Summer

School, which was held at Mackinac Island, Michigan, 27 May-3 June, 1992. This opportunity to interact with students and postdocs had a strong positive influence on the material presented here. This work was also supported in part by the National Science Foundation and by the Department of Energy.

April 1993

# 1 Prerequisites

This introductory section reviews a number of relevant facts about QCD, primarily its Lagrange density and Feynman rules, amplitudes and their renormalization, and the concepts of asymptotic freedom and infrared safety. We assume here a general familiarity with elementary methods in field theory. More detailed discussions of field theory topics may be found in textbooks. Asymptotic freedom, infrared safety and the renormalization group applied to QCD are also covered in a number of useful reviews [1.1].

## 1.1 Lagrangian

Quantum Chromodynamics is defined as a field theory by its Lagrange density,

$$\mathcal{L}_{\text{eff}}^{\text{QCD}} [\psi_f(x), A(x), c(x), \bar{c}(x); g, m_f] = \mathcal{L}_{\text{invar.}} + \mathcal{L}_{\text{gauge}} + \mathcal{L}_{\text{ghost}} , \quad (1.1)$$

which is a function of fields ( $\psi_f$  (quark),  $A$  (gluon) and  $c$  (ghost)) and parameters  $g$  and  $m_f$ .  $f$  labels distinct quark fields.  $\mathcal{L}_{\text{invar.}}$  is the classical density, invariant under local  $SU(N_c)$  gauge transformations, with  $N_c = 3$  for QCD.  $\mathcal{L}_{\text{invar.}}$  is of the form that was originally written down by Yang and Mills [1.2]

$$\begin{aligned} \mathcal{L}_{\text{invar.}} &= \sum_f \bar{\psi}_f [i \not{D} [A] - m_f] \psi_f - \frac{1}{4} F^2 [A] , \\ &= \sum_{f=1}^{n_f} \sum_{\alpha,\beta=1}^4 \sum_{i,j=1}^{N_c} \bar{\psi}_{f,\beta,j} \left[ i(\gamma)^{\mu}_{\beta\alpha} D_{\mu,ji} [A] - m_f \delta_{\beta\alpha} \delta_{ji} \right] \psi_{f,\alpha,i} \\ &\quad - \frac{1}{4} \sum_{\mu,\nu=0}^3 \sum_{a=1}^{N_c^2-1} F_{\mu\nu,a}[A] F^{\mu\nu}{}_a[A] . \end{aligned} \quad (1.2)$$

In the second expression, we have written out all indices explicitly, using the notations

$$D_{\mu,ij}[A] \equiv \partial_\mu \delta_{ij} + ig A_{\mu a} (T_a^{(F)})_{ij} , \quad (1.3)$$

and

$$F_{\mu\nu,a}[A] \equiv \partial_\mu A_{\nu a} - \partial_\nu A_{\mu a} - g C_{abc} A_{\mu b} A_{\nu c} . \quad (1.4)$$

Let us describe what these formulas represent, working backwards from Eq. (1.4).

$F_{\mu\nu,a}$  is the nonabelian *field strength* defined in terms of the *gluon* vector field  $A_b^\mu$ , with  $N_c^2 - 1$  group components  $b$ .  $g$  is the QCD (“strong”) coupling and the  $C_{abc}$ ,  $a, b, c = 1 \dots N_c^2 - 1$ , are real numbers, called the structure constants of  $SU(N_c)$ , which define its *Lie algebra*. As mentioned above, for QCD [1.3],  $N_c = 3$ , but for many purposes it is useful to exhibit the  $N_c$ -dependence explicitly.  $N_c$  is often called the “number of colors”.

The Lie algebra is defined by the commutation relations of the  $N_c^2 - 1, N_c \times N_c$  matrices  $(T_a^{(F)})_{ij}$  that appear in the definition of  $D$ , Eq. (1.3),

$$[T_a^{(F)}, T_b^{(F)}] = iC_{abc}T_c^{(F)}. \quad (1.5)$$

These commutation relations define the algebra. Here we have taken the  $T_a^{(F)}$  to be hermitian, which makes QCD look a lot like QED. Some useful facts about the algebra of generators are listed in Appendix A.

$D_{ij}^\mu[A]$  is the *covariant derivative* in the  $N_c$ -dimensional representation of  $SU(N_c)$ , which acts on the spinor *quark* fields in Eq. (1.2), with color indices  $i = 1 \dots N_c$ . There are  $n_f$  independent quark fields ( $n_f = 6$  in the standard model), labeled by *flavor*  $f (= u, d, c, s, t, b)$ . In QCD, they are distinguished only by their masses.

The quark fields all transform as

$$\psi'_{f,\alpha,j}(x) = U_{ji}(x)\psi_{f,\alpha,i}(x), \quad (1.6)$$

under local gauge transformations, where

$$U_{ji}(x) = \left[ \exp \left\{ i \sum_{a=1}^{N_c^2-1} \beta_a(x) T_a^{(F)} \right\} \right]_{ji}, \quad (1.7)$$

with  $\beta_a(x)$  real. Defined this way,  $U_{ij}(x)$  for each  $x$  is an element of the group  $SU(N_c)$ , which is the local invariance that has been built into the theory. The corresponding transformation for the gluon field is best expressed in terms of an  $N_c \times N_c$  matrix,  $A_\mu(x)$ ,

$$[A_\mu(x)]_{ij} \equiv \sum_{a=1}^{N_c^2-1} A_{\mu a}(x)(T_a^{(F)})_{ij}, \quad (1.8)$$

which is the form that occurs in the covariant derivative. The gluonic field is defined to transform as

$$A'_\mu(x) = U(x)A_\mu(x)U^{-1}(x) + \frac{i}{g}[\partial_\mu U(x)]U^{-1}(x). \quad (1.9)$$

With these transformation rules, the gauge invariance of  $\mathcal{L}_{invar}$  is not difficult to check.

The gauge invariance of  $\mathcal{L}_{invar}$  actually makes it somewhat difficult to quantize. This problem is solved by adding to  $\mathcal{L}_{invar}$  *gauge-fixing* and *ghost* densities,  $\mathcal{L}_{gauge}$  and  $\mathcal{L}_{ghost}$ , as in Eq. (1.1). The former may be chosen almost freely; the two most common choices being

$$\begin{aligned} \mathcal{L}_{gauge} &= -\frac{\lambda}{2} \sum_{a=1}^{N_c^2-1} (\partial_\mu A_a^\mu)^2 \quad 1 < \lambda < \infty, \\ \mathcal{L}_{gauge} &= -\frac{\lambda}{2} \sum_{a=1}^{N_c^2-1} (n \cdot A_a)^2 \quad \lambda \rightarrow \infty, \end{aligned} \quad (1.10)$$

where  $n^\mu$  is a fixed vector. The first defines the set of “covariant” gauges, the most familiar having  $\lambda = 1$ , the *Feynman gauge*. The second defines the “axial” or “physical” gauges [1.4], since taking  $\lambda$  to infinity eliminates the need for ghost fields. Here, picking  $n^\mu$  light-like,  $n^2 = 0$ , defines the *light-cone gauge*. For  $\lambda \rightarrow \infty$ , a nonzero value of  $n \cdot A$  leads to infinite action, and for this reason the physical gauges are often called “ $n \cdot A = 0$  gauges”.

Finally, in the covariant gauges we must add a ghost Lagrangian [1.5]

$$\mathcal{L}_{ghost} = (\partial_\mu \bar{c}_a)(\partial^\mu \delta_{ad} - g C_{abd} A_b^\mu) c_d, \quad (1.11)$$

where  $c_a(x)$  and  $\bar{c}_a(x)$  are scalar ghost and antighost fields. In the quantization procedure, ghost fields anticommute, despite their spin. In an  $SU(N_c)$  theory, the ghost fields ensure that the gauge fixing does not spoil the unitarity of the S-matrix.

## 1.2 Feynman Rules and Green Functions

The perturbation theory (Feynman) rules for QCD are summarized in Fig. 1.1. With our choice of (hermitian) generators  $T_a^{(F)}$ , the quark-gluon

coupling is just like the QED fermion-photon vertex, except for the extra matrix factor  $T_a^{(F)}$ . The remaining rules for vertices are not difficult to derive in detail, but their essential structure is already revealed by the correspondence  $(\partial_\rho \phi) \rightarrow -iq_\rho$ , where  $q_\rho$  is the momentum flowing into the vertex at field  $\phi$ .

As for the propagators, we pause only to notice some special features of physical gauges. In the  $n \cdot A = 0$  gauge, we have, from the propagator in Fig. 1.1,

$$k^\mu G_\mu^\nu(k, n) = i \left( \frac{n^\nu}{n \cdot k} - \frac{n^2 k^\nu}{(n \cdot k)^2} \right). \quad (1.12)$$

Note the lack of a pole at  $k^2 = 0$  on the right-hand side of this relation. This means that the unphysical gluon polarization that is proportional to its momentum does not propagate as a physical particle in these gauges. The lack of a pole for the gluon scalar polarization is the essential reason why ghosts are not necessary in physical gauges. This simplification also makes these gauges useful for many all-order arguments in pQCD. The price, however, is the unphysical poles at  $n \cdot k = 0$ , which are usually thought of as principal values,

$$P \frac{1}{(n \cdot k)^\alpha} \equiv \frac{1}{2} \left[ \frac{1}{(n \cdot k + i\epsilon)^\alpha} + \frac{1}{(n \cdot k - i\epsilon)^\alpha} \right]. \quad (1.13)$$

This definition, however, is awkward beyond tree level (when loops are present) [1.4], and it is perhaps best to back up results derived in physical gauges with calculations or arguments based on covariant gauge reasoning.

The Feynman rules allow us to define *Green functions* in momentum space. These are the vacuum expectation values of time-ordered products of fields,

$$(2\pi)^4 \delta(p_1 + \dots + p_n) G_{\alpha_1 \dots \alpha_n}(p_1, \dots, p_n) = \prod_{i=1}^n \int d^4 x_i e^{-ip_i \cdot x_i} \times \langle 0 | T[\phi_{\alpha_1}(x_1) \dots \phi_{\alpha_n}(x_n)] | 0 \rangle, \quad (1.14)$$

where the  $\alpha_i$  represent both space-time and group indices of the fields, collectively denoted by  $\phi$ . At any fixed order in perturbation theory,  $G_{\alpha_1 \dots \alpha_n}$  is given by the sum of all diagrams constructed according to the rules of Fig. 1.1. Corresponding to each of the fields in the matrix element, every diagram will have an external propagator carrying momentum  $p_i$  into the diagram, with a free external index  $\alpha_i$ . Essentially all of the physical information of the theory is contained in its Green functions.

## 1.3 From Green Functions to Experiment

The route from Feynman rules, through Green functions to experimentally observable quantities is straightforward, but involves a number of steps which it may be useful to outline. In what follows, we will briefly review the roles of the S-matrix, cross sections, renormalization schemes and regularization.

We do not address yet the issue of whether perturbation theory is of any use for reliable calculations of cross sections in QCD.

### 1.3.1 The S-matrix and Cross Sections

By themselves, Green functions are not always direct physical observables. For one thing, their external lines are not necessarily on-mass-shell, and, in a gauge theory, the Green functions are not even gauge invariant. The relation between Green functions and physical quantities like cross sections is, however, quite simple. Let us review the basic steps in a generic situation with fields  $\phi_\alpha$ .

First, a two-point Green function has a pole at  $p^2 = m^2$ . Near the pole, it has the form of a "free" propagator (Fig. 1.1) times a scalar constant  $R_\phi$ ,

$$G_{\alpha\beta}(p) \rightarrow R_\phi G_{\alpha\beta}(p)^{\text{free}} + \text{finite}. \quad (1.15)$$

If the particles under discussion are hadrons, then  $R_\phi$  and the physical mass  $M$  are not perturbatively calculable. If, instead, we discuss the perturbative S-matrix for quarks and gluons, then  $R_\phi$  and  $M$  can be computed as a power series in the coupling

$$\begin{aligned} R_\phi &= 1 + \mathcal{O}(g^2) \\ M &= m + \mathcal{O}(g^2). \end{aligned} \quad (1.16)$$

The *S-matrix* is the amplitude for the scattering of momentum eigenstates into momentum eigenstates. In particle physics, the most important S-matrix elements describe the scattering of two particles into a set of outgoing particles. The S-matrix is derived from Green functions by "reduction formulas", of the general form

$$S((p_1, s_1) + (p_2, s_2) \rightarrow (p_3, s_3) + \dots (p_n, s_n)) = \prod_i \psi(p_i, s_i)_{\alpha_i}$$

$$\left[ \frac{G_{\alpha_i \beta_i}^{-1}(p_i)^{\text{free}}}{R_\phi^{1/2}} \right] G_{\beta_1 \dots \beta_n}(p_1, p_2, -p_3, \dots, -p_n), \quad (1.17)$$

where now  $s_i$  represents the spin (and other quantum numbers) of particle  $i$ . Here  $\psi(p_i, s_i)_{\alpha_i}$  represents the wave function of external particle  $i$ , given by

$u(p, s)$	for an incoming Dirac particle
$\bar{u}(p, s)$	for an outgoing Dirac particle
$\bar{v}(p, s)$	for an incoming Dirac antiparticle
$v(p, s)$	for an outgoing Dirac antiparticle
$\epsilon(p, s)$	for an incoming vector particle
$\epsilon^*(p, s)$	for an outgoing vector particle .

(1.18)

Once again,  $G_{\alpha_i \beta_i}(p_i)^{\text{free}}$  is the free propagator, for field  $i$ , but with the correct physical mass of the corresponding particle.

From the S-matrix, it is customary to define the *transition matrix*  $T$  by

$$S = I + iT, \quad (1.19)$$

with  $I$  the identity matrix in the space of states. For momentum eigenstates,  $T$  contains an explicit momentum-conservation delta function, which it is convenient to separate explicitly,

$$\begin{aligned} iT((p_1, s_1) + (p_2, s_2) \rightarrow (p_3, s_3) + \dots (p_n, s_n)) &= \\ (2\pi)^4 \delta^4(p_1 + p_2 - p_3 - \dots - p_n) \\ \times \mathcal{M}((p_1, s_1) + (p_2, s_2) \rightarrow (p_3, s_3) + \dots (p_n, s_n)). \end{aligned} \quad (1.20)$$

It is  $\mathcal{M}$ -matrix elements that are used to derive cross sections, by integrating the general infinitesimal cross section,

$$\begin{aligned} d\sigma((p_1, s_1) + (p_2, s_2) \rightarrow (p_3, s_3) + \dots (p_n, s_n)) \\ = \frac{1}{4\sqrt{(p_1 \cdot p_2)^2 - m_1^2 m_2^2}} dPS_n \\ \times |\mathcal{M}((p_1, s_1) + (p_2, s_2) \rightarrow (p_3, s_3) + \dots (p_n, s_n))|^2, \end{aligned} \quad (1.21)$$

over  $n$ -particle phase space,

$$dPS_n = \prod_i \left( \frac{d^3 p_i}{2\omega_i (2\pi)^3} \right) N_i (2\pi)^4 \delta^4(p_1 + p_2 - \sum_{j=3}^n p_j). \quad (1.22)$$

Here  $N_i = 1$  for vector and scalar particles, as well as for Dirac particles when we normalize their wave functions according to  $\bar{u}(p, s)u(p, s) = 2m$ . For the other common choice,  $\bar{u}(p, s)u(p, s) = 1$ , we have  $N_i = 2m$  for Dirac fermions. If one integrates a differential cross section over the phase space for  $n$  identical particles, then one should include an additional factor of  $S_n = 1/n!$  that compensates for counting the same physical result  $n!$  times. When discussing the perturbative expansion of a cross section, it is often useful to work directly with diagrams for  $|\mathcal{M}|^2$ . The rules for this expansion are almost the same as for the S-matrix, and are summarized in Appendix B.

### 1.3.2 UV Divergences, Renormalization and Schemes

Green functions, and consequently cross sections, calculated according to the unmodified Feynman rules described above suffer a severe problem when we include diagrams with loops. These are the ultraviolet (UV) divergences, associated with infinite loop momenta. We may think of these divergences as due to virtual states in which energy conservation is violated by an arbitrarily large amount. Let us see how these problems come about, and review how they are usually solved in perturbative calculations.

A typical one-loop integral UV divergence is illustrated by the diagram with scalar lines in Fig. 1.2.

For scalar lines the diagram is given, before renormalization, by

$$\begin{aligned} \Gamma^{(un)}(p) &= \int \frac{d^4 k}{(2\pi)^4} \frac{1}{(k^2 - m^2)((p - k)^2 - m^2)} \\ &= \int_0^1 dx \int \frac{d^4 k}{(2\pi)^4} \frac{1}{(k^2 - 2xp \cdot k + xp^2 - m^2)^2} \\ &= \int_0^1 dx \int \frac{d^4 k'}{(2\pi)^4} \frac{1}{(k'^2 + x(1-x)p^2 - m^2)^2}. \end{aligned} \quad (1.23)$$

In the second equality, we have combined the two denominators into one by a trick known as *Feynman parameterization*. In the third, we have completed

the square in the denominator by the change of variable  $k' = k - xp$ . Of course, all this is purely formal, since the integral as it stands is divergent for  $k \rightarrow \infty$ , that is, in the ultraviolet. Nevertheless, let us consider a one loop integral of the generic form,

$$\Gamma^{(un)}(p) = \int \frac{d^4k}{(2\pi)^4} \frac{1}{(k^2 - M^2(p))^2}, \quad (1.24)$$

which is undefined because of a logarithmic divergence at infinity. We let  $M^2(p)$  denote the dependence on external momentum(a) of the diagram (and “Feynman parameters” like  $x$  above). In QCD there is also momentum dependence through Dirac traces and vector indices in the numerator, but they won’t affect the point we are trying to make right now.

The purpose of renormalization is to replace divergent integrals like the one above by finite expressions, in a systematic fashion. For the logarithmically divergent integrals at hand, renormalization consists of the replacement (suppressing the  $x$  integral)

$$\Gamma^{(un)}(p) \rightarrow \Gamma^{ren}(p, \mu) = \frac{-i}{(4\pi)^2} \ln \left( \frac{M^2(p)}{\mu^2} \right), \quad (1.25)$$

where  $\mu$  is a new mass, not included as a parameter in the original Lagrangian of the theory. Note that we can check Eq. (1.25) by differentiating Eq. (1.24) with respect to  $M^2$ , doing the (now convergent)  $k$  integral, and then integrating the result with respect to  $M^2$  to get Eq. (1.25) up to a constant. To begin with,  $\mu$  is completely arbitrary, and may differ from integral to integral. It is necessary to specify a set of rules to determine the value of  $\mu$  for each divergent diagram. Such a set of rules is called a *renormalization scheme*.

There are two basic kinds of schemes currently in wide use.

(i) In a *momentum subtraction* scheme we choose

$$\mu = M(p_0) \rightarrow \Gamma^{ren}(p_0) = 0, \quad (1.26)$$

with  $p_0$  some fixed set of external momenta, and  $\Gamma$  a particular divergent vertex function. This is what is done in quantum electrodynamics, for instance, when we renormalize so that all the one (and higher) loop corrections to the photon-electron vertex vanish at zero momentum transfer. (In this case  $p_0$  is any point where the photon momentum is zero, and the electrons are on-shell so that  $p_i^2 = m_e^2$ .)

- (ii) In the second generic renormalization scheme,  $\mu$  is chosen the same for *every* divergent integral, and appears as a free parameter in renormalized Green functions. This defines a *minimal subtraction* scheme. Because of its underlying simplicity, minimal subtraction is favored for many practical pQCD calculations. (See Appendix C). The precise scheme for minimal subtraction that is usually used is called the "modified minimal subtraction" or  $\overline{\text{MS}}$  scheme.

Clearly, what we have said so far is highly simplified. It can be shown that these renormalization schemes are flexible enough to handle not only logarithmically, but also quadratically divergent integrals, and apply to multi-loop as well as one-loop integrals. Suffice it to say that these issues may be handled, and the substitution we have just described captures the heart of the issue [1.6].

### 1.3.3 The Renormalization Scale and Experiment

The question now naturally arises, what can we do with a theory that has an arbitrary parameter  $\mu$  in it? The procedure for getting unique experimental predictions is this. For simplicity, let us assume we have a massless theory with only a single coupling constant  $g$ . We now compute a cross section — *any* cross section — which we will call  $\sigma(p, \mu)$ , with  $p$  denoting the momenta of the particles involved. The perturbation theory for  $\sigma$  will always have some UV divergent integrals in it, so its (renormalized) perturbation series will look like

$$\sigma(p, \mu) = \sum_{n=1}^A a_n(p, \mu) g^{2n}, \quad (1.27)$$

where  $A$  is the highest order which we have had the strength to compute, and the  $a_n$  are coefficients that are the results of the computation. Now first we go out and measure  $\sigma(p, \mu)$  for some particular momenta  $\bar{p}$ . Next we fix  $\mu$  to be whatever we like. Then we can *solve* Eq. (1.27) for  $g$ , with a result that we denote  $g(\mu)$ . ( $g(\mu)$  is implicitly also a function of  $\bar{p}$ , and also of  $A$ .) This may not seem to accomplish much, until we realize that we can now compute  $\sigma$  for *any* value of  $p$ . Thus, at the price of doing one experiment, we have predictions for a whole set of experiments. Not only that, but if  $g$  really is the only parameter in the theory, we have unique predictions for

every single cross section in the theory for which we are willing to compute a perturbative series.

Now, because  $\sigma(p, \mu)$  is a physical quantity it *must* be independent of our choice of  $\mu$ , which leads us to the equation

$$\mu \frac{d}{d\mu} \sigma(p, \mu) = 0, \quad (1.28)$$

where we must remember to keep the  $\mu$  dependence in  $g(\mu)$ . This equation holds exactly if we have the exact solution of the theory. If we apply it to the finite order approximation Eq. (1.27), then there will be errors of the order of the first uncomputed term in the perturbation expansion. This will be a useful approximation if the coupling is small, which leads us to our next topic, *asymptotic freedom*.

## 1.4 Asymptotic Freedom

The successes of QCD in describing the strong interactions are summarized by two terms: *asymptotic freedom* [1.7] and *confinement*. To understand the importance of these two attributes we should recall some facts about the strong interactions. Hadron spectra are very well described by the *quark model*, but quarks have never been seen in isolation. Any effort to produce single quarks in scattering experiments leads only to the production of the familiar mesons and baryons. Evidently, the forces between quarks are strong. Paradoxically, however, certain high energy cross sections are quite successfully described by a model in which the quarks do not interact at all. This is the *parton model* that we will describe in Section 2. *Asymptotic freedom* refers to the weakness of the short-distance interaction, while the *confinement* of quarks follows from its strength at long distances.

An extraordinary feature of QCD is its ability to accommodate both kinds of behavior. It does this by making the forces between quarks a rather complicated function of distance. Qualitatively, when two quarks are close together, the force is relatively weak (this is asymptotic freedom), but when they move farther apart the force becomes stronger (confinement). At some distance, it becomes easier to make new quarks and antiquarks, which combine to form hadrons, than to keep pulling against the ever-increasing force. The realization that a single theory might describe such a complicated be-

havior is commonplace nowadays, but it required a major reorientation in our way of thinking about fundamental forces.

The detailed evidence for the coexistence of asymptotic freedom and confinement in QCD is a complicated web of analytic and numerical results and inferences. In this handbook, we will be concerned mainly with the experimental consequences of asymptotic freedom. Nevertheless, in the following we will try and give the reader an idea of the origin of these properties of QCD, as they are embodied in the Feynman rules that we have just outlined.

#### 1.4.1 Forces in QCD and QED

A reasonably direct approach to asymptotic freedom and confinement is through a discussion of the effective forces that are implicit in the Feynman rules of the theory. To see what's involved, we can consider the more familiar case of quantum electrodynamics (QED), where we know quite well the basic force, the Coulomb force, derived from the potential between two particles at rest,

$$V(Q_1, Q_2, \mathbf{r}) = \frac{1}{4\pi} \frac{Q_1 Q_2}{|\mathbf{r}|}. \quad (1.29)$$

$Q_1$  and  $Q_2$  represent the sizes of two charges, separated by  $\mathbf{r}$ . The charges are measured in a system of units in which the permittivity of the vacuum ( $\epsilon_0$  in mks units) is unity. (This is the usual system of units for quantum field theory.) Let us see how this potential comes about in QED, which is the abelian version of the gauge theory with Lagrange density, Eq. (1.2).

The Coulomb potential may be derived by considering the scattering of two very heavy charged particles. If the particles are sufficiently heavy, we can ignore energy transfer compared to momentum transfer, and use a non-relativistic approximation ( $p^2/2M \ll M$ ). If we wanted to go into detail, we would compute the nonrelativistic scattered wave functions as functions of momentum transfer, from which we could infer a spatial potential. We will short-circuit this reasoning and just give the rule: the potential is the spatial Fourier transform of the gauge field propagator, considered as a function of three-momentum ( $|\mathbf{k}|$ ) only, multiplied by the coupling constants at the vertices and divided by  $-i$ . For equal charges,  $Q_i = e$ , this is

$$V(\mathbf{r}) = -e^2 \int \frac{d^3k}{(2\pi)^3} e^{-ik \cdot r} \frac{1}{-k^2}$$

$$= e^2 \frac{2}{(2\pi)^2} \int_0^\infty dk \frac{\sin(k|r|)}{k|r|}, \quad (1.30)$$

where the second equality comes from the angular integrals. That this is the Coulomb potential for unit charges follows from the integral formula,

$$\int_0^\infty dx \frac{\sin(x)}{x} = \frac{\pi}{2}. \quad (1.31)$$

The purpose of this simple exercise is to show how close the Feynman rules are to our ideas of potential and force. What we have verified so far is that the potential can be found from the lowest order diagram shown in Fig. 1.3.

Beyond lowest order in perturbation theory the potential will still be the Fourier transform of the scattering amplitude,

$$V(r) = \int \frac{d^3 k}{(2\pi)^3} e^{-ik \cdot r} A(k^2), \quad (1.32)$$

with  $A(k^2)$  given at lowest order by single-photon exchange as above.

Let's pursue our picture of the nonrelativistic scattering of heavy particles in perturbation theory a bit further, and discuss the effect of some of the perturbative corrections to Fig. 1.3, shown in Fig. 1.4.

These graphs describe  $O(e^4)$  contributions to the potential, whose momentum dependence may be different from the lowest order. We may think of the fermion loop in the first diagram as virtual "light" fermions, of a mass  $m \ll M$ . To define the potential at this order, we actually need to introduce an infrared cutoff, or to sum over soft photon emission, and to carry out renormalization. All this will not affect the main point we want to make here, however, and we shall assume that this has been done, without going into details. Rather, we shall concentrate on the physical picture.

Our basic problem is that we cannot separate experimentally the contributions of the various diagrams of Fig. 1.4, or those from yet higher orders, from the lowest order amplitude. As we shall see, the higher-order corrections modify the momentum dependence, and therefore the potential. How then, do we ever manage to determine the electromagnetic coupling? We do it by *defining* the amplitude at some fixed momentum transfer  $-k^2 = t_0$  to be

$$A(t_0) = \frac{\alpha(t_0)}{t_0}, \quad (1.33)$$

where the *fine structure constant*  $\alpha$  is

$$\alpha = \frac{e^2}{4\pi}. \quad (1.34)$$

Notice that this form says nothing yet about the momentum *dependence* of  $A(t)$ , only about what it is at a specific value of its argument. Since we define this to be the coupling divided by  $t_0$ , the value of the coupling that we find depends upon the  $t_0$  that we choose.

The qualitative effects of the corrections in Fig. 1.4 to  $e^2(t_0)$  are easily understood without explicit calculations. The main contribution is from the first diagram, in which the two incoming charges are linked by a virtual photon that includes a “self-energy” diagram consisting of a fermion-antifermion pair. The net charge of such pairs is zero, and they act to “screen” each charge, as seen by the other charge. We may think of each heavy charge as being surrounded by a cloud of charged pairs. If the incoming charges are far apart, each sees a very large cloud which serves to decrease the effective charge of the other. As  $t_0$  increases, however, the charges come closer together (by the uncertainty principle), get inside the clouds, and the screening becomes less effective. This we can summarize by

$$\frac{d}{dt_0} e^2(t_0) > 0, \quad (1.35)$$

at least for contributions from the first diagram. Actually, the next two diagrams, in which virtual photons are emitted and reabsorbed by one of the charges, do not change this result, because at this order, the emission of an extra virtual photon does not change the charge distribution at all. Explicit calculations show that Eq. (1.35) holds quite generally. It states that as the momentum transfer increases, the observed charge also increases. We will see how to make this observation quantitative in the next subsection. Clearly, this is a problem at extremely high energies. For QED, however, the charge, as observed in Coulomb scattering ( $t_0 = 0$ ) is so small, that  $e^2(t_0)$  does not become large until truly astronomical energies.

Now let us see what happens in QCD, where we define an effective charge  $g^2(t_0)$  by direct analogy to Eq. (1.33). We also define an effective fine structure ‘constant’ for QCD by

$$\alpha_s = \frac{g^2}{4\pi}. \quad (1.36)$$

The corrections of Fig. 1.4 are all present in QCD, with photons replaced by gluons. In addition, at the same order, we also have to include diagrams with three-gluon couplings, as in Fig. 1.5.

As in QED, the effect of virtual corrections is to surround our heavy (nonabelian) charged particles by clouds of charge. There is a very important difference, however. In the nonabelian case the emission of a gluon does *not* leave the nonabelian charge of the heavy particle unchanged. Although the total charge is conserved, it “leaks away” into the cloud of virtual particles. Thus, for small  $t_0$ , when the two heavy particles stay far apart, they are actually *more* likely to see each other’s true charge. As  $t_0$  increases, they penetrate further and further into each other’s charge clouds, and are less and less likely to measure the true charge. For this (only heuristic!) reason, we may expect “antiscreening” for the nonabelian theory, just the opposite of QED,

$$\frac{d}{dt_0} \alpha_s(t_0) < 0. \quad (1.37)$$

This means that as  $t_0$  increases, the observed coupling decreases. This is what we mean by *asymptotic freedom*. At the same time, as  $t_0$  decreases, the coupling increases. Again, explicit calculation verifies this behavior. Of course, it is easier to go to small energy than large, and we shall see that at low energies the effective coupling deduced from perturbation theory actually diverges. This shows that perturbation theory will not be applicable at low energies where, apparently, the interactions become very strong. In this fashion, a perturbative description at short distances and high energies is compatible with confinement at long distances and low energies.

Let us now go on to make these observations more quantitative, by introducing an explicit equation for the effective coupling. This discussion will also serve to introduce a very important concept for QCD, the *renormalization group*.

#### 1.4.2 The Renormalization Group and the Effective Coupling

Let’s see what the two-particle scattering amplitude looks like for momentum transfers not equal to  $t_0$ . As we have seen, it is necessary to introduce a unit of mass,  $\mu$ , called the *renormalization scale*. In the case at hand, for heavy-particle scattering with momentum transfer  $t_0$ , we may choose  $\mu$  as

$$\mu^2 = -t_0. \quad (1.38)$$

This notation is a generalization of the specific choice, Eq. (1.33), that we have made to define the amplitude. In fact, the latter is a special case of a “momentum subtraction scheme”, as introduced in Section 1.3.2. To define  $A(t_0)$  in perturbation theory, it is necessary to introduce a renormalization mass, and Eq. (1.33) is one way to do this.

In terms of  $\alpha_s(\mu^2)$ , the amplitude is of the form

$$A(\mathbf{k}^2) = \alpha_s(\mu^2) \frac{1}{\mathbf{k}^2} + a_{21}\alpha_s^2(\mu^2) \frac{\ln(\mathbf{k}^2/\mu^2)}{\mathbf{k}^2} + a_{20}\alpha_s^2(\mu^2) + \dots \quad (1.39)$$

with  $a_{21}$  a number and  $a_{20}$  a possibly complicated function of the masses and the infrared cutoff. Now here is the fundamental observation, upon which the *renormalization group* is based. The group consists of simply the set of all rescalings of  $\mu$ . The amplitude  $A(\mathbf{k}^2)$  is a *physical* quantity, that can, in principle, be measured by experiment. As such, it *cannot depend on our choice of  $\mu^2$* . This is equivalent to Eq. (1.28), or in this case,

$$\mu \frac{d[tA(t)]}{d\mu} = 0. \quad (1.40)$$

Then, from Eq. (1.39),

$$\mu \frac{d\alpha_s(\mu^2)}{d\mu} = -a_{21}\alpha_s^2(\mu^2) + \dots \quad (1.41)$$

Thus, we have derived an equation for the effective coupling, which determines its  $\mu$  dependence, so long as the coupling remains small enough that higher-order terms remain small. The solution to this equation is known as the *effective* or *running* coupling. According to our observations above, we will find that  $a_{21} > 0$ , so that the coupling decreases as  $\mu$  increases. Thus, asymptotic freedom is a quantifiable concept.

The conventional way of expressing asymptotic freedom is through the dependence of the linear coupling  $g(\mu) = \sqrt{4\pi\alpha_s(\mu^2)}$ ,

$$\mu \frac{dg(\mu)}{d\mu} = \beta(g(\mu)), \quad (1.42)$$

where the *beta function* is a power series in  $g$  beginning at  $O(g^3)$ ,

$$\beta(g) = -g \left( \frac{\alpha_s}{4\pi} \beta_1 + \left( \frac{\alpha_s}{4\pi} \right)^2 \beta_2 + \dots \right). \quad (1.43)$$

$\beta_1$  can be found directly from  $a_{21}$  calculated as above, or from any other physical quantity that depends on  $\mu$  in perturbation theory. It is, as expected, positive for QCD,

$$\beta_1 = 11 - 2n_f/3 = (11N_c - 2n_f)/3, \quad (1.44)$$

where  $n_f$  is the number of flavors of quarks and  $N_c$  the number of colors. The positive contribution, 11, comes mainly from the nonabelian diagrams, Fig. 1.5. The negative contribution,  $2n_f/3$ , which weakens asymptotic freedom, comes from the fermion loop diagram in Fig. 1.4. In these terms, the solution to the lowest order approximation to Eq. (1.42) can be written in terms of  $\alpha_s$  as

$$\alpha_s(\mu^2) = \frac{\alpha_s(\mu_0^2)}{1 + (\beta_1/4\pi)\alpha_s(\mu_0^2)\ln(\mu^2/\mu_0^2)} \quad (\text{lowest order}), \quad (1.45)$$

where the value of  $\alpha_s(\mu_0^2)$  gives the boundary condition for the solution of the differential equation. In this form, the running coupling seems to depend on both  $\alpha_s(\mu_0^2)$  and  $\mu_0^2$ , but in fact it has to be independent of where we start. Therefore, it is often convenient to write  $\alpha_s(\mu^2)$  in terms of a single variable,

$$\alpha_s(\mu^2) = \frac{4\pi}{\beta_1\ln(\mu^2/\Lambda^2)} \quad (\text{lowest order}), \quad (1.46)$$

where

$$\Lambda = \mu_0 e^{-2\pi/(\beta_1\alpha_s(\mu_0^2))} \quad (\text{lowest order}), \quad (1.47)$$

sets the scale for the running coupling. This scale is the famous  $\Lambda_{\text{QCD}}$  which is the subject of much measurement.

A more accurate solution for  $\alpha_s(\mu^2)$  is obtained by using the first two terms in the beta function. One conventionally writes  $\alpha_s(\mu^2)$  in an expansion in powers of  $1/\ln(\mu^2/\Lambda^2)$ , where the coefficient of  $[1/\ln(\mu^2/\Lambda^2)]^n$  is a polynomial in  $\ln(\ln(\mu^2/\Lambda^2))$ . Keeping  $\beta_1$  and  $\beta_2$  allows us to determine the coefficients of  $[1/\ln(\mu^2/\Lambda^2)]^2$ ,

$$\frac{\alpha_s(\mu^2)}{4\pi} = \frac{1}{\beta_1\ln(\mu^2/\Lambda^2)} - \frac{\beta_2\ln(\ln(\mu^2/\Lambda^2))}{\beta_1^3\ln^2(\mu^2/\Lambda^2)} + O\left(\frac{1}{\ln^3(\mu^2/\Lambda^2)}\right), \quad (1.48)$$

where  $\beta_2 = 102 - 38n_f/3$ . Notice that there is no contribution of the form  $c/\ln^2(\mu^2/\Lambda^2)$ . Such a contribution can be absorbed into a redefinition of  $\Lambda$ . One defines  $\Lambda$  by the condition that  $c = 0$ .

If, as is conventional, renormalization is carried out according to the  $\overline{\text{MS}}$  scheme, then  $\Lambda$  here is  $\Lambda_{\overline{\text{MS}}}$ .

## 1.5 Quark Masses

Having discussed the QCD coupling, we now turn to the other physical parameters in the Lagrange density, Eq. (1.1), the quark masses. When we compute higher order loop graphs in the theory, the corrections to the masses are divergent (infinite but temporarily controlled by some regularization process) and the masses themselves must be renormalized. The simplest renormalization scheme, “MS” involves the continuation of the theory into a dimension different from four (Appendix C). Let us illustrate this feature in QED, in the MS scheme. When we compute the one-loop change in the mass, we find, in  $4 - 2\epsilon$  dimensions,

$$m_0 = m \left\{ 1 + \frac{3e^2}{8\pi^2} \frac{1}{\epsilon} + O(e^4) \right\}, \quad (1.49)$$

where  $m_0$  is the mass parameter in the Lagrangian in the absence of interactions ( $e = 0$ ), and  $m$  is the parameter that we use in the interacting case. Note that both masses are still mathematical parameters. As expected, as  $\epsilon \rightarrow 0$  ( $n \rightarrow 4$ ) the difference between the two is infinite, corresponding to an infinite shift in the mass due to the interaction of the electron with its own electromagnetic field. This is not as bad as it sounds, since  $m_0$ , in particular, is not observable. The advantage of using this particular renormalization scheme is that  $m$  and  $m_0$  are related by a simple formula which involves an expansion in pole terms with residues which are powers in the renormalized coupling constant.

Note that neither  $m$  nor  $m_0$  is the physical mass of the electron. We must define the physical mass of the electron,  $m_e$ , as the position of the pole in the renormalized electron two-point Green function. An examination of the corrections to this propagator in perturbation theory yields the finite relation

$$m_e = m \left\{ 1 + \frac{e^2}{8\pi^2} \left( 2 - \frac{3}{2} \ln \frac{m^2}{\mu^2} \right) + O(e^4) \right\} \quad (1.50)$$

where  $\mu$  is an arbitrary mass scale. We thus know the identification between the mathematical parameter in the renormalized Lagrangian and the quantity which is measured in the laboratory.

For QCD this last step does not work. Color confinement is postulated to explain the absence in Nature of free quarks and therefore the physical mass is unobservable. In perturbation theory there is a parameter  $m_0$  and

a renormalized parameter  $m$ , which is treated in the renormalization group equation in the same way as the coupling constant. If we choose the mass independent renormalization scheme given above then the solution of the renormalization group equation follows from the introduction of a running coupling constant  $g(\mu)$  for the quark-gluon interaction and also a running mass  $m(\mu)$  for every quark flavor (up, down, strange,etc). In the theoretical analysis of deep inelastic scattering from “light-mass” quarks the only true scale is the quantity  $\Lambda_{QCD}$ . The running masses decrease as the scale increases so ratios such as  $m_u/\Lambda_{QCD}$ , are small for the up, down and strange quarks. Therefore we are justified in treating these quarks as massless. The running mass is evaluated at a scale where it is small, and therefore plays no role in the analysis of data.

In the case of the heavier quarks, such as charm, bottom and top the masses from spectroscopy are large  $\Lambda_{QCD} < m_c < m_b < m_t$ , so there are new scales in the theory. First we observe that when we choose the renormalization scale close to the mass  $m_Q$  of the heavy quark, the pole of the heavy quark propagator is close to  $p^2 = m_Q^2$  (with order  $\alpha_s(m_Q)$  corrections). At scales of virtuality well below the quark mass, the only effects of heavy-quark propagators are in loop corrections and of a form that they can be cancelled by adjustment of renormalization counterterms. This is the *decoupling theorem* of Appelquist, Carrazone and Symanzik [1.8]. When we work with virtualities well above the heavy quark mass, it is the mass that can be neglected: we treat the quark on the same footing as the light quark and the renormalization scale  $\mu$  is of order the large scale. Clearly we have two regimes: when  $\mu \gg m_Q$ , the heavy quark participates fully, and when  $\mu \ll m_Q$ , we should omit the heavy quark. Matching conditions are necessary. As Collins, Wilczek and Zee [1.9] showed, this can be done by a suitable choice of renormalization scheme. They use  $\overline{MS}$  for everything when  $\mu > m_Q$ , but they use zero-momentum subtraction for loops with heavy quarks when  $\mu < m_Q$ , and  $\overline{MS}$  for everything else. This method gives automatic decoupling of heavy quarks when it is applicable, and allows calculations at scales of order  $m_Q$  with all mass effects taken into account. At the break point  $\mu = m_Q$  the number of active quark flavors in the beta function is changed by exactly one, and the coupling is made continuous there. It can be shown by explicit calculation that, at the one-loop approximation, this break point is at  $\mu/m_Q = 1$  and not at some other ratio, provided that  $\overline{MS}$  renormalization is used. If desired, higher order corrections to this matching condition

can be calculated. It is not yet known how to make an accurate direct experimental measurement of a running quark mass, so we simply adjust  $m_Q$  to fit a physical quantity such as the production cross section. Therefore one should not be surprised when these masses do not exactly agree with the naive expectation of one-half the energy of the threshold for "open" heavy quark production.

## 1.6 Infrared Safety

With our solution for the running coupling, we now have an idea of how asymptotic freedom can help in a practical case. Let  $\sigma(p_i \cdot p_j / \mu^2, m_i^2 / \mu^2, g(\mu))$  represent some physical quantity that we can compute in perturbation theory,

$$\sigma\left(\frac{p_i \cdot p_j}{\mu^2}, \frac{m_i^2}{\mu^2} g(\mu)\right) = \sum_{n=0}^{\infty} a_n \left(\frac{p_i \cdot p_j}{\mu^2}, \frac{m_i^2}{\mu^2}\right) \alpha_s^n(\mu), \quad (1.51)$$

where the  $p_i$  denote external momenta and  $m_i$  the internal (quark) masses  $m_f$ , and any external invariants that are also small. It is quite common that the coefficients  $a_i$  are large, regardless of the value of  $\alpha_s(\mu)$ . In fact, almost all cross sections in perturbative QCD are infrared (IR) divergent, because of the vanishing gluon mass (see Section 4). That is, they are not even defined in the renormalized theory. Nevertheless, we will find that there is a large class of quantities which are *infrared safe* [1.10]. Infrared safe quantities are those which do not depend on the long-distance behavior of the theory. For such quantities, the  $a_n$  are infrared finite, and also possess a finite limit for vanishing  $m_i$ , so that

$$\sigma\left(\frac{Q^2}{\mu^2}, \frac{m_i^2}{\mu^2}, g(\mu)\right) = \sigma\left(\frac{Q^2}{\mu^2}, 0, g(\mu)\right) \left\{ 1 + O\left(\frac{m_i^2}{Q^2}\right) \right\}, \quad (1.52)$$

where  $Q^2$  is a scale characteristic of the large invariants among the  $p_i \cdot p_j$ . (When there is more than one such scale, the situation becomes more complicated, but can remain within the realm of pQCD.)

For an infrared safe quantity, Eq. (1.28) has the solution

$$\sigma\left(\frac{Q^2}{\mu^2}, 0, g(\mu)\right) = \sigma(1, 0, g(Q)), \quad (1.53)$$

in which *all* momentum dependence has been put in the couplings. When  $Q$  is large, the coupling decreases, and the perturbation series becomes better and better.

A major goal of perturbative QCD is to identify and analyze experimental quantities to which asymptotic freedom may be applied consistently. We will often find it necessary to reorganize the perturbation series to identify and compute infrared safe quantities. Typical of the results are the factorization theorems to be discussed in Section 3. Before reorganization, the coefficients in the perturbation series are so large that it is of no practical value to use them. After reorganization, we isolate factors for which low order perturbation theory is useful in practical applications.

## References

- [1.1] T. Muta, *Foundations of Perturbative QCD* (World Scientific, Singapore, 1987); *Perturbative QCD* ed. A.H. Mueller (World Scientific, Singapore, 1989); G. Sterman, *Introduction to Perturbative QCD* 1991 TASI lectures, Stony Brook preprint ITP-SB 91-55.
- [1.2] C.N. Yang and R.L. Mills, Phys. Rev. **96**, 191 (1954).
- [1.3] H. Fritzsch, M. Gell-Mann and H. Leutwyler, Phys. Lett. **B47**, 365 (1973); D.J. Gross and F. Wilczek, Phys. Rev. **D8**, 3633 (1973); S. Weinberg, Phys. Rev. Lett. **31**, 494 (1973).
- [1.4] G. Leibbrandt, Rev. Mod. Phys. **59**, 1067 (1987).
- [1.5] R.P. Feynman, Acta Physica Polonica **24**, 697 (1963); B.S. DeWitt, Phys. Rev. **162**, 1195, 1239 (1967); L.D. Faddeev and V.N. Popov, Phys. Lett. **B25**, 29 (1967); G. 't Hooft and M. Veltman, Nucl. Phys. **B50**, 318 (1972).
- [1.6] J.C. Collins, *Renormalization* (Cambridge University Press 1984).
- [1.7] D.J. Gross and F. Wilczek, Phys. Rev. Lett. **30**, 1343 (1973); H.D. Politzer, Phys. Rev. Lett. **30**, 1346 (1973).

- [1.8] K. Symanzik, Comm. Math. Phys. **34**, 7 (1973); T. Appelquist and J. Carrazone, Phys. Rev. **D11**, 2856 (1975); Nucl. Phys. **B120**, 77 (1977).
- [1.9] J. Collins, F. Wilczek and A. Zee, Phys. Rev. **D18**, 242 (1978); E. Witten, Nucl. Phys. **B104**, 445 (1976); H. Georgi and H.D. Politzer, Phys. Rev. **D14**, 1829 (1976).
- [1.10] G. Sterman and S. Weinberg, Phys. Rev. Lett. **39**, 1436 (1977); Yu. L. Dokshitzer, D.I. Dyakanov and S.I. Troyan, Phys. Rep. **58C**, 269 (1980).

(a) Propagators

Gluon, quark and ghost lines of momentum  $k$

$$\nu, a \rightsquigarrow \mu, b \quad i \frac{\delta_{ba}}{k^2 + i\epsilon} \left[ -g^{\mu\nu} + (1 - \frac{1}{\lambda}) \frac{k^\mu k^\nu}{k^2 + i\epsilon} \right] \text{ covariant gauge}$$

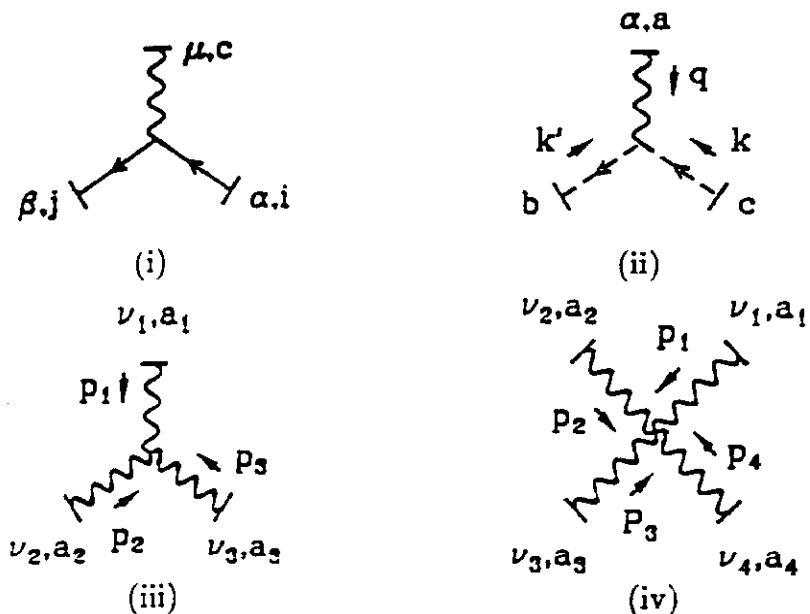
$$i \frac{\delta_{ba}}{k^2 + i\epsilon} \left[ -g^{\mu\nu} + \frac{k^\mu n^\nu + n^\mu k^\nu}{n \cdot k} - n^2 \frac{k^\mu k^\nu}{(n \cdot k)^2} \right] \text{ physical gauge}$$

$\vec{k} \rightarrow$

$$\alpha, i \longrightarrow \beta, j \quad i \frac{\delta_{ij}}{k^2 - m^2 + i\epsilon} [(\vec{k} + m)]_{\beta\alpha}$$

$$a \dashrightarrow b \quad i \frac{\delta_{ba}}{k^2 + i\epsilon}$$

(b) Vertices (all momenta defined to flow in)



$$(i) -ig(T_c^{(F)})_{ji}[\gamma_\mu]_{\beta\alpha}$$

$$(ii) gC_{abc}k'_\alpha$$

$$(iii) -gC_{a_1 a_2 a_3} [g^{\nu_1 \nu_2} (p_1 - p_2)^{\nu_3} + g^{\nu_2 \nu_3} (p_2 - p_3)^{\nu_1} + g^{\nu_3 \nu_1} (p_3 - p_1)^{\nu_2}]$$

$$(iv) -ig^2 [C_{ea_1 a_2} C_{ea_3 a_4} (g^{\nu_1 \nu_3} g^{\nu_2 \nu_4} - g^{\nu_1 \nu_4} g^{\nu_2 \nu_3})$$

$$+ C_{ea_1 a_3} C_{ea_4 a_2} (g^{\nu_1 \nu_4} g^{\nu_3 \nu_2} - g^{\nu_1 \nu_2} g^{\nu_3 \nu_4})$$

$$+ C_{ea_1 a_4} C_{ea_2 a_3} (g^{\nu_1 \nu_2} g^{\nu_4 \nu_3} - g^{\nu_1 \nu_3} g^{\nu_4 \nu_2})]$$

Figure 1.1. Perturbation theory rules for QCD.

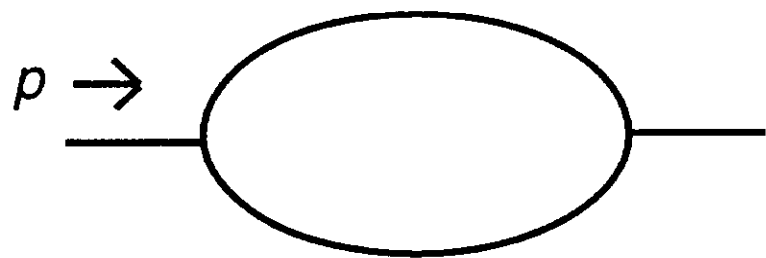


Figure 1.2. An ultraviolet divergent one-loop scalar diagram.

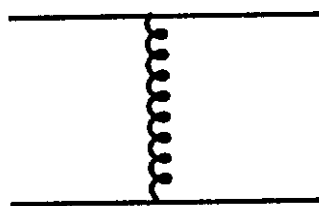


Figure 1.3. The lowest-order potential in QED.

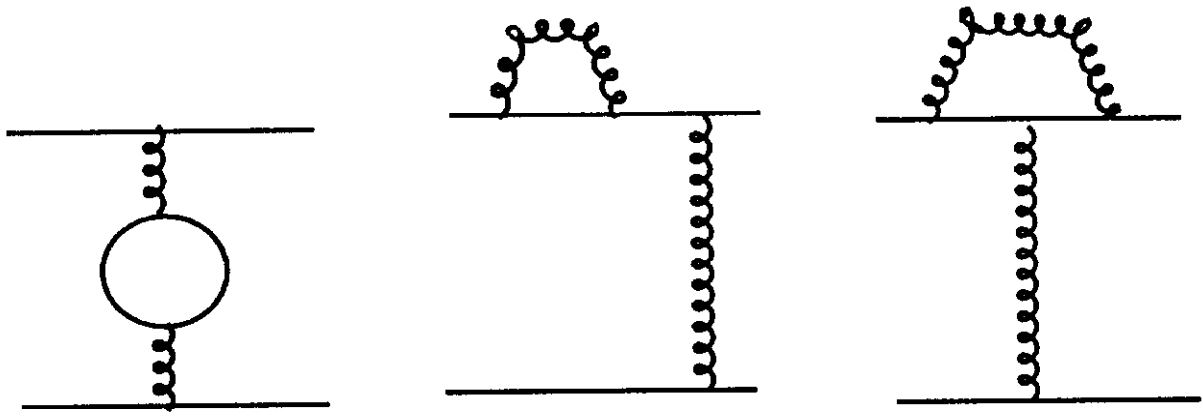


Figure 1.4. Field theory corrections to the potential in QED.

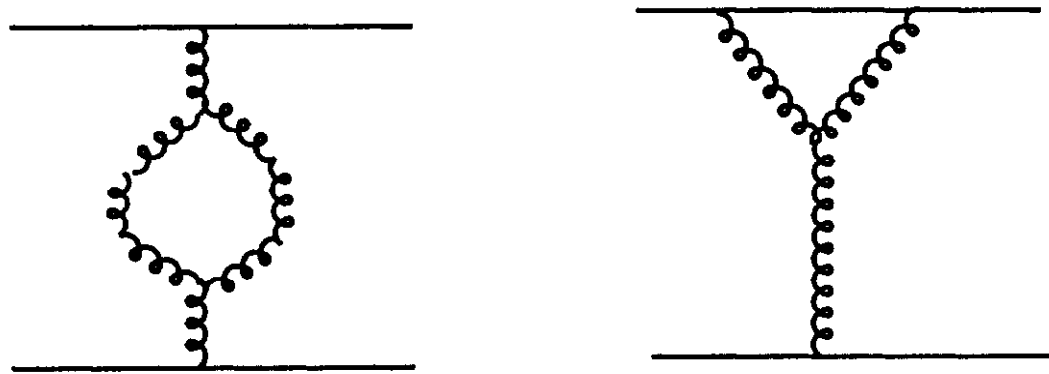


Figure 1.5. Nonabelian correction to the QCD potential.

## 2 The Parton Model: Fundamental Cross Sections

### 2.1 Overview.

The parton model is applicable, with varying degrees of success, to any hadronic cross section involving a large momentum transfer. The parton model is, in essence, a generalization of the impulse approximation. We assume that any physically observed hadron, of momentum  $p^\mu$  is made up of constituent particles, its “partons”, which we will identify with quarks and gluons. At high energy, we neglect the masses of hadrons and partons compared to the scale  $Q$  of the hard scattering. Furthermore, we assume that every relevant parton entering the hard scattering from an initial state hadron has momentum  $xp^\mu$ , with  $0 \leq x \leq 1$ ; here  $p^\mu$  is the momentum of the parent hadron and *within the hard scattering* we make the approximation  $p^2 = 0$ .

Parton model cross sections are calculated from the *tree graphs* (no loops) for partonic scattering, by combining them with *probability* densities, as follows. Consider collisions of hadrons  $A$  and  $B$  to make some suitable final state, e.g., one containing a dimuon pair of large invariant mass. (This particular case is the Drell-Yan process.) Then the parton model cross section for this process has the schematic form,

$$\sigma_{AB}(p, p') \sim \sum_{\text{partons } i,j} \int_0^1 dx dx' \hat{\sigma}_{ij}(xp, x'p') \phi_{i/A}(x) \phi_{j/B}(x') , \quad (2.1)$$

where  $\hat{\sigma}_{ij}$  is the corresponding Born approximation cross section for the scattering of partons  $i$  and  $j$  to produce the chosen final state, and  $\phi_{i/h}(x)$  is the probability density for finding parton  $i$  in the hadron  $h$ , carrying momentum  $xp$ ,  $0 \leq x \leq 1$ .  $\phi_{i/A}$  is called the *distribution* of parton  $i$  in hadron  $A$ .

Similarly, for a final-state hadron  $C$ , with momentum  $\ell$ , we relate hadronic to partonic cross sections by

$$d\sigma_C(\ell) = \sum_{\text{partons } k} \int_0^1 dz d\hat{\sigma}_k(\ell/z) D_{C/k}(z) , \quad (2.2)$$

where now  $D_{C/k}(z)$  is the *fragmentation function* that describes the probability for parton  $k$ , with momentum  $\ell^\mu/z$  to produce a hadron  $C(\ell^\mu)$  in the final state. A general parton model cross section will involve both initial- and final-state hadrons of definite momentum.

### 2.1.1 Heuristic justification

The physical insights behind the parton model are most easily seen in deeply inelastic lepton-hadron scattering. Fig. 2.1 gives a schematic picture of this process in the spirit of the parton model. Fig. 2.1a shows the system before the scattering, as seen in the center-of-mass frame. The hadron, say a nucleon, consists of a set of partons (denoted by  $\times$ 's), in some virtual state of definite fractional momenta  $\xi_i p$ . The central observation is that this virtual state is characterized by a lifetime  $\tau$  in the nucleon rest frame. The precise value of  $\tau$  depends on the details of nucleon structure. Let us suppose, however, that there is an effective lower bound,  $\tau > \tau_0$ , so that the nucleon is made up primarily of virtual states of non-zero lifetime in its own rest frame.

In the center-of-mass system, the nucleon suffers both Lorentz contraction and time dilation. Thus, in this frame, the lifetime of our virtual state is  $\tau(1 - v^*{}^2/c^2)^{-1/2} \gg \tau$ , with  $v^*$  the velocity. Combined with Lorentz contraction (indicated in the figure by a disc shape), this means that the time it takes the electron to cross the nucleon vanishes as the center-of-mass energy goes to infinity.

Therefore, at the time of collision, Fig. 2.1b, the electron sees a collection of partons that are effectively “frozen” during its transit. To exchange a large momentum  $q^\mu$  with one of the partons, the electron must come as close to it as  $O(1/Q)$  in the transverse direction, by the uncertainty principle. The details of the exchange depend on the underlying electron-parton interaction, such as QED.

Most importantly, if we assume that the partons are more-or-less randomly spread out over the disc, the probability of finding an *additional* parton near enough to take part in the hard scattering is suppressed by the

geometrical factor

$$\frac{1/Q^2}{\pi R_0^2}, \quad (2.3)$$

with  $R_0$  the radius of the nucleon. Such an estimate makes sense to the extent that the partons are effectively “frozen” during the short time it takes the electron to pass by. Then the cross section may be written as the probability of finding a parton with given momentum fraction, times the cross section for the interaction.

After the collision, Fig. 2.1c, anything may happen, and as the scattered electron recedes, the fragments of the nucleon interact, create quark pairs and eventually respect confinement. All this is assumed to take place on time scales that are also long compared with the electron’s collision with the nucleon. Then the process of “hadronization”, by which quarks and gluons coalesce into the observed particles, happens too late to influence the hard scattering itself. This assumption underlies the idea of treating the parton-electron scattering in the elastic Born approximation. We do not assume that the scattered quark is really on-shell, only that it is much closer to the mass shell than  $Q^2$ , and lives a much longer time than  $1/Q$ , as  $Q \rightarrow \infty$ .

In summary, the parton model rests upon two physical concepts: the Lorentz contraction and time dilation of internal states of the nucleon, and the long-time nature of hadronization. The “initial-state” interactions between partons happen too early to affect the basic scattering, and hence the inclusive cross section, while the “final-state” interactions between fragments happen too late. Up to kinematic factors, then, the scattering is directly proportional to the density of partons, which is frozen over the short scattering time scale.

To apply the parton model formulas, Eqs. (2.1) and (2.2), we need to calculate elastic scattering processes for these partons in the Born approximation. Of course, we don’t get something for nothing, and it will also be necessary to incorporate information on the structure of hadrons via the functions  $\phi_{i/h}(x)$ . The magic of the parton model is that it is *not* necessary to solve the problem of hadron binding completely. Instead, the required information will be available from experiment. To see how, we study cross

sections for the scattering of hadrons and leptons. Such cross sections will begin at order  $\alpha^2$ , with  $\alpha = e^2/4\pi$  the electromagnetic (or more generally electroweak) fine structure constant.

## 2.2 Lepton-Hadron Cross Sections

There are three standard lepton-hadron parton model cross sections, corresponding to the following underlying partonic reactions: lepton-parton elastic scattering, lepton pair annihilation into parton pairs, and parton pair annihilation into lepton pairs. They correspond, respectively, to *deeply inelastic scattering*,  *$e^+e^-$  annihilation* and the *Drell-Yan process*. At the (observable) hadronic level, these cross sections are all inclusive for hadrons in the final state. In this subsection we treat deeply inelastic scattering.

### 2.2.1 Deeply inelastic scattering kinematics.

A deeply inelastic scattering (DIS) process is generically of the form

$$\ell(k) + h(p) \rightarrow \ell'(k') + X , \quad (2.4)$$

where  $\ell(k)$  represents a lepton of momentum  $k^\mu$ ,  $h(p)$  a hadron of momentum  $p^\mu$ , and  $X$  an arbitrary hadronic state. Normally,  $h(p)$  will be a nucleon or nucleus. The process, illustrated in Fig. 2.2, is initiated by the exchange of vector boson  $V$ . The classic DIS experiment is totally inclusive in the hadronic final state, so that it is necessary only to observe the outgoing lepton, of momentum  $k'^\mu$ . The discussion of DIS, more than any other cross section, is couched in a rather specialized kinematic notation, which we will now briefly review. It should be kept in mind that the kinematics are much more general than the parton model, and even than pQCD.

In DIS, the momentum transfer between lepton and hadron,  $q$ , is space-like,

$$\begin{aligned} q^\mu &= k^\mu - k'^\mu , \\ -q^2 &= Q^2 . \end{aligned} \quad (2.5)$$

In addition, as the term implies, in DIS the hadronic final state  $X$  has an invariant mass much larger than that of the nucleon. This is normally parameterized in terms of the *Bjorken scaling variable*,  $x$ ,

$$x = \frac{-q^2}{2p \cdot q} = \frac{Q^2}{2m_h\nu}, \quad (2.6)$$

where  $\nu$  is the energy transferred from the lepton to the hadron in the hadron (target) rest frame,

$$\nu = p \cdot q / m_h = E_k - E_{k'} . \quad (2.7)$$

$\nu$  is naturally related to the dimensionless variable  $y$ ,

$$y = \frac{p \cdot q}{p \cdot k} = \frac{E_k - E_{k'}}{E_k}, \quad (2.8)$$

that measures the ratio of the energy transferred to the hadronic system to the total leptonic energy available in the target rest frame.

For a nucleus with atomic number  $A$ , it is usually convenient to rescale  $x$  by  $A$ , so that the denominator in Eq. (2.6) is still the mass of a nucleon. For fixed  $x$ , the mass of the hadronic final state is given by

$$W^2 = m_h^2 + \frac{Q^2}{x} (1 - x) . \quad (2.9)$$

Thus, for  $x$  fixed and  $Q^2$  large, the mass of the hadronic final state is also large.

The incoming lepton may be an electron, a muon or an (anti)neutrino [2.1], and the exchanged vector boson a photon,  $W^\pm$ , or  $Z$ . At lowest order in electroweak interactions, the cross section may be split into leptonic and hadronic parts,

$$d\sigma = \frac{d^3 k'}{2s|k'|} \frac{c_V^4}{4\pi^2(q^2 - m_V^2)^2} L_{lV}^{\mu\nu}(k, q) W_{\mu\nu}^{Vh}(p, q), \quad (2.10)$$

where  $V$  labels the exchanged vector boson, of mass  $m_V$ , and where

$$\begin{aligned} c_V &= e, \\ c_{W^\pm} &= \frac{g}{2\sqrt{2}}, \end{aligned} \quad (2.11)$$

for reasons which will become clear in a moment. (Note that each weak interaction coupling involves  $g = e/\sin\theta_W$ ). In this equation, we assume the form  $-g_{\alpha\beta}/(q^2 - m_V^2)$  for the vector boson propagator, neglecting gauge- and mass-dependent terms proportional to  $q_\alpha q_\beta$ . Corrections to this approximation vanish for  $V = \gamma$ , and are suppressed by the ratio  $m_\ell/m_V$  for  $V = W^\pm, Z$ .

The leptonic tensors can be evaluated explicitly (with a conventional but arbitrary normalization) from

$$L_{\ell V}^{\mu\nu}(k, q) = \frac{1}{2} \text{Tr} [ \not{k}\Gamma_{V\ell}^\mu (\not{k} - \not{q})\Gamma_{V\ell}^\nu ], \quad (2.12)$$

where  $\Gamma_{V\ell}$  is the perturbative vertex coupling lepton  $\ell$  to vector  $V$  and the (unique) outgoing lepton  $\ell'$ , but with the factor  $c_V^2$  removed. The factor  $1/2$  is for the spin average for unpolarized electrons: it should be removed for neutrino scattering. To be specific, we may take

$$\Gamma_{\gamma\ell^\pm}^\mu = \gamma^\mu, \quad (2.13)$$

$$\Gamma_{W^{+\nu}}^\mu = \gamma^\mu(1 - \gamma_5), \quad (2.14)$$

$$\Gamma_{W^{-\bar{\nu}}}^\mu = \gamma^\mu(1 + \gamma_5). \quad (2.15)$$

The hadronic tensor, on the other hand, is defined to all orders in the strong interaction in terms of the matrix elements

$$W_{\mu\nu}^{(Vh)}(p, q) = \frac{1}{8\pi} \sum_\sigma \sum_X \langle h(p, \sigma) | j_\mu^{V\dagger}(0) | X \rangle \langle X | j_\nu^V(0) | h(p, \sigma) \rangle \times (2\pi)^4 \delta^4(p + q - p_X). \quad (2.16)$$

Here,  $j_\mu^V(x)$  is the appropriate operator electroweak current, labeled by the corresponding vector boson, and divided by the appropriate  $c_V$  Eq. (2.11). (This procedure does *not* result in unit coupling for quarks; see Section 2.2.2). When appropriate, we average over the nucleon spin,  $\sigma$ , which simplifies our analysis (spin-dependence has lately emerged as a topic of interest and controversy [2.2], [2.3].) We have performed this average in Eq. (2.16), and the normalization factor includes a factor  $1/2$  for this average.

Symmetry properties give important restrictions on the form  $W_{\mu\nu}^{(Vh)}$  may take. These restrictions may be summarized by expanding the tensor in terms of scalar *structure functions*  $W_i^{(Vh)}$ . The general expansion may be expressed as

$$\begin{aligned} W_{\mu\nu}^{(Vh)} = & - \left( g_{\mu\nu} - \frac{q_\mu q_\nu}{q^2} \right) W_1^{(Vh)}(x, Q^2) \\ & + \left( p_\mu - q_\mu \frac{p \cdot q}{q^2} \right) \left( p_\nu - q_\nu \frac{p \cdot q}{q^2} \right) \frac{1}{m_h^2} W_2^{(Vh)}(x, Q^2) \\ & - i\epsilon_{\mu\nu\lambda\sigma} p^\lambda q^\sigma \frac{1}{m_h^2} W_3^{(Vh)}(x, Q^2). \end{aligned} \quad (2.17)$$

Note that there are a variety of conventions in the literature about the definitions of  $W_i$ , and of the variable  $\nu$ . This variation is less pronounced for the scaling structure functions  $F_i$  to be defined below. Our conventions for the  $F_i$ 's are consistent with those in the 1992 Review of Particle Properties [2.4] (taking into account the Erratum <sup>1</sup> to Ref. [2.4]!), and with the detailed derivation found in Chapter 6 of Ref. [2.5] (although our  $W_i$  differ from those of the latter).

The structure functions are generally parameterized in terms of  $x$  and  $Q^2$ . At this stage, there is no relation between the  $W_i^{(Vh)}$  for different bosons  $V$ , although parity invariance of the strong interactions implies that

$$W_3^{(\gamma h)}(x, Q^2) = 0 \quad (\text{for photon exchange only}). \quad (2.18)$$

The functions  $W_i$  of Eq. (2.17) are usually replaced, for the purposes of exhibiting data, by alternate, but equivalent, structure functions  $F_i$ , which will turn out to be particularly simple in the parton model,

$$\begin{aligned} F_1(x, Q^2) &= W_1(x, Q^2), \\ F_2(x, Q^2) &= \frac{\nu}{m_h} W_2(x, Q^2), \\ F_3(x, Q^2) &= \frac{\nu}{m_h} W_3(x, Q^2). \end{aligned} \quad (2.19)$$

---

<sup>1</sup>The erratum refers to the expression for  $F_3$  on page III.52 in [2.4]; it does not apply to the *Particle Properties Data Booklet*.

Yet another equivalent basis for the structure functions is inspired by assigning polarizations to the vector boson  $V$ , in the target rest frame:

$$\begin{aligned}\epsilon_R(q) &= \frac{1}{\sqrt{2}}(0; 1, -i, 0), \\ \epsilon_L(q) &= \frac{1}{\sqrt{2}}(0; 1, i, 0), \\ \epsilon_{long}(q) &= \frac{1}{\sqrt{Q^2}}(\sqrt{Q^2 + \nu^2}; 0, 0, \nu).\end{aligned}\quad (2.20)$$

These correspond to helicities of  $+1, -1$  and to longitudinal (sometimes called “scalar”) polarization for the exchanged particle, respectively. Up to corrections of order  $m_h^2/Q^2$ ,  $W_{\mu\nu}^{(Vh)}$  has the expansion,

$$W_{\mu\nu}^{(Vh)} = \sum_{\lambda} \epsilon_{\lambda}^*(q)_{\mu} \epsilon_{\lambda}(q)_{\nu} F_{\lambda}^{(Vh)}(x, q^2), \quad (2.21)$$

where  $\lambda = L, R, long$  labels the helicity. In this approximation, the “helicity” structure functions are related to the structure functions of Eq. (2.19) by the simple relations

$$F_{L,R} = F_1 \pm F_3, \quad F_{long} = \frac{F_2}{2x} - F_1. \quad (2.22)$$

The structure functions can be found directly from experiments in which only the outgoing lepton’s momentum is measured. For instance, the differential cross section in terms of the dimensionless variables  $x$  and  $y$  may be written in terms of incoming and outgoing lepton energies and scattering angle in the target rest frame as

$$\begin{aligned}\frac{d\sigma^{(\ell h)}}{dxdy} &= N^{(\ell V)} \left[ 2W_1^{(Vh)}(x, q^2) \sin^2(\theta/2) + W_2^{(Vh)}(x, q^2) \cos^2(\theta/2) \right. \\ &\quad \left. \pm W_3^{(Vh)}(x, q^2) \frac{E + E'}{m_h} \sin^2(\theta/2) \right],\end{aligned}\quad (2.23)$$

where the  $\pm$  corresponds to  $V = W^{\pm}$ , and where

$$\begin{aligned}N^{(\ell^{\pm} \gamma)} &= 8\pi\alpha^2 \frac{m_h E}{Q^4}, \\ N^{(\nu W^+)} &= N^{(\bar{\nu} W^-)} = \pi\alpha^2 \frac{m_h E}{2\sin^4(\theta_W)(Q^2 + M_W^2)^2}.\end{aligned}\quad (2.24)$$

Here  $\theta_W$  is the weak mixing angle, and  $\pi\alpha^2/(2M_W^4 \sin^4(\theta_W)) = G_F^2/\pi$ , with  $G_F$  the Fermi constant.

Other useful expressions for this cross section are given directly in terms of  $y$ ,

$$\frac{d\sigma^{(th)}}{dx dy} = N^{IV} \left[ \frac{y^2}{2} 2x F_1^{(Vh)} + \left(1 - y - \frac{m_h xy}{2E}\right) F_2^{(Vh)} + \delta_V \left(y - \frac{y^2}{2}\right) x F_3^{(Vh)} \right], \quad (2.25)$$

where  $\delta_V$  is  $+1$  for  $V = W^+$  (neutrino beam),  $-1$  for  $V = W^-$  (antineutrino beam) and zero for the photon.  $m_h$  is the target mass.

### 2.2.2 Cross Sections and Parton Distributions

Now let us see what the parton model has to say about DIS. As emphasized above, in the parton model the scattering of the nucleon is due entirely to the scattering of its individual constituents. If these constituents are quarks and gluons, then only quarks will couple to electroweak currents in the Born approximation. The DIS cross section is then given by the probability,  $\phi_{f/h}(\xi)$ , of finding a quark of flavor  $f$  and fractional momentum  $\xi$  in hadron  $h$ , times the cross section for the *elastic* scattering of that parton.

A typical parton model DIS cross section is therefore given by

$$\frac{d\sigma^{(th)}}{dE_k' d\Omega_k'}(p, q) = \sum_f \int_0^1 d\xi \frac{d\sigma_{Born}^{(tf)}}{dE_k' d\Omega_k'}(\xi p, q) \phi_{f/h}(\xi). \quad (2.26)$$

The distribution  $\phi_{f/h}$  is at this point undetermined. The perturbative equivalent of the parton model picture of DIS is illustrated, in “cut diagram” notation (Appendix B), in Fig. 2.3a.

We note the absence of diagrams such as Fig. 2.3b, in which the scattering of quark  $f$  with fraction  $\xi$  interferes with the scattering of a quark of fraction  $\xi'$ , the momentum being made up by an extra gluon. This feature is referred to as the “incoherence” of the parton model.

From Eqs. (2.10), (2.17) and (2.19) we derive relations for the structure functions  $F_i$  in the parton model,

$$F_a^{(Vh)}(x) = \sum_f \int_0^1 \frac{d\xi}{\xi} F_a^{(Vf)}(x/\xi) \phi_{f/h}(\xi) \quad (a = 1, 3), \quad (2.27)$$

$$F_2^{(Vh)}(x) = \sum_f \int_0^1 d\xi F_2^{(Vf)}(x/\xi) \phi_{f/h}(\xi). \quad (2.28)$$

Here the  $F_i^{(Vf)}$  are the structure functions at the parton level; they can be calculated from the Born diagram of Fig. 2.4. The factor of  $1/\xi$  in Eq. (2.27) arises from the normalization of the parton states as compared with the hadron states and from the factors of  $p$  in the definitions of the structure functions from  $W_{\mu\nu}$  — the vector  $p^\mu$  must be changed to  $\xi p^\mu$  for scattering off a parton.

For example, with electromagnetic scattering, we have

$$(W_{\mu\nu}^{(\gamma f)})_{Born} = \frac{1}{8\pi} \int \frac{d^3 p'}{(2\pi)^3 2\omega_{p'}} Q_f^2 \text{Tr}[\gamma_\mu(p' + q)\gamma_\nu p'] (2\pi)^4 \delta^{(4)}(p' - p - q), \quad (2.29)$$

where  $eQ_f$  is the electric charge of the quark of flavor  $f$ . A factor  $e$  has been absorbed into  $c_\gamma$  in Eq. (2.11). This gives

$$2F_1^{(\gamma f)}(x) = F_2^{(\gamma f)}(x) = Q_f^2 \delta(1 - x). \quad (2.30)$$

Substituting these functions into Eqs. (2.27) and (2.28), we find the electromagnetic structure functions in terms of quark distributions,

$$2x F_1^{(Vh)}(x) = F_2^{(Vh)}(x) = \sum_f Q_f^2 x \phi_{f/h}(x). \quad (2.31)$$

Two important aspects of these expressions are:

- (i) the structure functions depend on the Bjorken scaling variable  $x$  only, and not on the momentum transfer directly;
- (ii) the two functions satisfy the relation  $2xF_1 = F_2$ .

The first result is known as *scaling* [2.6]. Its observation [2.1] was the inspiration for the parton model. The second, known as the *Callan-Gross relation* [2.7] follows from the specifics of the Born diagram, Fig. 2.4, and as such is evidence for the spin-1/2 nature of charged partons (the quarks).

Evidently, measuring  $F_1$  or  $F_2$  immediately gives an experimental determination of the combination of distributions,  $\sum_f Q_f^2 \phi_{f/h}(x)$  for  $h$  a proton or a neutron. Now isospin invariance implies that

$$\phi_{u/p} = \phi_{d/n}, \quad \phi_{d/p} = \phi_{u/n}, \quad (2.32)$$

with  $u$  the up and  $d$  the down quark. In the approximation that the proton and neutron contain  $u$  and  $d$  quarks only, a measurement of  $F_2$  for  $p$  and  $n$ , combined with Eq. (2.32), determines the distributions  $\phi_{u/h}$  and  $\phi_{d/h}$ . These distributions can then be used to predict other DIS cross sections, such as neutrino scattering, to the same approximation.

Of course, in real life things are not so simple. Quantum mechanics tells us that virtual states will include quark-antiquark pairs of every flavor. The sum in Eq. (2.31) will therefore include the strange, charm, and even the bottom and top quarks, in addition to all the antiquarks. Although we may expect that the admixture of very heavy quark pairs in a nucleon is relatively small, we clearly need more information than is supplied by electromagnetic scattering alone, even to determine the distributions of light antiquarks, for instance. For this purpose, we will find neutrino and antineutrino scattering ideal.

The parton model cross sections for charged weak currents are almost as easy to compute as for the electromagnetic current, and the answers are just as satisfyingly simple. Quarks of definite mass — that is, the quarks of the strong interaction Lagrangian — are not eigenstates of the weak interaction Lagrangian. As a result, the basic vertex for  $u + W^- \rightarrow d$  is *almost* like the vertex for  $\nu_e + W^- \rightarrow e^-$ , i.e.,  $(1/2\sqrt{2}) g \gamma^\mu (1 - \gamma_5)$ , with  $g = (e/\sin \theta_W)$ , but not quite. Instead,  $g$  is replaced by  $g V_{ud}$ , where  $V_{ud}$  is an element in a three-by-three unitary matrix called the *Cabibbo-Kobayashi-Maskawa* mixing matrix. As a result of the mixing, the absorption of a  $W^-$  can change an up quark, not only into a down quark, with coupling  $g V_{ud}$  but also into a

strange quark, with coupling  $gV_{us}$ , or a bottom quark, with coupling  $gV_{ub}$ . The three mixing matrix elements  $V_{ud}$ ,  $V_{us}$  and  $V_{ub}$  form a row of the unitary matrix  $V$ , and hence satisfy

$$|V_{ud}|^2 + |V_{us}|^2 + |V_{ub}|^2 = 1 . \quad (2.33)$$

In practice,  $V_{ub}$  is relatively small, and

$$V_{ud} \sim \cos \theta_C, \quad V_{us} \sim \sin \theta_C , \quad (2.34)$$

where  $\theta_C$  is the same Cabibbo angle that was first introduced to relate strangeness changing to strangeness preserving weak decays.

We are now ready to compute the parton model hadronic tensor for charged weak currents acting on the up quark, through the exchange of a  $W^-$  from an incoming antiquark (of any flavor). We find (compare Eq. (2.29))

$$(W_{\mu\nu}^{(W^- u)})_{Born} = \frac{1}{8\pi} \int \frac{d^3 p'}{(2\pi)^3 2\omega_{p'}} \text{Tr} [\gamma_\mu (1 - \gamma_5) (\not{p} + \not{q}) \gamma_\nu (1 - \gamma_5) \not{p}] \times (2\pi)^4 \delta^4(p' - p - q) , \quad (2.35)$$

where we have used Eq. (2.33), and have, as usual, neglected the masses of the outgoing quarks. The factors of  $|V_{uj}|^2$  have summed to unity in the inclusive cross section, while the overall factors  $c_W$  are absorbed into the normalization of the cross section as in Eq. (2.11).

Computing the  $F$ 's for individual quarks and antiquarks, and hence for hadrons, is now a straightforward matter of taking traces. We won't give the details here, only quote the results. The relation to parton distributions is simplified for some purposes in terms of the sums and differences of neutrino and antineutrino structure functions,

$$F_i^{(W^h)} = \frac{1}{2} (F_i^{(W^+ h)} \pm F_i^{(W^- h)}) . \quad (2.36)$$

We now introduce the notation  $U_h(x)$  for the parton distribution for quark  $U$  of charge  $2/3$  (up, charm, top) in hadron  $h$ , and  $D_h(x)$  for quark  $D$  of charge  $-1/3$  (down, strange, bottom). Also, it is convenient to define *valence*

distributions for the  $U$  and  $D$  quarks by

$$\begin{aligned} U_h^v(x) &= U_h(x) - \bar{U}_h(x) , \\ D_h^v(x) &= D_h(x) - \bar{D}_h(x) . \end{aligned} \quad (2.37)$$

The motivation underlying these definitions is that for every extra antiquark produced in a virtual state there is also an extra quark. The valence distributions are what is left when the influence of these “extra” quarks (usually called sea quarks) is removed. (However, note that sea quarks and antiquarks need not necessarily have the same distribution in  $x$ .)

In these terms, the parton model results for charged weak interactions are remarkably informative. First of all, we find that the relation characteristic of spin-one half partons still holds,

$$2x F_{1\pm}^{(Wh)} = F_{2\pm}^{(Wh)} . \quad (2.38)$$

The explicit results for the sums of structure functions are

$$\begin{aligned} F_{2+}^{(Wh)} &= x \sum_D [ D_h(x) + \bar{D}_h(x) ] + x \sum_U [ U_h(x) + \bar{U}_h(x) ] , \\ F_{3+}^{(Wh)} &= \sum_D D_h^v(x) + \sum_U U_h^v(x) , \end{aligned} \quad (2.39)$$

while for the differences we get

$$\begin{aligned} F_{2-}^{(Wh)} &= x \sum_D D_h^v(x) - x \sum_U U_h^v(x) , \\ F_{3-}^{(Wh)} &= \sum_D [ D_h(x) + \bar{D}_h(x) ] - \sum_U [ U_h(x) + \bar{U}_h(x) ] . \end{aligned} \quad (2.40)$$

If we measure all four of these distributions, for both  $p$  and  $n$ , and assume isospin invariance and an isospin-symmetric sea (i.e.,  $\bar{u}(x) = \bar{d}(x) = \bar{s}(x)$ , with  $c(x) = b(x) = t(x) = 0$ ), the full set of cross sections becomes over-determined, and the self-consistency of the parton model may be tested. The sole one of these assumptions that is dangerous in QCD is the assumption of isospin-symmetry of the sea quarks.

For completeness, let us give the same results as above, in terms of neutrino ( $W^+$ ) and antineutrino ( $W^-$ ) structure functions directly,

$$F_2^{(W^+h)} = 2x \left( \sum_D D_h(x) + \sum_U \bar{U}_h(x) \right), \quad (2.41)$$

$$F_2^{(W^-h)} = 2x \left( \sum_D \bar{D}_h(x) + \sum_U U_h(x) \right), \quad (2.42)$$

and

$$F_3^{(W^+h)} = 2 \left( \sum_D D_h(x) - \sum_U \bar{U}_h(x) \right), \quad (2.43)$$

$$F_3^{(W^-h)} = 2 \left( -\sum_D \bar{D}_h(x) + \sum_U U_h(x) \right). \quad (2.44)$$

## 2.3 $e^+e^-$ Annihilation

Another fundamental cross section is the annihilation of lepton pairs into hadrons,  $e^+e^- \rightarrow \text{hadrons}$ . There are three variations on this theme for which we can derive predictions in the parton model: the total cross section, single-hadron inclusive cross sections and jet cross sections.

### 2.3.1 Total cross section

The total cross section for  $e^+e^-$  annihilation into hadrons falls immediately into the parton model framework, because it is completely inclusive in the hadronic final state. At the same time, there are no hadrons in the initial state, so the parton-model cross section is given immediately in terms of the lowest-order electromagnetic elastic cross section for  $e^+e^- \rightarrow q\bar{q}$ . This cross section is given by the “annihilation” Feynman diagrams, shown in Fig. 2.5, in which the lepton pair annihilates into a virtual photon or  $Z$  vector boson, which subsequently decays into the quark pair. The fermion-vector vertices are given by (compare Eq. (2.15))  $eQ_i\gamma^\mu$  for the photon, with  $Q_i$  the fractional electric charge of fermion  $i$ , and for the  $Z$ ,

$$e\Gamma^\mu = \frac{e}{\sin\theta_W \cos\theta_W} \gamma^\mu (V_i - A_i \gamma_5). \quad (2.45)$$

Here  $A_i$  and  $V_i$  characterize the vector and axial vector couplings, and are given by

$$\begin{aligned} A_i &= t_3 - 2Q_i \sin^2 \theta_W , \\ V_i &= t_3 , \end{aligned} \quad (2.46)$$

with  $t_3$  the weak isospin of (the left-handed component) of fermion  $i$  ( $t_3 = +1/2$  for neutrinos and up quarks,  $-1/2$  for negatively charged leptons and down quarks).

At energies much less than the  $Z$  mass, only the virtual photon is important, and we easily derive the cross section from the electromagnetic vertex alone,

$$\sigma(s)_{tot} = \frac{4N_c\pi\alpha^2}{3s} \left( \sum_f Q_f^2 \right) , \quad (2.47)$$

where  $N_c$  is the number of colors,  $s$  is the squared center-of-mass energy,  $\alpha (= e^2/4\pi)$  is the usual electromagnetic fine structure constant, and the sum is over all quarks with masses small enough to be produced at  $s$ .  $Q_f$  is the fractional electric charge of flavor  $f$ . In computing Eq (2.47), we have neglected quark masses compared to  $\sqrt{s}$ . Note that, because  $\sigma_{tot}$  is directly proportional to  $N_c$ , its measurement is a direct observation of the number of colors,  $N_c = 3$ , jointly with the fractional charge content of each flavor.

At very high energies, like those available at SLC and LEP, the  $Z$  becomes important, and gives the full parton model annihilation cross section,

$$\sigma(s)_{tot} = \frac{4N_c\pi\alpha^2}{3s} \sum_f Q_f^2 \left( 1 - 2\chi V_f^2 + [V_f^2 + A_f^2]^2 \chi^2 \right) , \quad (2.48)$$

where the sum is over the final-state quarks and leptons and where

$$\chi = \left( \frac{s}{s - M_Z^2} \right) \left( \frac{1}{4 \cos \theta_W \sin \theta_W} \right) . \quad (2.49)$$

### 2.3.2 Single-hadron inclusive annihilation

A stronger use of parton model methods is found in *single-hadron inclusive* (1PI) cross sections, for instance  $e^+e^- \rightarrow h(p) + X$ , in which all events

with a hadron of momentum  $p$  are included. The corresponding amplitudes, illustrated in Fig. 2.6, are the “crossed” versions of deeply inelastic scattering amplitudes for the hadronic antiparticle  $\bar{h}$ . The latter process is found from 1PI annihilation by transferring  $h$  from final to initial state, where it is identified with  $\bar{h}$ , and the positron from initial to final state, where it is identified as an electron.

The kinematics for 1PI annihilation processes are developed in an analogous manner to deeply inelastic scattering. The basic scale is set by the total momentum,

$$\begin{aligned} q &= \ell_1 + \ell_2 \\ q^2 &= Q^2 > 0, \end{aligned} \quad (2.50)$$

with  $\ell_1$  the incoming electron momentum. Two natural dimensionless variables, defined in terms of invariants, measure the energy and direction (relative to the electron momentum) of the produced particle in the center of mass system,  $\mathbf{q} = 0$ ,

$$\begin{aligned} x &= \frac{2p \cdot q}{q^2}, \\ y &= \frac{p \cdot \ell_1}{p \cdot q} = \frac{1}{2}(1 - \cos \theta_{p\ell_1}). \end{aligned} \quad (2.51)$$

These variables are the analogues of, but not identical to, the  $x$  and  $y$  defined in Eqs. (2.6) and (2.8).

For simplicity, we will specialize to 1PI through a photon, as is appropriate for energies well below the  $Z$  mass. In this case we have, analogous to Eq. (2.10) for DIS,

$$d\sigma_{e^+e^-}^h = \left( \frac{1}{q^2} \right) L_{e\gamma}^{\mu\nu}(\ell_i) \bar{W}_{\mu\nu}^{(\gamma h)}(p, q) dx dy, \quad (2.52)$$

with  $L^{\mu\nu}$  a leptonic tensor, given at order  $e^2$ , and  $\bar{W}_{\mu\nu}$  the hadronic tensor (compare Eq. (2.16)), defined by

$$\bar{W}_{\mu\nu}^{(\gamma h)}(p, q) = \frac{1}{4\pi} \sum_{\sigma, X} \langle 0 | j_\mu^\gamma(0) | X, h(p, \sigma) \rangle \langle X, h(p, \sigma) | j_\nu^\gamma(0) | 0 \rangle$$

$$\begin{aligned}
& \times (2\pi)^4 \delta^4(p + q - p_X) \\
= & -x(g_{\mu\nu} - \frac{q_\mu q_\nu}{q^2}) \bar{F}_1^{(\gamma h)}(x, q^2) \\
& + (p_\mu - q_\mu \frac{p \cdot q}{q^2})(p_\nu - q_\nu \frac{p \cdot q}{q^2}) \frac{1}{m_h^2} \bar{F}_2^{(\gamma h)}(x, q^2). \quad (2.53)
\end{aligned}$$

The  $\bar{F}$ 's are 1PI structure functions, in terms of which the cross section is given by

$$\frac{d\sigma_{e^+e^-}^h(x, y, q^2)}{dxdy} = N_c \frac{4\pi\alpha^2}{3q^2} \left( \frac{3}{2} \bar{F}_1^{(\gamma h)} - 3y(1-y) \bar{F}_2^{(\gamma h)} \right). \quad (2.54)$$

The factor  $N_c$  is, as usual, the number of colors, included so that we do not have to sum explicitly over the colors of partons below. Note, as in Eq. (2.25), the explicit nature of the  $y$  (angular) dependence.

The application of the parton model to 1PI cross sections is very straightforward. From Eq. (2.2) we have

$$\frac{d\sigma_{e^+e^-}^h(x, y, q^2)}{dxdy} = \sum_f \int dx' dy \frac{d\sigma_{e^+e^-}^f(x', y, q^2)}{dx'dy} D_f^{(\gamma h)}(z) \delta(x' - x/z), \quad (2.55)$$

where the sum is over quark flavors  $f$  (not including antiquarks), since in the Born approximation only quark pairs, and not gluons, are produced in the annihilation process.  $D_f^{(\gamma h)}(z)$  is the fragmentation function for quark  $f$  into hadron  $h$ , with the latter carrying fraction  $z$  of the momentum of the former. It now requires a very straightforward calculation, involving a single fermion trace, to derive the 1PI structure functions in the parton model,

$$\bar{F}_i^{(\gamma h)}(x) = Q_i^2 D_{h/i}(x), \quad (2.56)$$

or, in terms of the cross section,

$$\frac{d\sigma_{e^+e^-}^h(x, y, q^2)}{dxdy} = N_c \frac{\pi\alpha^2}{q^2} \sum_f Q_f^2 \left( 1 + \cos^2 \theta_{\ell_1 p} \right) D_{h/f}(x), \quad (2.57)$$

where, as above, the angle is measured in the overall center-of-mass frame.

### 2.3.3 Jet Cross Sections

From Eq. (2.57), we see that in the parton model the angular dependence of hadrons in the final state directly follows that of the underlying quarks. The  $1 + \cos^2 \theta$  dependence is characteristic of spin-1/2 particles (scalar quarks would have given  $\sin^2 \theta$ , for instance). This feature ranks with the Callan-Gross relation and the normalization of the total annihilation cross section, as fundamental evidence for quarks.

There is even more to it than that, however. If we really take Eq. (2.57) seriously, we may conclude that each and every hadron appears in the final state in the same direction as the virtual quark whose fragmentation product it is. This would mean that in any given event, every hadron with a nonzero fraction of the total energy would move either in the direction of the virtual quark or of the virtual antiquark. In such a final state, all hadrons would appear as part of one of two *jets* of parallel-moving particles. Indeed, from this point of view, we can compute a *jet cross section*, which in the parton model is identical with the differential Born cross section for  $e^+e^-$  annihilation into quark pairs,

$$\frac{d\sigma_{e^+e^-}^{(jet)}(\cos \theta, q^2)}{dx dy} = 2N_c \frac{\pi \alpha^2}{q^2} \left( \sum_f Q_f^2 \right) (1 + \cos^2 \theta) , \quad (2.58)$$

where now  $\theta$  is the angle between either of the jets and the incoming electron in the overall center-of-mass frame. The factor of 2 relative to Eq. (2.57) comes from counting both jets equally. The integral of this cross section over  $\theta$  from zero to  $\pi$  is the total cross section, (2.48).

Notice that this conclusion is *not* forced upon us by the parton model arguments of Section 2.1. There we only claimed that the cross section for a single hadron is closely related to the underlying partonic direction. It is clear that the extension to jet cross sections is approximate at best. As we shall see, however, this approximation becomes better and better as the energy increases. In fact, we will be able to reinterpret the underlying Born cross section in any inclusive parton model cross section as a cross section for jets, emerging in the directions of, and with the energies of, the outgoing partons. In this, lowest-order approximation, the jets are “ideal”, and consist

of a set of exactly parallel-moving hadrons. In realistic cross sections it will be necessary to define what we mean by jets more carefully.

## 2.4 Drell-Yan Production

The production in hadronic collisions of a lepton pair with large invariant mass ( $e^+ e^-$ ,  $\mu^+ \mu^-$ ,  $\mu^+ \nu_\mu$ ,  $\mu^- \bar{\nu}_\mu$ , etc.) yields complementary information to that revealed in deeply inelastic collisions and electron-positron collisions.

Since the theoretical framework for the analysis of these processes was originally proposed by Drell and Yan [2.8], [2.9] these reactions are commonly referred to as hadronic Drell-Yan (DY) production.

The study of massive lepton pair production started with the Columbia-BNL experiment on proton-nucleus collisions [2.10]. Reviews of the early work can be found in [2.11]. Since the lepton pairs have no direct interactions with hadrons they are really the manifestation of the production of virtual gauge particles,  $\gamma$ ,  $W^\pm$ ,  $Z$ , which couple to lepton pairs through electromagnetic or weak interactions. As the virtual gauge bosons are timelike, any on-mass-shell vector meson resonances which couple to virtual photons, such as the  $J/\psi$  [2.12] and the  $\Upsilon$  [2.13], are produced. The intermediate bosons  $W^\pm$  and  $Z$  can also be produced as physical particles when the center of mass energy is large enough. In the case of the intermediate bosons, the DY cross sections are largest when the particles are actually produced on-mass-shell. Given their well-known branching ratios into leptonic channels, the detection of single leptons at large  $p_t$  is the characteristic signal for the production of  $W^\pm$  [2.14] and  $Z$  [2.15].

Let us consider first the basic electromagnetic reaction written as the production of a virtual photon followed by its decay into a lepton pair

$$\begin{aligned} A(p) + B(p') &\rightarrow \gamma^*(q) + X \\ &\rightarrow \ell(k) + \ell'(k') + X, \end{aligned} \tag{2.59}$$

where  $X$  labels all the undetected hadrons in the final state so that the process is inclusive. The notation is the same as in the previous sections. Since the virtual photon is timelike,  $q = k + k'$  satisfies  $q^2 = Q^2 > 0$ . One of

the easiest variables to measure experimentally is  $q^2$ , the invariant mass of the pair. It is convenient to introduce the DY scaling variable

$$\tau = q^2/s, \quad (2.60)$$

where the total center of mass energy of the hadronic collision is determined from  $s = (p + p')^2$ .

The parton-model interpretation of the DY process is that in the hadronic collision two partons, say a quark-antiquark pair, annihilate to produce the virtual photon. In this case we write the hadronic DY cross section as a product of the partonic DY cross section for the reaction  $q(\xi p) + \bar{q}(\xi' p') \rightarrow \ell(k) + \ell'(k')$ , times two parton distribution functions

$$\frac{d\sigma_{AB}^{(PM)}(p, p', q)}{dq^2} = \sum_f \int_0^1 d\xi d\xi' \phi_{f/A}(\xi) \frac{d\sigma_{AB}^{(\text{Born})}(\xi p, \xi' p', q)}{dq^2} \phi_{\bar{f}/B}(\xi'). \quad (2.61)$$

The distributions  $\phi(\xi)$  and  $\phi(\xi')$  are assumed to be the same “universal” functions as measured in deeply inelastic scattering. The hard scattering is the Born approximation for quark-antiquark annihilation into a virtual photon, averaged over the color degrees of freedom of the initial quark and antiquark. The resulting differential cross section is

$$\frac{d\sigma_{ff}^{(\gamma)}(\xi p, \xi' p', q)}{dq^2} = Q_f^2 \frac{4\pi\alpha^2}{3N_c q^2} \delta(q^2 - (\xi p + \xi' p')^2). \quad (2.62)$$

Substituting this result and the definition of  $\tau$  into Eq. (2.61) we find for the photon

$$\frac{d\sigma_{AB}^{(\gamma)}(p, p', q)}{dq^2} = \frac{4\pi\alpha^2}{3N_c q^2 s} \sum_f Q_f^2 \int_0^1 d\xi d\xi' \phi_{f/A}(\xi) \delta(\tau - \xi\xi') \phi_{\bar{f}/B}(\xi'). \quad (2.63)$$

The general inclusive DY cross section is of the form,

$$\frac{d\sigma_{AB}^{(V)}}{dq^2} = \sigma_0^V(q^2) W_{AB}^V(\tau), \quad (2.64)$$

with  $V = \gamma, W^\pm, Z$ . The factor  $\sigma_0^V$  contains the overall dimensions, while the dimensionless function  $W_{AB}^V$  is defined as the integral over the appropriate

product of distribution functions times couplings (in units of  $e$ ), which we denote by  $PD_{AB}^V$ ,

$$W_{AB}^V(\tau) = \int_0^1 d\xi \int_0^1 d\xi' \delta(\tau - \xi\xi') PD_{AB}^V(\xi, \xi') . \quad (2.65)$$

In the electromagnetic case we have

$$\sigma_0^\gamma = \frac{4\pi\alpha^2}{3N_c q^2 s} , \quad (2.66)$$

while  $W_{AB}^\gamma$  is computed with

$$PD_{AB}^\gamma(\xi, \xi') = \sum_q Q_q^2 \{ \phi_{q/A}(\xi) \phi_{\bar{q}/B}(\xi') + \phi_{\bar{q}/A}(\xi) \phi_{q/B}(\xi') \} . \quad (2.67)$$

For intermediate boson production, we only have to change  $\sigma_0^V$  and  $PD_{AB}^V$ . In the case of Z, we have

$$\sigma_0^Z = \tau \frac{\pi\alpha^2}{192N_c \sin^4 \theta_W \cos^4 \theta_W} \frac{1 + [1 - 4 \sin^2 \theta_W]^2}{(q^2 - M_Z^2)^2 + M_Z^2 \Gamma_Z^2} \quad (2.68)$$

for the reaction  $q\bar{q} \rightarrow e^+e^-$ , where  $\Gamma_Z$  is the total width of the Z boson,

$$\Gamma_Z = \frac{\alpha M_Z}{24 \sin^2 \theta_W \cos^2 \theta_W} [1 - 4 \sin^2 \theta_W + 8 \sin^4 \theta_W] . \quad (2.69)$$

The relevant product of distributions is

$$PD_{AB}^Z(\xi, \xi') = \sum_q C_q \{ \phi_{q/A}(\xi) \phi_{\bar{q}/B}(\xi') + \phi_{\bar{q}/A}(\xi) \phi_{q/B}(\xi') \} \quad (2.70)$$

for production in the  $q\bar{q}$  channel, where  $C_q = 1 + \{1 - 4|Q_q| \sin^2 \theta_W\}^2$ .

The total Z production rate is found by integrating over  $q^2$ , in the “narrow width approximation”  $\Gamma_Z \ll M_Z$ ,

$$\sigma_{tot}^{(Z)} = \frac{\pi^2 \alpha_S}{12 \sin^2 \theta_W \cos^2 \theta_W} \frac{1}{s} W_Z(\tau = \frac{M_Z^2}{s}, q^2 = M_Z^2) . \quad (2.71)$$

The corresponding results for  $V = W^-$  are

$$\sigma_W = \tau \frac{\pi\alpha^2}{12N_c \sin^4 \theta_W} \frac{1}{(q^2 - M_W^2)^2 + M_W^2 \Gamma_W^2} , \quad (2.72)$$

$$\begin{aligned}
PD_{AB}^W(\xi, \xi') = & \cos^2 \theta_C \{ \bar{u}_A(\xi) d_B(\xi') + \bar{c}_A(\xi) s_B(\xi') \} , \\
& + \sin^2 \theta_C \{ \bar{u}_A(\xi) s_B(\xi') + \bar{c}_A(\xi) d_B(\xi') \} \\
& +(A \leftrightarrow B),
\end{aligned} \tag{2.73}$$

$$\Gamma_W = \frac{\alpha M_W}{12 \sin^2 \theta_W}, \tag{2.74}$$

where  $\bar{u}_A \equiv \phi_{\bar{u}/A}$ , etc. As usual,  $\theta_W$  and  $\theta_C$  are the weak mixing and Cabibbo mixing angles respectively. Then the total  $W^-$  production rate is

$$\sigma_{tot}^{(W)} = \frac{\pi^2 \alpha_s}{3 \sin^2 \theta_W \cos^2 \theta_W} \frac{1}{s} W_Z(\tau = \frac{M_W^2}{s}, q^2 = M_W^2). \tag{2.75}$$

## 2.5 $O(\alpha \alpha_s)$ Processes

The next level in complexity for parton model cross sections are those for which the partonic scattering involves the inelastic emission or absorption of a photon. The Born cross section will then be of order  $\alpha \alpha_s$ , instead of  $\alpha^2$ , as above. These processes are photoproduction and direct photon production processes, respectively [2.16].

Once again, the cross section at the hadron level is given in terms of a convolution of parton distribution functions, the hard scattering parton-level subprocess cross sections, and the appropriate fragmentation functions. The inclusive invariant cross section of the type  $A + B \rightarrow C + X$  is given by

$$\begin{aligned}
E_C \frac{d^3 \sigma}{dp_C^3}(AB \rightarrow C + X) = & \sum_{abcd} \int dx_a dx_b dz_c \phi_{a/A}(x_a) \phi_{b/B}(x_b) \\
& \times \frac{\hat{s}}{z_c^2 \pi} \frac{d\sigma}{dt} (ab \rightarrow cd) D_{C/c}(z_c) \delta(\hat{s} + \hat{t} + \hat{u}),
\end{aligned} \tag{2.76}$$

where in our case  $a \dots d$  label partons and/or the photon. Hatted variables,  $(\hat{s})$  etc., refer to invariants of the partonic subprocess. As is conventional, we have explicitly exhibited the  $\delta$  function in partonic cross section appearing in Eq. (2.76), associated with the phase space for the two-body scattering of

massless particles. The other kinematic factor,  $(\hat{s}/z_c^2\pi)$ , is associated with the difference between the hadronic differential  $E_C d/dp_C^3$ , and the partonic differential  $(d/d\hat{t})$ .

Now consider the process of direct photon production in hadron-hadron collisions. The term “direct photon” refers to those photons which are produced in the hard-scattering subprocess and are not decay products of some particle. There are two two-body subprocesses which can produce direct photons: the QCD Compton subprocess  $gq \rightarrow \gamma q$  and the annihilation subprocess  $q\bar{q} \rightarrow \gamma g$ . The cross sections for these are

$$\frac{d\sigma}{d\hat{t}}(gq \rightarrow \gamma q) = -\frac{\pi\alpha\alpha_s}{\hat{s}^2} \frac{e_q^2}{3} \left( \frac{\hat{u}}{\hat{s}} + \frac{\hat{s}}{\hat{u}} \right), \quad (2.77)$$

and

$$\frac{d\sigma}{d\hat{t}}(q\bar{q} \rightarrow \gamma g) = \frac{\pi\alpha\alpha_s}{\hat{s}^2} \frac{8}{9} e_q^2 \left( \frac{\hat{u}}{\hat{t}} + \frac{\hat{t}}{\hat{u}} \right), \quad (2.78)$$

where  $e_q$  is the fractional electric charge of the quark  $q$ . Note that the running coupling,  $\alpha_s$ , is a function of the renormalization scale  $\mu$ . For transverse momenta of the order of  $\sqrt{\hat{s}}$ , these two subprocesses provide the dominant contribution to direct photon production. In other kinematic regions, it may be necessary to incorporate bremsstrahlung effects, which are QED corrections to purely hadronic two-body scattering. We shall discuss this issue in a later section. Here, we only note that we must also construct fragmentation functions of photons in partons, like  $D_{\gamma/q}(z)$ .

The case of photoproduction is quite similar, since at the parton level one is just the time reversed version of the other. Accordingly, the subprocess expressions differ only by color factors associated with the interchange of the initial and final states. The two basic subprocesses are QCD Compton scattering and photon-gluon fusion, the cross sections for which are given by

$$\frac{d\sigma}{d\hat{t}}(\gamma q \rightarrow gq) = -\frac{\pi\alpha\alpha_s}{\hat{s}^2} \frac{8e_q^2}{3} \left( \frac{\hat{u}}{\hat{s}} + \frac{\hat{s}}{\hat{u}} \right), \quad (2.79)$$

and

$$\frac{d\sigma}{d\hat{t}}(\gamma g \rightarrow q\bar{q}) = \frac{\pi\alpha\alpha_s}{\hat{s}^2} e_q^2 \left( \frac{\hat{u}}{\hat{t}} + \frac{\hat{t}}{\hat{u}} \right). \quad (2.80)$$

These subprocess expressions may be used in Eq.(2.76) without fragmentation functions, in which case one obtains the cross section for jet production. On the other hand, inserting the appropriate hadronic fragmentation function enables one to calculate the cross section for the photoproduction of that type of hadron.

## 2.6 The Parton Model and Experiment

Historically, the parton model, or more traditionally, the Quark-Parton Model (QPM), was motivated by high energy experimental results of the late 1960's, especially the famous deep inelastic scattering experiment at SLAC [2.17][2.18]. The subsequent success of this picture in providing a unified description of a wide variety of high energy processes gave strong impetus to the search for a theoretical foundation for its validity, resulting in the discovery of asymptotic freedom and the formulation of perturbative QCD as the basic framework for describing all high energy physics processes. In this section, we summarize the main features of the QPM which have been successfully compared with experiments. It is useful to keep in mind that the significance of QPM stems not from any specific triumph, but from the coherent framework it provides to correlate a wide range of processes. To review, in the QPM large classes of (physically measurable) high energy cross-sections are related to the corresponding (theoretically calculable) partonic cross-sections through a set of universal parton distribution functions.

### 2.6.1 Deep Inelastic Scattering

There are a number of reviews of DIS experiments and comparisons of the measured structure functions  $F_i^\ell(x, Q^2)$  (where  $\ell = \mu(e), \nu, \bar{\nu}$  and  $i = 1, 2, 3$  (or  $L$ , for *longitudinal*)) with the QPM and QCD [2.19]. We shall only describe briefly the main features of this rather extensive area of experimental and phenomenological work. The expressions for  $F_i^\ell(x, Q^2)$  in terms of the universal parton distribution functions  $\phi_{a/A}(x, Q^2)$ , where  $(a, A)$  label the parton and hadron (mostly nucleon) respectively, are given in many textbooks [2.20], review articles [2.21] and in Section 2.2.3 above.

**Scaling:** The most striking feature of the first SLAC DIS data [2.17][2.18] was *scaling*: the approximate independence of the measured structure functions  $F_i(x, Q^2)$  of  $Q^2$  – an indication of scattering from point-like constituents analogous to the classic Rutherford experiment on atomic structure. The basic idea of the QPM originated from this observed fact, which has since been corroborated by similar observations in *all* high energy *hard* processes.

**Quarks as Partons:** The identification of the “partons” with the previously known quarks (from hadron spectroscopy, which concerns physics at an altogether different energy scale) was cemented by a series of seminal experiments and phenomenological analyses: (i) the near vanishing of the longitudinal structure function in  $eN$  scattering suggested that the spin of the parton is  $1/2$  – the Callan-Gross relation (Eq. (2.31)); (ii) the measured value of the ratio of total cross-sections for neutrino to antineutrino scattering on isoscalar nuclei (i.e., nuclei with equal numbers of protons and neutrons, and hence of  $u$  and  $d$  quarks) is about 3. This result can be derived by integrating the differential cross sections Eq. (2.25), using the QPM expressions Eq. (2.42) and Eq. (2.44) for the structure functions with all antiquark distributions set to zero. (The corresponding cross section ratio for scattering of neutrinos and antineutrinos from atomic electrons is also about 3 [2.22]). This striking fact strongly suggests that the nucleon consists primarily of spin  $1/2$  partons, rather than anti-partons, which couple to the intermediate vector bosons the same way as the leptons; (iii) the subsequent detailed measurements of the differential cross-section  $d^2\sigma/dxdy$ , Eq. (2.25), and hence of the full structure functions  $F_i^{(th)}(x, Q^2)$ , have consistently confirmed this interpretation and yielded a wealth of information on the distribution of these partons inside the nucleon.

**The charge ratio:** The structure function  $F_2^\ell(x, Q^2)$  measured in neutral-current (virtual)  $\gamma$  exchange processes ( $\ell = e, \mu$ ) and in charged current  $W^\pm$  exchange processes ( $\ell = \nu, \bar{\nu}$ ) are in principle different. In the QPM, they are related to the same set of parton distribution functions – in fact, as a simple sum of the latter, each multiplied by an appropriate coupling

constant (the squared charge for  $\gamma^*$  and an appropriate weak isospin matrix element for  $W^\pm$  exchange). After summing over parton flavors, one expects  $F_2^{(eA)}(x, Q^2)/F_2^{(\nu A + \bar{\nu} A)}(x, Q^2) = 5/18$  for scattering off an iso-scalar target,  $A$ . This “charge ratio”, valid for all  $(x, Q^2)$  where QPM applies, has been verified to a great degree of accuracy in the very high statistics DIS experiments, for example BCDMS and CCFR after appropriate small corrections [2.23].

**Quark number sum rules:** The “valence quark” distributions of the proton satisfy the obvious quark number sum rules:

$$N_u = \int_0^1 dx (u(x) - \bar{u}(x)) = 2; \quad N_d = \int_0^1 dx (d(x) - \bar{d}(x)) = 1$$

In the QPM, linear combinations of these integrals are related to various integrals of measurable structure functions, e.g.

$$\int_0^1 \frac{dx}{2x} [F_2^{\nu n} - F_2^{\nu p}] = N_u - N_d = 1 \quad (\text{Adler Sum Rule})$$

$$\int_0^1 \frac{dx}{2x} [xF_3^{\nu n} - xF_3^{\nu p}] = N_u + N_d = 3 \quad (\text{Gross - Llewellyn Smith Sum Rule})$$

These sum rules have been extensively checked by all relevant deep inelastic scattering experiments. Within the experimental accuracy (and, by now, known QCD corrections to the latter), they are verified – the measured integral for the Adler sum rule is [2.24]  $1.01 \pm 0.20$ ; and for the GLS sum rule it is [2.23]  $2.50 \pm 0.08$ . (There is an expected QCD correction to the naive QPM value for the GLS sum rule of approximately  $-0.34$ .)

### 2.6.2 Electron-positron Annihilation into Hadrons

**Total cross-section and scaling** The total cross-section for hadron final states in  $e^+e^-$  annihilation normalized to the point-like cross-section for  $e^+e^- \rightarrow \mu^+\mu^-$  behaves roughly as step-functions in the center-of-mass energy, [2.25] staying constant (see Eq. (2.47)) over certain ranges (now known to correspond to regions between heavy quark flavor thresholds). This is the analogue of scaling behavior for DIS, and suggests that the underlying interaction mechanism is  $e^+e^- \rightarrow$  parton–anti-parton pair. The absolute value of

this ratio is proportional to the sum of the squared charges of the partons. The overall constant is 1 for spin 1/2 partons and 1/4 for spin 0 partons. The measured values agree well with the assumption that partons are quarks with the usual assigned charges.

**Two-jet final states as evidence for underlying partons** The most direct evidence for the existence of partons perhaps come from the clear emergence of jet-like hadronic final states in experiments done at the PETRA and PEP  $e^+e^-$  colliders [2.25]. The dominance of these events gave the first visual evidence for the underlying parton-anti-parton pair final state previously inferred indirectly from the total cross-section measurements and from DIS.

**Angular distribution and spin of the parton** If we assume that the underlying parton picture, the angular distribution of the two-jet final states gives direct evidence on the angular distribution of the created parton pair, which is sensitive to the spin of the parton and its coupling to the virtual photon. The measured distribution agrees very well with the canonical  $(1 + \cos^2\theta)$  distribution for spin 1/2 partons, Eq. (2.58) and Ref. [2.25].

### 2.6.3 Lepton-pair Production (Drell-Yan Process)

The most convincing evidence that the QPM provides the correct framework for high energy processes in general came (historically) from its success in accounting for features of the measured lepton-pair production ( $A + B \rightarrow \ell^+\ell^- + X$ ) cross-sections, using the same simple parton picture and the same parton distributions determined from deep inelastic scattering.

In the QPM, lepton-pair production proceeds through the basic quark-anti-quark annihilation  $q\bar{q} \rightarrow \ell^+\ell^-$ , the Drell-Yan process. The QPM cross-section at fixed center-of-mass pair rapidity,  $y = (1/2)\ln(x_1/x_2)$ , is given by

$$Q^4 \frac{d\sigma}{dy dQ^2} = \left[ \frac{4\pi\alpha^2}{9} x_1 x_2 \right] \sum_q e_q^2 (\phi_{q/A}(x_1) \phi_{\bar{q}/B}(x_2) + \phi_{\bar{q}/A}(x_1) \phi_{q/B}(x_2)),$$

where  $x_{1,2} = (Q/\sqrt{s})e^{\pm y}$  are scaling variables. The main features of this formula are:

**Scaling:** The fact that the right-hand side is independent of any energy scale (say,  $Q$ ) – i.e. the dimensionless cross-section satisfies *scaling* – is again evidence for the underlying point-like interaction [2.26][2.27]. This feature allows one to predict the cross-section at higher energies from low energy measurements. We must re-emphasize that scaling is exactly true in the QPM, and that it is somewhat violated in QCD.

**Color factor:** The overall factor in this formula contains a “color factor” 3 in the denominator which played an important role in determining *Quantum Chromodynamics* to be the underlying fundamental theory for strong interactions when parton distribution functions measured in deep inelastic scattering experiments were used in the above formula to test against lepton-pair cross-sections. To get quantitative agreement with experiment, the higher order corrections in  $\alpha_s(Q)$  predicted by QCD are essential.

**Cross-section ratios:** The above QPM formula for lepton-pair production leads to many simple predictions on cross-section ratios which agree well with experiment and were instrumental in establishing the credibility of the QPM during its infancy. For instance:

$$\frac{\sigma(\pi^+ N \rightarrow \mu^+ \mu^-)}{\sigma(\pi^- N \rightarrow \mu^+ \mu^-)} \rightarrow \left(\frac{e_d}{e_u}\right)^2 = \frac{1}{4} \text{ as } \tau \rightarrow 1,$$

where  $N$  denotes an “isoscalar” target. This is indeed found to be true. This is the region where the “valence quark” is presumed to dominate. In contrast the ratio rises toward 1 for  $\tau \rightarrow 0$ , where  $\pi^\pm$  contain equal amounts of  $\bar{u}$  and  $\bar{d}$  quarks [2.28].

**Angular distribution of the leptons:** Since the underlying fundamental process for lepton-pair production,  $q\bar{q} \rightarrow \ell^+\ell^-$ , is very similar to  $e^+e^- \rightarrow$

$\mu^+ \mu^-$ , the angular distribution of the outgoing leptons in their center-of-mass frame is expected to be  $\sim (1 + \cos^2 \theta)$  – just like for the latter – if the QPM is correct. Experiments amply confirm this fact [2.26], [2.27], [2.28].

#### 2.6.4 Other Hard Processes

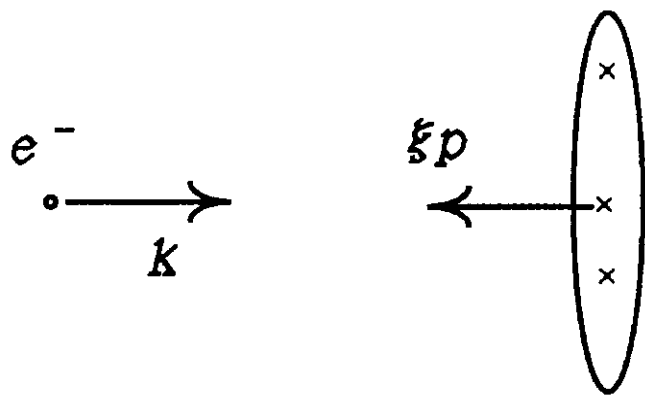
The basic features of QPM are also observed in other high energy “hard processes”, e.g. production of high transverse momentum direct photons and production of high transverse momentum jets. Although the three processes described in previous sections played a more crucial role in establishing the QPM picture historically, all the hard processes are highly relevant in current studies of the QCD-improved parton model, which provides the foundation for the quantitative formulation of high energy processes in the Standard Model and beyond.

## References

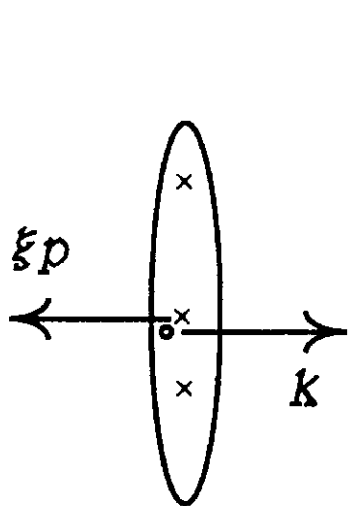
- [2.1] E.D. Bloom *et al.*, Phys.Rev.Lett. **23**, 930 (1969); M. Breidenbach *et al.*, Phys.Rev.Lett. **23**, 935 (1969); J.I. Friedman and H.W. Kendall, Ann. Rev. Nucl. Sci. **22**, 203 (1972); For recent references consult: Proceedings of the Workshop on “Hadron Structure Functions and Parton Distributions”, Fermilab 1990; eds. D.F. Geesaman, J. Morfin, C. Sazama and W-K. Tung, World Scientific (1991).
- [2.2] J. Ashman *et al.*, Phys.Lett. **B206**, 364 (1988); Nucl. Phys. **B328**, 1 (1989); M.J. Alguard *et al.*, Phys. Rev. Lett. **37**, 1261 (1978); **41**, 70 (1978); G. Baum *et al.*, Phys.Rev.Lett. **51**, 1135 (1983).
- [2.3] A.V. Efremov and O.V. Teryaev, JINR Dubna preprint E2-88-287 (1988); G. Altarelli and G.G. Ross, Phys. Lett. **B212**, 391 (1988); R.D. Carlitz, J.C. Collins and A.H. Mueller, Phys. Lett. **B214**, 229 (1988); G.T. Bodwin and J. Qiu, Phys. Rev. **D41**, 2755 (1990); R.L. Jaffe and A. Manohar, Nucl. Phys. **B337**, 509 (1990); M. Glück and E. Reya, Phys. Lett. **B270**, 65 (1991).

- [2.4] Review of Particle Properties, Phys. Rev. **D45**, S1 (1992); and Erratum.
- [2.5] *Field Theory in Particle Physics* by B. de Wit and J. Smith, Elsevier Science Publishers, Amsterdam 1986.
- [2.6] J.D. Bjorken, Phys. Rev. **179**, 1547 (1969).
- [2.7] C.G. Callan and D.G. Gross, Phys. Rev. Lett. **22**, 156 (1969).
- [2.8] S.D. Drell, D.J. Levy and T.M. Yan, Phys. Rev. Lett. **22**, 744 (1969); Phys. Rev. **187**, 2159 (1969); Phys. Rev. **D1**, 1035 (1970); T.M. Yan and S.D. Drell, Phys. Rev. **D1**, 2402 (1970).
- [2.9] S.D. Drell and T.M. Yan, Phys. Rev. Lett. **25**, 316 (1970); Ann. Phys. **66**, 578 (1971).
- [2.10] J.H. Christenson, G.S. Hicks, L.M. Lederman, P.J. Limon, B.G. Pope and E. Zavattini, Phys. Rev. Lett. **25**, 1523 (1970); Phys. Rev. **D8**, 2016 (1973).
- [2.11] L.M. Lederman, Phys. Rep. **C26**, 149 (1976); N.S. Craigie, Phys. Rep. **C47**, 1 (1978); R. Stroynowski, Phys. Rep. **C71**, 1 (1981).
- [2.12] J.J. Aubert et al, Phys. Rev. Lett. **33**, 1404 (1974).
- [2.13] S.W. Herb et al, Phys. Rev. Lett. **39**, 252 (1977); W.R. Innes et al., Phys. Rev. Lett. **39**, 1240 (1977).
- [2.14] UA1 collaboration: G. Arnison et al., Phys. Lett. **B122**, 103 (1983);  
UA2 collaboration: M. Banner et al., Phys. Lett. **B122**, 476 (1983);  
P.Bagnia et al., Phys. Lett. **B129**, 130 (1983).
- [2.15] UA1 collaboration: C. Albajar et al., Phys. Lett. **B198**, 271 (1987);  
UA2 collaboration: R. Ansari et al., Phys. Lett. **B194**, 158 (1987).
- [2.16] J.F. Owens, Rev. Mod. Phys. **59**, 465 (1987).

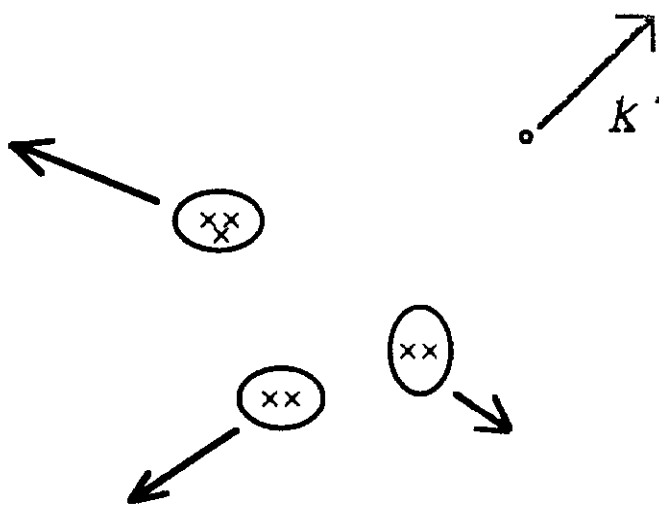
- [2.17] W.K.H. Panofsky, in *International Conf on High Energy Physics*, Vienna, ed. J. Prentki and J. Steinberger (CERN, Geneva); Bloom *et al.*, Phys. Rev. Lett. **23**, 930 (1969); M. Breidenbach *et al.*, Phys. Rev. Lett. **23**, 935 (1969).
- [2.18] R.P. Feynman, Phys. Rev. Lett., **23**, 1415 (1969); *Photon-Hadron Interactions*, W.A. Benjamin, New York (1972).
- [2.19] For instance, F. Sciulli in Proceedings of *Workshop on Hadron Structure Functions and Parton Distributions*, Fermilab, Ed. Geesaman *et al.*, World Scientific, 1990; S. Mishra and F. Sciulli, Annu. Rev. Nucl. Part. Sci. **39**, 259 (1989).
- [2.20] For instance, *The Structure of the Proton*, by R.G. Roberts, Cambridge Univ. Press, 1990.
- [2.21] For instance, Wu-Ki Tung *et al.*, in *High Energy Physics in the 1990's (Snowmass 88)*, Ed. S. Jenson, World Sci. Pub. (1989).
- [2.22] Gargamelle Collaboration, T. Eichten *et al.*, Phys. Lett. **B46**, 281 (1973).
- [2.23] S. Mishra, SLAC Summer School lecture, 1991.
- [2.24] D. Allasia *et al.*, Phys. Lett. **B135**, 231 (1985); Z. Phys. **C28**, 321 (1985).
- [2.25] For a comprehensive review, see S.L. Wu, Phys. Rep. **C107**, 59 (1984).
- [2.26] L. Lederman, *Proc. XIX Int. Conf. on High Energy Physics*, Tokyo, 1978; R. Stroynowski, Phys. Rep. **C71**, 1 (1981).
- [2.27] For a recent high-statistics experiment, see C.N. Brown *et al.*, Phys. Rev. Lett. **63**, 2637 (1989).
- [2.28] J. Pilcher, *Proc. 1979 Int. Symp. on Lepton and Photon Interactions at High Energies*, Fermilab, (1979).



(a)



(b)



(c)

Figure 2.1. Schematic parton model picture for DIS.

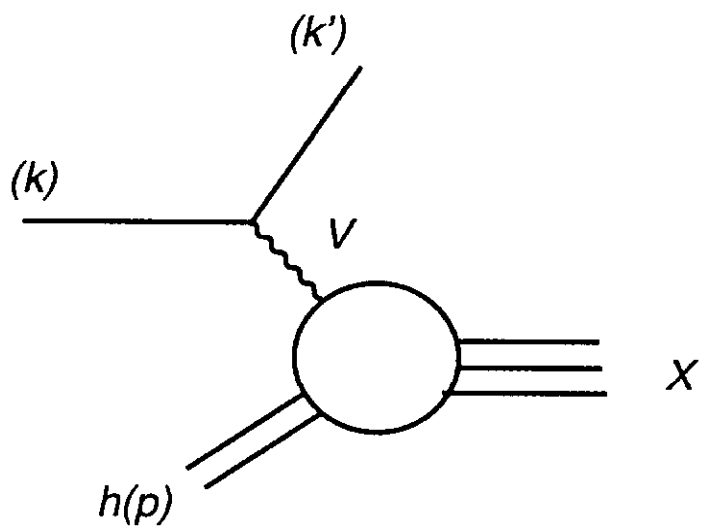


Figure 2.2. Deeply Inelastic Scattering

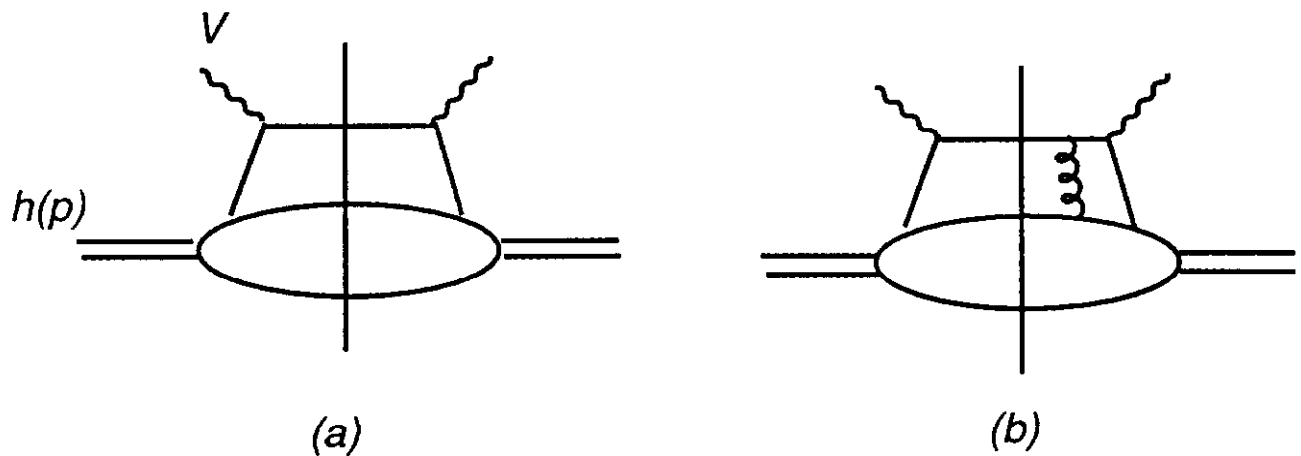


Figure 2.3. (a) Parton model scattering. (b) Interference graph.

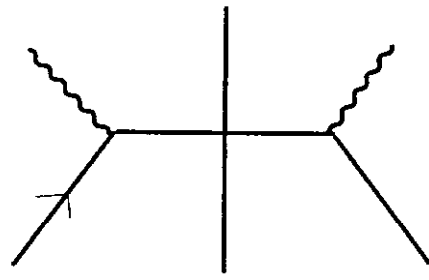


Figure 2.4. Born diagram.

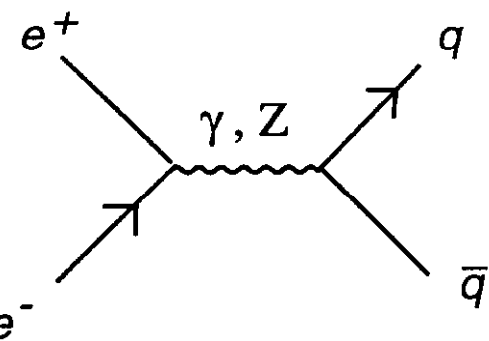


Figure 2.5. Born diagrams for  $e^+e^-$  annihilation.

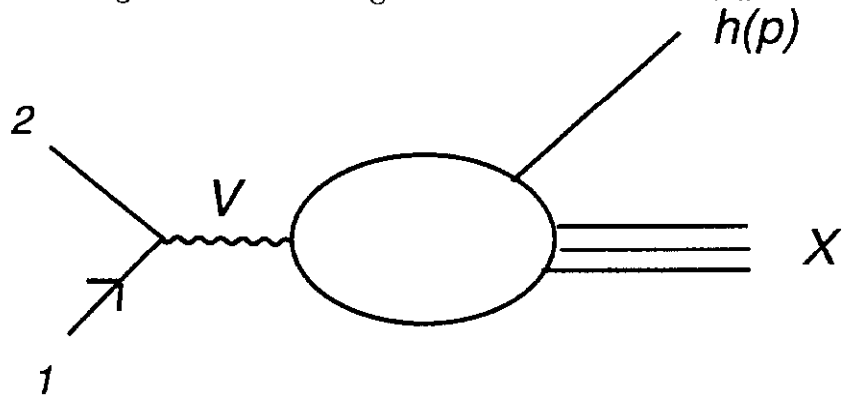


Figure 2.6. Inclusive single hadron production in  $e^+e^-$  annihilation.

## 3 Perturbative QCD: Fundamental Theorems

The first goal of perturbative QCD is to find a justification of the parton model in field theory, and to identify systematic procedures for improving upon parton model predictions. This program is conveniently summarized in terms of a series of fundamental theorems, which we describe below. We will motivate each of these basic results from the parton model cross sections of the previous section. It should be kept in mind, however, that the methods developed below allow us to address a wider range of problems than can be systematically treated in the parton model, and, although perturbative QCD is in some sense a descendent of the parton model, it has a life of its own. Moreover, many of the results of perturbative QCD have been derived from the fundamental Langrangian of QCD. Thus they must be regarded as real predictions of the theory, and not just as a model.

### 3.1 Infrared Safety in $e^+e^-$ Annihilation

The first set of theorems that we will discuss apply to  $e^+e^-$  annihilation. Here the results are simplified by the lack of hadrons in the initial state. We shall treat the perturbative QCD generalizations of parton model expressions for the total and jet cross sections.

#### 3.1.1 Total Cross Section

The simplest of the parton model cross sections is the total cross section for  $e^+e^-$  annihilation into hadrons, Eq. (2.47). In this case, no phenomenologically determined parton distribution or fragmentation functions are necessary. Instead we have an absolute prediction which is in quite good agreement with experiment. Yet, Eq. (2.47) is the Born cross section for the production of a quark pair, not of physical hadrons, and it is hadrons that we observe in experiment, not free quarks. The success of this prediction is understandable because the total cross section is *infrared safe* in the sense described in Section 1.6 above. Recall that an infrared safe quantity becomes independent of the masses of light partons (gluons and light quarks)

in the high-energy limit, and is dominated by highly off-shell virtual states in perturbation theory. In configuration space, an infrared safe quantity is correspondingly dependent only on the short-distance behavior of QCD, not on the long-distance dynamics that produce confinement and the details of the hadronic spectrum. Such a quantity possesses a perturbative expansion in the running coupling that is free of logarithms or other sensitive functions which depend on large ratios, such as  $Q/m$ , with  $m$  a parton mass and  $Q$  the overall momentum scale.

Thus, our first theorem of perturbative QCD is that the total  $e^+e^-$  annihilation cross section is infrared safe,

$$\sigma_{tot}(Q^2, \mu^2, m^2/\mu^2, \alpha_s(\mu)) = \frac{1}{Q^2} \Pi(Q^2/\mu^2, 0, \alpha_s(\mu)) \left\{ 1 + O(m^2/Q^2) \right\}, \quad (3.1)$$

where  $m$  labels the fixed mass scales in the theory,  $\mu$  is the renormalization scale (Section 1.3.2), and where we have factored out an overall factor  $Q^{-2}$ , leaving behind dependence on dimensionless variables in the function  $\Pi$ . An important result is that, because of its IR safety, the total cross section may be computed in *massless* QCD, up to corrections that vanish as a power of the energy as far as the light quarks are concerned.

Now  $\sigma_{tot}$  is a physical quantity, and is consequently independent of the renormalization scale  $\mu$ . In particular, we have

$$\Pi(Q^2/\mu^2, \alpha_s(\mu^2)) = \Pi(1, \alpha_s(Q^2)), \quad (3.2)$$

where we have suppressed the mass argument, since we are working in massless perturbation theory. Technically speaking, the cross section satisfies the renormalization group equation,

$$\left( \mu \frac{\partial}{\partial \mu} + \beta(g) \frac{\partial}{\partial g} \right) \Pi(Q^2/\mu^2, \alpha_s(\mu)) = 0, \quad (3.3)$$

but the content of this equation is the same as Eq. (3.2).

When the perturbative total cross section is exhibited, it is usually the right-hand side of Eq. (3.2) that is given as a power series in  $\alpha_s(Q)$ , in which

the coefficients are pure numbers, since all energy dependence is absorbed into the running coupling,

$$\Pi(1, \alpha_s(Q^2)) = N_c \frac{4\pi\alpha^2}{9} \left( \sum_f Q_f^2 \right) \sum_{n=0}^{\infty} s_n \alpha_s^n(Q). \quad (3.4)$$

Here we have factored out the parton model result, Eq. (2.47), so that the first term in the series is

$$s_0 = 1. \quad (3.5)$$

We will discuss the calculation of higher terms in Section 4 below.

For large  $Q$  the running coupling, Eq. (1.48),

$$\frac{\alpha_s(Q)}{4\pi} = \frac{1}{\beta_1 \ln(Q^2/\Lambda^2)} - \frac{\beta_2 \ln \ln(Q^2/\Lambda^2)}{\beta_1^3 \ln^2(Q^2/\Lambda^2)} + O\left(\frac{1}{\ln^3 Q^2/\Lambda^2}\right), \quad (3.6)$$

falls off, and remaining terms in the series are small corrections. Here is the reason that the parton model result works so well.

The formal proof of the infrared safety of  $\Pi(Q^2/\mu^2)$  follows from the famous theorem of Kinoshita and Lee and Nauenberg [3.1], that fully inclusive transition probabilities are finite in the zero-mass limit. Actually, the arguments of Ref. [3.1] require one to sum over all degenerate initial as well as final states, but in this case, because there are no hadrons in the initial state, a simple sum over final states will do. The extension of these results to QCD was discussed in [3.2].

The relevant physical observation that justifies infrared safety is that the creation of a quark pair is a short-distance phenomenon, and is not expected to interfere quantum mechanically with the long-distance processes that produce hadrons from quarks. Consequently, the cross section can be thought of as a product of probabilities, one for quark pair creation (Born diagram plus calculable corrections), the other for the evolution of quarks to hadrons. In the fully inclusive cross section, we sum over all final states. Then, because of the absence of interference between short- and long-distance effects, the probabilities for hadrons to be produced from quarks sum to unity, since, without further electroweak corrections, off-shell quarks *always* produce on-shell hadrons. This will happen in perturbation theory (where

the role of hadrons is played by on-shell quarks and gluons), as well as in the real world (where hadrons are the physically observed particles). Thus, any infrared sensitivity which may be present in perturbation theory should cancel after the sum over final states, leaving only the short-distance cross section for producing the pair in the first place.

### 3.1.2 Other infrared safe quantities in $e^+e^-$ annihilation

The infrared safety of  $\sigma_{tot}$  can be extended to a large class of cross sections that can be measured in  $e^+e^-$  annihilation. To understand what quantities are infrared safe and why, one should consider a perturbative calculation in which the quarks as well as the gluons are massless. Then any sensitivity to long distance effects will show up as an infrared divergence in the calculation.

How would such a divergence arise? A detailed analysis given in Ref. [3.3] yields a simple answer: the potential divergences are related to soft or collinear momentum configurations. First, a massless on-shell particle with momentum  $p^\mu$  can emit a massless particle with momentum  $q^\mu = 0$  and remain on-shell. Integration over momenta  $q^\mu$  near to  $q^\mu = 0$  produces *soft divergences* in cross sections. Second, a massless on-shell particle with momentum  $p^\mu$  can emit a massless particle with momentum  $q^\mu = zp^\mu$  and remain on-shell. Integration over momenta  $q^\mu$  near to  $q^\mu = zp^\mu$  produces *collinear divergences* in cross sections.

When the total cross section for  $e^+e^-$  annihilation is calculated perturbatively, individual terms are infinite, but the infinities cancel for reasons based on unitarity, as discussed in the previous subsection. There are other quantities for which a similar cancellation occurs. Consider a quantity  $\mathcal{I}$  that is defined in the style of [3.4] in terms of parton cross sections and functions  $S_n$  by

$$\begin{aligned} \mathcal{I} = & \frac{1}{2!} \int d\Omega_2 \frac{d\sigma[2]}{d\Omega_2} S_2(p_1^\mu, p_2^\mu) \\ & + \frac{1}{3!} \int d\Omega_2 dE_3 d\Omega_3 \frac{d\sigma[3]}{d\Omega_2 dE_3 d\Omega_3} S_3(p_1^\mu, p_2^\mu, p_3^\mu) \\ & + \frac{1}{4!} \int d\Omega_2 dE_3 d\Omega_3 dE_4 d\Omega_4 \frac{d\sigma[4]}{d\Omega_2 dE_3 d\Omega_3 dE_4 d\Omega_4} S_4(p_1^\mu, p_2^\mu, p_3^\mu, p_4^\mu) \end{aligned}$$

$$+ \dots \quad (3.7)$$

The functions  $\mathcal{S}_n$  specify the measurement to be made. An example of  $\mathcal{I}$  is the total cross section, for which all of the  $\mathcal{S}_n$  equal 1. Another example is the thrust distribution  $d\sigma/dT$  where, for an event containing  $n$  particles, the thrust  $T$  is [3.5]

$$T_n(p_1^\mu, \dots, p_n^\mu) = \max_{\vec{u}} \frac{\sum_{i=1}^n |\vec{p}_i \cdot \vec{u}|}{\sum_{i=1}^n |\vec{p}_i|}. \quad (3.8)$$

Here the  $\vec{u}$  is a unit vector defining the “thrust axis,” which is chosen to maximize the thrust. To calculate  $d\sigma/dT$ , one uses eq. (3.7) with

$$\mathcal{S}_n(p_1^\mu, \dots, p_n^\mu) = \delta(T - T_n(p_1^\mu, \dots, p_n^\mu)). \quad (3.9)$$

Perhaps the most important examples of  $\mathcal{I}$  are the various jet cross sections, to be discussed in Sects. 4 and 7.

Under what conditions will the cancellation of infrared infinities that occurred for the total cross section also occur for the quantity  $\mathcal{I}$ ? Without loss of generality, we may assume that the  $\mathcal{S}_n$  are invariant under interchange of their  $n$  arguments  $p_n^\mu$ . Then the discussion above of collinear and soft divergences should make it clear that one needs

$$\mathcal{S}_{n+1}(p_1^\mu, \dots, (1-\lambda)p_n^\mu, \lambda p_n^\mu) = \mathcal{S}_n(p_1^\mu, \dots, p_n^\mu) \quad (3.10)$$

for  $0 \leq \lambda \leq 1$ . That is to say, the measurement should not distinguish between a final state in which two particles are collinear and the final state in which these two particles are replaced by one particle carrying the sum of the momenta of these collinear particles. Similarly, the measurement should not distinguish between a final state in which one particle has zero momentum and the final state in which this particle is omitted entirely.

The argument that a cross section specified by functions  $\mathcal{S}$  with this property does not have infrared divergences may be understood as an extension of the KLN theorem [3.1]. The heuristic arguments given above for the total cross section apply in this case as well. We need only observe that long-distance interactions (and hence infrared sensitivity) arise from interactions that occur over a long time period. These are just the interactions involving

parallel-moving particles or very low momentum particles. As long as the measured quantity is not sensitive to whether such a long-time interaction has occurred, one can still cancel the divergences in perturbation theory using unitarity: the sum of the probabilities that the interaction does or does not occur is unity.

On the level of QCD calculations, infrared safety means that the quantity can be calculated in perturbation theory without obtaining infinity. Since the infrared infinities come from long distance physics, the physical interpretation is that infrared safe quantities are insensitive to long distance physics.

## 3.2 Factorization Theorems in Deeply Inelastic Scattering

In this subsection, we introduce two of the basic ideas of perturbative QCD, *factorization*, which enables us to derive and generalize the parton model, and *evolution*, which enables us to compute scale-breaking effects systematically.

### 3.2.1 Factorization for structure functions

*Theorem.* The field theory realization of the parton model is the theorem of *factorization* of long-distance from short-distance dependence for deeply inelastic scattering [3.6]. This theorem states that the sum of all the diagrammatic contributions to the structure functions is a direct generalization of the parton model results, Eq. (2.27) and Eq. (2.28), given by

$$F_a^{(Vh)}(x, Q^2) = \sum_{i=f, \bar{f}, G} \int_0^1 \frac{d\xi}{\xi} C_a^{(Vi)}(x/\xi, Q^2/\mu^2, \mu_f^2/\mu^2, \alpha_s(\mu^2)) \times \phi_{i/h}(\xi, \mu_f, \mu^2), \quad (a = 1, 3) \quad (3.11)$$

$$F_2^{(Vh)}(x, Q^2) = \sum_{i=f, \bar{f}, G} \int_0^1 d\xi C_2^{(Vi)}(x/\xi, Q^2/\mu^2, \mu_f^2/\mu^2, \alpha_s(\mu^2)) \times \phi_{i/h}(\xi, \mu_f, \mu^2). \quad (3.12)$$

Here  $i$  denotes a sum over all partons: quarks, antiquarks and gluons.

We note, compared to the parton model formula, dependence on two mass scales,  $\mu$  and  $\mu_f$ . The former is the renormalization scale, which is necessary in any perturbative computation. The latter, however, is specific to factorization calculations, and is called the factorization scale. It serves to define the separation of short-distance from long-distance effects. Roughly speaking, any propagator that is off-shell by  $\mu_f^2$  or more will contribute to  $C_a^{(Vi)}$ . Below this scale, it will be grouped into  $\phi_{i/h}$ . The precise definition of  $\mu_f$  is made when we give a formal definition of the parton distributions. It appears in the definition of the parton distributions in a fashion very similar to the way the renormalization scale  $\mu$  appears in renormalization.

Often, it will be convenient to choose the two scales  $\mu$  and  $\mu_f$  to be equal, but this need not be done in general.

The substance of factorization is contained in the following properties of the functions  $C_a^{(Vi)}$  and  $\phi_{i/h}$ .

- i. Each hard-scattering function

$$C_a^{(Vi)}(x/\xi, Q^2/\mu^2, \mu_f^2/\mu^2, \alpha_s(\mu^2)), \quad a = 1, 2, 3, \quad (3.13)$$

is *infrared safe*, calculable in perturbation theory. It depends on the label  $a$ , on the electroweak vector boson  $V$ , on the parton  $i$ , and on the renormalization and factorization scales, but it is *independent* of long-distance effects. In particular it is independent of the identity of hadron  $h$ . For example, it is the same in the DIS of a proton and a neutron and, for that matter, in the DIS of a pion or kaon. It is a generalization of the Born elastic scattering cross section in the parton model formula, Eq. (2.30).

- ii. The parton distribution,  $\phi_{i/h}(\xi, \mu, \mu_f, \alpha_s(\mu^2))$ , on the other hand, contains *all* the infrared sensitivity of the original cross section. It is specific to the hadron  $h$ , and depends on  $\mu_f$ . On the other hand it is *universal*, that is, it is independent of the particular hard scattering process that we treat: it is the same for the different structure functions  $F_1$  and  $F_2$ , for example, and it depends on neither  $a$  nor  $V$ , nor even  $Q^2$ , unless we pick  $\mu^2 = Q^2$ . It is a direct generalization of the parton model quark distribution.

*Use and interpretation.* The use of factorization is also a generalization of the parton model. The  $C$ 's are to be computed in perturbation theory, and the  $\phi$ 's are to be measured by comparing Eq. (3.11) and Eq. (3.12) to experiment, given explicit expressions for the  $C$ 's. Once enough information is amassed to determine the parton distributions from some standard set of cross sections, we can use factorization to provide predictions for other factorizable cross sections, and for the same process at other  $Q^2$ .

The essential question is therefore to give a method of computation for the hard scattering functions  $C_a^{(Vh)}$ . To do so, we use the fact that the  $C$ 's are independent of the external hadron. We can therefore calculate them in perturbation theory, with the external hadron replaced by a parton. This will require us to consider the distribution of a parton in a parton:  $\phi_{i/j}$ , where we have a parton label instead of a hadron label. Then we will need a prescription for computing the cross sections or structure functions with a parton target and separating out the hard scattering from the parton distributions  $\phi_{i/j}$ .

Such a prescription obviously involves a degree of choice. A set of rules that makes the choices is often called a “factorization scheme”, by analogy to renormalization scheme. Such a scheme defines at the same time the hard scattering functions and the parton distributions. Once this has been done, we can discard the perturbative parton distributions, which have no particular meaning since they are dominated by infrared effects and thus by infrared parameters that we cannot measure. Nevertheless, the factorization theorem insures that the hard scattering functions determined in this calculation are insensitive to infrared scales and parameters, and are applicable to cross sections computed with phenomenologically determined hadronic parton distributions.

Explicit results for hard-scattering functions may be found in Section 5, along with a discussion of the mechanics of their calculation for the archetypical factorized cross section: the electromagnetic DIS structure functions of a quark,  $F_a^{(\gamma f)}$ .

*Generalizations.* So far, we have discussed factorization for the fully inclusive structure functions. Essentially the same factorization theorem applies,

however, to any DIS cross section defined by a sum over hadronic final states that satisfies the same condition Eq. (3.10) that implies infrared safety in  $e^+e^-$  annihilation [3.7]. Other generalizations apply to non-scaling, “higher-twist” contributions which fall off as powers of  $Q^2$  [3.8] and to spin-dependent distributions [3.9].

### 3.2.2 Factorization Schemes

Even before we discuss how to define the distribution  $\phi_{f/f}$  perturbatively, it is clear that in the absence of interactions, it should enable the factorization formula to reproduce the Born cross section. We must therefore have

$$\phi_{f/f}^{(0)}(\xi) = \delta(1 - \xi). \quad (3.14)$$

(Here and below, we use a notation  $f^{(i)}$  to denote the  $i$ th order in the perturbation expansion of a quantity  $f$ , which in the above equation is  $\phi$ .) Then we find by direct substitution in Eq. (3.11) and Eq. (3.12) that, for  $a = 1, 2$ ,

$$F_a^{(\gamma f)(0)}(x) = Q_f^2 \delta(1 - x) = C_a^{(\gamma f)(0)}(x), \quad (3.15)$$

just as in Eq. (2.30).

Beyond lowest order in perturbation theory there is considerable ambiguity in separating the hard scattering functions from their corresponding parton distributions. In general, any choice for the parton distributions that satisfies Eq. (3.14) at lowest order, and that absorbs all long-distance effects at higher order, is acceptable. Short-distance “finite parts” at higher orders may be apportioned arbitrarily between the  $C$ ’s and  $\phi$ ’s. A prescription that eliminates this ambiguity is what we mean by a factorization scheme. The choice of scheme is a matter of taste and convenience, but it is absolutely crucial to use schemes consistently, and to know in which scheme any given calculation, or comparison to data, is carried out. The two most commonly used schemes, called DIS and  $\overline{\text{MS}}$  reflect two different uses to which the freedom in factorization may be put.

The DIS scheme is appealing for its close correspondence to experiment [3.10]. In this scheme, we demand that, order-by-order in perturbation theory, all corrections to the structure functions  $F_2^{(V^h)}$  be absorbed into the

distributions of the quarks and antiquarks. This means that at  $\mu = \mu_f = Q$ , the hard scattering functions are exactly equal to their parton-model values:

$$\begin{aligned} C_2^{(Vq)}(x) &= Q_q^2 \delta(1-x), \\ C_2^{(V\bar{q})}(x) &= Q_{\bar{q}}^2 \delta(1-x), \\ C_2^{(Vg)}(x) &= 0, \end{aligned} \quad (3.16)$$

to all orders of perturbation theory. Of course, it is possible to do this for only one of the structure functions. The other structure functions will receive corrections at order  $\alpha_s$  and beyond. Note that this definition does not fix the gluon distribution.

The  $\overline{\text{MS}}$  scheme, on the other hand, is appealing for its theoretical elegance and calculational simplicity. In this scheme the parton distributions are defined directly in terms of hadronic matrix elements [3.11]. In their simplest form, these matrix elements may be given in terms of operators  $b_i(xp, \mathbf{k}_T)$  and  $b_i^\dagger(xp, \mathbf{k}_T)$ , which annihilate and create parton  $i$ , with longitudinal momentum  $xp$  and transverse momentum  $\mathbf{k}_T$ , in hadron  $h$  of momentum  $p$ ,

$$\phi_{i/h}(x, \mu^2) = \int \frac{d^2 \mathbf{k}_T}{(2\pi)^2} \langle h(p) | b_i^\dagger(xp, \mathbf{k}_T) b_i(xp, \mathbf{k}_T) | h(p) \rangle. \quad (3.17)$$

The first (rightmost) operator absorbs the parton from the hadronic state, and the second emits it again. This parton distribution is, in essence, the expectation value of a number operator in the hadronic state. A little sophisticated footwork reexpresses the matrix element in Eq. (3.17) in terms of the quantum field corresponding to parton  $i$ . Thus, for instance, the  $\overline{\text{MS}}$  distribution for a quark of flavor  $f$  is given by

$$\begin{aligned} \phi_{f/h}(x, \mu^2) &= \int_{-\infty}^{\infty} \frac{dy^-}{4\pi} e^{-ixp^+y^-} \langle h(p) | \bar{\psi}(y^-, 0^+, \mathbf{0}_T) \gamma^+ \\ &\quad \times \psi(0^-, 0^+, \mathbf{0}_T) | h(p) \rangle, \end{aligned} \quad (3.18)$$

where an average over the spin of  $h(p)$  is understood. Similar explicit expressions can be give for the antiquark (in which the roles of  $\psi$  and  $\bar{\psi}$  are exchanged) and for the gluon, for which the relevant field is  $F^{+T} \equiv$

$(1/\sqrt{2})(F^{0T} + F^{3T})$  where  $T$  labels the transverse components relative to the momentum  $\mathbf{p}$ . (There are some complications due to gauge invariance that we have ignored in definition (3.18). See Section 3.4)

More insight into these two “canonical” ways of defining parton distributions can be gained from the explicit one-loop calculations described in Section 5.4 below .

### 3.2.3 Evolution

Everything in the process just described was carried out for fixed  $Q^2$ . But even a single DIS experiment supplies data over a range of momentum transfers. A remarkable consequence of factorization is that measuring parton distributions for one scale  $\mu$  allows their prediction for *any* other scale  $\mu'$ , as long as both  $\mu$  and  $\mu'$  are large enough that both  $\alpha_s(\mu)$  and  $\alpha_s(\mu')$  are small. This result, called the *evolution* of structure functions, increases the power of pQCD enormously. Thus, for instance, measuring  $F_2^{(\gamma h)}(x, Q^2)$  is enough to predict, not only  $F_1^{(\gamma h)}(x, Q^2)$ , but also  $F_1^{(\gamma h)}(x, Q'^2)$  and  $F_2^{(\gamma h)}(x, Q'^2)$  for all large  $Q'^2$ . We have skipped over the point that to make precise predictions, we need analogous information from neutrino scattering to perform the flavor separation of the parton densities.

The evolution of the parton distributions is most often, and most conveniently, described in terms of integro-differential equations,

$$\mu \frac{d}{d\mu} \phi_{i/h}(x, \mu, \mu^2) = \sum_{j=f, \bar{f}, G} \int_x^1 \frac{d\xi}{\xi} P_{ij} \left( \frac{x}{\xi}, \alpha_s(\mu^2) \right) \phi_{j/h}(\xi, \mu, \mu^2) . \quad (3.19)$$

We have chosen  $\mu = \mu_f$ . This equation is known as the Gribov-Lipatov-Altarelli-Parisi evolution equation [3.12] [3.13]. The *evolution kernels*  $P_{ij}(x)$  are given by perturbative expansions, beginning with  $O(\alpha_s)$ . Their explicit forms will be discussed in Section 5 below. The one-loop terms in the kernels are independent of the scheme used to define the parton distributions.

Note that the integral on the right-hand side of Eq. (3.19) begins at  $x$ . Thus, it is only necessary to know  $\phi_{j/h}(\xi, Q_0^2)$  for  $\xi > x$  at some starting value of the scale  $\mu = Q_0$ , in order to derive  $\phi_{j/h}(x, \mu^2)$  at a higher value

$\mu = Q$ . This is a great simplification, since data at small  $x$  are hard to come by at moderate energies.

Without going into the details of the evolution kernels, we can get some insight into their use by applying Eq. (3.19) to a parton state  $h = j$  and expanding to first order in  $\alpha_s$ , using Eq. (3.14),

$$\mu \frac{d}{d\mu} \phi_{i/h}^{(1)}(x, \mu, \mu^2) = \sum_{j=f, \bar{f}, G} P_{ij}^{(1)}(x). \quad (3.20)$$

From this relation, we already see that the evolution kernels show up as the coefficients of the logarithmic factorization-scale dependence in one-loop calculations.

The evolution equations control the dependence of parton distributions on the factorization scale. If we choose  $\mu = \mu_f = Q$ , the momentum transfer in DIS, then there are no large ratios in the arguments of the hard-scattering functions  $C_a$  in the factorization theorem. Under these circumstances, we *expect* the perturbative series for the  $C$ 's to be well under control, with no large coefficients of  $\alpha_s$  at first order and beyond, at the same time that  $\alpha_s$  itself is relatively small. Of course, this means that most of the information on  $Q^2$ -dependence has simply been shuffled into the parton distributions. The beauty of the evolution equations is that they tell us how to compute this dependence, given only that we have measured the parton distributions at one scale  $Q_0$ . In the language of the parton model, the evolution equation enables us to compute the  $Q^2$ -dependence of the parton distributions, and hence the “scale-breaking” of the structure functions themselves.

It is relatively easy to derive the evolution equations (3.19) directly from the factorization theorem, Eq. (3.11) and Eq. (3.12). This instructive derivation also enables us to introduce the famous analysis of scale breaking in DIS in terms of *moments* of structure functions.

Evolution is directly related to our freedom in choosing the renormalization and factorization scales. We notice first that the value of  $\mu_f$  in the factorization theorem Eq. (3.11) and Eq. (3.12) is free. A natural choice for DIS is  $\mu_f = \mu = Q$ , so that the  $C_a^{(Vi)}$ , as well as the  $\phi_{i/h}$ , are functions of  $\alpha_s(Q^2)$ . With this choice, the evolution of parton distributions is sufficient to evolve the complete structure functions.

The derivation of evolution is simplified in so-called *nonsinglet* structure functions, the simplest of which are

$$F_a^{(VNS)} \equiv F_a^{(Vp)} - F_a^{(Vn)}, \quad (3.21)$$

where  $p$  is the proton and  $n$  the neutron. For the following discussion, we suppress the label  $V$ , and choose  $\mu_f = \mu$ .  $F_1^{(NS)}$ , for instance, satisfies the factorization theorem,

$$\begin{aligned} F_1^{(NS)}(x, Q^2) &= \int_0^1 \frac{d\xi}{\xi} C_1^{(NS)} \left( \frac{x}{\xi}, \frac{Q^2}{\mu^2}, \alpha_s(\mu^2) \right) \\ &\quad \times \phi_{NS}(\xi, \alpha_s(\mu^2)), \end{aligned} \quad (3.22)$$

where  $\phi_{NS}$  is a “valence” quark distribution. More properly it is the difference between  $p$  and  $n$  quark distributions,

$$\phi_{NS}(x, \mu^2) = \sum_f Q_f^2 [\phi_{f/p}(x, \mu^2) - \phi_{f/n}(x, \mu^2)], \quad (3.23)$$

where we have absorbed the quark charges into its definition, which makes the short-distance function independent of  $f$ .

The term “valence” refers to our expectation that the distributions of gluons, and of “sea” quarks, produced in pairs by gluons, should be the same in the proton as in the neutron. These contributions, which are singlets under the isospin group  $SU(2)$ , cancel in the difference in Eq. (3.21). Note that this result holds exactly only for electromagnetic structure functions, since the electromagnetic interactions respect charge conjugation, which exchanges the roles of quarks and antiquarks. What remains is almost entirely due to the difference in the “valence”  $u$  and  $d$  quark content of the proton and neutron. The simplification in Eq. (3.21) relative to Eq. (3.11) and Eq. (3.12) is that the result is a single convolution, rather than a sum of convolutions.

Now both the functions on the right of Eq. (3.22) are functions of  $\mu$ , but the physical quantity  $F_1^{(NS)}$  on the left is not,

$$\frac{d}{d\mu} F_1^{(NS)} = 0. \quad (3.24)$$

Thus, the  $\mu$ -dependence in  $C_1^{(NS)}$  must compensate that of  $\phi_{\text{NS}}$ . The information contained in this observation may be brought out clearly by introducing *moments* of the structure functions,

$$\begin{aligned}\bar{F}_1^{(NS)}(n, Q^2) &\equiv \int_0^1 dx x^{n-1} F_1^{(NS)}(x, Q^2) \\ &= \bar{C}_1^{(NS)} \left( n, \frac{Q^2}{\mu^2}, \alpha_s(\mu^2) \right) \bar{\phi}_{\text{NS}}(n, \mu, \mu^2),\end{aligned}\quad (3.25)$$

where  $\bar{C}^{(NS)}$  and  $\bar{\phi}_{\text{NS}}$  are

$$\begin{aligned}\bar{C}_1^{(NS)}(n) &\equiv \int_0^1 d\eta \eta^{n-1} C_1^{(NS)}(\eta), \\ \bar{\phi}_{\text{NS}}(n) &\equiv \int_0^1 d\xi \xi^{n-1} \phi_{\text{NS}}(\xi).\end{aligned}\quad (3.26)$$

Now, applying moments to Eq. (3.22), we find that

$$\begin{aligned}\mu \frac{d}{d\mu} \ln \bar{\phi}_{\text{NS}}(n, \mu, \mu^2) &= -\gamma_n^{(NS)}(\alpha_s(\mu^2)) \\ &= -\mu \frac{d}{d\mu} \ln \bar{C}_1^{(NS)} \left( n, \frac{Q^2}{\mu^2}, \mu^2 \right),\end{aligned}\quad (3.27)$$

where  $\gamma_n^{(NS)}(\alpha_s(\mu^2))$  is a function of  $\alpha_s$  only, since this is the only variable that  $\phi_{\text{NS}}$  and  $\bar{C}^{(NS)}$  have in common. (Note that the ratio  $Q/\mu_f$  in  $C$ , for instance, is independent of the  $\mu_f$ -dependence in  $\phi$ , because the latter would occur in ratios like  $\mu/\lambda$ , with  $\lambda$  an infrared cutoff.)  $\gamma_n^{(NS)}$  is known as an *anomalous dimension*, since it acts like a factor  $\mu^{-\gamma_n}$  in the (dimensionless!) function  $\ln \bar{\phi}_{\text{NS}}(n, \alpha_s(\mu^2))$ .

The anomalous dimensions  $\gamma_n$  can be constructed directly from the one-loop value of the parton distribution. (At one loop  $\phi_{f/f}$  and  $\phi_{\text{NS}}$  are the same for an external quark.) Although  $\phi_{f/f}$  is certainly not IR safe,  $\gamma_n^{(NS)}$  is, because it is also a derivative of  $C^{(NS)}(n)$ . The derivative of  $\phi_{f/f}^{(1)}$  is particularly simple, however,

$$\begin{aligned}\gamma_n^{(NS)} &= \mu \frac{d}{d\mu} \ln \bar{\phi}_{\text{NS}}(n, \mu, \alpha_s(\mu^2)) \\ &= -\frac{\alpha_s}{\pi} \int_0^1 dx x^{n-1} P_{qq}^{(1)}(x) + O(\alpha_s^2),\end{aligned}\quad (3.28)$$

with  $P_{qq}^{(1)}(x)$  found from Eq. (3.20). To give substance to these rather abstract considerations, let us exhibit the explicit integral from which we find  $\gamma_n^{(NS)}$ , which may be found directly from the explicit form for  $P_{qq}(x)$ , given in Section 5,

$$\begin{aligned}\gamma_n^{(NS)} &= -\frac{\alpha_s}{\pi} C_2(F) \int_0^1 dx \left\{ \frac{(1+x^2)x^{n-1} - 2}{1-x} \right. \\ &\quad \left. - x^{n-1} \frac{3}{2} \delta(1-x) \right\}, \\ &= \frac{\alpha_s}{2\pi} C_2(F) \left\{ 4 \sum_{m=2}^n \frac{1}{m} - \frac{2}{n(n+1)} + 1 \right\}. \end{aligned} \quad (3.29)$$

We note an important subsidiary result

$$\gamma_1^{(NS)} = 0, \quad (3.30)$$

which states that the integral of the NS distribution,

$$M_1 \equiv \int_0^1 d\xi \phi_{NS}(\xi, \mu^2, \mu^2), \quad (3.31)$$

is independent of the factorization scale. This is gratifying, since  $M_1$  measures the number of valence quarks. For  $n > 1$ , the  $\gamma_n$ 's are all positive and increase in size with  $n$ . This means that higher moments, which test the size of  $\phi_{NS}(x)$  near  $x = 1$ , vanish more rapidly than lower moments as  $Q^2 \rightarrow \infty$ . Along with  $\gamma_1^{(NS)} = 0$ , this implies a “softening” of  $\phi_{NS}$  with  $Q^2$ , in which the average  $x$  decreases as  $Q^2$  increases. This behavior is characteristic of all parton distributions.

The formal solution to the evolution equation Eq. (3.27) gives the behavior of  $\bar{\phi}_{NS}(n, Q^2)$  as a function of  $Q^2$  and hence of  $\bar{F}_a^{(NS)}(n, Q^2)$ ,

$$\begin{aligned}\bar{\phi}_{NS}(n, Q^2) &= \bar{\phi}_{NS}(n, \mu_0, \alpha_s(Q_0^2)) \\ &\quad \times \exp \left\{ -\frac{1}{2} \int_0^{\ln \frac{Q^2}{Q_0^2}} dt \gamma_n(\alpha_s(Q_0^2 e^t)) \right\}, \\ \bar{F}_1^{(NS)}(n, Q^2) &= \bar{C}_1^{(NS)}(n, \alpha_s(Q^2)) \bar{\phi}_{NS}(n, Q_0^2) \\ &\quad \times \exp \left\{ -\frac{1}{2} \int_0^{\ln \frac{Q^2}{Q_0^2}} dt \gamma_n(\alpha_s(Q_0^2 e^t)) \right\}. \end{aligned} \quad (3.32)$$

The  $Q^2$  behavior thus determined depends on whether or not our theory is asymptotically free. Writing

$$\gamma_n^{(NS)} = \frac{\alpha_s}{\pi} \gamma_n^{(1)}, \quad (3.33)$$

and using Eq. (1.46) for the one-loop running coupling in QCD, we find

$$\tilde{F}_a^{(NS)}(n, Q^2) \sim \left[ \frac{\ln Q^2/\Lambda^2}{\ln Q_0^2/\Lambda^2} \right]^{-2\gamma_n^{(1)}/4|\beta_1|}. \quad (3.34)$$

This is a relatively mild logarithmic  $Q^2$ -dependence, which is consistent with an approximate scaling over the limited range of  $Q^2$  in early experiments [3.14]. It is to be contrasted with the behavior in a hypothetical “fixed-point” theory, in which

$$\alpha_s(\mu^2) \xrightarrow[\mu \rightarrow \infty]{} \alpha_0, \quad (3.35)$$

with  $\alpha_0 \neq 0$ . In the latter case we would have a *power* scale-breaking

$$F_a^{(NS)}(n, Q^2) \sim \left( \frac{Q^2}{Q_0^2} \right)^{-\frac{\alpha_0}{2\pi} \gamma_n^{(1)}}. \quad (3.36)$$

The evolution result, Eq. (3.32) was known for some time [3.15] before asymptotic freedom was discovered [3.16]. The inconsistency of experimentally-observed scaling behavior with strong scale breaking like Eq. (3.36) seemed to make the application of field theory to the strong interactions problematic. The derivation of approximate scaling from asymptotic freedom was therefore a very important result [3.17].

*Physical Content of Evolution.* In the parton model,  $\phi_{i/h}(x)$  has the direct interpretation of the density of partons of type  $i$  and fractional momentum  $x$  in hadron  $h$ . In pQCD,  $\phi_{i/h}(x, \bar{\mu}^2)$  has essentially the same interpretation, but with the added restriction that the parton be off-shell by approximately no more than the scale  $\bar{\mu}^2$ . Beyond this limit, a parton would be incorporated into the hard-scattering functions  $C_a^{(i)}$  in Eq. (3.11) and Eq. (3.12).

Now if QCD had a natural *maximum* off-shellness  $Q_0^2$  for its virtual partons, then we would have

$$\phi_{i/h}(x, Q^2) = \phi_{i/h}(x, Q_0^2) \quad (3.37)$$

for all  $Q^2 > Q_0^2$ , and the theory would exhibit true scaling behavior. Note the close correspondence of this assumption to the assumption  $\tau > \tau_0$  for the lifetimes of virtual states in our heuristic justification of the parton model in Section 2.1.1. In a renormalizable theory, however, this *never* happens: there are always states of arbitrarily short lifetimes, and lines that are arbitrarily far off-shell. That is the reason the theory must be renormalized to begin with. The evolution of  $\phi_{i/h}(x, Q^2)$ , therefore, measures the distribution of off-shell partons. The rather weak evolution of an asymptotically free theory, Eq. (3.34), shows that production of these partons is not strong.

### 3.3 Other Factorization Theorems

#### 3.3.1 Drell-Yan

The factorization theorem for the Drell-Yan process is typical of factorization theorems for more general hard scattering processes, and it is formulated as follows.

The process is the inclusive production of a lepton pair of high invariant mass via an electroweak particle in hadron-hadron collisions. The classical case is a high-mass virtual photon:  $A + B \rightarrow \gamma^* + \text{anything}$ , with  $\gamma^* \rightarrow e^+e^-$  or  $\gamma^* \rightarrow \mu^+\mu^-$ . Here  $A$  and  $B$  are two incoming hadrons. Essentially identical theorems apply to the production of W or Z bosons.

We let  $s$  be the square of the total center-of-mass energy and  $q^\mu$  be the momentum of the  $\gamma^*$ . The kinematic region to which the theorem applies is where  $\sqrt{s}$  and  $Q$  large, with  $Q^2/s$  fixed. ( $Q$  is  $\sqrt{q^2}$ .) The transverse momentum  $q_\perp$  of the  $\gamma^*$  is either of order  $Q$  or is integrated over.

In the case that  $q_\perp$  is integrated over, the factorization theorem for the unpolarized Drell-Yan cross section reads:

$$\begin{aligned} \frac{d\sigma}{dQ^2 dy d\Omega} = & \sum_{a,b} \int_{x_A}^1 d\xi_A \int_{x_B}^1 d\xi_B \phi_{a/A}(\xi_A, \mu^2) \\ & \times H_{ab} \left( \frac{x_A}{\xi_A}, \frac{x_B}{\xi_B}, \theta, \phi, Q; \frac{\mu}{Q}, \alpha_s(\mu) \right) \phi_{b/B}(\xi_B, \mu^2) \\ & + \text{remainder ,} \end{aligned} \quad (3.38)$$

where  $y$  is the rapidity of the virtual photon in the overall center-of-mass frame and  $d\Omega$  is the element of solid angle for the lepton pair: the polar and azimuthal angles for this decay are  $\theta$  and  $\phi$  respectively relative to some chosen axes. The remainder is suppressed by  $Q^{-2}$  compared to the term shown. The sums over  $a$  and  $b$  are over parton species, and we write

$$x_A = e^y \sqrt{\frac{Q^2}{s}}, \quad x_B = e^{-y} \sqrt{\frac{Q^2}{s}}. \quad (3.39)$$

The function  $H_{ab}$  is the ultraviolet-dominated hard scattering cross section, computable in perturbation theory. It plays the role of a parton level cross section and is often written as

$$H_{ab} = \frac{d\hat{\sigma}}{dQ^2 dy d\Omega}. \quad (3.40)$$

The parton distribution functions,  $\phi$ , are the same as in deeply inelastic scattering. Fig. 3.1 illustrates the factorization theorem.

As in DIS, extensions to more specific final states are possible. For instance, jet cross sections, defined by analogy to  $e^+e^-$  annihilation, obey factorization formulas of the same form as Eq. (3.38) [3.7]. Other extensions, to first nonleading power in  $Q^2$  [3.18], and to polarized scattering [3.19] are also possible.

### 3.3.2 Single-Particle Inclusive Cross Sections

We consider high  $p_\perp$  inclusive single particle production in hadron-hadron collisions  $A + B \rightarrow C + X$ . This is the most complicated of the single-particle inclusive cross sections. Applications to  $e^+e^-$  annihilation and to DIS are straightforward variations on this theme. Let the initial-state hadrons have momenta  $p_A$  and  $p_B$ , and let the observed hadron have momentum  $p_C$ . The factorization theorem reads

$$\begin{aligned} E_C \frac{d\sigma}{d^3 p_C} &= \sum_{abc} \int d\xi_A d\xi_B \frac{dz}{z} \phi_{a/A}(\xi_A, \mu) \phi_{b/B}(\xi_B, \mu) \\ &\times |\vec{k}_c| \frac{d\hat{\sigma}}{d^3 k_c}(p_c/z\sqrt{s}, \mu) D_{C/c}(z, \mu^2), \end{aligned} \quad (3.41)$$

which is illustrated in Fig. 3.2. ( The sum is over the various flavors of partons (quarks, antiquarks and gluons) that can participate in the hard scattering process, while  $\phi_{a/A}$  and  $\phi_{b/B}$  are the parton densities for the initial hadrons, and  $D_{C/c}(z)$  is the fragmentation function. The hard scattering function  $|\vec{k}|d\hat{\sigma}/d^3k_c$  is for the scattering  $a+b \rightarrow c+X$  at the parton level; it is a purely ultraviolet function, free of all mass singularities, so that it can be calculated perturbatively. The variable  $z$  represents the fractional momentum of the measured hadron relative to its parent quark, so that we set  $\vec{k}_c = z\vec{p}_C$ , when we use the center-of-mass frame of the hard scattering. For DIS the corresponding theorem has only a single parton distribution, while for  $e^+e^-$  there are none.

It can be checked that with the normalizations indicated, the fragmentation function can be interpreted by saying that  $zD_{C/c}(z)dz$  is the number of hadrons of type  $C$  in a parton of type  $c$  that have fractional momentum  $z$  to  $z + dz$ . Because of the factor  $z$ , it is common to define the fragmentation function to be  $d_{C/c}(z) \equiv zD_{C/c}(z)$ , rather than  $D$ . However, the behavior of  $D$  under Lorentz transformations is simpler, and this is important, since we can define a function for the fragmentation into two observed hadrons, for example.

It might appear that we have neglected the possibility that the hadron  $C$  has transverse momentum relative to the parton  $c$ . However, this is not so. In accordance with the derivation of Eq. (3.41), we have actually integrated over all small values of this transverse momentum, while realizing that the dependence of the hard scattering on small changes in the transverse momentum vanishes as  $Q \rightarrow \infty$ . Large values of this transverse momentum are correctly taken care of by the higher order corrections to the hard scattering function.

Like parton distributions  $\phi(x, \mu^2)$ , the fragmentation functions  $D(z, \mu^2)$  evolve in  $\mu$ , according to equations very similar to Eq. (3.19) [3.20]. The evolution kernels are closely related to, but not identical with, those for the parton distributions.

## 3.4 Operator Definitions of Parton Distribution and Fragmentation Functions

In this section, we collect together the operator definitions of the parton distribution and fragmentation functions for reference. These include the spin dependent cases. All the definitions have ultraviolet divergences, and these must be renormalized away to define finite parton distributions and fragmentation functions to be used in the factorization formulas. Although these definitions are not necessary for all phenomenological uses, they are needed to make precise the rules for Feynman graph calculations, for example.

### 3.4.1 Quark Distribution Functions

The distribution function for a quark of flavor  $i$  in a hadron  $h$  with momentum  $p_\mu$  in the plus direction is

$$\phi_{i/h}(\xi) \equiv \int \frac{dy^-}{2\pi} e^{i\xi p^+ y^-} \langle p | \bar{\psi}_i(0, y^-, 0_\perp) \frac{\gamma^+}{2} P e^{-ig \int_0^{y^-} dy'^- A_a^+(0, y'^-, 0) t_a} \psi_i(0) | p \rangle. \quad (3.42)$$

The path ordered exponential of the gluon field is needed to make the definition gauge invariant. Here and below,  $t_a$  denotes the generator  $T_a^{(F)}$ . We see that the simplified distributions of Eq. (3.18) are exact only in the  $A^+ = 0$  gauge.

In the case that the hadron can have polarization, the helicity asymmetry of a quark in a hadron is defined by

$$\begin{aligned} \lambda \Delta_L \phi_{i/h}(\xi) &\equiv \int \frac{dy^-}{2\pi} e^{i\xi p^+ y^-} \langle p | \bar{\psi}_i(0, y^-, 0_\perp) \frac{\gamma_5 \gamma^+}{2} \\ &\quad \times P e^{-ig \int_0^{y^-} dy'^- A_a^+(0, y'^-, 0) t_a} \psi_i(0) | p \rangle, \end{aligned} \quad (3.43)$$

where  $\lambda$  is the helicity of the hadron, normalized so that  $\lambda = \pm 1$  corresponds to a fully polarized nucleon.

A hadron may also have a component of spin transverse to the collision axis. We define a *transversity asymmetry*,  $\Delta_T \phi_{i/h}$ , of the quark by

$$s_\perp^\mu \Delta_T \phi_{i/h}(\xi) \equiv \int \frac{dy^-}{2\pi} e^{i\xi p^+ y^-}$$

$$\begin{aligned} & \times \langle p | \bar{\psi}_i(0, y^-, 0_\perp) \frac{\gamma^+ \gamma_5 \gamma^\mu_\perp}{2} \\ & \times P e^{-ig \int_0^{y^-} dy'^- A_a^+(0, y'^-, 0_\perp) t_a} \psi_i(0) | p \rangle, \end{aligned} \quad (3.44)$$

where  $s_\perp^\mu$  is the transverse part of the hadron's Pauli-Lubanski spin vector, normalized so that 100% transverse polarization corresponds to  $s_\perp^\mu s_{\perp\mu} = -1$ .

### 3.4.2 Gluon Distribution Functions

Operator definitions for the distribution of gluons in a hadron are made in an analogous fashion to those for quarks:

$$\begin{aligned} \phi_{g/h}(\xi) &\equiv \sum_{j=1}^2 \int \frac{dy^-}{2\pi\xi p^+} e^{i\xi p^+ y^-} \langle p | G^{+j}(0, y^-, 0_\perp) \mathcal{P} G^{+j}(0) | p \rangle, \\ \lambda_{g/h} \Delta_L f_{g/h}(\xi) &\equiv \sum_{j,j'=1}^2 P_{jj'}^{\text{hel}} \int \frac{dy^-}{2\pi\xi p^+} e^{i\xi p^+ y^-} \langle p | G^{+j}(0, y^-, 0_\perp) \mathcal{P} G^{+j'}(0) | p \rangle, \\ s_{g/h\perp} \Delta_T f_{g/h}(\xi) &\equiv \sum_{j,j'=1}^2 P_{\perp jj'}^{\text{tran}} \int \frac{dy^-}{2\pi\xi p^+} e^{i\xi p^+ y^-} \\ & \quad \times \langle p | G^{+j}(0, y^-, 0_\perp) \mathcal{P} G^{+j'}(0) | p \rangle, \end{aligned} \quad (3.45)$$

where  $G_{\mu\nu}$  is the gluon field strength tensor and  $\mathcal{P}$  denotes the path-ordered exponential of the gluon field along the light-cone that makes the operators gauge-invariant, in exact analogy to Eq. (3.42)

$$\mathcal{P} \equiv P \exp \left[ \int_0^{y^-} dy'^- A_a^+(0, y'^-, 0_\perp) T_a \right], \quad (3.46)$$

where  $T_a = T_a^{(A)}$  are the generating matrices for the adjoint representation of color  $SU(N_c)$ . The  $j$  index runs over the two transverse dimensions, and the spin projection operators are defined by

$$\begin{aligned} P_{11}^{\text{hel}} &\equiv P_{22}^{\text{hel}} = 0, \\ P_{12}^{\text{hel}} &\equiv -P_{21}^{\text{hel}} = i, \\ P_{n,jj'}^{\text{tran}} &\equiv n_j n_{j'} - \delta_{jj'}/2. \end{aligned} \quad (3.47)$$

By angular momentum conservation, the linear polarization of a gluon is zero in a spin- $\frac{1}{2}$  hadron [3.21]. (The reason is that the linear polarization is measured by an operator that flips helicity by two units. Since no helicity is absorbed by the space-time part of the definition of the parton densities (the integrals are azimuthally symmetric), the helicity flip in the operator must correspond to a helicity flip term in the density matrix for the hadron.

### 3.4.3 Fragmentation Functions

The unpolarized fragmentation function to find a hadron  $h$  in the decay products of a quark of flavor  $c$  is

$$D_{h/c}(z) \equiv \sum_X \int \frac{dy^-}{12\pi} e^{ik^+y^-} \text{Tr} \gamma^+ \langle 0 | \psi(0, y^-, y_\perp) | hX \rangle \langle hX | \bar{\psi}(0) | 0 \rangle. \quad (3.48)$$

We have ignored here the path-ordered exponential of the gluon field that is needed to make this a gauge invariant definition. The sum is over all final states containing the chosen hadron.

## References

- [3.1] T. Kinoshita, Jour. Math. Phys. **3**, 650 (1962); T.D. Lee and M. Nauenberg, Phys. Rev. **B133**, 1549 (1964).
- [3.2] E.C. Poggio and H.R. Quinn, Phys. Rev. **D14**, 578 (1976); G. Sterman, Phys. Rev. **D14**, 2123 (1976).
- [3.3] G. Sterman, Phys. Rev. **D17**, 2773, 2789 (1978).
- [3.4] Z. Kunszt and D. E. Soper, Phys. Rev. **D46**, 192 (1992).
- [3.5] E. Fahri, Phys. Rev. Lett. **39**, 1587 (1977).
- [3.6] J.C. Collins, D.E. Soper and G. Sterman, in *Perturbative Quantum Chromodynamics*, ed. A.H. Mueller (World Scientific, Singapore, 1989) and references therein.

- [3.7] S.B. Libby and G. Sterman, Phys. Rev. **D18**, 3252 (1978).
- [3.8] R.K. Ellis, W. Furmanski and Petronzio, Nucl. Phys. **B207**, 1 (1982); **B212**, 29 (1983); R.L. Jaffe, Nucl. Phys. **B229**, 205 (1983); J. Qiu, Phys. Rev. **D42**, 30 (1990); J. Qiu and G. Sterman, Nucl. Phys. **B353**, 105 (1991); M. Okawa, Nucl. Phys. **B187**, 71 (1981); E.V. Shuryak and A.L. Vainshtein, Phys. Lett. **B105**, 65 (1981); R.L. Jaffe and M. Soldate, Phys. Rev. **D26**, 49 (1982); S.P. Luttrell and S. Wada, Nucl. Phys. **B197**, 290 (1982).
- [3.9] X. Artru and M. Mekhfi, Z. Phys. **C45**, 669 (1990); Proceedings of the *Polarized Collider Workshop*, ed. J.C. Collins, S. Heppelmann and R. Robinett (American Institute of Physics, New York, 1991); J.C. Collins, Penn State preprint PSU/TH/100 (1992).
- [3.10] G. Altarelli, R.K. Ellis and G. Martinelli, Nucl. Phys. **B157**, 461 (1979).
- [3.11] W.A. Bardeen, A.J. Buras, D.W. Duke and T. Muta, Phys. Rev. **D18**, 3998 (1978); G. Curci, W. Furmanski and R. Petronzio, Nucl. Phys. **B175**, 27 (1980); J.C. Collins and D.E. Soper, Nucl. Phys. **B194**, 445 (1982).
- [3.12] V.N. Gribov and L.N. Lipatov, Sov. J. Nucl. Phys. **15**, 675 (1972).
- [3.13] G. Altarelli and G. Parisi, Nucl. Phys. **B126**, 298 (1977).
- [3.14] J.I. Friedman and H.W. Kendall, Ann. Rev. Nucl. Sci. **22**, 203 (1972).
- [3.15] N. Christ, B. Hasslacher and A.H. Mueller, Phys. Rev. **D6**, 3543 (1972).
- [3.16] D.J. Gross and F. Wilczek, Phys. Rev. Lett. **30**, 1343 (1973); H.D. Politzer, Phys. Rev. Lett. **30**, 1346 (1973).
- [3.17] D.J. Gross and F. Wilczek, Phys. Rev. **D8**, 3633 (1973) **D9**, 980 (1974); H. Georgi and H.D. Politzer, Phys. Rev. **D9**, 416 (1974).

- [3.18] J. Qiu and G. Sterman, Nucl. Phys. **B353**, 137 (1991).
- [3.19] J.P. Ralston and D.E. Soper, Nucl. Phys. **B152**, 209 (1979); R.L. Jaffe and X. Ji, Phys. Rev. Lett. **67**, 552 (1991); J. Qiu and G. Sterman, Phys. Rev. Lett. **67**, 2664 (1991).
- [3.20] V.N. Gribov and L.N. Lipatov, Sov. J. Nucl. Phys. **15**, 438 (1972); A.H. Mueller, Phys. Rev. **D18**, 3705 (1978); J.C. Collins and D.E. Soper, Ref. [3.11].
- [3.21] X. Artru and M. Mekhfi, Z. Phys. **C45**, 669 (1990).

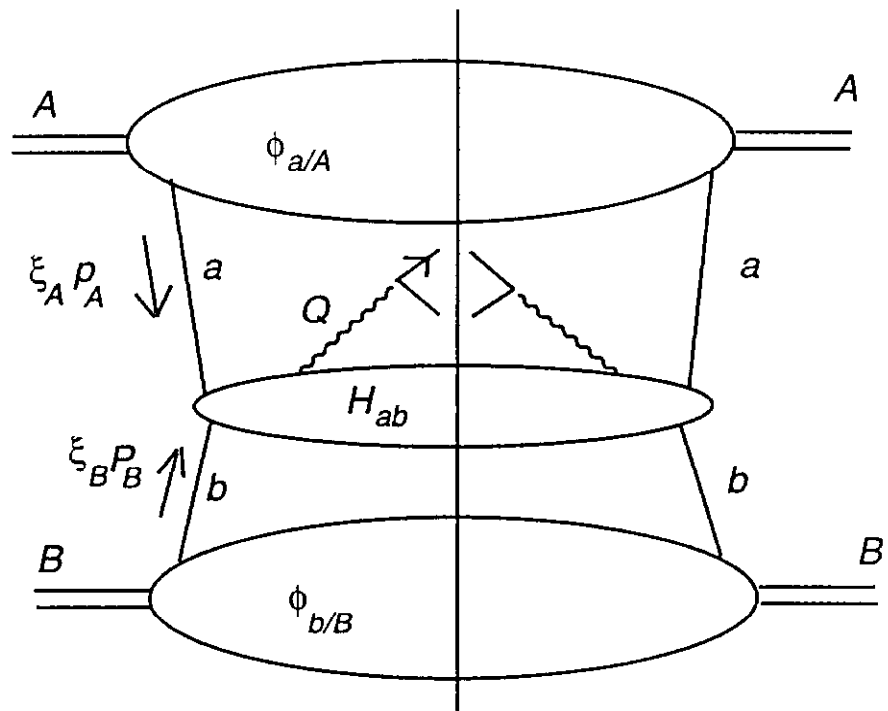


Figure 3.1. Factorization theorem for Drell-Yan cross section.

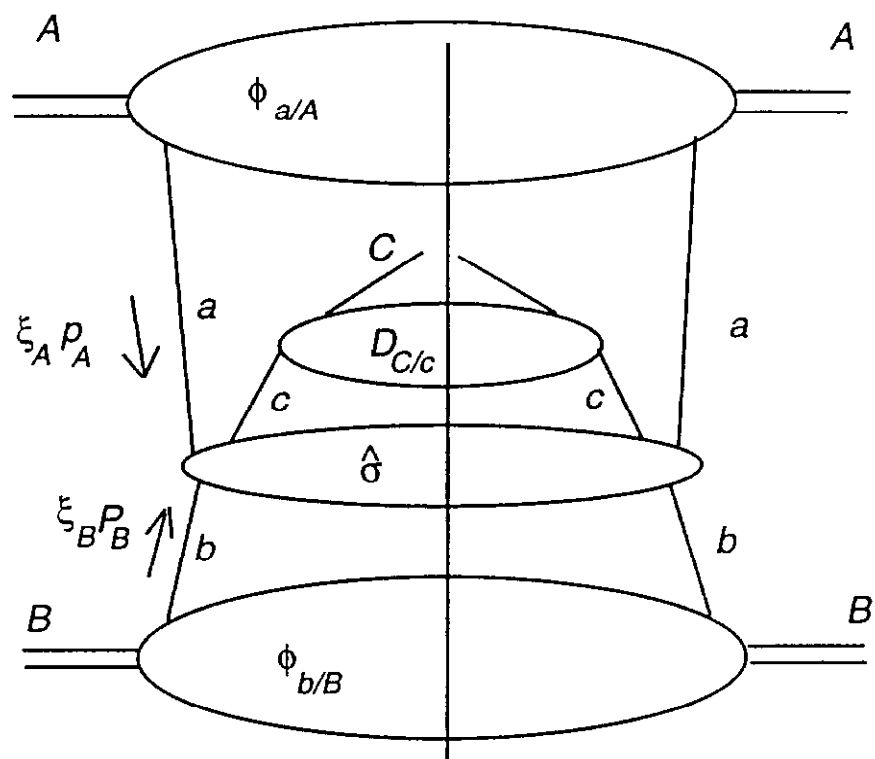


Figure 3.2. Factorization theorem for single particle production in hadron-hadron collisions.

## 4 $e^+e^-$ Annihilation

Among the most basic of the concepts of perturbative QCD is infrared safety. As discussed in Section 3, total and jet cross sections in  $e^+e^-$  annihilation are themselves infrared safe, without factorization into long- and short-distance components. In this section, we review explicit low-order results for these IR safe quantities.

### 4.1 Total Cross Section

The basic squared amplitudes for the total cross section in  $e^+e^-$  annihilation are illustrated in Fig. 4.1 at one loop, in the cut diagram notation of Appendix B.

At this level, the ultraviolet (UV) divergences in the self-energies cancel those in the vertex corrections. This cancellation is related to the manner in which quantum electrodynamics is renormalized: at zero photon momentum, all radiative corrections to the charge must vanish. That QCD respects the renormalization conditions of QED was a necessary condition for it to be a viable theory of the strong interactions. At a technical level, the result follows from  $[\mathcal{H}_{QCD}, \hat{Q}] = 0$ , with  $\mathcal{H}_{QCD}$  the Hamiltonian and  $\hat{Q}$  the operator for electromagnetic charge.

Because of this cancellation the one-loop cross section is independent of the scheme that we specify to renormalize QCD, and the result is identical in all schemes. Beyond one loop, however, it is necessary to specify a renormalization scheme, and results will, in general, differ from scheme to scheme.

The total cross section for  $e^+e^-$  annihilation at center-of-mass energy  $Q$  (in the one-photon approximation) has now been computed up to three loops with massless quarks in an  $\overline{\text{MS}}$  renormalization scheme [4.1]. Here is what it looks like,

$$\begin{aligned}
\sigma(Q^2) = \sigma_0 & \left\{ \begin{aligned}
& 1 + \frac{\alpha_s(Q^2)}{4\pi} (3C_F) \\
& + \left( \frac{\alpha_s(Q^2)}{4\pi} \right)^2 \left[ -C_F^2 \left( \frac{3}{2} \right) + C_F C_A \left( \frac{123}{2} - 44\zeta(3) \right) \right. \\
& \quad \left. + C_F T n_f (-22 + 16\zeta(3)) \right] \\
& + \left( \frac{\alpha_s(Q^2)}{4\pi} \right)^3 \left[ C_F^3 \left( -\frac{69}{2} \right) \right. \\
& \quad \left. + C_F^2 C_A (-127 - 572\zeta(3) + 880\zeta(5)) \right. \\
& \quad \left. + C_F C_A^2 \left( \frac{90445}{54} - \frac{10948}{9}\zeta(3) + \frac{440}{3}\zeta(5) \right) \right. \\
& \quad \left. + C_F^2 T n_f (-29 + 304\zeta(3) - 320\zeta(5)) \right. \\
& \quad \left. + C_F C_A T n_f \left( -\frac{31040}{27} + \frac{7168}{9}\zeta(3) + \frac{160}{3}\zeta(5) \right) \right. \\
& \quad \left. + C_F T^2 n_f^2 \left( \frac{4832}{27} - \frac{1216}{9}\zeta(3) \right) \right. \\
& \quad \left. - C_F \pi^2 \left( \frac{11}{3}C_A - \frac{4}{3}T n_f \right)^2 \right. \\
& \quad \left. + \frac{(\sum_f Q_f)^2}{(N \sum_f Q_f^2)} \frac{D}{16} \left( \frac{176}{3} - 128\zeta(3) \right) \right] \} .
\end{aligned} \right. \tag{4.1}
\end{aligned}$$

In this expression,  $\sigma_0$  is the parton model total cross section, Eq. (2.47),

$$\sigma_0 = \frac{4N\pi\alpha^2}{Q^2} \left( \sum_f Q_f^2 \right), \tag{4.2}$$

$n_f$  is the number of quark flavors and  $N$  is the number of colors. The group invariants,  $C_F^3$ ,  $C_F^2 C_A$ , etc., give structure to the otherwise unremitting sequence of integers, fractions and “zeta functions” in the three-loop result. For simplicity, we have written,  $C_F \equiv C_2(F)$ , etc., and from Appendix A, we have  $C_F = 4/3$ ,  $C_A = 3$ ,  $T = 1/2$ ,  $D = 40/3$  in QCD.  $\zeta(m)$  is the Riemann zeta function, beloved of mathematicians,

$$\zeta(x) = \sum_{n=0}^{\infty} \frac{1}{n^x}, \tag{4.3}$$

whose specific values encountered above are

$$\begin{aligned}\zeta(3) &= 1.2020569 \\ \zeta(5) &= 1.0369278.\end{aligned}\quad (4.4)$$

Using these values, the numerical coefficients for SU(3) with five quark flavors are

$$\sigma(Q^2) = \sigma_0(Q^2) \left( 1 + \frac{\alpha_s}{\pi} + 1.409 \left( \frac{\alpha_s}{\pi} \right)^2 - 12.805 \left( \frac{\alpha_s}{\pi} \right)^3 \right). \quad (4.5)$$

We note that the coefficient  $-12.805$  represents a second try; previously published results gave an uncomfortably large incorrect value of about 60. These results are for electron-positron annihilation via a virtual photon. In the LEP experiments, a virtual  $Z$  is involved and modifications in the formula are required. Most of the pieces of the modified formula are known, but some order  $\alpha_s^3$  terms involving heavy quark loops remain uncalculated.

## 4.2 $e^+e^-$ Total Cross Section at One Loop

The explicit calculations that lead to the  $O(\alpha_s^3)$  results are, like the results themselves, extremely complicated, and can be carried out only with the aid of computers. The  $O(\alpha_s)$  corrections, however, already exhibit some of the basic problems of pQCD, and their resolution through infrared safety.

At lowest order, the total cross section is given by the Born diagram, zeroth order in  $\alpha_s$ . The diagrams that contribute to the total cross section at  $O(\alpha_s)$  are of two kinds, those in which a gluon appears in the final state (Fig. 4.1a), and those which are the interference between an amplitude with an  $O(\alpha_s)$  virtual loop correction and the zeroth order (Fig. 4.1b). The leptonic and hadronic parts of these diagrams are connected by only a single photon (which we may take in Feynman gauge, with propagator  $-g_{\alpha\beta}/Q^2$ ), and it is consequently natural to write the cross section as a product of leptonic  $L^{\mu\nu}(k_1, k_2)$ , and hadronic,  $H_{\mu\nu}(q)$  tensors,

$$\sigma_{tot} = L^{\mu\nu}(k_1, k_2) H_{\mu\nu}(q). \quad (4.6)$$

Here  $k_1$  and  $k_2$  are the leptons' momenta and  $q = k_1 + k_2$ ,  $q^\mu q_\mu = Q^2$ . We define  $L$  to absorb the photon propagator, and the overall kinematic normalization of the cross section,  $1/8Q^2$ , where we neglect the lepton mass and average over spins. Similarly we absorb the integral over final-state phase space into  $H$ . The leptonic part is then given by the Dirac trace

$$\begin{aligned} L^{\mu\nu}(k_1, k_2) &= \frac{1}{8Q^2} \frac{e^2}{(Q^2)^2} \text{Tr}[k_1 \gamma_\mu k_2 \gamma_\nu] \\ &= \frac{e^2}{2(Q^2)^2} (k_1^\mu k_2^\nu + k_2^\mu k_1^\nu - (Q^2/2) g^{\mu\nu}) . \end{aligned} \quad (4.7)$$

The calculation of  $\sigma_{tot}$  is simplified by employing conservation of the electromagnetic current, which, as we mentioned above, is respected by QCD,

$$q^\mu H_{\mu\nu}(q) = H_{\mu\nu} q^\nu = 0 . \quad (4.8)$$

Now, because  $H$  is a symmetric tensor that can only depend on the total momentum  $q$ , we find that it has the form

$$H_{\mu\nu} = (q_\mu q_\nu - Q^2 g_{\mu\nu}) H(Q^2) , \quad (4.9)$$

with  $H(Q^2)$  a scalar function that can be found by

$$H(Q^2) = \frac{1}{3Q^2} (-g^{\mu\nu} H_{\mu\nu}) . \quad (4.10)$$

Combining these results, it is easy to show that

$$\sigma_{tot} = \frac{e^2}{6(Q^2)^2} (-g^{\mu\nu}) H_{\mu\nu}(Q) . \quad (4.11)$$

Thus, it is only necessary to compute the contraction of the hadronic tensor with  $g_{\mu\nu}$  to compute the total cross section.

To compute the hadronic tensor, we write it as the integral over three-particle phase space of the squared matrix element for gluon emission,

$$\begin{aligned} -g^{\mu\nu} H_{\mu\nu}(Q) &= \frac{1}{4(2\pi)^5} \int \frac{d^3 p_1}{|p_1|} \frac{d^3 k}{|k|} \delta([q - p_1 - k]^2) |\mathcal{M}(k, p_1)|_r^2 . \end{aligned} \quad (4.12)$$

Here  $p_1$  is the quark's,  $k$  the gluon's, and  $q = p_1 - k$  the antiquark's momentum, while  $|\mathcal{M}(k, p_1)|_r^2$  represents the contribution of Fig 4.1a to the squared matrix element. The subscript  $r$  denotes that this contribution is real as apposed to those from Fig 4.1b,d which involve virtual loops and are therefore complex. In this (spin-averaged) case,  $|\mathcal{M}|_r^2$  is independent of the direction of  $p_1$  and of the azimuthal angle  $\mathbf{k}$  about  $\mathbf{p}_1$ . We may then evaluate these angular integrals to give

$$\begin{aligned} & -g^{\mu\nu} H_{\mu\nu}(Q) \\ &= \frac{2}{(2\pi)^3} \int_0^\infty dp_1 p_1 \int_0^\infty dk k \int_{-1}^1 du \\ &\quad \times \delta(Q^2 - 2Q \cdot (p_1 + k) + 2|\mathbf{p}_1||\mathbf{k}|(1-u)) |\mathcal{M}(k, p_1)|_r^2 , \end{aligned} \quad (4.13)$$

where  $u$  is the cosine of the angle between  $\mathbf{p}_1$  and  $\mathbf{k}$  and  $Q = \sqrt{Q^2}$ .

Next let's have a look at the hadronic tensor corresponding to Fig. 4.1a. Because the fermions are now quarks, it includes the product of a Dirac trace times a color trace, given by

$$\begin{aligned} |\mathcal{M}(p_1, k)|_r^2 &= 2\text{Tr}[T_a^{(F)} T_a^{(F)}] g^2 e^2 \sum_f Q_f^2 \\ &\quad \times \left[ \frac{1}{(2p_1 \cdot k)(2p_2 \cdot k)} \text{Tr}[\gamma_\mu \not{p}_1 \gamma^\alpha (\not{p}_1 + \not{k}) \gamma^\mu \not{p}_2 \gamma_\alpha (-\not{p}_2 - \not{k})] \right. \\ &\quad \left. + \frac{1}{(2p_1 \cdot k)^2} \text{Tr}[\gamma_\mu (\not{p}_1 + \not{k}) \gamma^\alpha (\not{p}_1) \gamma_\alpha (\not{p}_1 + \not{k}) \gamma^\mu (\not{p}_2)] \right] . \end{aligned} \quad (4.14)$$

It is at this point that we see the kind of problems one encounters in a perturbative calculation. They are exactly of the sort anticipated in Section 3.1.1.

There are two denominator factors, corresponding to the propagators for the two virtual fermions in each diagram. Consider, for instance,

$$p_1 \cdot k = |\mathbf{p}_1||\mathbf{k}|(1-u) . \quad (4.15)$$

This factor vanishes at two generic points in phase space

$$\begin{aligned} k &= 0 \leftrightarrow k^\mu \text{ soft} , \\ u &= 1 \leftrightarrow \mathbf{k} \text{ collinear to } \mathbf{p}_1 . \end{aligned} \quad (4.16)$$

It is easy to check that the integral over phase space is divergent in both of these limits: the *soft* limit, where the gluon momentum vanishes, and the *collinear* limit, where it becomes parallel to the quark's momentum. In these two limits, the  $k$  and  $u$  integrals become, respectively,

$$\begin{aligned} \int_0^{\infty} \frac{dk}{k} &\leftrightarrow k^\mu \text{ soft ,} \\ \int^1 \frac{du}{1-u} &\leftrightarrow \mathbf{k} \text{ collinear to } \mathbf{p}_1 . \end{aligned} \quad (4.17)$$

Not surprisingly, there is yet another region where the integral diverges, for  $\mathbf{k}$  collinear to  $\mathbf{p}_2$ ,

$$p_2 \cdot k = |\mathbf{p}_2| |\mathbf{k}| (1+u) + O((1+u)^2) . \quad (4.18)$$

Thus, soft and collinear divergences are already present at one loop in massless QCD.

In Section 3.1.1 we argued that infrared sensitivity cancels between different final states. At this order, there are only two final states to choose from, the quark-antiquark state, and the quark-antiquark-gluon state. It is possible to show that if the integrands for these contributions to  $\sigma_{tot}$  are combined, all sources of divergence cancel, before any integrals are done [4.2]. For many purposes, however, it is useful to do the integrals in an *infrared regularized* theory, in which the soft and collinear divergences have been rendered finite by some modification of the theory, in much the same spirit as for UV divergences. It is important to realize that an infrared regulated theory is *not* the same as the original theory, because infrared regulation changes the long-distance behavior. But, in the limit that the regulator is taken away, the infrared-regulated theory should give the same predictions as the real theory for infrared safe quantities, which don't depend on the long-distance behavior anyway.

Actually, it is not so easy to find a completely satisfactory infrared regulator for QCD, one that doesn't affect the short distance behavior at some high order. Interestingly enough, dimensional regularization (Appendix C) provides such a regulator. In this case, we (formally) carry out all integrals in  $4 - 2\epsilon$  dimensions. Divergences appear as poles at vanishing regulator scale  $\epsilon$

(i.e. at four dimensions). There are some subtle points here, especially since the same method is also used to regulate UV divergences. Nevertheless, one may apply it consistently. Another method, that works well at least to one loop, is to assign a small mass,  $m_g$ , to the gluon (in Feynman gauge, for simplicity). Here infrared and collinear divergences appear as logarithms of  $m_g$ . This method may be dangerous beyond one loop, because a gluon mass breaks gauge invariance, but it works well enough at this level.

Let us quote the results for the two-particle and three-particle cross sections represented by Fig. 4.1. For the two-particle final state, the cross sections are, at one loop

$$\begin{aligned}\sigma_2^{(m_g)} &= \sigma_0 C_F \left( \frac{\alpha_s}{\pi} \right) \left[ -2\ln^2(Q/m_g) + 3\ln(Q/m_g) - \frac{7}{4} + \frac{\pi^2}{6} \right] \\ \sigma_2^{(\epsilon)} &= -\sigma_0 C_F \left( \frac{\alpha_s}{\pi} \right) \left( \frac{3(1-\epsilon)^2}{(3-2\epsilon)\Gamma(2-2\epsilon)} \right) \\ &\quad \times \left( \frac{4\pi\mu^2}{Q^2} \right)^{2\epsilon} \left( \frac{1}{\epsilon^2} + \frac{3}{2\epsilon} - \frac{\pi^2}{2} + 4 \right),\end{aligned}\tag{4.19}$$

for gluon-mass and dimensional regularization, respectively. Notice that, although the two expressions share some features, they are vastly different, and each depends upon one of the unphysical parameters,  $m_g$  or  $\epsilon$ . This is a sign that the long-distance behaviors of the regulated theories are different.

The three-particle final state gives these results at one loop:

$$\begin{aligned}\sigma_3^{(m_g)} &= \sigma_0 C_F \left( \frac{\alpha_s}{\pi} \right) \left[ 2\ln^2(Q/m_g) - 3\ln(Q/m_g) + \frac{5}{2} - \frac{\pi^2}{6} \right], \\ \sigma_3^{(\epsilon)} &= \sigma_0 C_F \left( \frac{\alpha_s}{\pi} \right) \left( \frac{3(1-\epsilon)^2}{(3-2\epsilon)\Gamma(2-2\epsilon)} \right) \\ &\quad \times \left( \frac{4\pi\mu^2}{Q^2} \right)^{2\epsilon} \left( \frac{1}{\epsilon^2} + \frac{3}{2\epsilon} - \frac{\pi^2}{2} + \frac{19}{4} \right).\end{aligned}\tag{4.20}$$

Comparing the two- and three-particle results for each choice of regularization, we find that most of their respective terms cancel, leaving behind exactly the simple  $O(\alpha_s)$  correction of Eq. (4.1). This demonstrates explicitly that the total cross section is independent of long distance behavior, at

least to this approximation. The explicit calculations of Ref. [4.1] show that it is possible to verify this result much more dramatically.

### 4.3 Energy-Energy Correlation

The total cross section for  $e^+e^-$  annihilation, being an infrared safe quantity, see Section 3.1, can be used to study the short distance behavior of the Standard Model without complications from long-distance physics. However, it is by no means the only such quantity. By looking at infrared safe quantities that probe the hadronic final states produced in  $e^+e^-$  annihilation, we can learn about the structure of the interaction Lagrangian that controls the short distance physics.

We have discussed in Section 4.1 how certain measurements can involve the final state in such a way that the measured quantity is not sensitive to collinear parton branching or the emission of soft partons (see Eqs. (3.7), (3.10)). There we used as an example the thrust distribution  $d\sigma/dT$  defined in Eqs. (3.8), (3.9). Another frequently used quantity is the energy-energy correlation function [4.3],

$$\frac{1}{\sigma_T} \frac{d\Sigma}{d \cos \chi}. \quad (4.21)$$

A convenient way to express the definition of  $\Sigma$  is to use the general equation (3.7). If we let  $\mathcal{I}$  in (3.7) be  $d\Sigma/d \cos \chi$  then the functions  $\mathcal{S}_n$  that define the contribution from an  $n$  particle final state are

$$\mathcal{S}_n(p_1^\mu, \dots, p_n^\mu) = \sum_{i=1}^n \sum_{j=1}^n \frac{E_i E_j}{s} \delta(\cos \chi - \cos \chi_{ij}), \quad (4.22)$$

where  $\chi_{ij}$  is the angle between particles  $i$  and  $j$ . Recall that the normalization of the  $\mathcal{S}_n$  is such that  $\mathcal{S}_n = 1$  for all  $n$  gives the total cross section. Then since  $\sum_i E_i = \sqrt{s}$ , the normalization for  $\Sigma$  is

$$\frac{1}{\sigma_T} \int_{-1}^1 d \cos \chi \frac{d\Sigma}{d \cos \chi} = 1. \quad (4.23)$$

The energy-energy correlation function is infrared safe. To verify that the required condition (3.10) is satisfied, consider  $\mathcal{S}_{n+1}(p_1^\mu, \dots, (1-\lambda)p_n^\mu, \lambda p_n^\mu)$ .

We have

$$\begin{aligned}
& \mathcal{S}_{n+1}(p_1^\mu, \dots, (1-\lambda)p_n^\mu, \lambda p_n^\mu) \\
&= \sum_{i=1}^{n-1} \sum_{j=1}^{n-1} \frac{E_i E_j}{s} \delta(\cos \chi - \cos \chi_{ij}) \\
&\quad + 2 \sum_{i=1}^{n-1} \frac{E_i [\lambda E_n + (1-\lambda)E_n]}{s} \delta(\cos \chi - \cos \chi_{in}) \\
&\quad + \frac{[\lambda E_n + (1-\lambda)E_n]^2}{s} \delta(\cos \chi - \cos \chi_{nn}) \\
&= \mathcal{S}_n(p_1^\mu, \dots, p_n^\mu). \tag{4.24}
\end{aligned}$$

There are other distributions besides the thrust distribution and the energy-energy correlation that probe the shape of the hadronic energy distribution. Jet cross sections, to which we now turn, fall into this class. Concise descriptions of other, related quantities, with calculations and references, may be found in ref. [4.4].

#### 4.4 Jets

In a typical electron-positron annihilation event at LEP or SLC, two, or sometimes three or more, sprays of particles are produced. The more energetic of the particles within each spray are typically confined to an angular range of a few tenths of a radian. These sprays of particles are called jets, and various measurable cross sections to produce jets are studied [4.5], [4.6]. For instance, one can measure the inclusive cross section to make two jets with given energies and angles, plus anything else. Most commonly, one measures the cross section for the final state to contain exactly 2,3,4 ... jets.

One thinks of a jet as consisting of the decay products of a single off-shell parton, a quark or gluon, that was produced in the annihilation by a short-distance process. It is not, however, completely straightforward to define precisely how many jets are present in a given final state and what their momenta and energies are. The physical problem is that the decay products from an energetic parton are not infinitely well collimated, and, in particular, will generally include the remnants of some rather soft gluons

that are emitted at large angles. Worse, because partons can join as well as divide, and because of quantum interference, a given hadron can be a “decay product” of more than one hard parton at once. Thus a jet cross section is to some extent an artifact.

If a jet cross section is an artifact, so be it. One must simply give a careful definition how the jet content of the final state is to be measured. Then, one must calculate (perturbatively) the cross section to make jets in a given configuration according to this definition. In order that the cross section reflect short distance physics, one must arrange the jet definition so that the corresponding jet cross sections are infrared safe in the sense of Eq. (3.10).

The possibility of calculating and measuring infrared safe jet cross sections was first explored in Ref. [4.6]. The definition given there involved cones, something like the cones often used to define jets in hadron-hadron collisions, as described in Section 7. The definitions used nowadays for electron-positron collisions involve an algorithm for successively combining hadrons into jets, using some function of momenta as a measure of “jettiness”. (In the corresponding calculation, one uses the same algorithm to successively combine partons into jets.) Here, we shall describe the original example of this class, the so-called JADE algorithm [4.7]. There are several variations that are used, of which we may mention particularly the Durham algorithm [4.8]. A summary may be found in [4.9].

The successive combination algorithms are iterative. At each stage, two jets from a list of jets are combined into one. One begins with a list of jets that are just the observed particles. At each stage of the iteration, one considers two jets  $i$  and  $j$  as candidates for combination into a single jet according to the value of a dimensionless “jettiness” variable  $y_{ij}$ . Pairs with small  $y_{ij}$  are considered to be the most jetlike. For the JADE algorithm,

$$y_{ij} = \frac{2E_i E_j (1 - \cos \theta_{ij})}{s}. \quad (4.25)$$

The pair  $i,j$  with the smallest value of  $y_{ij}$  is combined first. When two jets are combined the four-momentum  $p^\mu$  of the new jet is determined by a combination formula. For the JADE algorithm, the combination formula is

simply

$$p^\mu = p_i^\mu + p_j^\mu. \quad (4.26)$$

After this joining, there is a new list of jets. The process continues until every remaining  $y_{ij}$  is larger than a preset cutoff,  $y_{\text{cut}}$ . In this way, each event is classified as containing two, three, four, etc. jets, where the number of jets depends on the cutoff  $y_{\text{cut}}$  chosen.

Notice that this algorithm is infrared safe, because it satisfies Eq. (3.10). A particle that has only an infinitesimal energy will not affect the final number of jets, or their four-momenta, since it will contribute only an infinitesimal amount to the final four-momentum of the jet in which it is included. Similarly, if two particles are nearly collinear, with  $p_i^\mu \approx \lambda p^\mu$  and  $p_j^\mu \approx (1 - \lambda)p^\mu$ , then the first step of the algorithm is to combine them into one jet with momentum close to  $p^\mu$ .

## 4.5 Calculations

One can categorize the possible infrared safe quantities in electron-positron annihilation as “ $N$ -jet like” by considering the functions  $S_n$ , eq. (3.7), that define the measurement. If  $S_2 \neq 0$ , we say that the quantity is “two-jet like.” If  $S_2 = 0$  but  $S_3 \neq 0$ , we say that the quantity is “three-jet like.” With this nomenclature, the total annihilation cross section is two-jet like. Quantities such as the cross section to make exactly three jets (for a given  $y_{\text{cut}}$ ) or the energy-energy correlation function away from  $\chi = 0, \pi$  are “three jet-like”.

As we have seen in Section 4.1, the total cross section has been calculated to order  $\alpha_s^3$ . Since this is three orders beyond the Born approximation, the comparison of the prediction to data can provide an extraordinarily stringent test of the Standard Model. However, there is an experimental limitation of the usefulness of a two-jet like quantity like the total cross section as a way to measure  $\alpha_s$ , or to provide a test of the QCD part of the Standard Model. The limitation is that the Born approximation to such a quantity is independent of  $\alpha_s$ ; QCD enters only in the higher order corrections. Thus extraordinary experimental accuracy is required in order to measure the QCD contribution precisely.

With three-jet like quantities, one is measuring something that, in the Born approximation, is proportional to  $\alpha_s$ . Thus the experimental demands are less stringent. However, the theoretical difficulties are greater. Non-perturbative effects are estimated to play a larger role than in the completely inclusive total cross section. (See, for example, ref. [4.9].) More importantly, the perturbative calculations are more complicated. The calculation depends on realizing cancellations of collinear and soft divergences between contributions from four parton final states and from three parton final states with virtual loop corrections. (The results for the virtual loop graphs are generally taken from the work of Ellis, Ross, and Terrano [4.10].) There are calculations of individual three-jet like quantities at order  $\alpha_s^2$  in the literature. References may be found in [4.4]. There is now also a computer program by Kunszt and Nason [4.4] that can calculate any infrared finite three-jet quantity at order  $\alpha_s^2$ . Basically, one has only to supply suitable computer code for the functions  $S_2$  and  $S_3$  that specify the measurement.

## References

- [4.1] L.R. Surguladze and M.A. Samuel, Phys. Rev. Lett. **66**, 560 (1991); S.G. Gorishny, A.L. Kataev and S.A. Larin, Phys. Lett. **B259**, 144 (1991).
- [4.2] G. Sterman, Phys. Rev. **D17**, 2773 (1978).
- [4.3] C. L. Basham, L. S. Brown, S. D. Ellis, and S. T. Love, Phys. Rev. **D19**, 2018 (1979); L. S. Brown and S. D. Ellis, Phys. Rev. **D24**, 2383 (1981).
- [4.4] Z. Kunszt, P. Nason, G. Marchesini and B. R. Webber, in G. Altarelli, R. Kleiss and C. Verzegnassi, eds, *Z Physics at LEP 1*, Volume 1: Standard Physics, (CERN, Geneva, 1989).
- [4.5] G. Sterman, Phys. Rev. **D17**, 2773, 2789 (1978).
- [4.6] G. Sterman and S. Weinberg, Phys. Rev. Letters, **39**, 1436 (1977).

- [4.7] JADE Collab., S. Bethke *et al.*, Phys. Lett. **B213**, 235 (1988).
- [4.8] Yu. L. Dokshitzer, contribution to *Workshop on Jets at LEP and HERA*, Durham, December 1990.
- [4.9] S. Bethke, Z. Kunszt, D. E. Soper and W. J. Stirling, Nucl. Phys. **B370**, 310 (1992).
- [4.10] R. K. Ellis, D. A. Ross and A. E. Terrano, Nucl. Phys. **B178**, 421 (1981).

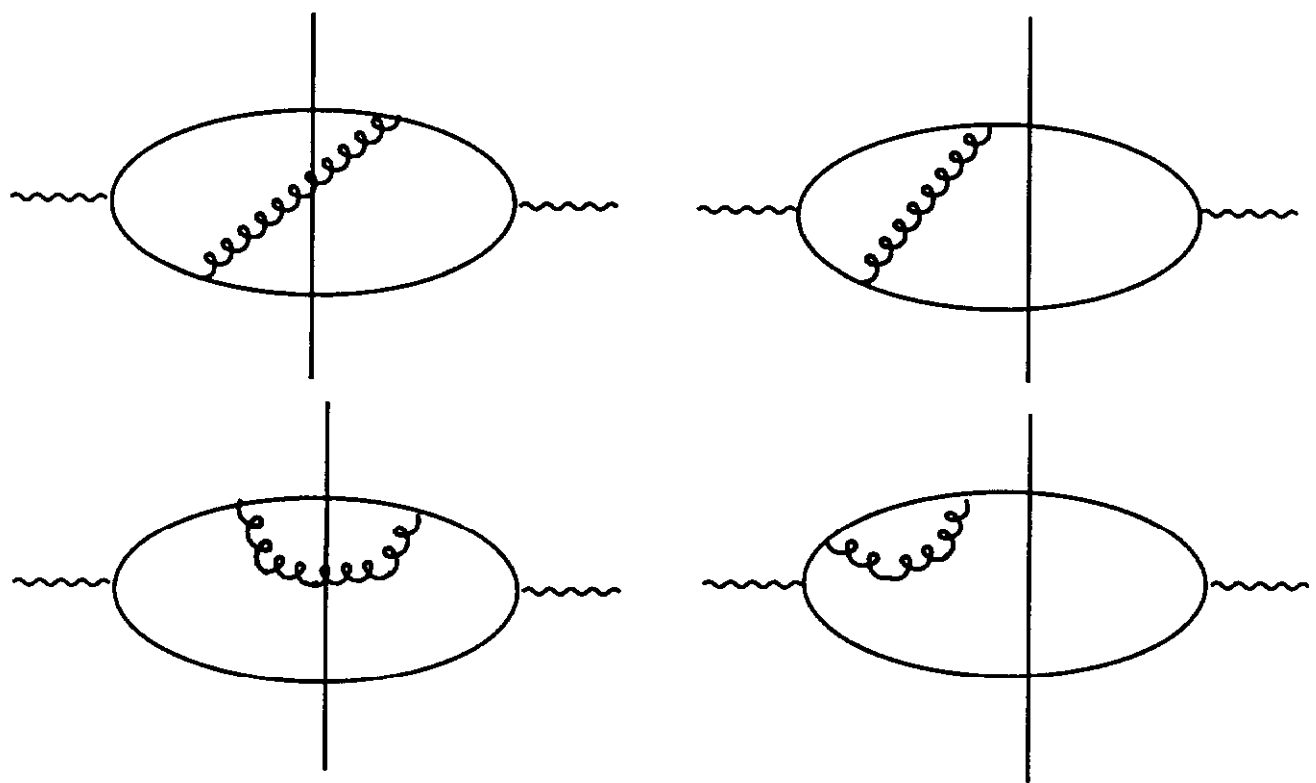


Figure 4.1. One-loop corrections to the  $e^+e^-$  annihilation cross section.

7

## 5 Deeply Inelastic Scattering

### 5.1 Use of Perturbative Corrections in DIS

The use of parton distributions in pQCD is similar to their use in the parton model. The basic facts are still: (i) that the IR safe short-distance functions  $C_a^{(Vi)}$  are independent of the external hadron  $h$  and (ii) that the distributions  $\phi_{i/h}$  are “universal”, for instance, the same for  $F_1$  as for  $F_2$ . For convenience, we reproduce here the DIS factorization theorems, Eq. (3.11) and Eq. (3.12),

$$\begin{aligned} F_a^{(Vh)}(x, Q^2) &= \sum_{i=f, \bar{f}, G} \int_0^1 \frac{d\xi}{\xi} C_a^{(Vi)}(x/\xi, Q^2/\mu^2, \alpha_s(\mu^2)) \\ &\quad \times \phi_{i/h}(\xi, \mu^2), \quad (a = 1, 3) \\ F_2^{(Vh)}(x, Q^2) &= \sum_{i=f, \bar{f}, G} \int_0^1 d\xi C_2^{(Vi)}(x/\xi, Q^2/\mu^2, \alpha_s(\mu^2)) \\ &\quad \times \phi_{i/h}(\xi, \mu^2) \end{aligned} \quad (5.1)$$

(where we have set the factorization scale equal to the renormalization scale  $\mu$ ), and the evolution equation Eq. (3.19),

$$\mu \frac{d}{d\mu} \phi_{i/h}(x, \mu, \alpha_s(\mu^2)) = \sum_{j=f, \bar{f}, G} \int_x^1 \frac{d\xi}{\xi} P_{ij} \left( \frac{x}{\xi}, \alpha_s(\mu^2) \right) \phi_{j/h}(\xi, \mu, \alpha_s(\mu^2)). \quad (5.2)$$

With these results in hand, we can make predictions by combining perturbative calculations with experimental input. In this section, we discuss how this works in low order corrections.

Unlike an infrared safe total cross section, the hard-scattering coefficient functions of DIS factorization are *not* simple finite functions of  $\alpha_s$ . Instead, they must be defined as infrared safe “distributions”, generalized functions which give finite answers when convoluted with smooth functions. The most familiar example of a distribution is a delta function. Here, we introduce the “plus” distribution, denoted

$$\left[ \frac{g(x)}{1-x} \right]_+, \quad (5.3)$$

whose integral with a smooth function  $f(x)$  is defined by

$$\int_z^1 dx f(x) \left[ \frac{g(x)}{1-x} \right]_+ = \int_z^1 dx \frac{(f(x) - f(1))g(x)}{1-x} - f(1) \int_0^z dx \frac{g(x)}{1-x}. \quad (5.4)$$

A plus distribution corresponds to a divergent integral that is regularized by a divergent subtraction, in this case  $f(1)$  times the integral from 0 to 1. (Note that the second term on the right vanishes when  $z = 0$ .) Plus distributions are ubiquitous in both hard-scattering functions and parton distributions, for all nontrivial factorization theorems in QCD. The manner in which they arise in one-loop corrections is discussed in Section 5.4 below.

The three basic quantities in the factorization and evolution theorems above are: the coefficient functions  $C_a^{(\gamma i)}$ , the evolution kernels  $P_{ij}$ , and the parton distributions  $\phi_{i/h}$ . Of these, the first two are computable as power series in  $\alpha_s$  as realistic, infrared-safe quantities. The distributions, on the other hand, are directly computable only for  $\phi_{i/j}$ , with both  $i$  and  $j$  partons, and then only in an infrared-regulated version of the theory. Such unphysical parton distributions, however, enable us to isolate the physical coefficient functions and evolution kernels. Let us review how this works.

*Combining Theory and Experiment.* As an example, consider the relation between the structure functions  $F_a^{(Vh)}$ ,  $V = \gamma, W^\pm$ , and the physical parton distributions  $\phi_{i/h}(x, \mu^2)$ . The procedure can be summarized as:

- (a) Compute the regulated distributions  $\phi_{i/q}$  and  $\phi_{i/g}$  to some order in perturbation theory.
- (b) Compute  $F_a^{(Vj)}$ , with  $j = q, g$  to the same order.
- (c) Combine the results of (a) and (b) to derive  $C_a^{(Vj)}$  to this order.
- (d) Combine  $C_a^{(Vj)}$  with experimentally determined  $F_a^{(Vh)}$  to derive the non-perturbative  $\phi_{j/h}$  to the same order in perturbation theory by applying the factorization theorem.

These distributions, in turn, can be combined with hard scattering functions from other processes to derive predictions from the theory. Note that the

parton distributions and coefficient functions are factorization-scheme dependent, in the sense described in Section 3.2. The evolution kernels,  $P_{ij}$ , however, are scheme-independent in the one-loop approximation.

At  $O(\alpha_s)$  the procedure we have just described is particularly straightforward. For instance, in the electromagnetic case Eq. (3.11) and Eq. (3.12) yield,

$$F_a^{(Vf)(1)}(x, Q^2) = \phi_{f/f}^{(1)}(x, \mu^2) + C_a^{(Vf)(1)} \left( x, \frac{Q^2}{\mu^2}, \alpha_s(\mu) \right). \quad (5.5)$$

Here and below, we suppress an overall factor  $Q_f^2$  (the fractional charge of the quark) in  $F_a$  for electromagnetic scattering.

## 5.2 One-Loop Corrections in DIS

$\overline{\text{MS}}$  scheme. In the  $\overline{\text{MS}}$  scheme, the distributions are defined by matrix elements as in Section 3.4, and are simple at one loop in perturbation theory, although the resulting coefficient functions tend to be a bit complicated. They are also convention dependent. To compare the following results with the literature it is necessary to check not only the definitions of the  $F_a$  Eq. (2.15) but also the explicit factorization formulas (5.1). For instance the results below for  $C_2$  differ from those quoted in [5.2] by a factor  $x$ .

From the procedure just described, the explicit nonzero one-loop coefficient functions for DIS are given in the  $\overline{\text{MS}}$  factorization scheme by [5.2] [5.3]

$$\begin{aligned} C_2^{(Vq)(1)} &= C_2(F) \frac{x}{2} \left[ \frac{1+x^2}{1-x} \left( \ln \frac{(1-x)}{x} - \frac{3}{4} \right) + \frac{1}{4}(9+5x) \right]_+, \\ C_1^{(Vq)(1)} &= \frac{1}{2x} C_2^{(Vq)(1)} - C_2(F) \frac{1}{2} x, \\ C_3^{(Vq)(1)} &= \frac{1}{x} C_2^{(Vq)(1)} - C_2(F)(1+x), \\ C_2^{(Vg)(1)} &= T(F) n_f x \left[ (x^2 + (1-x)^2) \ln \left( \frac{1-x}{x} \right) - 1 + 8x(1-x) \right], \\ C_1^{(Vg)(1)} &= \frac{1}{2x} C_2^{(VG)(1)} - T(F) n_f [4x(1-x)], \end{aligned} \quad (5.6)$$

where  $n_f$  is the number of quark flavors,  $C_2(F) = 4/3$  for  $N_c = 3$  and  $T(F) = 1/2$  (see Appendix A). Similarly, the one-loop kernels are given by  $(\alpha_s/2\pi)P_{ij}^{(1)}$ , with [5.4]

$$\begin{aligned} P_{qq}^{(1)}(x) &= C_2(F) \left[ (1+x^2)(\frac{1}{1-x})_+ + \frac{3}{2}\delta(1-x) \right] , \\ P_{qg}^{(1)}(x) &= 2T(F) \left[ (1-x)^2 + x^2 \right] , \\ P_{gg}^{(1)}(x) &= C_2(F) \frac{(1-x)^2 + 1}{x} , \\ P_{gg}^{(1)}(x) &= 2C_2(A) \left[ \frac{x}{(1-x)_+} + \frac{1-x}{x} + x(1-x) \right] \\ &\quad + (\frac{11}{6}C_2(A) - \frac{2}{3}T(F)n_f)\delta(1-x) , \end{aligned} \quad (5.7)$$

where  $C_2(A) = 3$  and  $T(F) = 1/2$  in QCD (Appendix A). Finally, the  $\overline{\text{MS}}$  distributions for partons in partons are (with  $\epsilon \equiv 2 - n/2$ )

$$\phi_{i/j}(x, \epsilon) = -\frac{1}{\epsilon} \frac{\alpha_s}{2\pi} \left( \frac{\mu^2}{M^2} \right)^\epsilon P_{ij}^{(1)}(x) , \quad (5.8)$$

where we conventionally choose

$$M^2 = \mu^2 e^{\gamma_E - \ln 4\pi} , \quad (5.9)$$

with  $\gamma_E$  Euler's constant. This choice corresponds to a natural definition for the renormalized matrix elements that define the distributions (see Section 3.4).

*DIS scheme.* The DIS scheme is defined to *all* orders in perturbation theory by Eq. (3.16),

$$\begin{aligned} C_2^{(Vq)}(x) &= \delta(1-x) , \\ C_2^{(V\bar{q})}(x) &= \delta(1-x) , \\ C_2^{(Vg)}(x) &= 0 . \end{aligned} \quad (5.10)$$

That is we renormalize the parton densities so that the parton model is exact at  $\mu = Q$ . This gives somewhat more complicated results for one-loop

distributions of partons in partons [5.1], which however, are determined in terms of the  $\overline{\text{MS}}$  distribution to one loop by

$$\phi_{q/h}(x, \mu^2)^{(\text{DIS})} = [1 + \alpha_s(\mu) C_2^{(Vq)(\overline{\text{MS}})}] \otimes \phi_{q/h}^{(\overline{\text{MS}})} + \alpha_s(\mu) C_2^{(Vg)(\overline{\text{MS}})} \otimes \phi_{g/h}^{(\overline{\text{MS}})} / 2n_f , \quad (5.11)$$

where  $\otimes$  represents the convolution in Eq. (5.1). Here the effect of the gluon distribution in  $F_2$  is shared evenly by the  $n_f$  quark flavors (the same number as is used in the beta function at this momentum scale, see Section 1.5). Similarly, a frequently-used (but nonunique) definition for the DIS gluon distribution in terms of the  $\overline{\text{MS}}$  distributions at order  $\alpha_s$  is

$$\phi_{g/h}(x, \mu^2)^{(\text{DIS})} = [1 - \alpha_s(\mu) C_2^{(Vg)(\overline{\text{MS}})}] \otimes \phi_{g/h}^{(\overline{\text{MS}})} - \alpha_s(\mu) \sum_q C_2^{(Vq)(\overline{\text{MS}})} \otimes \phi_{q/h}^{(\overline{\text{MS}})} . \quad (5.12)$$

These relations holds to order  $\alpha_s$  for  $h$  a parton or a physical hadron.

Because of the relation Eq. (5.5), the remaining coefficient functions in the DIS scheme are trivially found from those in the  $\overline{\text{MS}}$  scheme. The reward for the somewhat complicated partonic distributions in the DIS scheme (remember, they are unphysical anyway), is much simpler one-loop coefficient functions; in addition to the defining equations, Eq. (5.10) we find (see, for instance, Ref. [5.4]),

$$C_1^{(Vq)(1)}(x) = -\frac{1}{2} C_2(F) x , \quad (5.13)$$

$$C_1^{(Vg)(1)}(x) = -T(F)n_f 4x(1-x) , \quad (5.14)$$

$$C_3^{(Vq)(1)}(x) = -C_2(F)(1+x) . \quad (5.15)$$

### 5.3 Two-Loop Corrections

Recently, DIS coefficient functions have been calculated in DIS and  $\overline{\text{MS}}$  schemes by van Neerven and coworkers [5.3]. This, of course, requires the determination of perturbative parton distributions and evolution functions at two loops as well. The full expressions are bulky, and we shall not reproduce them here. To give the flavor of the results, however, it may be useful to give the two-loop evolution kernel for the nonsinglet distributions (Section 3.2.3),

$P_{ij}^{NS}(x)$ , [5.4]:

$$\begin{aligned}
P_{qq}^{NS}(x, \alpha_s) = & \frac{\alpha_s}{2\pi} C_F \left( \frac{1+x^2}{1-x} \right)_+ + \left( \frac{\alpha_s}{2\pi} \right)^2 \left\{ C_F^2 \left[ -2 \left( \frac{1+x^2}{1-x} \right) \ln x \ln(1-x) \right. \right. \\
& - 5(1-x) - \left( \frac{3}{1-x} + 2x \right) \ln x - \frac{1}{2}(1+x) \ln^2 x \left. \right] \\
& + \frac{1}{2} C_F C_A \left[ \left( \frac{1+x^2}{1-x} \right) \left( \ln^2 x - \frac{11}{3} \ln \frac{1-x}{x^2} + \frac{367}{16} - \frac{\pi^2}{3} \right) \right. \\
& + 2(1+x) \ln x + \frac{61}{12} - \frac{215}{12} x \left. \right] \\
& + \frac{2}{3} C_F T \left[ \left( \frac{1+x^2}{1-x} \right) \left( \ln \frac{1-x}{x^2} - \frac{29}{12} \right) + \frac{1}{4} + \frac{13}{4} x \right] \}_+ \\
& \left. + \delta(1-x) \int_0^1 dx Q_{q\bar{q}}(x, \alpha_s) + O(\alpha_s^3) \right\}_+,
\end{aligned} \tag{5.16}$$

where

$$\begin{aligned}
Q_{q\bar{q}}(x, \alpha_s) = & \left( \frac{\alpha_s}{2\pi} \right)^2 \left( C_F - \frac{1}{2} C_A \right) C_F \left[ 2(1+x) \ln x + 4(1-x) \right. \\
& \left. + \frac{1+x^2}{1+x} \left( \ln^2 x - 4 \ln x \ln(1+x) - 4 \text{Li}_2(-x) - \frac{\pi^2}{3} \right) \right].
\end{aligned} \tag{5.17}$$

## 5.4 Computation of One-Loop DIS Correction

Typical (cut) Feynman diagrams that contribute to  $W_{\mu\nu}^{(\gamma f)}$  are shown in Fig. 5.1. At lowest order, they involve either gluon emission, or one-loop radiative corrections. Here we will give just enough detail on the gluon emission process to illustrate the physical content of factorization. For more details, see [5.5].

Since we are interested in structure functions, it is convenient to use the contractions

$$\begin{aligned}
-g^{\mu\nu} W_{\mu\nu}^{(\gamma f)(1)} &= \frac{1}{x} F_2^{(\gamma f)(1)} - \frac{3}{2} \left( F_2^{(\gamma f)(1)} - 2x F_1^{(\gamma f)(1)} \right), \\
p^\mu p^\nu W_{\mu\nu}^{(\gamma f)(1)} &= \frac{Q^2}{8x^3} \left( F_2^{(\gamma f)(1)} - 2x F_1^{(\gamma f)(1)} \right).
\end{aligned} \tag{5.18}$$

Of these, the first is by far the more demanding to calculate, because the Dirac equation may be used to eliminate all but one of the diagrams shown in Fig. 5.1 for  $p^\mu p^\nu W_{\mu\nu}$ . (We should note that when these calculations are carried out using the method of dimensional regularization these identities become somewhat more complicated. See Appendix C.)

Let's have a look at the real-gluon contribution to  $-g^{\mu\nu}W_{\mu\nu}$ . It can be computed as if the diagrams described the Born approximation for the two-to-two process  $\gamma^* + f \rightarrow f + g$ , with  $g$  a gluon,

$$-g^{\mu\nu}W_{\mu\nu}^{(\gamma f)(1)} = \int_{PS} (|\mathcal{M}^{(\gamma f)}(s, t, q^2)|^2)^{(1)}, \quad (5.19)$$

where  $\mathcal{M}$  is the squared matrix element for this process, normalized according to Eq. (2.16), and averaged over the spin of the initial-state quark.  $\int_{PS}$  denotes the integral over two-particle phase space. The matrix element is described in terms of the usual kinematic variables,

$$s = (p+q)^2, \quad t = (p-k)^2, \quad u = (q-k)^2, \quad s+t+u = -Q^2, \quad (5.20)$$

in terms of which it is given explicitly by (recall, we are suppressing  $Q_f$ )

$$(|\mathcal{M}^{(\gamma f)}(s, t, q^2)|^2)_{real}^{(1)} = 4\alpha_s \frac{4}{3} \left( \frac{s}{-t} + \frac{-t}{s} - \frac{2uq^2}{st} \right). \quad (5.21)$$

The phase space integral is particularly simple in the center of mass frame, where it reduces to an integral over  $\xi = \cos\theta$ , with  $\theta$  the angle between  $\mathbf{p}$  and  $\mathbf{k}$ . In this frame,  $t$ ,  $u$  and  $s$  are given by

$$t = \frac{-Q^2(1-\xi)}{2x}, \quad u = \frac{-Q^2(1+\xi)}{2x}, \quad s = \frac{Q^2(1-x)}{x}. \quad (5.22)$$

As usual,  $x = Q^2/2p \cdot q$ . Collecting these expressions in Eq. (5.19), we have

$$(-g^{\mu\nu}W_{\mu\nu})_{real}^{(1)} = \frac{\alpha_s}{4\pi} \frac{4}{3} \int_{-1}^1 d\xi \left( \frac{2(1-x)}{1-\xi} + \frac{1-\xi}{2(1-x)} + \frac{2x(1+\xi)}{(1-x)(1-\xi)} \right). \quad (5.23)$$

As it stands this expression has problems of two kinds, closely related to those found at one loop in  $e^+e^-$  annihilation.

First, the unmodified integral diverges at  $\xi = 1$ , that is, when the gluon is parallel to the initial-state quark. This is the familiar collinear divergence, associated with the degeneracy of on-shell single-quark and parallel-moving quark-gluon states. It is just the sort of contribution that corresponds to the evolution of an isolated quark long before the interaction takes place, and should be absorbed into the distribution  $\phi_{f/f}$ . In a careful calculation, we would regularize the collinear divergence dimensionally, or by giving the quark a mass. We can even cut off the angular integral at some minimum angle: each of these choices will only show up in the precise definition of the infrared sensitive part of  $\phi_{f/f}$ , which we are going to discard anyway. We will therefore assume that regularization has been carried out, and not modify the explicit expressions below. Thus we may assume that the expression for  $W^{(1)}$  is well-defined for all  $x \neq 1$ .

The divergences as  $x \rightarrow 1$  are our second problem. Given that  $s = Q^2(1 - x)/x$ , they are evidently associated with a vanishing mass for the final state, which happens if the emitted gluon has either zero momentum (soft divergence), or is collinear to the outgoing quark. Divergences of this sort are not candidates for absorption into the parton distribution, because they depend on details of the momentum transfer and the final state. On the other hand, an unmitigated divergence of this kind cannot be pushed into the hard-scattering functions  $C(z)$  either, because a pole at  $z = 1$  in  $C(z)$  would lead to a singularity in the basic factorization integral, Eq. (5.1), whenever  $x = \xi$ . If factorization is going to work, the  $x = 1$  poles must be canceled.

As in  $e^+e^-$  annihilation, we look to virtual processes to cancel divergences associated with real-gluon emission. There is an important difference, however, in the kinematics of DIS and the annihilation processes. The virtual diagrams of Fig. 5.1 can only contribute at  $x = 1$  precisely; in fact, they are proportional to a factor  $\delta(1 - x)$ , which comes from the mass-shell delta function  $\delta([p + q]^2)$ . Thus, as anticipated above, the complete answer will be infrared finite as a distribution, rather than as a function.

Let's now skip to the answer. It will consist of plus distributions in  $x$ , in addition to finite terms. Collinear-divergent integrals will remain, which will have to be absorbed in the parton distributions. To compare real and virtual-

gluon corrections, we will change variables from the cosine  $\xi$  to the transverse momentum of the gluon,  $\mathbf{k}_T$ , relative to the direction of the incoming quark. In the center of mass frame, the relation between the two variables is

$$k_T^2 = Q^2 \frac{1-x}{x} (1-\xi^2). \quad (5.24)$$

Leaving the divergent  $k_T^2$  integral explicit, the one-loop electromagnetic structure functions are

$$\begin{aligned} F_2^{(\gamma f)(1)}(x) &= \frac{\alpha}{2\pi} \left\{ \int_0^{Q^2} \frac{dk_T^2}{k_T^2} \left( \left[ \frac{1+x^2}{1-x} \right]_+ + \frac{3}{2}\delta(1-x) \right) \right. \\ &\quad \left. + C_2(F) \left[ \frac{1+x^2}{1-x} \left( \ln \frac{(1-x)}{x} - \frac{3}{2} \right) + \frac{1}{4}(9+5x) \right]_+ \right\}, \\ 2xF_1^{(\gamma f)(1)} &= F_2^{(\gamma f)(1)} - C_2(F) \frac{\alpha}{2\pi} 2x. \end{aligned} \quad (5.25)$$

In the expression for  $F_2$ ,  $[9+5x]_+$  is defined by direct analogy to Eq. (5.4). We see explicitly the collinear divergent  $\mathbf{k}_T$  integral, which will be absorbed into  $\phi_{f/f}^{(1)}$  according to Eq. (5.5), and the evolution kernel

$$\left[ \frac{1+x^2}{1-x} \right]_+ + \frac{3}{2}\delta(1-x) \equiv P_{qq}^{(1)}(x), \quad (5.26)$$

which is of central importance in determining the  $Q^2$  dependence of the DIS cross section (Section 3.2.3).

As promised, all  $x \rightarrow 1$  divergences have canceled in Eq. (5.25), a necessary condition for factorization. Also, we note that  $F_2$  and  $F_1$  differ by an infrared safe function. This means that the same parton distribution  $\phi_{f/f}$  will absorb the infrared sensitivity of both structure functions. This is another prerequisite for factorization. Thus the calculation of DIS structure functions at one loop gives us two highly nontrivial checks of the factorization formulas, Eq. (5.1).

The explicit forms of one-loop corrections suggest the two standard choices of parton distributions, discussed in Section 5.2 above,

$$\phi_{f/f}^{(1)}(x, Q^2)_{\overline{\text{MS}}} = \frac{\alpha_s(Q^2)}{2\pi} \int_0^{\mu_f^2} \frac{dk_T^2}{k_T^2} P_{qq}(x), \quad (5.27)$$

$$\phi_{f/f}^{(1)}(x, Q^2)_{\text{DIS}} = F^{(\gamma f)(1)}(x, \alpha_s(Q^2)). \quad (5.28)$$

The first, “ $\overline{\text{MS}}$ ”, distribution, (Eq. (5.27)), absorbs as little as possible into  $\phi$ , that is, only the collinear divergent term, leaving the remainder to the  $C_a$ ’s. It is particularly simple in dimensional regularization, where the divergent term may be identified as the coefficient of a pole like  $1/(n - 4)$ , with  $n$  the “number” of dimensions. Alternately, in the second, “DIS” distribution, (Eq. (5.28)), we absorb as much as we can in the parton distribution, the standard choice being *all* of  $F_2^{(\gamma f)}(x, Q_0^2)$ , at the momentum scale  $Q_0^2 = \mu_f^2$ .

## 5.5 Review of DIS Experiments

### 5.5.1 Historical perspective

Early work on electron-nuclei scattering led to the discovery of the *scaling property* of the structure functions [5.6]. This scaling property demonstrated the existence of point-like constituents—partons—within the proton; these partons are now identified as the quarks and gluons. In a sense, DIS experiments of the 1960’s established the sub-structure of the proton in the same manner that the Rutherford scattering experiments established the sub-structure of the atom in 1911.

DIS experiments provided the experimental foundation for the parton model, Section 2, which, for the case of lepton-hadron scattering, can be summarized by the following formula:  $\sigma(\ell h \rightarrow \ell' X) = \phi_{a/h} \otimes \hat{\sigma}(\ell a \rightarrow \ell' X)$ , where  $\phi_{a/h}$  is the parton distribution function (PDF),  $\hat{\sigma}(\ell a \rightarrow \ell' X)$  is the hard scattering cross section, and  $\otimes$  represents convolution in momentum fraction. The implicit assumption in the parton model is that the lepton scatters *incoherently* from the parton constituents. The principal achievement of the parton model is that we have taken a physical cross section which is difficult to calculate directly, and divided it into a term that we can calculate in perturbation theory,  $\hat{\sigma}(\ell a \rightarrow \ell' X)$ , and a term that we extract from experiment,  $\phi_{a/h}$ .

Obviously, the utility of the parton model relies on our ability to determine  $\phi_{a/h}$ , or equivalently,<sup>2</sup> the structure functions,  $F_i$ . The basic pro-

---

<sup>2</sup>Note, to leading order, the structure functions are simply related to the parton distributions. However, beyond leading-order, the relations are more complex.

cedure used is to compute  $\hat{\sigma}(\ell a \rightarrow \ell' X)$  in perturbation theory, measure  $\sigma(\ell h \rightarrow \ell' X)$  experimentally, and thereby extract  $\phi_{a/h}$ . Unfortunately, this is easier said than done, as we must unfold the convolution to find  $\phi_{a/h}$ .

Presently, the data from DIS experiments provide the most precise determination of the functions  $\phi_{a/h}$ . The advantage of the DIS process is apparent when contrasted with a hadron-hadron scattering process where the parton model formula would read  $\sigma = \phi \otimes \hat{\sigma} \otimes \phi$ , and we would have to unfold *two* convolutions to extract  $\phi$ .

Although an important goal of DIS experiments is the extraction of PDF's, these experiments cover a wide range of topics, including the precision measurements of  $\sin \theta_W$ , Cabibbo-Kobayashi-Maskawa matrix elements, quark masses, and branching ratios. We will limit the scope of our discussion, however, primarily to the extraction of PDF's.

The generic DIS scattering experiment consists of a lepton beam ( $e$ ,  $\mu$ , or  $\nu$ ) incident on a nucleon target. In the simplest version of this experiment (totally inclusive DIS), only the final state lepton is observed, and the hadron remnants are ignored. For example, the SLAC-MIT group [5.7] scattered an electron beam of energy 7 GeV to 17 GeV from a hydrogen target. The energy of the outgoing electron was measured using a large magnetic spectrometer for scattering angles  $\theta = 6^\circ$  and  $10^\circ$ .

In the QCD parton model, we assume that the DIS process occurs via the exchange of a virtual boson ( $W^\pm$  for charged current reactions,  $\gamma$  or  $Z^0$  in neutral current events) with momentum  $q^\mu = k^\mu - k'^\mu$ . The momentum of the exchanged boson defines the energy scale, and the momentum fraction is given by Bjorken scaling variable  $x$ :

$$\begin{aligned} Q^2 &= -q^2 &= 4E_k E_{k'} \sin^2(\theta/2) \\ x &= \frac{Q^2}{2q \cdot P} &= \frac{2E_k E_{k'} \sin^2(\theta/2)}{m_h(E_k - E_{k'})} \end{aligned} \quad . \quad (5.29)$$

Therefore, by measuring only the final state lepton energy ( $E_{k'}$ ) and angle ( $\theta$ ) in the target rest frame, we can determine  $Q^2$  and  $x$ , and thereby extract the structure functions.

The surprising discovery by the SLAC-MIT group was that the structure

functions were insensitive to  $Q^2$ , and only depended on the scaling variable  $x$ . In the context of QCD, we now know that there is a logarithmic  $Q^2$  dependence which spoils the exact scaling. Therefore, the goal of modern experiments is to measure the structure functions in terms of both  $Q^2$  and  $x$ .

### 5.5.2 The Experiments

We shall present a selective survey of the DIS experiments [5.8]. The DIS experiments can be divided into two categories: charged ( $e, \mu$ ) and neutral ( $\nu_e, \nu_\mu$ ) lepton beams.

We will consider four neutrino-induced DIS experiments. At CERN, both CDHS (CERN, Dortmund, Heidelberg, and Saclay) [CERN-WA-001] and CHARM (CERN, Hamburg, Amsterdam, Rome, Moscow) [CERN-WA-018] used a  $\nu_\mu/\bar{\nu}_\mu$  beam with an energy  $\leq 260$  GeV. These experiments were completed in 1984. At Fermilab, CCFR (Chicago, Columbia, Fermilab, Rochester) [FNAL-770] used a  $\nu_\mu/\bar{\nu}_\mu$  beam with an energy  $\leq 600$  GeV, and was completed in 1988. FMMF (Fermilab, Michigan State, MIT, and University of Florida) [FNAL-733] had a  $\nu_\mu/\bar{\nu}_\mu$  beam with an energy  $\leq 500$  GeV, and was completed in 1988. CDHS and CCFR used massive (about 7g/cc) Fe calorimeters which yielded a larger statistical sample. CHARM and FMMF used lighter (about 2g/cc) “fine-grained” calorimeters which yielded good pattern recognition, but lower statistics.

The major charged-lepton-induced DIS experiments include the following. EMC (European Muon Collaboration) [CERN-NA-028] used a  $\mu$  beam with an energy  $\leq 325$  GeV, and was completed in 1983. NMC (New Muon Collaboration) [CERN-NA-037] used the EMC detector to extend the kinematic range to  $x = [0.005, 0.75]$  and  $Q^2 = [1, 200]$  GeV $^2$ , and was completed in 1989. SMC (Spin Muon Collaboration) [CERN-NA-047] is a third reincarnation of the EMC detector designed to measure the spin-dependent asymmetries of longitudinally polarized muons scattering from polarized targets. SMC began operation in 1991. BCDMS (Bologna, CERN, Dubna, Munich, Saclay) [CERN-NA-004] used a  $\mu$  beam with an energy  $100 \text{ GeV} \leq E_\mu \leq 280 \text{ GeV}$ , and was completed in 1985.

Finally, there is a new class of experiments which has only become reality in the past year: lepton-hadron colliders. The HERA collider at DESY began taking data in 1992, colliding 26.7 GeV electrons on 820 GeV protons for a  $\sqrt{s} = 296$  GeV. With two experiments called H1 and ZEUS this facility will be capable of measuring structure functions in the range  $x \geq 10^{-5}$  and  $Q^2 \leq 30,000$  GeV $^2$ .

### 5.5.3 Outstanding Issues in DIS

The DIS process is by far the most accurate experiment for measuring the quark distributions; however, since there is no direct lepton-gluon coupling, the DIS process is only sensitive to the gluon distributions at next-to-leading-order. Given the significant role that the gluons play in the QCD parton model, it is important to obtain their PDF in a separate process, such as direct-photon production.

DIS experiments are performed with a variety of nuclear targets; however, to compare structure functions among experiments, we prefer to convert the nuclear structure functions to isoscalar structure functions. This necessary conversion is non-trivial, and can introduce significant uncertainties.

We have sketched the process for extracting the structure functions summed over parton flavors; however, the extraction of the PDF's is more complicated. In principle we can use proton and neutron scattering data to separately extract the up and down distributions, but this is not straightforward.

A further complication arises when we try to determine the sea-quark distributions. For example, the  $s$ -quark distribution is determined using the sub-process  $s + W \rightarrow c$  with the final state  $c$ -quark observed. Unfortunately, this process is sensitive to threshold effects arising from the charm quark mass, as well as large non-leading order contributions arising from the mixing of the gluon and strange quark distributions.

New high precision DIS data, as well as improved higher-order theoretical calculations, force us to go beyond leading-order perturbation theory. When we carry our calculations and data analysis beyond the leading-order of perturbation theory, all the subtleties of the renormalization scheme and scale dependence arise.

## 5.6 Experimental Status of Parton Distributions

In this section we review some properties of parton distribution functions (PDF's) as currently determined from experiment. We begin with overall features, and go on to discuss the experimental status of scaling violation, evolution and the determination of  $\Lambda_{\text{QCD}}$ .

### 5.6.1 General Features

In neutrino scattering the built-in flavor selection, as described for the parton model in Section 2, provides a powerful means of extracting PDF's. Nevertheless, neutrino experiments on light targets (H or D) suffer in statistical precision. In the following, we briefly review the results of neutrino experiments on hydrogen, and dwell primarily upon the precision measurements from neutrino scattering off isoscalar targets.

#### (1) Quark Densities from $\nu$ -H Scattering

Neutrino measurements of quark densities from a hydrogen target are in agreement between the two experiments, CDHS [5.9] and WA21 (BEBC) [5.10], at about the 15% level. Figure 5.2 shows the ratio of quark and antiquark components as measured by the two groups. (It should be noted that the CDHS data have been adjusted in overall normalization to reflect this group's recent cross section measurement [5.11].)

#### (2) Valence Quark Densities in the Proton

The present status of separate valence quark components,  $xu_V(x)$  and  $xd_V(x)$ , is summarized in Fig. 5.3.a and Fig. 5.3.b. As noted in [5.12], while there is general agreement on  $xu_V(x)$  between the muon experiment (EMC) and neutrino experiments (WA21, WA25, and CDHS), there is a distinct discrepancy in the shape of  $xd_V(x)$ . The precise reason for the discrepancy is not known. It is hoped that the recent muon experiment data by the BCDMS and NMC collaborations on hydrogen and deuterium might resolve this experimental conflict.

### (3) Valence Quark Densities in an Isoscalar Target

The valence quark density for an isoscalar target (i.e., the average of neutron and proton), which is the non-singlet structure function  $x F_3(x, Q^2)$ , is much more accurately determined in high statistics neutrino experiments. The CCFR collaboration [5.13] has presented new measurements on  $x F_3(x, Q^2)$ . These are compared with the CDHSW data [5.14] in Fig. 5.4. The  $Q^2$ -averaged ratio of the CDHSW to the CCFR values of  $x F_3$  are plotted as a function of  $x$ . The figure illustrates that within the systematic error of the overall normalization ( $\approx 2.5\% - 3\%$ ) the two measurements of  $x F_3$  are in agreement. There are, however, differences in the  $Q^2$ -dependence at a given  $x$  between the two data sets. This has important ramifications for the test of scaling violation in  $x F_3(x, Q^2)$  as discussed below.

### (4) Antiquark Densities in an Isoscalar Target

The antiquark densities as measured in light targets by three different groups, WA21, WA25, and CDHS, are in agreement as shown in Fig. 5.5.a (for details see [5.12]). The new high statistics measurement of  $x \bar{q}(x, Q^2)$  measured in the Fe target by the CCFR collaboration [5.13] is shown in Fig. 5.5.b. The data show that  $x \bar{q}(x) \neq 0$  up to  $x \leq 0.40$ .

### (5) Strange Quark Content of an Isoscalar Nucleon Sea

Neutrino-induced opposite sign dimuons,  $\mu^- \mu^+$ , offer the most promising measurement of the strange quark content  $s(x)$  [ $\bar{s}(x)$ ] of the nucleon sea. In addition, these events permit determination of the electroweak parameters  $V_{cd}$  (the Kobayashi-Maskawa matrix element: this is the only direct determination of this parameter), and  $m_c$  (the mass parameter of the charm quark: this is precisely the parameter which at present limits the precision of  $\sin^2 \theta_W$  determination in  $\nu$ -N scattering). The CDHS [5.15] and CCFR [5.16] [5.17] leading order analyses agree in their determination of the fractional strangeness content of the nucleon sea ( $\kappa = 2s/(\bar{u} + \bar{d})$ ); the average of the two measurements is:

$$\kappa = 0.52 \pm 0.07 \quad (5.30)$$

A noteworthy feature of the CCFR data (see [5.17]) is that the measured  $s(x)$  [ $\bar{s}(x)$ ] is somewhat softer than the non-strange sea (obtained from the single muon CC events). This is illustrated in Fig. 5.6. Two new developments are underway: (a) CCFR has quadrupled its sample of  $\mu^+\mu^-$  events by including data from two separate runs (FNAL E744 and E770), and by imposing a softer muon momentum cut on the second muon ( $E_\mu > 4\text{GeV}$ ); (b) It has been shown that, within the perturbative QCD framework, it is necessary to perform the analysis at least to order  $\alpha_s$  to achieve consistency [5.18]. It is hoped that these developments may help answer the question: is the strange sea *different* from the non-strange sea?

### 5.6.2 Evolution

Within the framework of DIS scattering described in Section 4 there are elegant and unambiguous QCD predictions that can be verified experimentally. In DIS there is no fragmentation uncertainty since one deals with inclusive final state hadrons; the scale, which is the four-momentum transfer  $Q^2$ , is well defined; the higher order corrections are small and the scaling violations are well described by the evolution equations [5.19]. Also the measurements yield structure functions at different values of  $x$  and  $Q^2$ , and thus afford a system of tests of evolution (Section 3.2.3).

Among the elegant predictions of perturbative QCD are slopes of structure functions with respect to  $Q^2$  as a function of  $x$  and the absolute magnitude and dependence of  $R(x, Q^2) = \sigma_L/\sigma_T$  on  $x$  and  $Q^2$ . Below we examine the status of these tests.

#### (1) Measurements of $R(x, Q^2)$ versus QCD

The  $R$  parameter of deep inelastic scattering is defined as the ratio of the absorption cross section of the longitudinally to transversely polarized virtual boson,  $R(x, Q^2) = \sigma_L/\sigma_T$ , and is related to the structure functions  $F_2$ , and  $F_1$  as:

$$R = \frac{\sigma_L}{\sigma_R} = \frac{F_2 - 2xF_1}{2xF_1} \equiv \frac{F_L}{2xF_1}. \quad (5.31)$$

where  $F_L$  is the longitudinal structure function, and the other symbols have their usual meaning [5.12]. Perturbative QCD predicts the magnitude of  $R$  and its dependence on  $x$  and  $Q^2$  (due to gluon radiation and quark pair production) to be [5.20]:

$$R(x, Q^2) = \frac{\alpha_s(Q^2)}{2\pi} \frac{x^2}{2xF_1(x, Q^2)} \int_x^1 \frac{dz}{z^3} \left[ \frac{8}{3}F_2(z, Q^2) + 4f(1 - \frac{x}{z})zG(z, Q^2) \right], \quad (5.32)$$

where  $f$  is the number of flavors if the incident lepton is a neutrino, and the sum of the squares of quark charges if the incident lepton is a muon or an electron;  $G(z, Q^2)$  is the gluon structure function. Numerous experiments have measured  $R(x, Q^2)$  and claimed consistency with the theoretical prediction. Nevertheless, from recent measurements at SLAC [5.21] and a simple model for higher twist effects, it is argued in Ref. [5.22] that the present cumulative deep inelastic scattering data are *consistent* with but *do not demonstrate*  $R = R_{\text{QCD}}$ . Precise measurements of  $R(x, Q^2)$  at sufficiently high  $Q^2$  (e.g.  $Q^2 > 10 - 15$  (GeV/c)<sup>2</sup>) in next generation deep inelastic experiments [5.23] [5.24] will provide a compelling test of perturbative QCD.

## (2) Evolution of Non-singlet Structure Function

In the DIS scheme, we can combine Eqs. (5.1), (5.2) and Eq. (5.10) to find evolution equations for the singlet and nonsinglet functions  $F_2^{(S)}$  and  $F_2^{(NS)}$ ,

$$\frac{dF_2^{(NS)}(x, Q^2)}{d \ln Q^2} = \int_x^1 P_{qq}(z, \alpha_s) F_2^{(NS)}\left(\frac{x}{z}, Q^2\right) dz \quad (5.33)$$

$$\frac{dF_2^{(S)}(x, Q^2)}{d \ln Q^2} = \int_x^1 \left[ P_{qq}(z, \alpha_s) F_2^{(S)}\left(\frac{x}{z}, Q^2\right) + P_{qG}(z, \alpha_s) \phi_{g/N}\left(\frac{x}{z}, Q^2\right) \right] dz \quad (5.34)$$

where the  $P_{ij}$  are the usual evolution kernels, given at one loop Eq. (5.7). Thus in the DIS scheme, the non-singlet (NS) evolution of  $F_2$  involves only the structure function itself, the known splitting function, and  $\alpha_s$ . The singlet (S) equation is coupled with that of the gluons and is hence

less directly related to experiment. An analysis of the kernels shows, however, that the slope of  $F_2^{(S)}$  is expected (at leading order) to pass through zero at about  $x = 0.1$ , as shown in Fig. 5.7.a.

In a manner similar to  $F_2^{(S)}$ , the evolution equation for  $x F_3$  can be written in the form

$$\frac{d \ln x F_3(x, Q^2)}{d \ln Q^2} = \alpha_s(Q^2) \psi(x, Q^2). \quad (5.35)$$

The term  $\psi(x, Q^2)$  involves an integral of  $x F_3(z, Q^2)$  for  $z > x$ ; the integral is evaluated using the known splitting function  $P_{qq}$  (which has been calculated to next-to-leading order). Thus, the only unknown on the right hand side of the above equation is the strong coupling constant: the logarithmic slope of  $x F_3$  is proportional to  $\alpha_s$  at each  $x$ .

Neutrino experiments on heavy targets can perform this test with the non-singlet structure function,  $x F_3$ . The high statistics CDHSW data [5.14] do not agree well with the predicted dependence of the scaling violations on  $x$ , although the authors state that the discrepancies are within their systematic errors. Previous CCFR data lacked the statistical power to offer a conclusive test [5.25]. The recent CCFR non-singlet data show an evolution consistent with the pQCD prediction, and provides an accurate determination of  $\alpha_s$  [5.26].

Measurements of the scaling violations are sensitive to miscalibrations of either the hadron or muon energies. For example, a 1% miscalibration can cause a 50 MeV mismeasurement of  $\Lambda_{QCD}$ , but hadron and muon errors enter with opposite signs. Thus if both hadron and muon energies were in error by the same amount, the error in  $\Lambda_{QCD}$  would be small. Therefore, while it is important that the hadron and muon energy calibrations and resolution functions be well known, it is crucial that the energy scales be cross-calibrated to minimize energy uncertainty as a source of error.

The Figure 5.7.b shows that the CCFR data have an evolution of  $x F_3$  consistent with the pQCD prediction. The pQCD prediction is a next-to-leading order (NLO) calculation in the modified minimal subtraction

( $\overline{\text{MS}}$ ) scheme. A  $Q^2 > 15$  ( $\text{GeV}/c$ )<sup>2</sup> cut was applied to eliminate the non-perturbative region, and another  $x < 0.7$  cut to remove the highest  $x$  bin (where resolution corrections are sensitive to Fermi motion). The best QCD fits to the data were obtained as illustrated in the figure.

### (3) Determination of $\Lambda_{QCD}$

A good visual representation of structure function evolution compares the magnitude of the  $Q^2$ -dependence of the data in each  $x$ -bin with the dependence predicted by the fit. This is shown by plotting the “slopes” ( $= d \ln x F_3 / d \ln Q^2$ ) as a function of  $x$ . Figure 5.7.c. shows the CCFR data along with the curve through the points predicted by the theory. More specifically the values shown in Fig. 5.7.c result from power law fits to both data and theory over the  $Q^2$  range of the data. The logarithmic slopes of the data agree well with the QCD prediction throughout the entire  $x$ -range. This observation is independent of calibration adjustments within reasonable limits. At low- $x$  values the data agree well with predictions independent of the value of  $\Lambda_{QCD}$ .

The value of  $\Lambda_{QCD}$  resulting from the fit to  $x F_3$  data is  $179 \pm 36$  MeV, with a  $\chi^2$  of 53.5 for 53 degrees of freedom ( $\chi^2=53.5/53$ ). Varying the  $Q^2$  cuts does not significantly change  $\Lambda_{QCD}$ ; for  $Q^2 > 10$  ( $\text{GeV}/c$ )<sup>2</sup>, the best fit gives  $\Lambda_{QCD} = 171 \pm 32$  MeV ( $\chi^2=66.4/63$ ); and for  $Q^2 > 5$  ( $\text{GeV}/c$ )<sup>2</sup>,  $\Lambda_{QCD} = 170 \pm 31$  MeV ( $\chi^2=83.8/80$ ).

More precise determinations of  $\Lambda_{QCD}$  from the non-singlet evolution is obtained by substituting  $F_2$  for  $x F_3$  at large values of  $x$ . The evolution of  $F_2$  should conform to that of a non-singlet structure function in a region,  $x > x_{cut}$ , so long as  $x_{cut}$  is large enough that the effects of antiquarks, gluons, and the longitudinal structure function are negligible on its  $Q^2$  evolution. The “best” value of  $\Lambda_{QCD}$  from non-singlet evolution is obtained by substituting  $F_2$  for  $x F_3$  for  $x > 0.5$ . (The slopes for  $F_2$  in this region are also shown in Fig. 5.8.c.) This non-singlet fit yields:

$$\Lambda_{QCD} = 210 \pm 28 \text{ MeV for } Q^2 > 15(\text{GeV}/c)^2. \quad (5.36)$$

Varying the  $x_{cut}$  from 0.5 to 0.4 does not significantly change  $\Lambda_{QCD}$ ; the above substitution yields,  $\Lambda_{QCD} = 216 \pm 25$  MeV with good fit. Using  $2xF_1$  instead of  $F_2$  in this fit changes  $\Lambda_{QCD}$  by +1 MeV.

#### (4) Evolution of Singlet Structure Function

We note (for details see Ref. [5.12]) that there were some experimental conflicts in  $F_2$ -evolution: whereas the BCDMS data showed lovely agreement with the theory (see Fig. 5.8.a and Fig. 5.8.b), the EMC and the CDHSW data on  $F_2$ -slopes were steeper than the prediction (Fig. 5.8.c and Fig. 5.8.d). The CCFR data on  $F_2$  show an evolution consistent with the pQCD. Figures 5.8.e and 5.8.f illustrate this consistency. It should be noted, however, that for the  $F_2$  evolution the functional form of the  $x$ -dependence of the gluons must be assumed, and its coefficient must be determined from the data.

We point out that, assuming the QCD evolution is unequivocally verified in the non-singlet evolution, the singlet evolution permits the extraction of the gluon structure function. In neutrino experiments, *the simultaneous evolution of  $F_2$  and  $xF_3$*  permits a very powerful constraint on the gluon degrees of freedom [5.25].

## 5.7 Status of DIS Sum Rules

### 5.7.1 Introduction

The invariant structure functions which parameterize the deep inelastic scattering cross section are related to the densities of quarks constituting the nucleon by the Quark Parton Model (QPM)(Section 2). Quark Parton Model sum rules are thus consistency conditions that relate appropriate integrals of measured quark densities to the total number and charges of the constituent quarks. In the following, we review from a phenomenological perspective the sum rules and the experimental challenges and tests of certain important sum rules in DIS experiments [5.27] [5.12]. Sum rules establish relationships

among the total integrated quark and antiquark densities. For simplicity, we consider the contributions of the first generation quark densities. (Higher generation quark densities generally cancel in the sum rules.) If we denote the total u-quark and d-quark densities by:

$$\begin{aligned} U_p &= \int_0^1 u(x)dx, \\ D_p &= \int_0^1 d(x)dx, \end{aligned} \quad (5.37)$$

it follows from the isospin invariance that the total density of the u-quark in the proton must be equal to the total density of the d-quark in the neutron:

$$\begin{aligned} U &= U_p = D_n \\ D &= D_p = U_n \\ \bar{U} &= \bar{U}_p = \bar{D}_n \\ \bar{D} &= \bar{D}_p = \bar{U}_n. \end{aligned} \quad (5.38)$$

The above simple relationships follow directly from the assigned baryon and isospin quantum numbers of the nucleon, and no violation of these relations have been reported to date.

The experimental challenges in precision tests of QPM sum rule predictions spring from two sources:

- (1) **Low- $x$  Region:** The experiments measure momentum densities of the partons, *i.e.*,  $xq(x)$ ; the sum rules involve integration over the number of quarks. The sums are thus obtained by integrating over the measured momentum densities *divided* by  $x$ , which weights the low- $x$  region heavily. A good experimental resolution and a good understanding of the resolution functions of the measured quantities in the low- $x$  region are necessary for accurate tests.
- (2) **Relative Normalization:** Sum rules involve differences of structure functions or cross-sections. The relative normalization between relevant cross-sections, therefore, must be accurately measured. Furthermore, as can be seen below, differences often must vanish at  $x = 0$ , or the

sum rule will become divergent. This imposes an additional emphasis upon measuring the relative normalization well.

### 5.7.2 Gross-Llewellyn Smith Sum Rule

The Gross-Llewellyn Smith (GLS) sum rule is the most accurately tested of sum rules. The GLS sum rule predicts that the number of valence quarks in a nucleon, up to finite  $Q^2$  corrections, is three [5.29]. It involves an integration over the non-singlet neutrino structure function,  $x F_3(x, Q^2)/x$ , which is obtained by subtracting the antineutrino differential cross section on an isoscalar target from the corresponding neutrino cross section. In the QPM, the GLS sum rule is:

$$S_{\text{GLS}} = \int_0^1 \frac{x F_3^{\nu N}}{2x} dx = (U - \bar{U}) + (D - \bar{D}) = 3. \quad (5.39)$$

To verify this result, see Eq. (2.44), recall that  $F^{(\nu h)} = F^{(W^{+h})}$  for  $h = p, n$  and use isospin invariance, Eq. (5.38). The integrand of the sum rule is the coefficient of  $1 - (1 - y)^2$  in the difference of the two differential cross sections.

The effects of scaling violations modify this sum rule. Perturbative QCD predicts a calculable deviation of the GLS sum rule from 3. In next-to-leading order,  $S_{\text{GLS}}$  is given by:

$$S_{\text{GLS}} = \int_0^1 \frac{x F_3^{\nu N}}{2x} dx = 3 \left\{ 1 - \frac{\alpha_s(Q^2)}{\pi} + \frac{G}{Q^2} + \mathcal{O}(Q^{-4}) \right\}. \quad (5.40)$$

The QPM relates the parity violating structure function,  $x F_3$ , to the valence quark density of the nucleon, and the sum rule follows. The second term in the equation corresponds to the known perturbative QCD correction, while the third term corresponds to an estimate of power suppressed (twist-4) contribution to the sum rule [5.30]. Using perturbative QCD with  $\Lambda_{\text{QCD}} = 200$  MeV the sum rule therefore predicts  $S_{\text{GLS}} = 2.66$  at  $Q^2 = 3$  (GeV/c) $^2$ . The order  $\alpha_s$  result may be derived from  $C_3^{(Vq)}$  in Eq. (5.6). This computation is greatly simplified by using the fact that the integral from 0 to 1 of a plus distribution vanishes.

Due to the  $1/x$  weighting in the integrand, the small  $x$  region ( $x < 0.1$ ) is particularly important; 90% of the integral comes from the region  $x \leq 0.1$ . It follows that the most important issues to assure small systematic errors are (a) accurate determination of the muon direction; and (b) accurate determination of the relative  $\bar{\nu}/\nu$  flux. Since  $x F_3$  is obtained from the difference of  $\nu$  and  $\bar{\nu}$  cross-sections, small relative normalization errors can become magnified by the weighting in the integral. The absolute normalization uses an average of  $\nu$ -N cross-section measurements.

As an example, in the CCFR measurement of  $S_{\text{GLS}}$ , the values of  $x F_3$  are interpolated or extrapolated to  $Q_0^2 = 3$  (GeV/c)<sup>2</sup>, which is approximately the mean  $Q^2$  of the data in the  $x$ -bin which contributes most heavily to the integral. The resulting  $x F_3$  is then fit to a function of the form  $f(x) = Ax^b(1-x)^c$  ( $b > 0$ ). The integral of the fit weighted by  $1/x$  gives  $S_{\text{GLS}}$ . The estimated systematic error due to fitting on  $S_{\text{GLS}}$  is  $\pm 0.040$ . The dominant systematic error of the measurement comes from the uncertainty in determining the absolute level of the flux, 2.2%. The other two systematic errors are 1.5% from uncertainties in relative  $\bar{\nu}$  to  $\nu$  flux measurement and 1% from uncertainties in muon energy calibration. The reported CCFR value for  $S_{\text{GLS}}$  is [5.28]:

$$S_{\text{GLS}} = \int_x^1 \frac{x F_3^{\nu N}}{2x} dx = 2.50 \pm 0.018(\text{ stat.}) \pm 0.078(\text{ syst.}) \quad (5.41)$$

The theoretical prediction of  $S_{\text{GLS}}$ , for the measured  $\Lambda = 213 \pm 50$  MeV from the evolution of the non-singlet structure function, is  $2.66 \pm 0.04$  (see Eq.( 5.40)). The prediction, assuming negligible contributions from higher twist effects, target mass corrections, [5.32] and higher order QCD corrections, is within 1.8 standard deviations of the measurement. The current status of  $S_{\text{GLS}}$  measurements is shown in Fig. 5.9.

The 3% accuracy of the GLS sum rule at  $Q^2 = 3$  GeV<sup>2</sup> raises theoretical concerns on nonleading contributions, which are discussed in [5.30] and [5.31].

### 5.7.3 Adler Sum Rule

The Adler sum rule predicts the integrated difference between neutrino-neutron and neutrino-proton structure functions. Unlike the GLS sum rule,

this sum rule is exact, and is expected to be valid to all orders of perturbation theory. It states [5.33]

$$S_A = \int_0^1 \frac{(F_2^{\nu n} - F_2^{\nu p})}{2x} dx = 1. \quad (5.42)$$

As for the one-loop correction to  $S_{\text{GLS}}$ , the vanishing of the one-loop correction to  $S_A$  follows immediately from the fact that  $C_2^{(Vq)}(x)/x$  in Eq. (5.6) is a plus distribution. In terms of the total number of u- and d-quarks, the sum rule implies (see Eq. (2.42)):

$$\begin{aligned} S_A &= \int_0^1 [d_n(x) + \bar{u}_n(x) - d_p(x) - \bar{u}_p(x)] dx \\ &= D_n + \bar{U}_n - D_p - \bar{U}_p \\ &= (U - \bar{U}) - (D - \bar{D}) \end{aligned} \quad (5.43)$$

The prediction follows from the last equation.

The WA25 (BEBC) collaboration [5.34] has used neutrino data on a light target to obtain this sum rule. Their measurement, averaged over  $1 < Q^2 < 40$  (GeV/c) $^2$  and assuming the Callan-Gross relation, yields:

$$S_A = 1.01 \pm 0.08 \text{ (stat.)} \pm 0.18 \text{ (syst.)}, \quad (5.44)$$

which is consistent with the prediction at the 20% precision. Figure 5.10 presents the WA25 measurement of  $S_A$  at various  $Q^2$  cuts. It should be pointed out however that the WA25 collaboration used a value for the total  $\nu N$  cross section which is lower than the current consistent value (see Refs. [5.35], [5.36].) The central value of the sum rule, therefore, should be adjusted:  $S_A = 1.08 \pm 0.08 \pm 0.18$ .

The Adler sum rule is particularly difficult to test accurately. Obtaining statistically accurate neutrino data on a light target would require a very intense neutrino beam; good low- $x$  resolution, and accurate relative normalization between proton and neutron (deuterium) targets impose additional constraints. No new effort is in view to improve upon the present 20% measurement of  $S_A$ .

### 5.7.4 Gottfried Sum Rule

The Gottfried sum rule is the “Adler sum rule analogue” for charged lepton probes. The sum rule involves the difference of  $F_2$  measured in proton and neutron targets using a muon beam [5.37]:

$$S_G = \int_0^1 \frac{(F_2^{ep} - F_2^{en})}{x} dx = \frac{1}{3}. \quad (5.45)$$

As in the case of the Adler sum rule, it is instructive to express this sum rule in terms of contributions (integrals) from individual quark densities (see Eq. (2.31)):

$$\begin{aligned} S_G &= \frac{1}{9} [4(U_p + \bar{U}_p) + (D_p + \bar{D}_p) - 4(U_n + \bar{U}_n) - (D_n + \bar{D}_n)] \\ &= \frac{1}{3} [(U + \bar{U}) - (D + \bar{D})]. \end{aligned} \quad (5.46)$$

If one assumes [5.12] that the total number of anti-up and anti-down quarks inside a proton is the same, *i.e.*  $\bar{U} = \bar{D}$ , then the sum rule predicts a value of  $(1/3)$ . Analogous to the Adler sum rule, the Gottfried sum rule is exact: the expected QCD correction to  $S_G$  is very small. This has been shown in Ref. [5.38].

It is the assumption  $\bar{U} = \bar{D}$  inside the proton that is seriously impugned by the recent NMC measurement of  $S_G$  [5.40]. Before discussing the experiment, let us analyze the contribution of various quark species to  $S_G$ .

When written in terms of u- and d-quark contributions, this is the first sum rule where the contributions of quark and anti-quark of the same type *add* — for all other sum rules, Gross-Llewellyn Smith, Adler, Bjorken, the contribution of say u-quark and antiquark *subtract*.

There is no a priori reason to believe that the total number of  $\bar{u}$  be the same as  $\bar{d}$  inside a proton. That the proton has 2 valence u-quarks, and 1 valence d-quark implies that the number of  $u\bar{u}$  pairs will be less than the corresponding number of  $d\bar{d}$  pairs in the nucleon sea — the suppression of u-quarks in the sea will be due to the exclusion principle [5.39]. Isospin symmetry does not predict equality. Exploiting the Adler sum rule (5.43),

however  $S_G$  can be cast in the form:

$$\begin{aligned} S_G &= \frac{1}{3} [(U - \bar{U}) - (D - \bar{D})] + \frac{2}{3} [\bar{U} - \bar{D}] \\ &= \frac{1}{3} + \frac{2}{3} [\bar{U} - \bar{D}] . \end{aligned} \quad (5.47)$$

If  $\bar{U} < \bar{D}$ , then it follows that  $S_G < (1/3)$ . This was found by the NMC [5.40]. Prior to these data, earlier measurement lacked precision in the critical low- $x$  region to provide a conclusive test of the sum rule. The  $S_G$  measurements by SLAC [5.41], EMC [5.42], and BCDMS [5.43] groups were all consistent with the naive prediction of  $(1/3)$  within their large errors (typically 20%). The earlier measurements, however, did show consistently a central value of  $S_G$  that was lower than the prediction. The NMC experiment had the commensurate statistics and resolution in the low- $x$  region enabling them to measure well  $F_2^p/F_2^n$  ratio down to small values of  $x$  [5.44]. Using this measured ratio, and the world-average of  $F_2$ (Deuterium), they obtained  $F_2^p - F_2^n$ :

$$F_2^p - F_2^n = 2F_2(\text{Deuterium}) \times \frac{1 - F_2^n/F_2^p}{1 + F_2^n/F_2^p}. \quad (5.48)$$

The NMC measurement of  $(F_2^p - F_2^n)$  dark-symbols (right-scale), and that of the corresponding integral,  $\int (F_2^p - F_2^n) dx$ , as open-symbols (left-scale) are shown in Fig. 5.11. as a function of  $x$ . The “circles” and “triangles” are two distinct methods of obtaining these data; their agreement reveals consistency. The lowest measured  $x$ -bin was 0.004; and over the measured  $x$ -region, they reported:

$$S_G = \int_0^1 \frac{(F_2^{up} - F_2^{dn})}{x} dx = 0.227 \pm 0.007 \pm 0.014 \text{ for } 0.004 \leq x \leq 0.8. \quad (5.49)$$

The measured  $x$ -dependence, just like the  $xF_3$  in the GLS measurement, is consistent with a power-law fit in  $x$ . This fit could be extrapolated to the unmeasured region in  $x$  below 0.004. The corrected sum rule is:

$$S_G = 0.240 \pm 0.016 \text{ for } 0 \leq x \leq 1. \quad (5.50)$$

This precise measurement of  $S_G$  is more than five-standard deviations higher than the naive prediction of 1/3.

The discrepancy has engendered a lot of interest. Some authors have postulated large asymmetry in the nucleon sea [5.45]; others have attributed the cause of disagreement to extrapolation to the unmeasured region in  $x$  [5.46]. Eichten *et al.* [5.47] have interpreted this discrepancy to be an interesting property of the nucleon. That there is an asymmetry in u- versus d-sea in the proton is not surprising; perhaps the startling feature is the possible magnitude of the asymmetry.

### 5.7.5 Bjorken Sum Rule

Polarized hard scattering is a rich subject, with many recent developments [5.48]. Here we discuss the extra structure functions that exist in polarized deep inelastic scattering. For a spin half target, there are two polarized structure functions,  $g_1$  and  $g_2$ . QCD predicts that  $g_2$  is higher twist and therefore gives a small contribution to the cross section. The only measurements to date are of  $g_1$ : for polarized protons at SLAC [5.49] and by EMC [5.50], and recently for polarized deuterium by SMC [5.51].

Consider the scattering of polarized muons (or electrons) off a polarized nucleon, with the axis of the polarization being the collision axis. We let  $\sigma(\uparrow\uparrow)$  ( $\sigma(\uparrow\downarrow)$ ) be the cross section when the target polarization is parallel (antiparallel) to the beam polarization. Then

$$\frac{d^2[\sigma(\uparrow\uparrow) - \sigma(\uparrow\downarrow)]}{dxdy} = \frac{e^4}{2\pi Q^2} (1 - y/2) g_1(x, Q), \quad (5.51)$$

where we have dropped terms that are suppressed by a power of  $Q^2$  in the Bjorken limit. The perturbative QCD prediction for  $g_1$  is

$$g_1(x, Q) = \frac{1}{2} \sum_f e_f^2 (\phi_f^\uparrow - \phi_f^\downarrow) + O(\alpha_s), \quad (5.52)$$

where the  $O(\alpha_s)$  corrections are known [5.52]. Here,  $\phi_f^\uparrow$  ( $\phi_f^\downarrow$ ) represents the number density of partons of flavor  $f$  that are polarized parallel (antiparallel) to the initial hadron.

The Bjorken sum rule [5.53] relates the difference between  $g_1$  for the proton and neutron to the nucleon vector and axialvector couplings  $g_V$  and  $g_A$

$$\begin{aligned} S_{\text{Bj}} &\equiv \Gamma_1^p - \Gamma_1^n = \int_0^1 [g_1^p(x) - g_1^n(x)] dx \\ &= \frac{1}{6} \frac{g_A}{g_V} \left( 1 - \frac{\alpha_s}{\pi} + O(\alpha_s^2) \right) \\ &= 0.191 \pm 0.002, \end{aligned} \quad (5.53)$$

where  $\Gamma_1$  denotes the first moment of  $g_1$ . The sum rule arises because the first moment of a polarized quark density plus the antiquark density is the expectation value of an axial current operator:

$$\Delta f \equiv \int_0^1 [\phi_f^\uparrow - \phi_f^\downarrow + \phi_{\bar{f}}^\uparrow - \phi_{\bar{f}}^\downarrow] dx = \langle N | \bar{\psi}_f \gamma^+ \gamma_5 \psi_f | N \rangle / (2p^+). \quad (5.54)$$

The Bjorken sum rule is a firm prediction of QCD, since it rests on established perturbative methods and on isospin invariance. It has recently been tested at low accuracy by the SMC [5.51]. With the aid of the EMC result [5.50]

$$\Gamma_1^p(\text{EMC}) = 0.114 \pm 0.012(\text{stat.}) \pm 0.026(\text{syst.}), \quad (5.55)$$

the SMC deuterium data give

$$\Gamma_1^n(\text{SMC}) = -0.08 \pm 0.04(\text{stat.}) \pm 0.04(\text{syst.}), \quad (5.56)$$

so that

$$S_{\text{Bj}}(\text{SMC}) = 0.20 \pm 0.05(\text{stat.}) \pm 0.05(\text{syst.}), \quad (5.57)$$

in agreement with the theoretical prediction Eq. (5.53)

Ellis and Jaffe [5.54] derived sum rules for  $g_1^p$  and  $g_1^n$  separately. Their critical assumption was that the strange quarks in the nucleon are unpolarized, so that in the notation of (5.54)  $\Delta s = 0$ . This hypothesis is plausible but it is by no means a prediction of QCD. In addition, the derivation used flavor SU(3) symmetry to relate the nonsinglet matrix elements in the operator product expansion to semi-leptonic decay rates of strange baryons; this is less accurate than isospin invariance. Modern values then predict [5.50]

$$\Gamma_1^p(\text{EJ}) = 0.189 \pm 0.005, \quad \Gamma_1^n(\text{EJ}) = -0.002 \pm 0.005. \quad (5.58)$$

The EMC and SMC results violate the Ellis-Jaffe sum rules. The EMC result, plus weak interaction measurements and SU(3) invariance, imply that

$$\Delta u = 0.74 \pm 0.10, \quad \Delta d = -0.54 \pm 0.10, \quad \Delta s = -0.20 \pm 0.11. \quad (5.59)$$

Taken at face value, these numbers imply that the strange sea quarks have substantial polarization and that the quarks carry little of the spin of the proton (since  $\Delta u + \Delta d + \Delta s = 0.01 \pm 0.29$ ).

It is possible to evade this conclusion: for example, one may question the direct identification of the  $\Delta f$ 's in Eq. (5.59) with spin fractions carried by quarks in a quark model wave function [5.55]. Then there could be a large spin asymmetry in the gluons. In any event, if the violation of the Ellis-Jaffe sum rule is confirmed, then it implies some surprising features of the nucleon wave function and of the associated nonperturbative physics. There is interesting work still to be done [5.48], particularly in a flavor separation of the spin dependent parton densities.

## References

- [5.1] J.F. Owens and W.-K. Tung, Annu. Rev. Nucl. Par. Sci. **42**, 291 (1992).
- [5.2] W. Furmanski and R. Petronzio, Z. Phys. **C11**, 293 (1982).
- [5.3] E.B. Zijlstra and W.L. van Neerven, Nucl. Phys. **B383**, 525 (1992); W.L. van Neerven and E.B. Zijlstra, Phys. Lett. **B272**, 127 (1991); E.B. Zijlstra and W.L. van Neerven, *ibid* **B273**, 476 (1991); W.L. van Neerven and E.B. Zijlstra, Nucl. Phys. **B382**, 11 (1992); T. Matsuura, R. Hamberg and W.L. van Neerven, Nucl. Phys. **B345**, 331 (1990); R. Hamberg, W.L. van Neerven and T. Matsuura, Nucl. Phys. **B359**, 343 (1991); R. Hamberg, Second Order Gluonic Contributions to Physical Quantities, Ph.D. thesis submitted to the University of Leiden, (1991).
- [5.4] G. Altarelli, Phys. Rep. **C81**, 1 (1982).
- [5.5] G. Altarelli, R. K. Ellis and G. Martinelli, Nucl. Phys. **B143**, 521 (1978), (E) **B146**, 544 (1978); *ibid* **B157**, 461 (1979); J. Kubar-Andre and F. E. Paige, Phys. Rev. **D19**, 221 (1979); K. Harada, T. Kaneko and N. Sakai, Nucl. Phys. **B155**, 169 (1979); (E) **B165**, 545 (1980); J. Abad and B. Humpert, Phys. Lett. **B80**, 286 (1979). B. Humpert and W.L. van Neerven, Nucl. Phys. **B184**, 225 (1981).
- [5.6] For a broader historical perspective, see:  
*The Experimental Foundations of Particle Physics*, R.N. Cahn and G. Goldhaber, Cambridge Univ. Press, 1989.
- [5.7] M. Breidenbach *et al.*, Phys. Rev. Lett. **23**, 935 (1969);  
E.D. Bloom *et al.*, Phys. Rev. Lett. **23**, 930 (1969).
- [5.8] For lack of space we can neither cite all experiments, nor all references. For those experiments discussed, the experiment number is given so that the interested reader can find a complete list of publications in the following reference. Note that this information is also available on

the SPIRES database.

*Current Experiments in Elementary Particle Physics: Particle Data Group*, H. Galic *et al.*, LBL-91-REV-1992, June 1992.

- [5.9] H. Abramowicz *et al.*, Z. Phys., **C25**, 29 (1984).
- [5.10] G.T. Jones *et al.*, WA21(BEBC) Preprint 87, Rec. Jul(1987).
- [5.11] P. Berge *et al.*, Z. Phys., **C35**, 443 (1987).
- [5.12] S.R. Mishra and F. Sciulli, “Deep Inelastic Lepton Nucleon Scattering”, Ann. Rev. of Nucl. and Part. Sci., **39**, 259 (1989).
- [5.13] S.R. Mishra *et al.*, Nevis Preprint # 1459 (1992).
- [5.14] CDHSW: P. Berge *et al.*, Z. Phys. **C49**, 187 (1991).
- [5.15] H. Abramowicz *et al.*, Z. Phys., **C17**, 19 (1982).
- [5.16] K. Lang *et al.*, Z. Phys., **C33**, 483 (1987).
- [5.17] C. Foudas *et al.*, Phys. Rev. Lett., **64**, 1207 (1990).
- [5.18] M.A. Aivazis, F.I. Olness and W.K. Tung, Phys. Rev. Lett., **65**, 2339 (1990).
- [5.19] G. Altarelli and G. Parisi, Nucl. Phys. **B26**, 298 (1977).
- [5.20] G. Altarelli and G. Martinelli, Phys. Lett. **B76**, 89 (1978); M. Glück and E. Reya, Nucl. Phys. **145**, 24 (1978).
- [5.21] S. Dasu *et al.*, Phys. Rev. Lett. **61**, 1061 (1988); L.W. Whitlow *et al.*, Phys. Lett. **B250**, 193 (1990).
- [5.22] S.R. Mishra and F. Sciulli, “Do Present Deep Inelastic Scattering Data Demonstrate  $R = R_{QCD}$ ?”, Phys. Lett. **B244**, 341 (1990).

- [5.23] S.R. Mishra, “A 2<sup>nd</sup> Generation Neutrino Deep Inelastic Scattering Experiment at the FNAL Tevatron”; presented at the workshop, “Fermilab in the 1990’s”, at Breckenridge, Colorado. A summary is to appear in the conference proceedings, eds. R.Brock and H.Montgomery.
- [5.24] C. Guyot *et al.*, “A New Fixed Target Experiment for a Precise Test of QCD”, Saclay Print-88-0741, Sep., 1988.
- [5.25] E. Oltman *et al.*, Z. Phys. **C53**, 51 (1992).
- [5.26] P.Z. Quintas *et al.*, Nevis Preprint # 1461 (1992). Also see P.Z. Quintas, Ph.D. Thesis, Columbia University, 1991.
- [5.27] F. Sciulli, “Review of Lepton Hadron Interactions”, in *Proc. of 1985 International Symposium on Lepton and Photon Interactions*, Kyoto, Aug.1985. For a historical perspective of the DIS experiments, see F.Sciulli, “Lepton-Hadron Scattering from Scaling Violations to HERA”, in *Proc. of the SLAC Summer Institute*, Aug. 1991.
- [5.28] W.C. Leung *et al.*, Nevis Preprint # 1460 (1992). Also see W.C. Leung, Ph.D. Thesis, Columbia University, 1991.
- [5.29] D.J. Gross and C. Llewellyn Smith, Nucl. Phys. **B14**, 337 (1969); M.A.B. Beg, Phys. Rev., **D11**, 1165 (1975).
- [5.30] B.A. Iijima, M.I.T. Preprint CTP993 (1983) (unpublished); R.Jaffe private communication.
- [5.31] E.V. Shuryak and A.L. Vianshtein, Phys. Lett. **B105**, 65 (1981).
- [5.32] S.R. Mishra, “Probing Nucleon Structure with  $\nu$ -N Experiments”, Review talk presented at “Workshop on Hadron Structure Functions and Parton Distributions”, at Fermilab, Batavia, April (1990).
- [5.33] S.L. Adler, Phys. Rev., **143**, 1144 (1966).
- [5.34] D. Allasia *et al.*, Phys. Lett. **B135**, 231 (1984); Z. Phys., **C28**, 321 (1985).

- [5.35] R. Blair *et al.*, Phys. Rev. Lett. **51**, 343 (1983).
- [5.36] P. Berge *et al.*, Z. Phys. **C35**, 443 (1987).
- [5.37] K. Gottfried, Phys. Rev. Lett. **18**, 1154 (1967).
- [5.38] D.A. Ross and C.T. Sachrada, Nucl. Phys. **B149**, 497 (1979).
- [5.39] R.D. Field and R.P. Feynman, Phys. Rev. **D15**, 2590 (1977).
- [5.40] P. Amaudruz *et al.*, Phys. Rev. Lett. **66**, 2712 (1991).
- [5.41] A. Bodek *et al.*, Phys. Rev. Lett. **30**, 1087 (1973).
- [5.42] J.J. Aubert *et al.*, Nucl. Phys. **B293**, 740 (1987).
- [5.43] A.C. Benvenuti *et al.*, Phys. Lett. **B237**, 592 (1990); A.C. Benvenuti *et al.*, Phys. Lett. **B237**, 599 (1990).
- [5.44] D. Allasia *et al.*, Phys. Lett. **B249**, 366 (1990).
- [5.45] P. Radcliff *et al.*, preprint submitted to Phys. Rev. Lett. (1991).
- [5.46] A.D. Martin *et al.*, Phys. Lett. **B252**, 653 (1990).
- [5.47] E.J. Eichten, I. Hinchliffe and C. Quigg, Phys. Rev. **D45**, 2269 (1992); *ibid* **D47**, 747 (1993).
- [5.48] References to recent work can be found in *Proceedings of the Polarized Collider Workshop*, ed. J.C. Collins, S. Heppelmann and R. Robinett, AIP Conference Proceedings 223 (AIP, New York, 1991), and in G. Bunce, J.C. Collins, S. Heppelmann, R. Jaffe, S.Y. Lee, Y. Makdisi, R.W. Robinett, J. Soffer, M. Tannenbaum, D. Underwood, A. Yokosawa, Physics World **3** (1992) 1. See also V.W. Hughes and J. Kuti, Annu. Rev. Nucl. Part. Sci. **33**, 611 (1983).
- [5.49] M.J. Alguard *et al.*, 41, 70 (1978); G. Baum *et al.*, Phys. Rev. Lett. **51**, 1135 (1983).

- [5.50] EMC, J. Ashman *et al.*, Phys. Lett. **B206**, 364 (1988) and Nucl. Phys. **B328**, 1 (1989).
- [5.51] SMC, B. Adeva *et al.*, Phys. Lett. **B302**, 533 (1993).
- [5.52] J. Kodaira, S. Matsuura, K. Sasaki and T. Uematsu, Nucl. Phys. **B159**, 99 (1979); J. Kodaira, Nucl. Phys. **B165**, 129 (1980).
- [5.53] J.D. Bjorken, Phys. Rev. **148**, 1467 (1966) and **D1**, 1376 (1970).
- [5.54] J. Ellis and R.L. Jaffe, Phys. Rev. **D9**, 1444 (1984)
- [5.55] A.V. Efremov and O.V. Teryaev, JINR Report E2-88-287 (1988); R.D. Carlitz, J.C. Collins and A.H. Mueller, Phys. Lett. **B214**, 229 (1988); G. Altarelli and G.G. Ross, Phys. Lett. **B212**, 391 (1988).
- [5.56] J.G. Morfín and W-K. Tung, Z. Phys. **52**, 13 (1991).

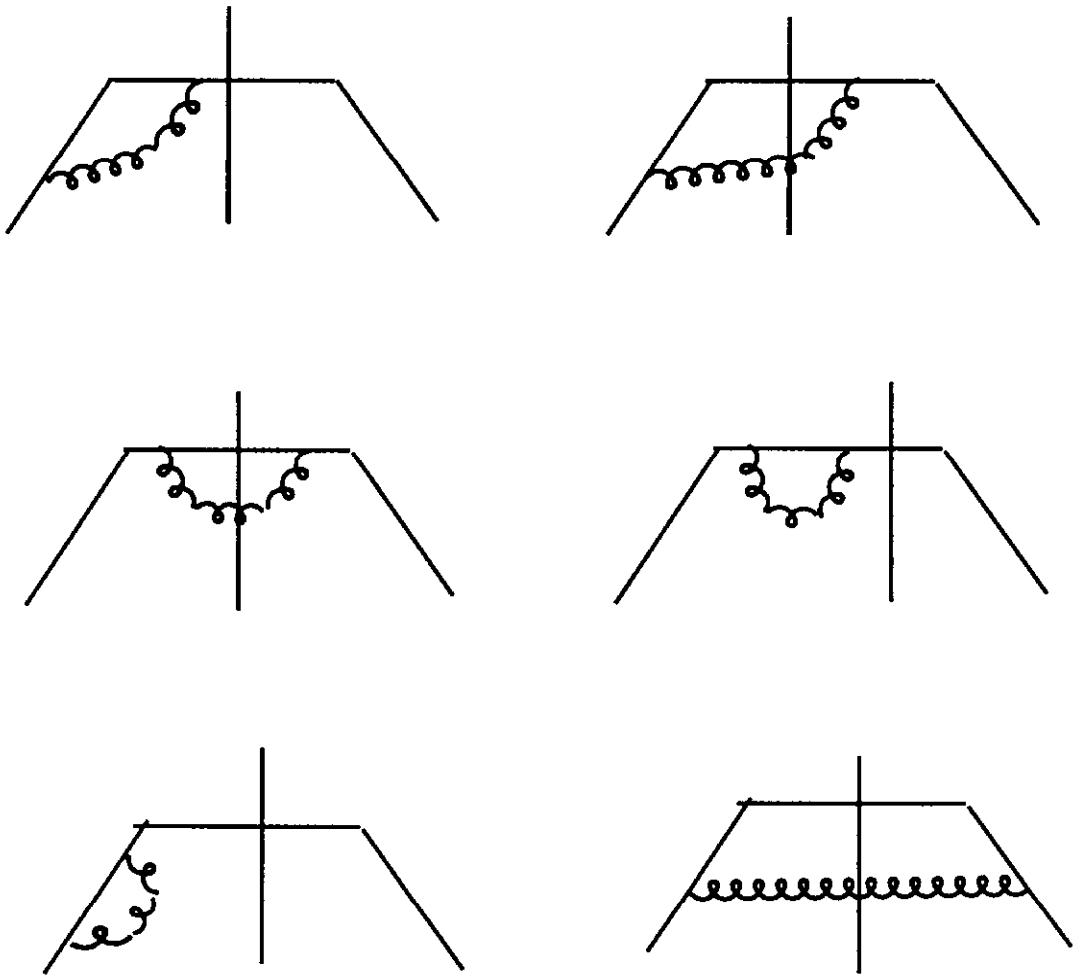


Figure 5.1. Low order diagrams for DIS.

BEBC-WA21/CDHS:  $\nu - \text{H}_2$

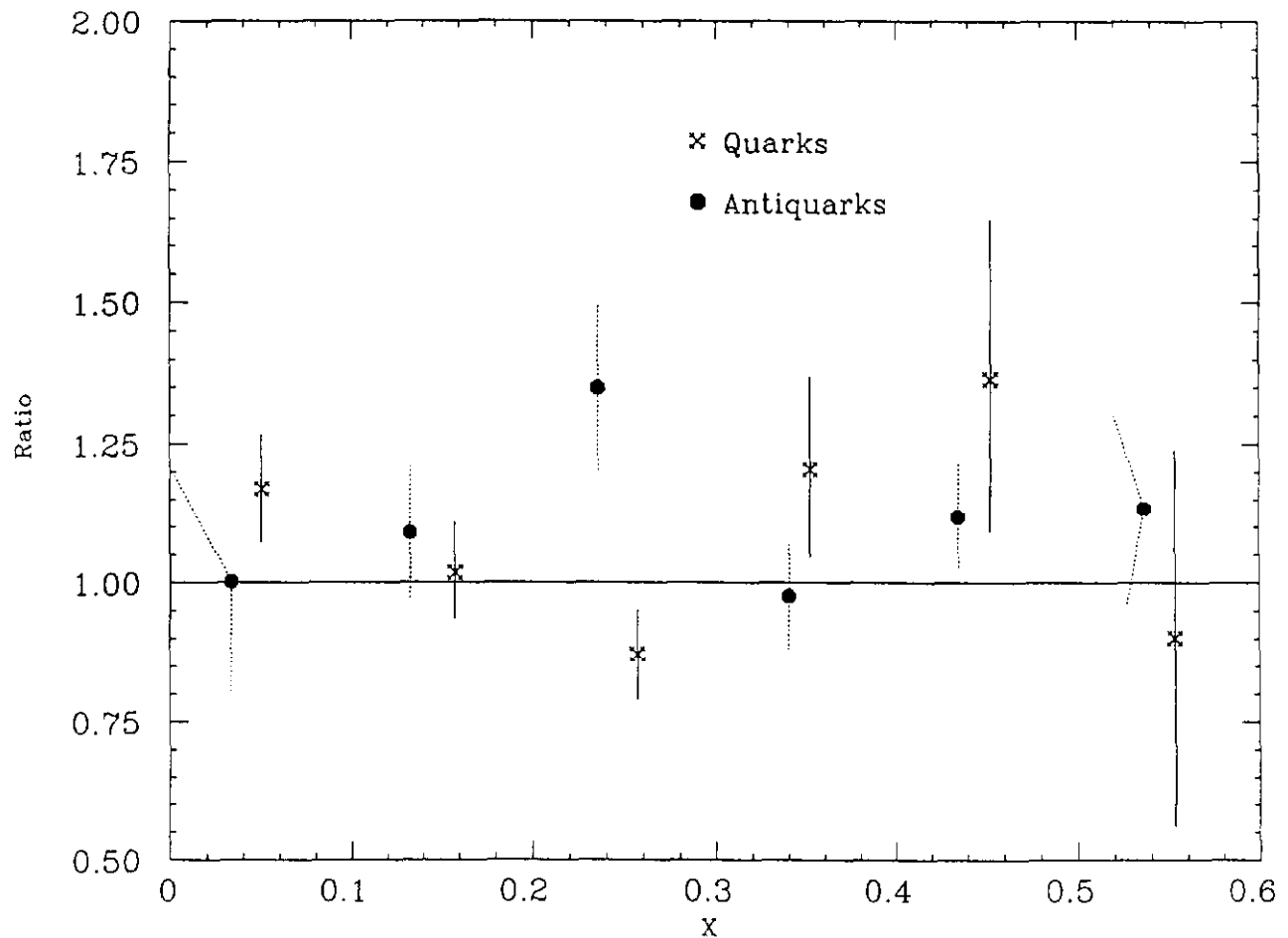


Figure 5.2. Ratios of the WA21 (BEBC) and CDHS data for quarks (crosses) and antiquarks (solid circles).

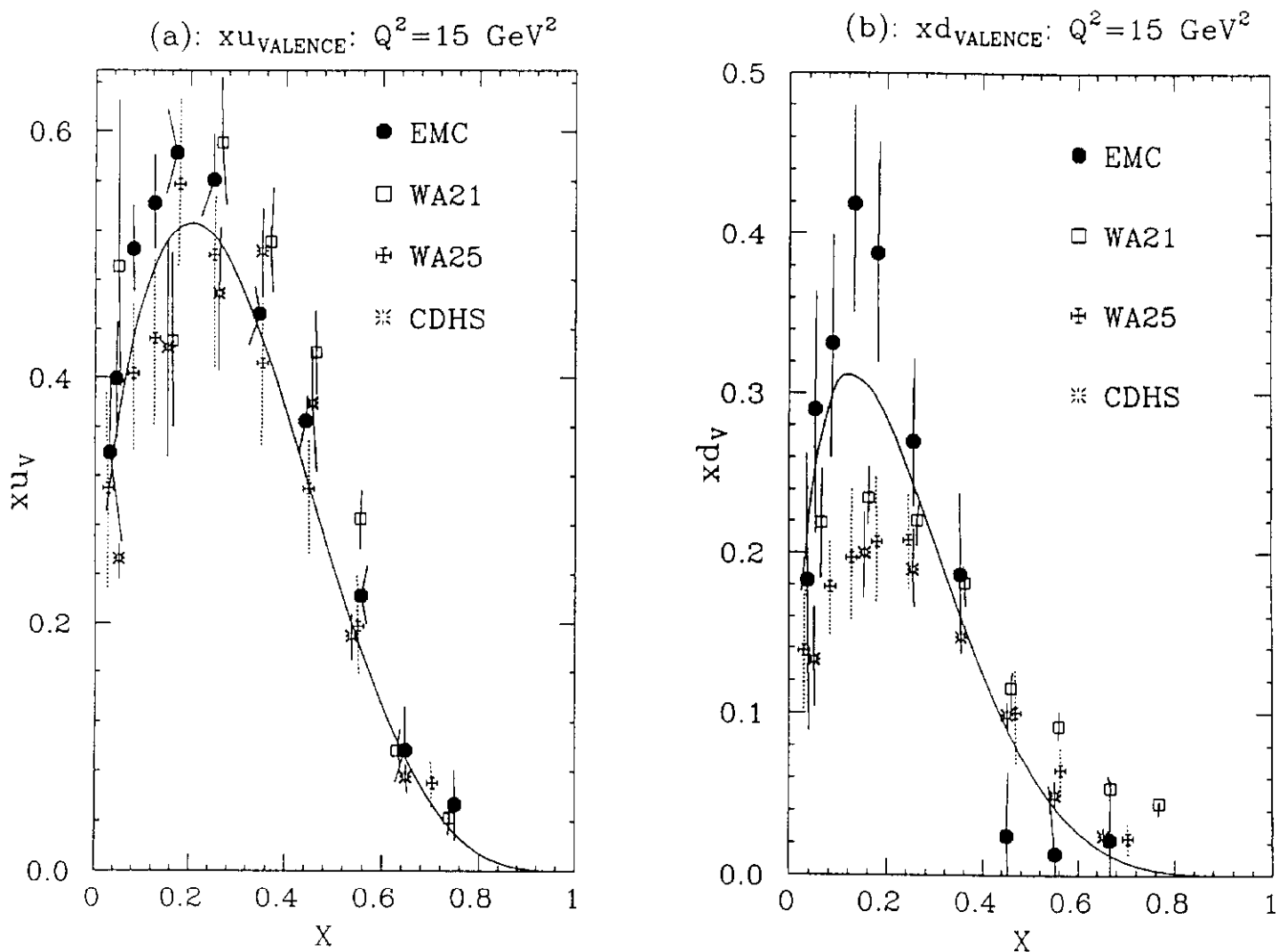


Figure 5.3. Valence quark densities in a proton: (a)  $xu_v$ , (b)  $xd_v$  as a function of  $x$ . The solid curve is the [5.56] parameterization.

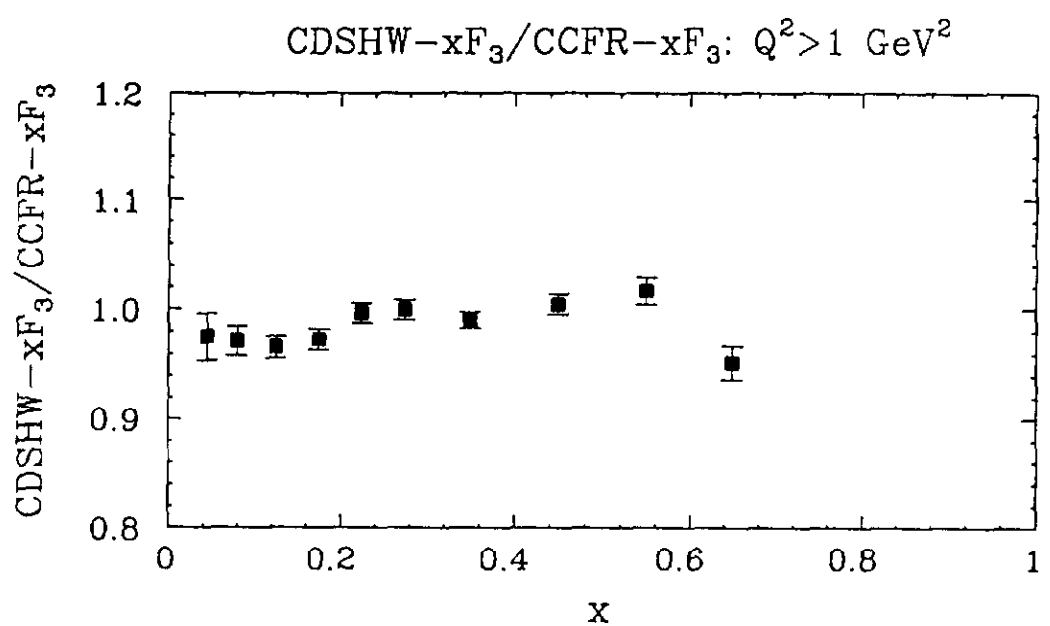


Figure 5.4. The ratio, CDHSW- $x F_3$ /CCFR- $x F_3$ , with  $Q^2 > 1$  GeV $^2$ , as a function of  $x$  with statistical errors only.

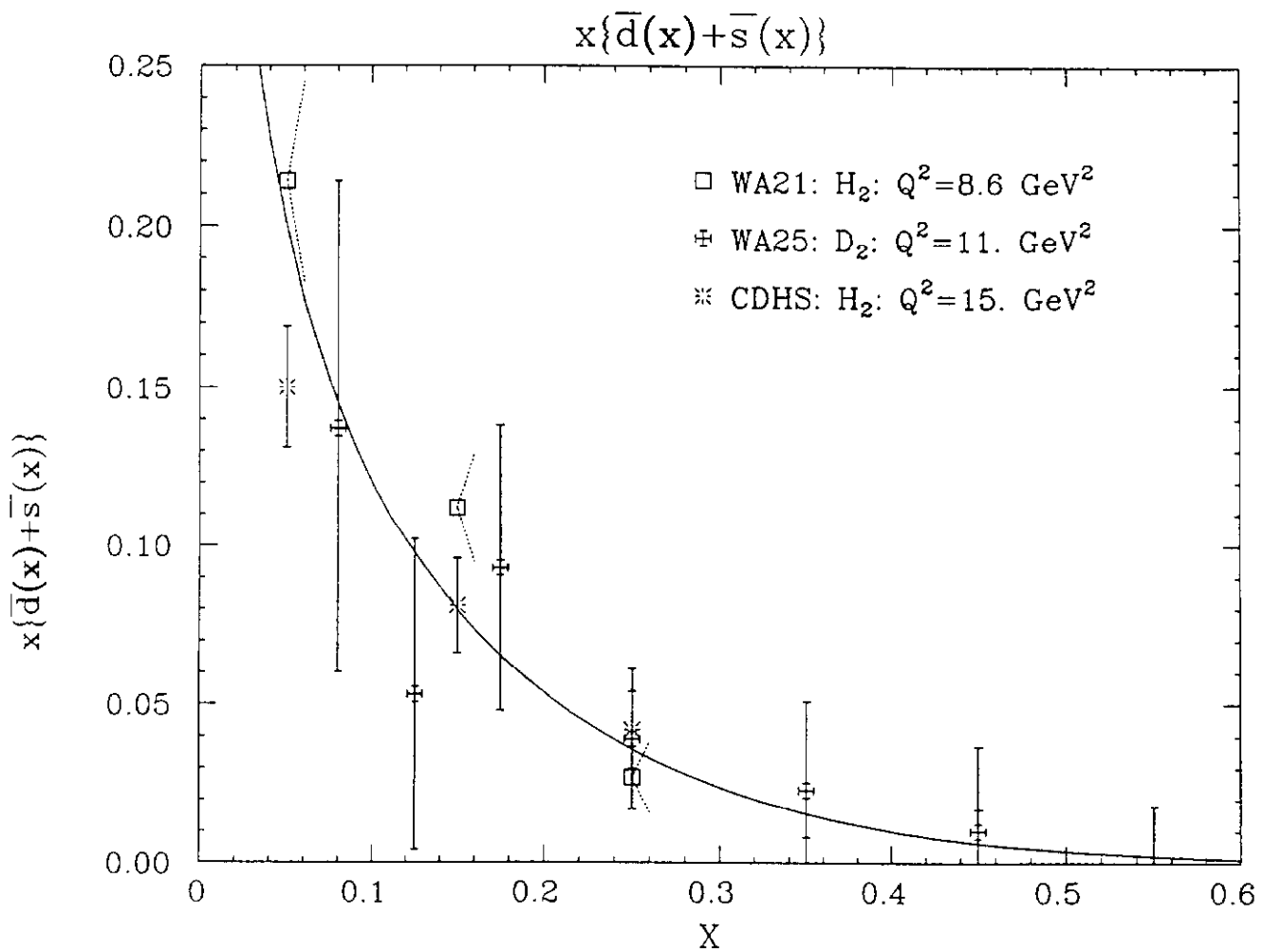


Figure 5.5.a. The antiquark component of the proton as measured by three neutrino experiments.

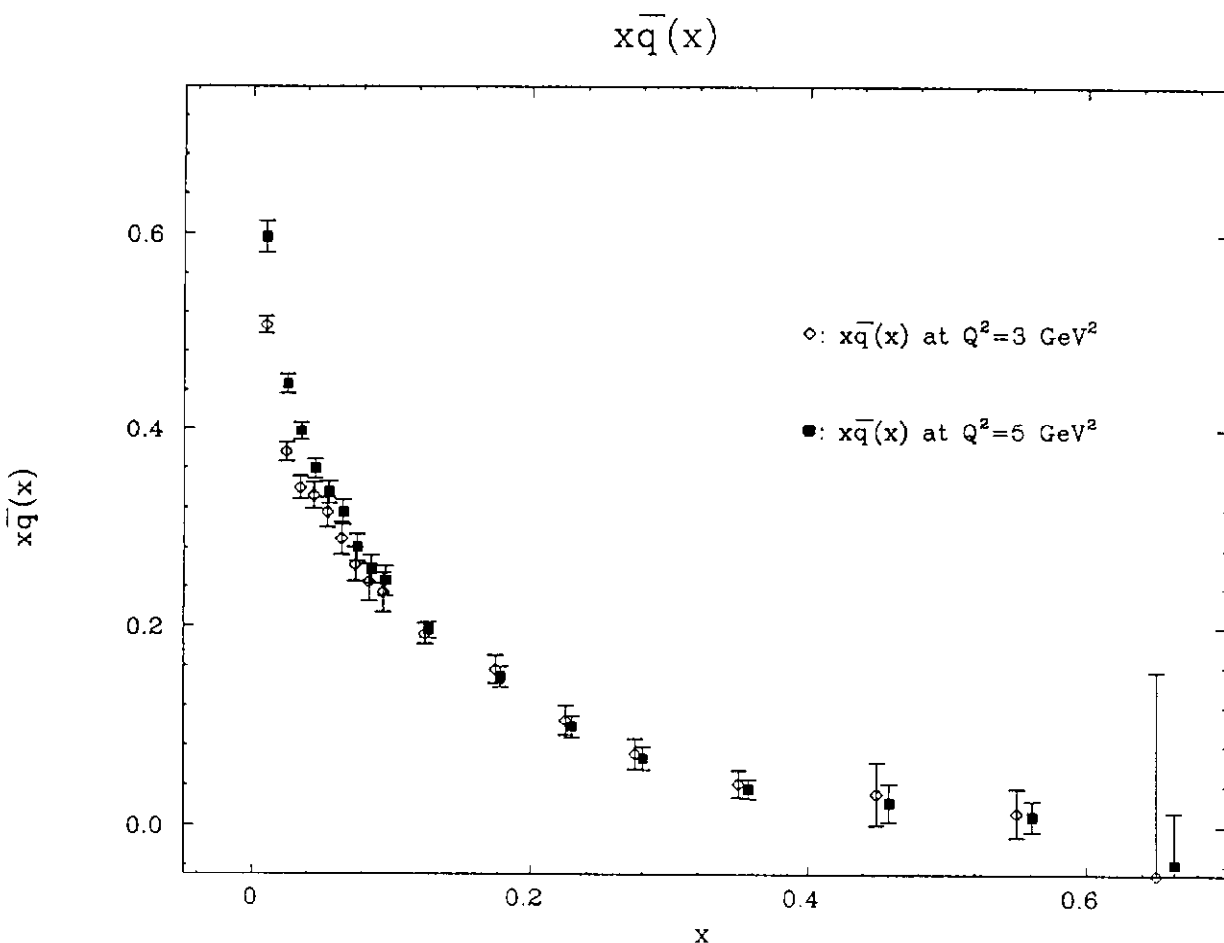


Figure 5.5.b. The antiquark component of a nucleon measured in an isoscalar target ( $\nu$ -Fe) by the CCFR collaboration.  $\bar{q}(x)$  as a function of  $x$  is shown for two values of  $Q^2$ :  $3 \text{ GeV}^2$  and  $5 \text{ GeV}^2$ .

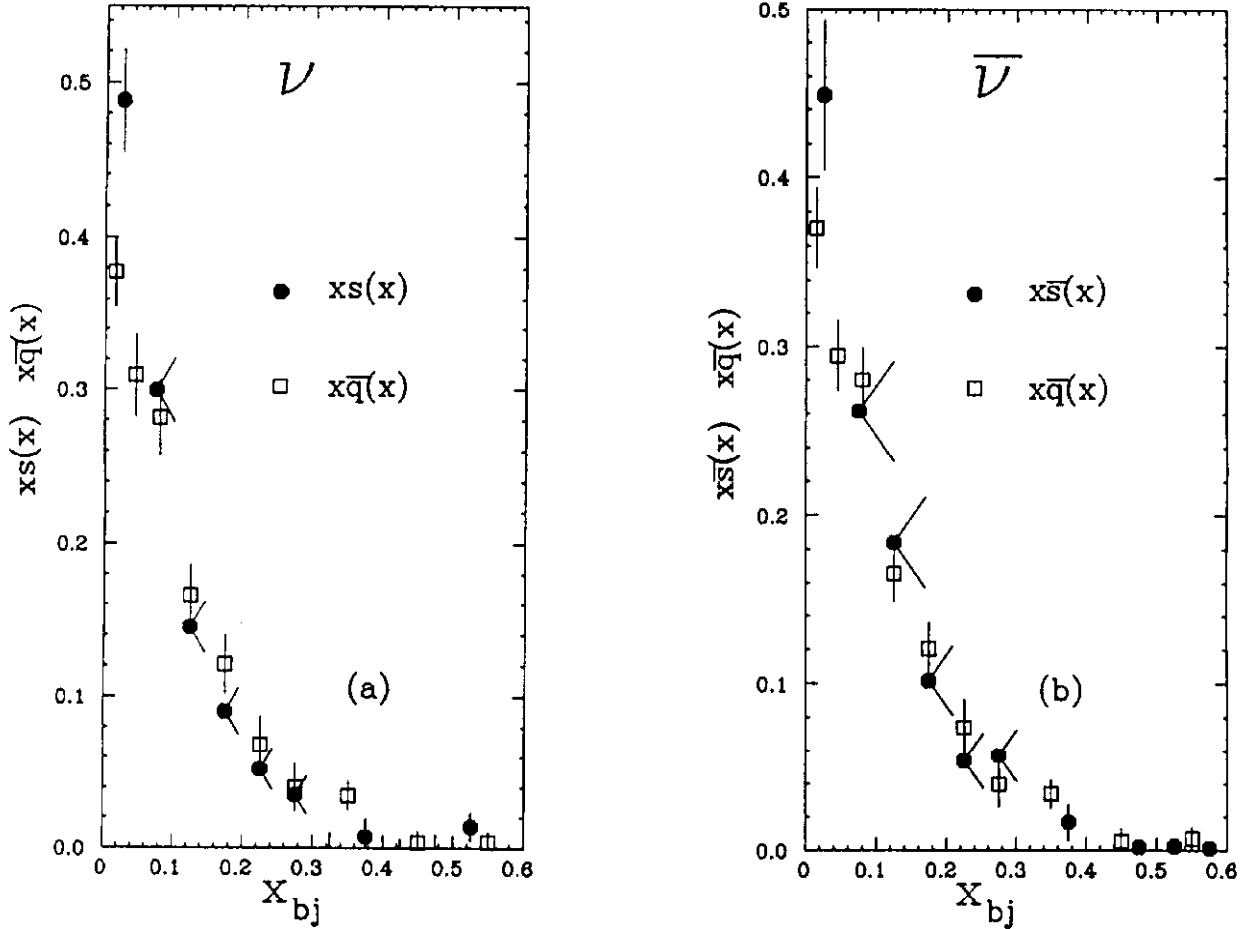


Figure 5.6. The strange sea component of the nucleon measured by analysing the CCFR  $\nu_\mu$ - and  $\bar{\nu}_\mu$ -induced opposite sign dimuons. The  $s(x)$  and  $\bar{s}(x)$  are compared to the non-strange  $\bar{q}(x)$  obtained from ordinary single muon events. To illustrate the “shape-difference”, the total  $\bar{q}(x)$  are normalized to the respective strange sea distribution.

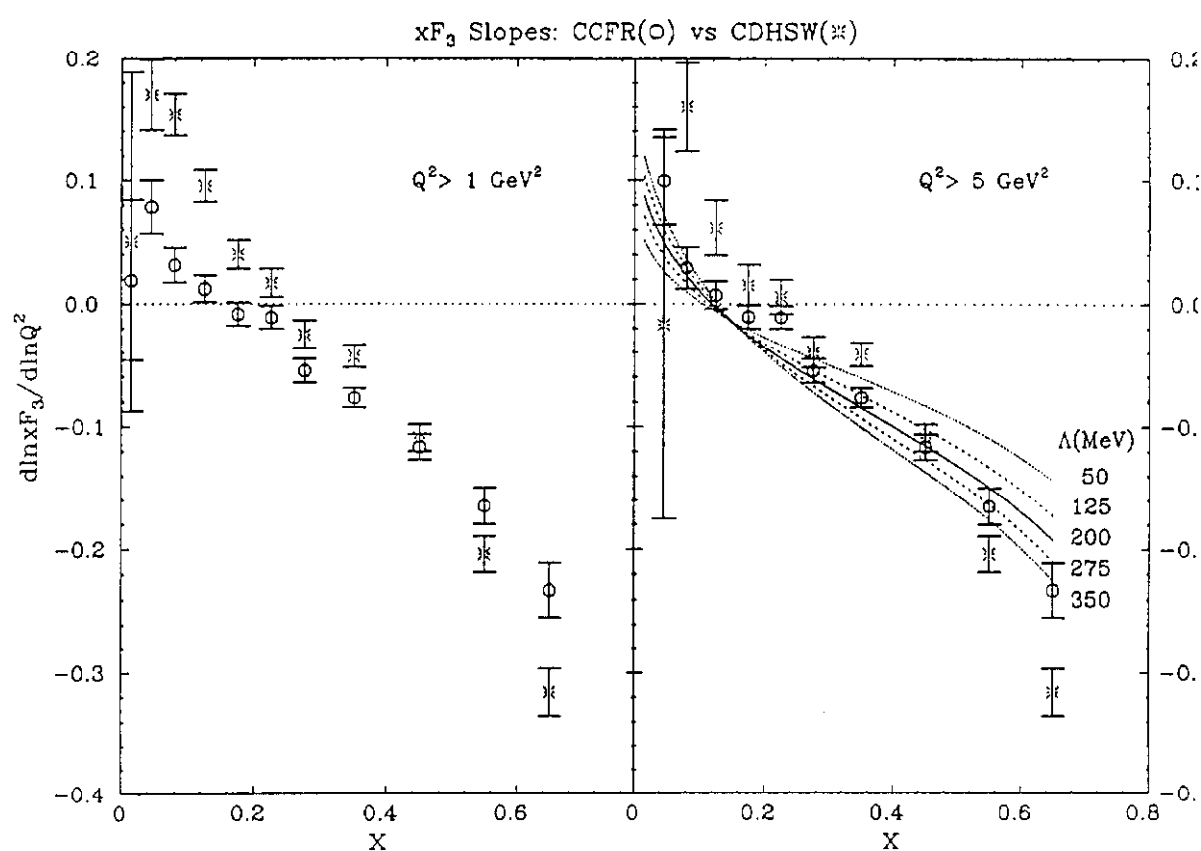


Figure 5.7.a. The logarithmic slopes of  $x F_3$  for the CDHSW and CCFR data, with (a)  $Q^2 > 1 \text{ GeV}^2$ , and (b)  $Q^2 > 5 \text{ GeV}^2$ . Only statistical errors are shown. The curves for  $Q^2 > 5 \text{ GeV}^2$  are QCD predictions for various values of  $\Lambda_{QCD}$ .

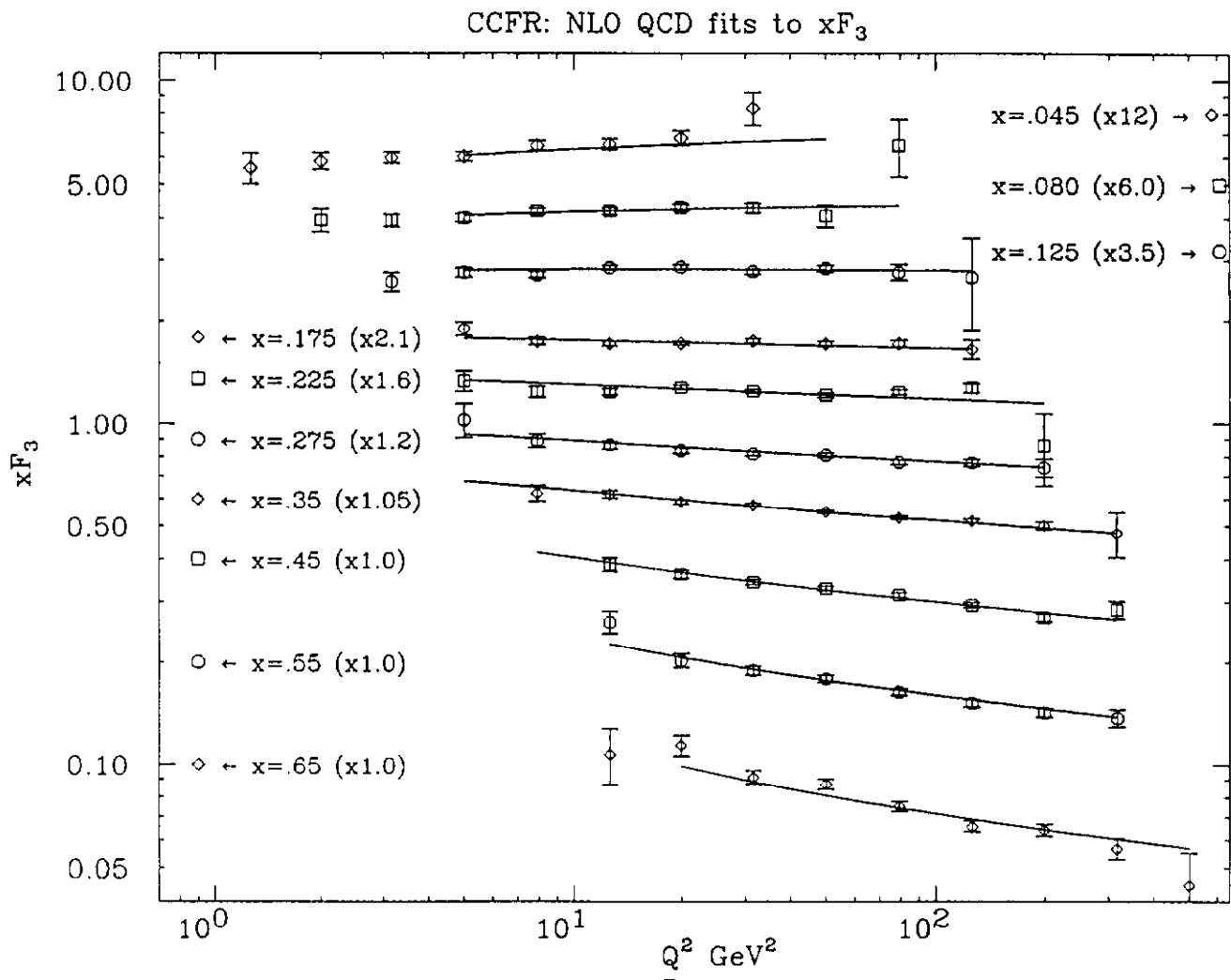


Figure 5.7.b. The  $x F_3$  data and the best NLO QCD fit. Cuts of  $Q^2 > 5$   $\text{GeV}^2$  and  $x < 0.7$  were applied for a next-to-leading order fit including target mass corrections.

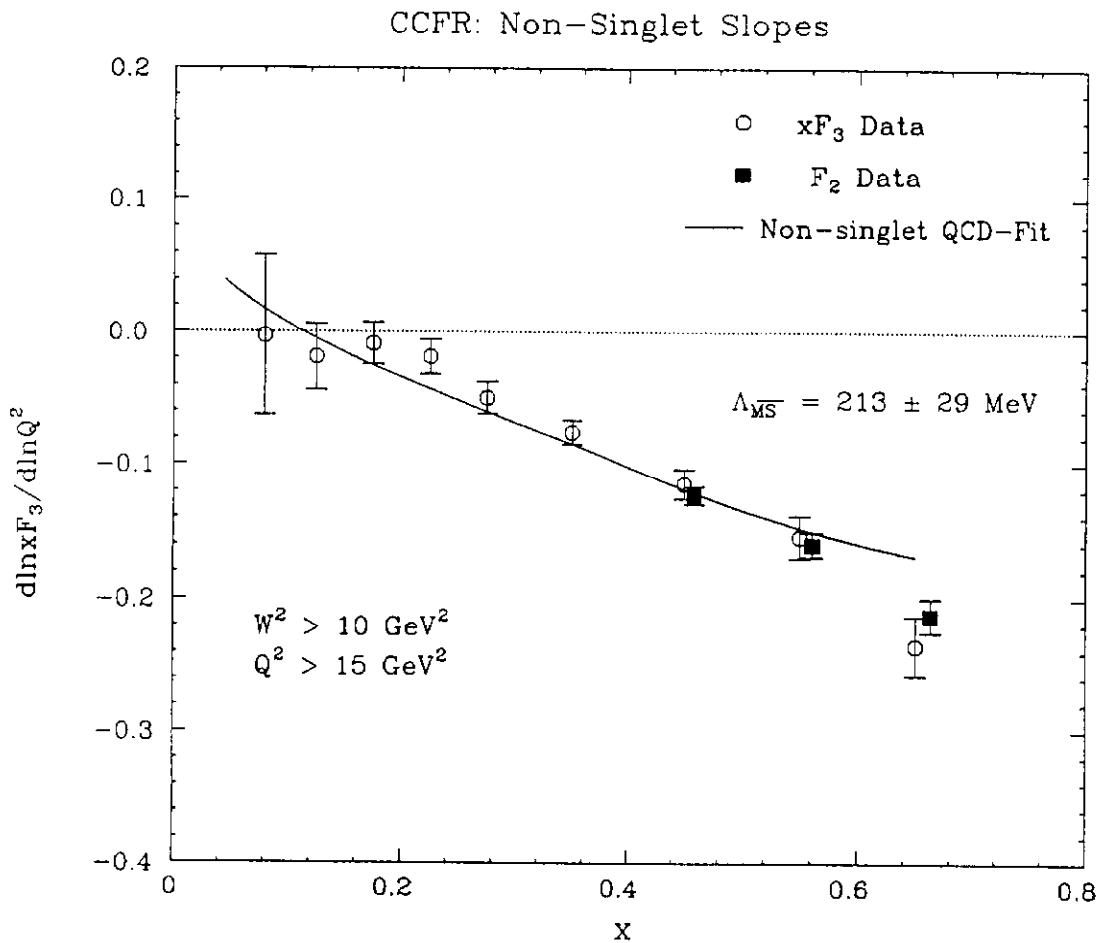


Figure 5.7.c. The slopes of  $xF_3$  ( $= d \ln xF_3 / d \ln Q^2$ ) for the CCFR data are shown in circles. The curve is a prediction from perturbative QCD with target mass correction. The slopes for  $F_2$  (squares) in the region  $x > 0.4$  are also shown (with  $x$  values shifted by +2% for clarity).

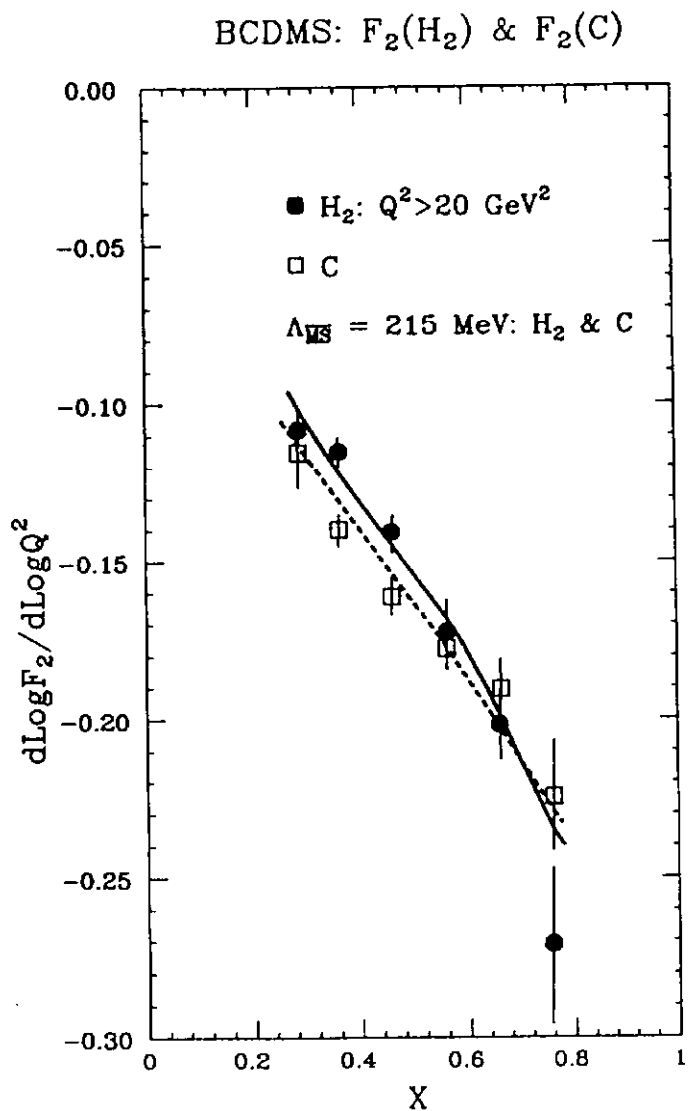


Figure 5.8.a. The BCDMS measurement of the logarithmic derivative of  $F_2$  with respect to  $Q^2$ ,  $d\log F_2 / d\log Q^2$ , as a function of  $x$  with hydrogen (solid symbols) and carbon (open symbols). The best NLO QCD non-singlet fits to these data are also shown. It is assumed that for  $x > 0.25$  the  $F_2$  data essentially evolve as non-singlets.

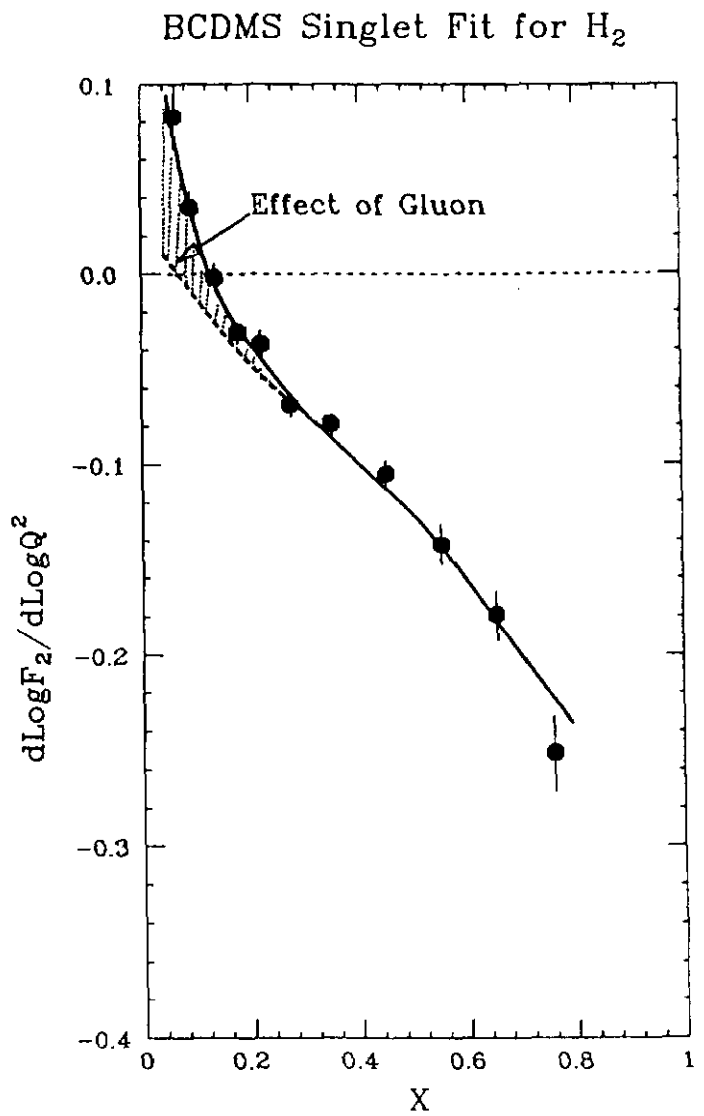


Figure 5.8.b. The singlet evolution of the BCDMS measurement of  $F_2$  in a hydrogen target. The effect of gluons, prominent at low  $x$ , is shown by the hatched region between the singlet (solid), and non-singlet (dotted) QCD fits.

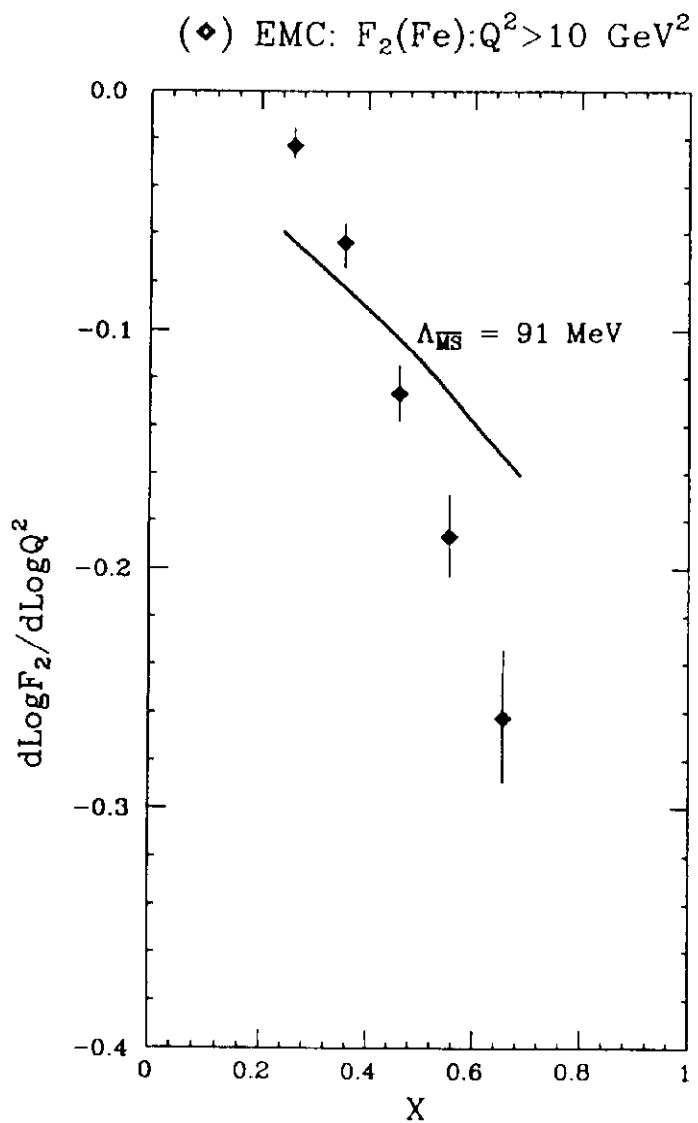


Figure 5.8.c. The EMC measurement of the logarithmic derivative of  $F_2$  with respect to  $Q^2$ ,  $d\log F_2 / d\log Q^2$ , as a function of  $x$  with iron target. The NLO QCD curve with typical value of  $\Lambda_{QCD}$  as analysed by the BCDMS collaboration is also shown.

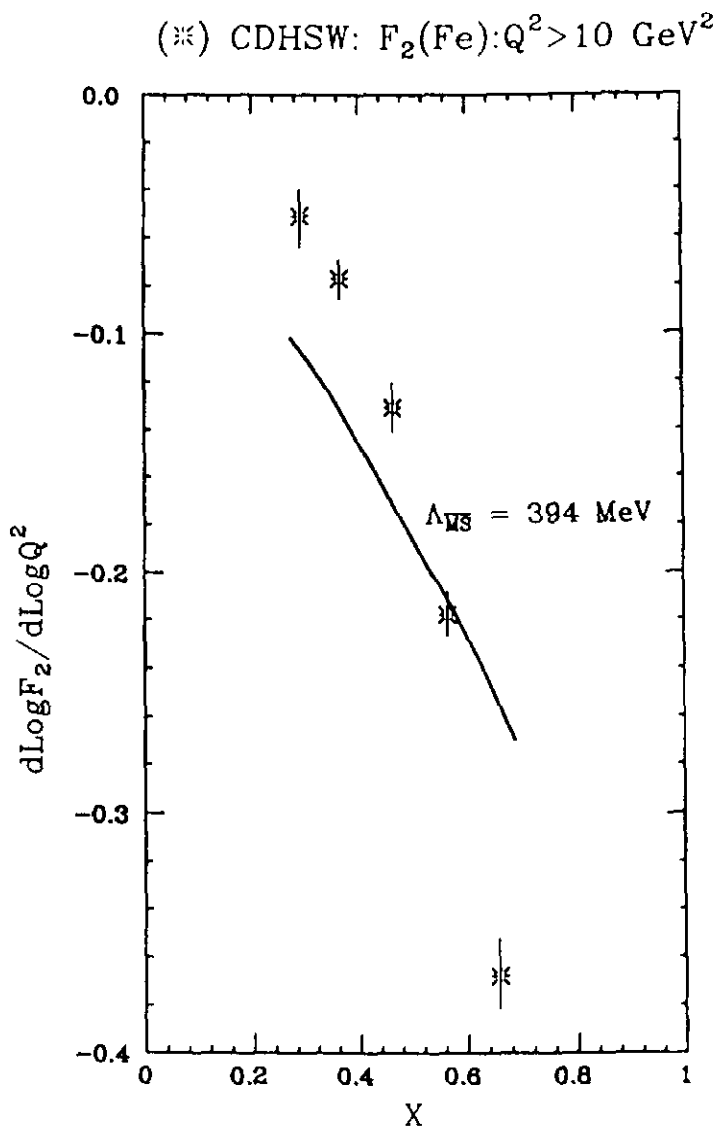


Figure 5.8.d. The CDHSW measurement of the logarithmic derivative of  $F_2$  with respect to  $Q^2$ ,  $d\log F_2 / d\log Q^2$ , as a function of  $x$  with an iron target. The NLO QCD curve with typical value of  $\Lambda_{QCD}$  as analysed by the BCDMS collaboration is also shown.

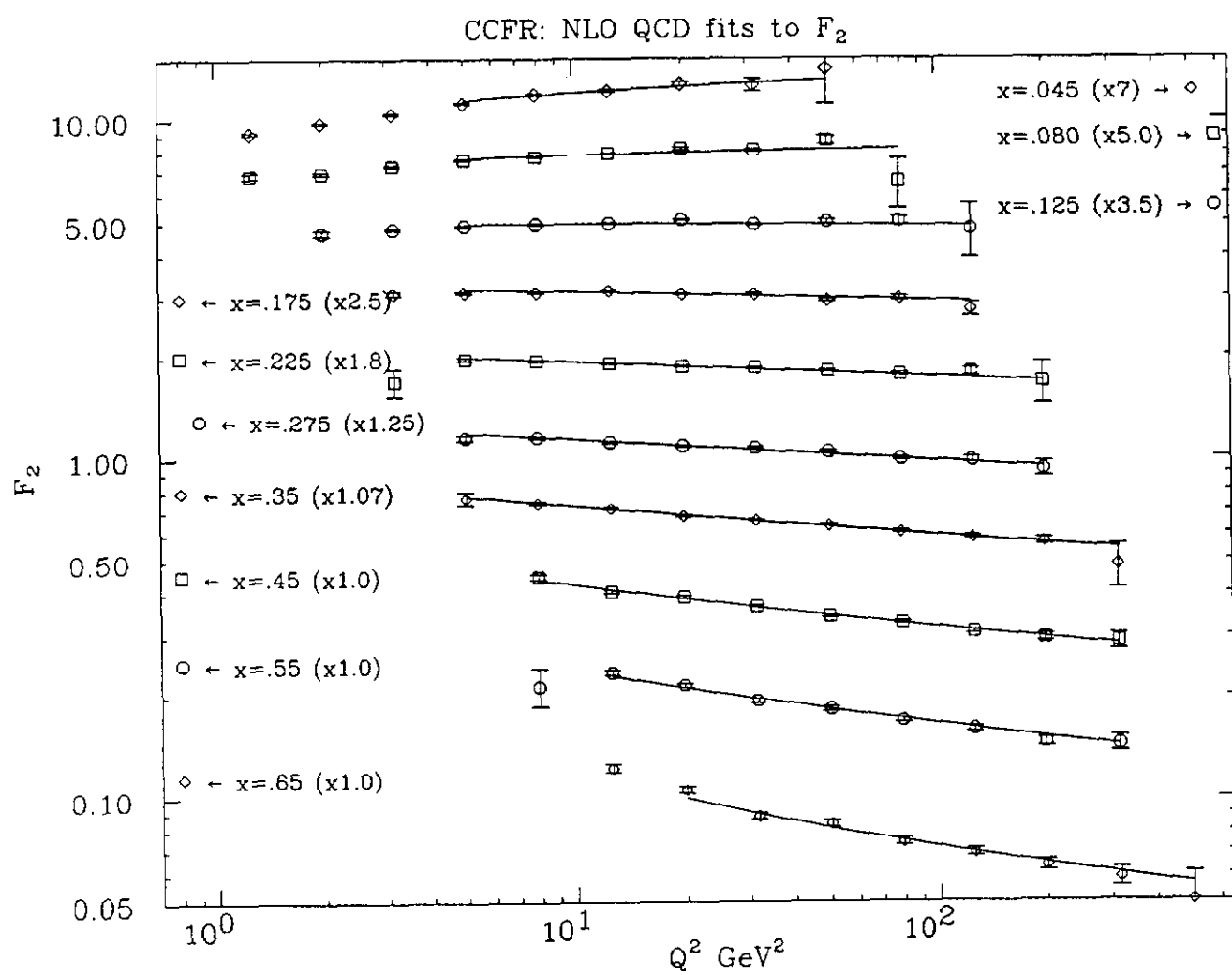


Figure 5.8.e. The  $F_2$  data of CCFR and the best NLO QCD fit. Cuts of  $Q^2 > 5 (\text{GeV}/c)^2$  and  $x < 0.7$  were applied for a next-to-leading order fit including target mass corrections.

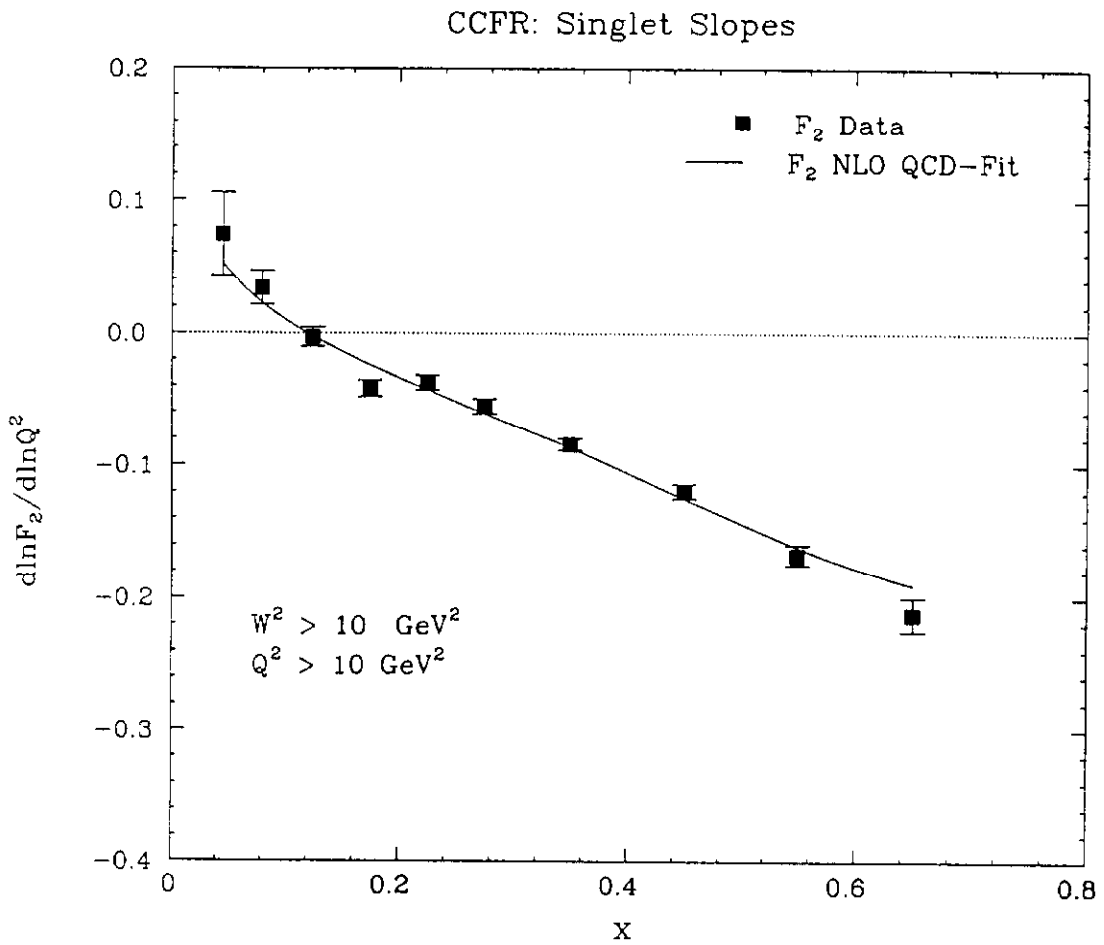


Figure 5.8.f. The slopes of  $F_2$  ( $= d \log F_2 / d \log Q^2$ ) for the CCFR data are shown (squares). The curve is a prediction from perturbative QCD.

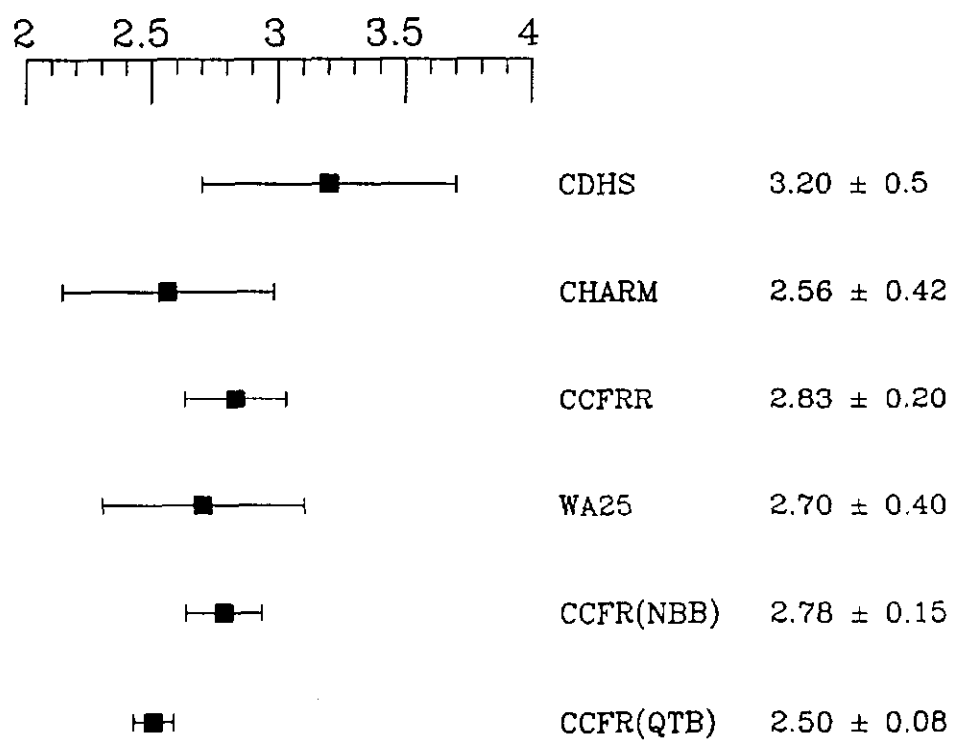


Figure 5.9. The world status of GLS sum rule measurement.

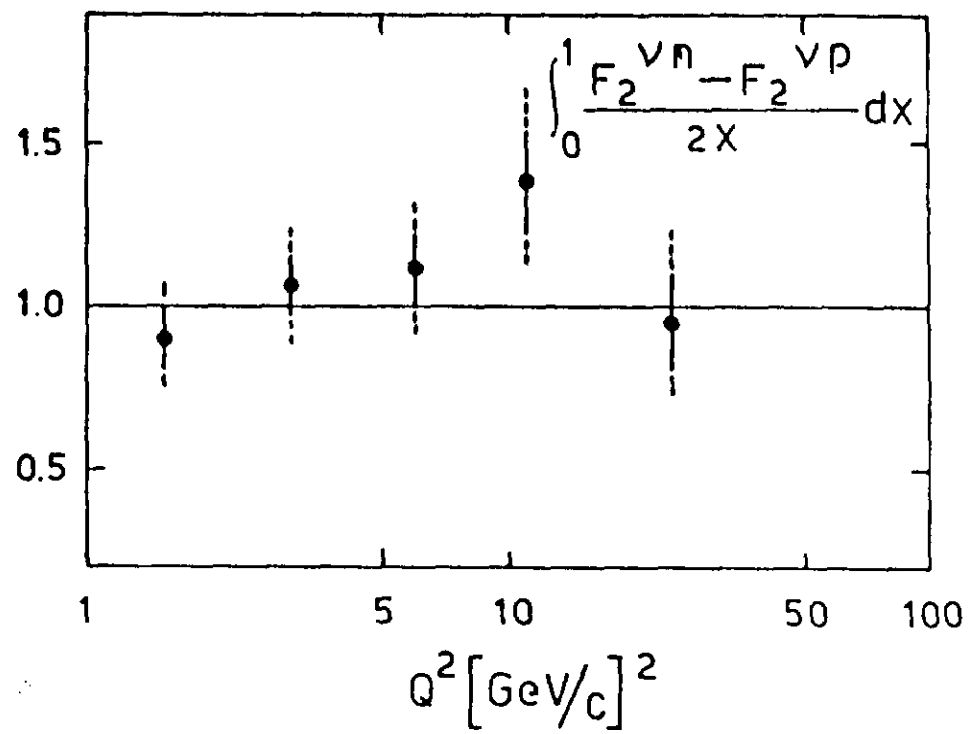


Figure 5.10. The WA25 measurement of the Adler sum rule with various  $Q^2$  cuts.

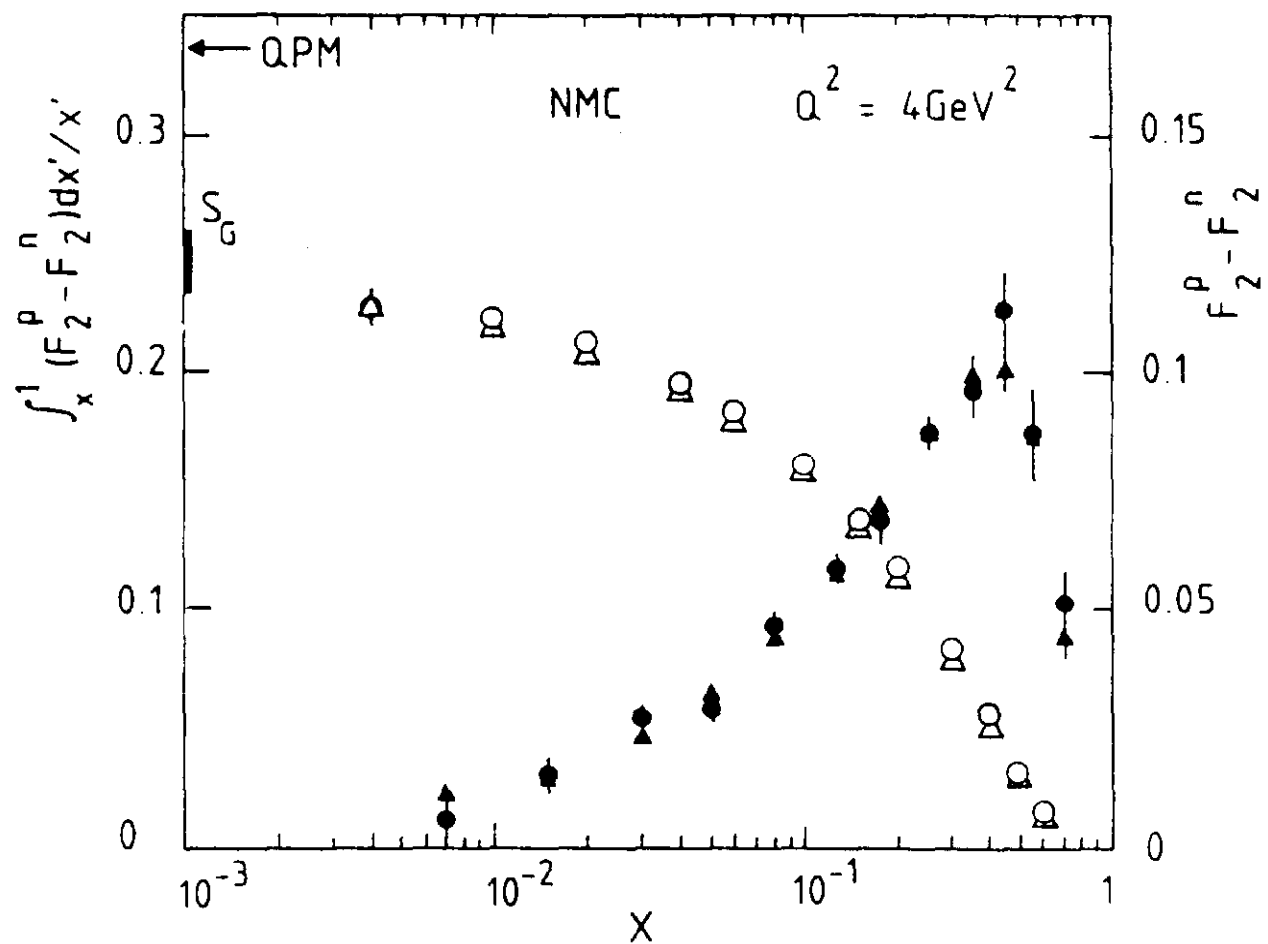


Figure 5.11. The NMC measurement of  $F_2^P - F_2^n$  — dark symbols and the right scale, as a function of  $x$ , and that of the integral  $\int (F_2^P - F_2^n) dx$  — open symbols and left scale, leading to the Gottfried sum rule. The “circles” and “triangles” represent two different methods of extraction.

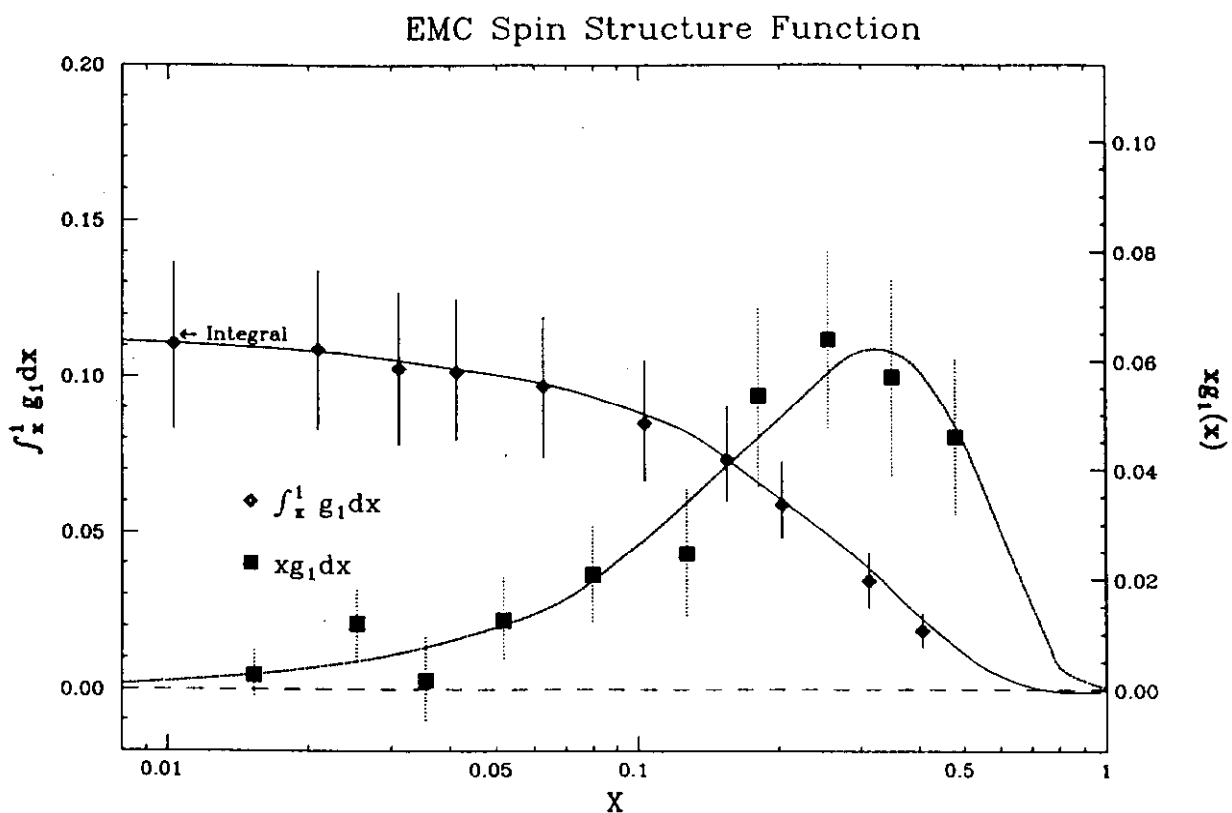


Figure 5.12. The EMC measurement of the spin structure function of proton  $g_1^p(x)$  — squares and right scale, and that of the integral  $\int g_1^p(x)dx$  — diamonds and left scale as a function of  $x$ .

## 6 Hadron-Hadron Cross Sections

The factorization program is fully realized in hadron-hadron cross sections. The underlying hard scattering may be initiated by electroweak interactions, as in Drell-Yan or direct photon production, or may be pure QCD processes, as in jet and heavy-quark production. In this section, we discuss hard scattering corrections in the simplest electroweak processes.

### 6.1 Hard-Scattering Corrections in the Drell-Yan Cross Section

The Drell-Yan process was introduced in Section 2.4. We will present the one-loop correction, noting that the inclusive Drell-Yan cross section is probably the only realistic hadronic cross section that is simple enough to present in detail. For definiteness, we limit ourselves to the purely electromagnetic process.

The basic factorization theorem for the unpolarized cross section was introduced in Section 3.3.1 and illustrated in Fig.3.1. Since the electromagnetic production of lepton pairs by a virtual photon only involves lowest order QED, the angular dependence in  $\theta$  and  $\phi$  can be calculated later. Although Eq. (3.38) holds for the double differential cross section, the generalization is straightforward, and here we only consider the corrections to the single differential cross section  $d\sigma/dQ^2$  written in the form

$$\frac{d\sigma(\tau, Q^2)}{dQ^2} = \sum_{a,b} \int_0^1 d\eta_A \int_0^1 d\eta_B \int_0^1 dz \delta(\tau/\eta_A \eta_B - z) \times \phi_{a/A}(\eta_A, \mu) H_{ab}(z, \alpha_s(\mu)) \phi_{b/B}(\eta_B, \mu), \quad (6.1)$$

where the parton-parton cross section  $H_{ab}$  is evaluated at the scaled variable  $z = Q^2/\eta_A \eta_B s$ , with  $\sqrt{s}$  is the center of mass energy of the hadron-hadron system . The theoretical justification for this result is analyzed in [6.1].

The hard scattering cross section  $H_{ab}$  has a perturbative expansion in  $\alpha_s$  of the form

$$H_{ab} = \sigma_0(H_{ab}^{(0)} + \frac{\alpha_s}{\pi} H_{ab}^{(1)} + \dots), \quad (6.2)$$

where  $\sigma_0$  contains the overall dimensions. In lowest order of perturbation theory, the only channel allowed is  $q + \bar{q} \rightarrow \gamma^*$ , where  $q$  labels a quark with charge  $Q_q$  and the photon is virtual.  $H^{(0)}$  is therefore given by the parton-model (Born) cross section. At higher order we proceed as in Section 5.1 for DIS. The hard-scattering cross section is independent of the nature of the external hadrons, so we can compute it from Eq. (6.1) by considering a particular case: namely we apply Eq. (6.1) to the parton-parton reaction. Then the functions  $\phi(\eta)$  measure the parton content of the external partons. In this case, the quantity on the left-hand-side is an  $n$ -dimensional scattering cross section which contains poles as  $\epsilon \rightarrow 0$ . As in DIS, perturbative expansions for the distributions  $\phi_{i/j}$  enable us to solve for the hard scattering functions  $H$ .

In  $O(\alpha_s)$  we have to consider both the virtual corrections to this basic vertex diagram and the gluon bremsstrahlung reaction  $q + \bar{q} \rightarrow \gamma^* + g$ . In addition there are new channels  $q + g \rightarrow q + \gamma^*$  and  $\bar{q} + g \rightarrow \bar{q} + \gamma^*$ . The latter reactions are very interesting from the experimental point of view, because they make the cross section sensitive to the gluon density in the hadron.

### 6.1.1 $O(\alpha_s)$ Corrections to the Drell-Yan Reaction

The calculation of one-loop corrections proceeds much as for DIS. The cut graphs are shown in Fig. 6.1. We recognize that they are the crossed versions of the diagrams for deeply inelastic scattering.

If we regularize the ultraviolet and infrared divergences by working in  $n$ -dimensions, then all pole terms cancel, apart from the collinear poles due to gluon radiation parallel to the directions of the incoming quark and anti-quark. As in the DIS cross section, Section 5.4, this is the cancellation of final state interactions, which is necessary for the factorization theorem Eq. (6.1) to hold. The remaining collinear divergences can be absorbed into the perturbative parton distributions, leaving behind the hard-scattering function. To make this explicit, we expand (6.1) with external partons  $a$  and  $b$ , to order  $\alpha_s$ , using  $\phi_{i/j}^{(0)}(x) = \delta_{ij}\delta(1-x)$  (Eq. (3.14)). We find

$$\begin{aligned}
\frac{d\sigma}{dQ^2}{}_{ab}^{(0)}(\tau, Q^2, \epsilon) + \frac{\alpha_s}{\pi} \frac{d\sigma}{dQ^2}{}_{ab}^{(1)}(\tau, Q^2, \epsilon) = \\
H_{ab}^{(0)}(\tau, Q^2, \epsilon) + \frac{\alpha_s}{\pi} H_{ab}^{(1)}(\tau, Q^2, \epsilon) \\
- \frac{\alpha_s}{\pi} \sum_c \int_{x_A}^1 d\eta_A \phi_{c/a}^{(1)}(\eta_A, \epsilon) H_{ab}^{(0)}(\tau, Q^2, \epsilon) \\
- \frac{\alpha_s}{\pi} \sum_d \int_{x_B}^1 d\eta_B \phi_{d/b}^{(1)}(\eta_B, \epsilon) H_{ad}^{(0)}(\tau, Q^2, \epsilon). \quad (6.3)
\end{aligned}$$

Thus, to extract the one-loop hard scattering, we need the (regulated) one-loop cross section and the (regulated) one-loop parton distributions, given in Section 5.2 for the  $\overline{\text{MS}}$  and DIS schemes. Actually, because  $H_{ab}^{(0)}$  is nonzero only for quark-antiquark scattering, with (see Eq. (2.62))

$$H_{q\bar{q}}^{(0)}(z) = Q_f^2 \frac{4\pi\alpha^2}{3Nq^2 s} \delta(1-z), \quad (6.4)$$

we only need  $\phi_{q/q}^{(1)} = \phi_{\bar{q}/\bar{q}}^{(1)}$  and  $\phi_{q/g}^{(1)} = \phi_{\bar{q}/g}^{(1)}$  at this level. For simplicity we use  $N$  for the number of colors.

The explicit quark-antiquark cross section at one loop is given by

$$\begin{aligned}
\left(\frac{\alpha_s}{\pi}\right) \frac{d\sigma}{dQ^2}{}_{q\bar{q}}^{(1)}(\tau, Q^2, \epsilon) = Q_f^2 \frac{4\pi\alpha^2}{3Nq^2 s} \left(\frac{\alpha_s}{\pi}\right) \left(\frac{4\pi\mu^2}{Q^2}\right)^\epsilon \\
\times \left\{ -\left(\frac{1}{\epsilon} - \gamma_E\right) P_{qq}^{(1)} + w_{q\bar{q}}^{(1)}(x) \right\}, \quad (6.5)
\end{aligned}$$

where

$$\begin{aligned}
w_{q\bar{q}}^{(1)}(x) = \delta(1-x) C_F [2\zeta(2) - 4] \\
+ C_F \left[ 4\mathcal{D}_1(x) - 2(1+x) \ln(1-x) - \frac{(1+x^2)}{1-x} \ln x \right]. \quad (6.6)
\end{aligned}$$

and where  $P_{qq}^{(1)}$  is the one-loop evolution kernel (splitting function) given in Eq. (5.7), and where we define

$$\mathcal{D}_m(z) = \left[ \frac{\ln^m(1-z)}{1-z} \right]_+. \quad (6.7)$$

Note that we take  $\epsilon \equiv 2 - n/2$ . Other conventions, of course, change the formulas somewhat.

The other partonic reaction  $q+g \rightarrow \gamma+q$ , which starts at  $O(\alpha_s)$ , is where

$$\begin{aligned} \left(\frac{\alpha_s}{\pi}\right) \frac{d\sigma}{dQ^2_{qg}}^{(1)}(\tau, Q^2, \epsilon) &= Q_f^2 \frac{4\pi\alpha^2}{3Nq^2s} \left(\frac{\alpha_s}{\pi}\right) \left(\frac{4\pi\mu^2}{Q^2}\right)^\epsilon \\ &\times \left\{ -\frac{1}{2} \left( \frac{1}{\epsilon} - \gamma_E \right) P_{qg}^{(1)} + w_{qg}^{(1)}(x) \right\}, \end{aligned} \quad (6.8)$$

with

$$w_{qg}^{(1)}(x) = C_F \left[ (1 - 2x + 2x^2) \ln \frac{(1-x)^2}{x} + \frac{1}{2}(3 + 2x - 3x^2) \right], \quad (6.9)$$

where again  $P_{qg}^{(1)}$  is the one-loop splitting function.

The determination of the one-loop hard scattering functions is now a simple matter. For “ $\overline{\text{MS}}$ ” distributions (Eqs. (5.8) and (5.9), for instance), we use

$$\phi_{a/b}(x, \epsilon) = \delta_{ab} \delta(1-x) - \frac{1}{\epsilon} \frac{\alpha_s}{2\pi} P_{a/b}^{(1)}(x) + O(\alpha_s^2), \quad (6.10)$$

in which the residues of the pole terms are the splitting functions. Substituting Eq. (6.10) into the general expanded formula Eq. (6.3), and comparing the results with Eqs. (6.5) and (6.8), we find simply,

$$H_{q\bar{q}}^{\overline{\text{MS}}(1)} = w_{q\bar{q}}^{(1)}, \quad (6.11)$$

$$H_{qg}^{\overline{\text{MS}}(1)} = w_{qg}^{(1)}. \quad (6.12)$$

For the DIS scheme, the parton distributions, Eqs. (5.11) and (5.12), are a bit more complicated, because they have picked up various infrared safe corrections from the one-loop deeply inelastic scattering cross section. The principles are the same, however, and we find in this scheme [6.2],

$$\begin{aligned} H_{q\bar{q}}^{\text{DIS}(1)} &= C_F \left\{ (1+z^2) D_1(z) + 3D_0 + \left( \frac{4\pi^2}{3} + 1 \right) \delta(1-z) - 6 - 4z \right\}, \\ H_{qg}^{\text{DIS}(1)} &= \frac{1}{4} \left\{ (z^2 + (1-z)^2) \ln(z-z) + \frac{9}{2}z^2 - 5z + \frac{3}{2} \right\}. \end{aligned} \quad (6.13)$$

Both Eqs. (6.12) and (6.13) provide absolute predictions for the Drell-Yan cross section, when combined with parton distributions in Eq. (6.1). It

is important, of course, to use distributions that have been determined in the corresponding scheme, usually from deeply inelastic scattering (see Section 2). As a practical matter, the hard scattering corrections at one loop turn out to be substantial; sometimes as large as the zeroth order (parton model) cross section. This is the theoretical side of the “K-factor” problem for Drell-Yan (see below). In Section 6.3 we shall see that the experimental situation is consistent with large perturbative corrections relative to the parton model. Considerable progress has been made in understanding the origin of large corrections for values of  $\tau = Q^2/s$  not too small [6.3] [6.4], but it is fair to say that the problem is not yet solved .

## 6.2 Drell-Yan at Two Loops

Along with DIS, the inclusive Drell-Yan cross section has been fully analyzed at two loops in a series of papers by van Neerven and his collaborators, in both the DIS scheme and the  $\overline{\text{MS}}$  scheme [6.5] [6.6] [6.7] [6.8] [6.9] [6.10] [6.11]. The full results for the hard-scattering functions at two loops are quite lengthy; but it is perhaps useful to exhibit here the full plus and delta-function distributions, as they occur in the quark-antiquark two-loop hard scattering function:

$$\begin{aligned}
H_{q\bar{q}}^{(2),S+V}(z) = & \left(\frac{\alpha_s}{4\pi}\right)^2 \delta(1-z) \\
& \times \left\{ C_A C_F \left[ \left[ \frac{193}{3} - 24\zeta(3) \right] \ln\left(\frac{Q^2}{M^2}\right) - 11 \ln^2\left(\frac{Q^2}{M^2}\right) \right. \right. \\
& - \frac{12}{5} \zeta(2)^2 + \frac{592}{9} \zeta(2) + 28\zeta(3) - \frac{1535}{12} \Big] + C_F^2 \left[ \left[ 18 - 32\zeta(2) \right] \ln^2\left(\frac{Q^2}{M^2}\right) \right. \\
& + \left[ 24\zeta(2) + 176\zeta(3) - 93 \right] \ln\left(\frac{Q^2}{M^2}\right) + \frac{8}{5} \zeta(2)^2 - 70\zeta(2) - 60\zeta(3) + \frac{511}{4} \Big] \\
& + n_f C_F \left[ 2 \ln^2\left(\frac{Q^2}{M^2}\right) - \frac{34}{3} \ln\left(\frac{Q^2}{M^2}\right) + 8\zeta(3) - \frac{112}{9} \zeta(2) + \frac{127}{6} \right] \Big\} \\
& + C_A C_F \left[ - \frac{44}{3} \mathcal{D}_0(z) \ln^2\left(\frac{Q^2}{M^2}\right) + \left[ (\frac{536}{9} - 16\zeta(2)) \mathcal{D}_0(z) \right. \right. \\
& \left. \left. + \frac{16}{3} \zeta(2)^2 - \frac{16}{9} \zeta(2) - \frac{16}{3} \zeta(3) + \frac{16}{9} \right] \right]
\end{aligned}$$

$$\begin{aligned}
& - \frac{176}{3} \mathcal{D}_1(z) \left] \ln \left( \frac{Q^2}{M^2} \right) - \frac{176}{3} \mathcal{D}_2(z) + \left[ \frac{1072}{9} - 32\zeta(2) \right] \mathcal{D}_1(z) + \left[ 56\zeta(3) \right. \right. \\
& + \frac{176}{3}\zeta(2) - \frac{1616}{27} \left] \mathcal{D}_0(z) \right] + C_F^2 \left[ \left[ 64\mathcal{D}_1(z) + 48\mathcal{D}_0(z) \right] \ln^2 \left( \frac{Q^2}{M^2} \right) \right. \\
& + \left[ 192\mathcal{D}_2(z) + 96\mathcal{D}_1(z) - (128 + 64\zeta(2))\mathcal{D}_0(z) \right] \ln \left( \frac{Q^2}{M^2} \right) \\
& \left. \left. + 128\mathcal{D}_3(z) - (128\zeta(2) + 256)\mathcal{D}_1(z) + 256\zeta(3)\mathcal{D}_0(z) \right] \right. \\
& + n_f C_F \left[ \frac{8}{3}\mathcal{D}_0(z) \ln^2 \left( \frac{Q^2}{M^2} \right) + \left[ \frac{32}{3}\mathcal{D}_1(z) - \frac{80}{9}\mathcal{D}_0(z) \right] \ln \left( \frac{Q^2}{M^2} \right) \right. \\
& \left. \left. + \frac{32}{3}\mathcal{D}_2(z) - \frac{160}{9}\mathcal{D}_1(z) + (\frac{224}{27} - \frac{32}{3}\zeta(2))\mathcal{D}_0(z) \right]. \quad (6.14)
\end{aligned}$$

To these results are added various smooth functions of the variable  $z$ . We may note that it is only in quark-antiquark scattering that distributions that are singular at  $z = 1$  occur. Note that there are plus distributions up to  $\mathcal{D}_3(z)$ .

### 6.3 Drell-Yan Cross Sections: Experimental Review

The production of dileptons in high energy collisions has been a staple of all hadron machines in the world for more than two decades. Lepton pairs in hadronic collisions were first observed at Brookhaven by Lederman and his group (see [6.12] and [6.13]). See Fig. 6.2 for the invariant mass spectrum of this original experiment. This early experiment was conceived as a scheme for searching for the carrier of the charged weak process, the intermediate vector boson (IVB). This technique has contributed greatly to the high energy physics landscape, including: the discovery of two new quarks (more below), as a source of information on parton distributions of the nucleon, as the essentially sole arbiter of parton distributions of mesons, and as a benchmark for a host of naive parton model predictions as well as sophisticated QCD calculations.

### 6.3.1 Massive Photon Production

The parton-model picture of the Drell Yan reaction has been described above in Section 2.4. In the collision of, say, two protons, a quark from one proton seeks out and annihilates with an antiquark from the other proton to form a single, off-shell photon which subsequently converts into the observable lepton pairs. The term “Drell-Yan” has been extended to include the production of any spin-1 virtual particle produced by electroweak interactions.

*General experimental techniques.* The choice of experimental technique depends on the physics and the beam configuration. Because of the low cross section, and of the desirability for high rate studies of a continuum cross section, fixed target experiments at the highest available energies or colliding beam experiments utilizing the highest possible luminosities are advantageous. At Brookhaven, the original fixed target experiment with incident nucleon and pion beams was utilized to produce dimuon pairs. At Fermilab, Brookhaven, and CERN, such experiments were carried out for many years, only recently culminating with E605 at Fermilab. It was with electron pairs, however, that the Brookhaven experiment discovered the  $J/\psi$  in a follow-up to the original dimuon approach. Electrons were used with this double-arm spectrometer because of better mass resolution (a few percent). For a review of this experiment, see Ref. [6.14].

Simultaneous with the early fixed target experiments, the CERN ISR mounted experiments using the collision of two proton beams in the center of mass. Presently, the tradition of high energy colliding hadron beams is active with the final analysis of the CERN SPS facility and with the ongoing Fermilab Tevatron program, both proton-antiproton colliding beam machines. This tradition should be continued into the anticipated SSC and LHC, proton colliding beam facilities.

Because of the high intensities necessary, most fixed target experiments have concentrated on muon final states. This is because the production of background leptons from decays and of the “punchthrough” of interaction and beam-related particles can be suppressed through the utilization of heavy hadron absorbers directly downstream from the target. Muons tra-

verse such dumps with ease and may be momentum analyzed in a magnetic spectrometer, while electrons would be totally invisible. The negative feature of such an approach is that the momentum resolution for muons is degraded through multiple scattering (by about 15%). Large air-core, rather than iron, magnets have been used to suppress this degradation. Colliding beam experiments are much cleaner in this regard and have concentrated on the better resolution obtainable with electromagnetic calorimetry. Consequently, the IVB-production, and the early ISR experiments were able to concentrate on electron final states, and key universality tests were performed in the early days. At the highest energies, and in the forward direction, where backgrounds from decays are severe, electron measurements are still superior, as generally iron toroids are utilized for muon analysis in those regions. In either approach, mass resolution is important in order to distinguish the continuum from the resonant dilepton states or, as is the case with the IVB experiments, to precisely measure the mass of the decaying particle.

*Significant results.* Among the notable achievements utilizing this technique of looking at dilepton final states are the discovery of new quark species, determination of parton distributions, and the measurement of the normalization of the cross section.

*New quarks.* Production of dileptons have served well as the indicator for the  $q\bar{q}$  resonant states - the ‘onia’ of charm and beauty, in particular. Most recently, the technique was extended to the highest energies and resulted in the discovery of the bottom quark resonant state,  $\Upsilon$ . Of course, the original discovery, at both SPEAR and Brookhaven, of the  $J/\psi$  was nearly scooped by the original Drell-Yan Brookhaven experiment which missed the interpretation of a shoulder in the invariant mass spectrum (Fig. 6.2). This story is one of the famous tales of high energy physics.

*Parton distributions.* The earliest utility of continuum dilepton production was as an important test of the parton model and, with the acceptance of the parton model, determination of the momentum distributions of the partons participating in the collision, especially the quark “sea”.

*Nucleon distributions.* With incident proton beams, the parton distributions of the proton can be extracted in a manner not dissimilar from the

procedure in deeply inelastic scattering. Through the comparison of incident proton and antiproton beams, NA3 at CERN was able to extract both the valence and sea quark momentum content.

By parameterizing a scaling set of valence and sea distributions by shape parameters,

$$\begin{aligned} u(x) &= Ax^\alpha(1-x)^{\beta_v} \\ d(x) &= 0.57u(x) \\ S(x) &= C(1-x)^{\beta_s} \end{aligned}$$

NA3 found (see [6.15]) the results in table 6.1. For comparison, the CDHS results from neutrino scattering are also shown as are the results of E288 from Fermilab, which made DIS-inspired parameterizations of the valence distributions.

	CDHS	NA3	E288
$\alpha$	$0.51 \pm 0.07$	$0.60 \pm 0.08$	
$\beta_v$	$2.38 \pm 0.09$	$3.59 \pm 0.14$	
$\beta_s$	$8.0 \pm 0.7$	$9.03 \pm 0.30$	$7.62 \pm 0.08$

Table 6.1. Representative shape parameters for parton distributions [6.16].

*Pion distributions.* With incident pion beams and assumptions about the nucleon parton distributions, NA3 also fit for the parton distributions of quarks inside a pion. Again, they parameterized the distributions with a form

$$\begin{aligned} V(x) &= A_V x^\alpha(1-x)^\beta \\ S(x) &= A_S(1-x)^{\beta_s}. \end{aligned}$$

They found  $\alpha = 0.41 \pm 0.04$  and  $\beta = 0.95 \pm 0.05$ . More up-to-date fits to parton distributions also employ Drell-Yan data (see Section 8).

*Scaling.* The parton model suggests that the cross section for lepton pairs of invariant mass  $Q$  should scale as a function of the variable,  $\sqrt{\tau} = Q/\sqrt{s}$ . Fig. 6.3 shows a variety of data, over a moderate range of  $\sqrt{s}$ . The scaling

behavior is reasonably demonstrated. The cross section below the Z mass at  $\sqrt{s} = 630$  GeV is determined to be  $\sigma = 405 \pm 51 \pm 84$  pb by UA2 [6.17]. This is in rough agreement with  $O(\alpha_s^2)$  calculations. CDF has also measured the integral cross section for electron pairs below the Z mass (see [6.18]).

*The K-factor.* The fact that the normalization of the cross section in the parton model is off by large factors is consistent with theoretical results (see Section 6.1.1). Table 6.2 shows a variety of experiments and their measured “K-factor” - the correction required of the naive theory to match the data.

Group	Beam/target	cm Energy	K
E288	p/Pt	27.4	1.7
E439	p/W	27.4	$1.6 \pm 0.3$
CHFMNP	p/p	44,63	$1.6 \pm 0.2$
AABCSY	p/p	44,63	1.7
NA3	p/Pt	27.4	$3.1 \pm 0.5 \pm 0.3$
E537	antip/W	15.3	$2.45 \pm 0.12 \pm 0.20$
NA3	(p-antip)/Pt	16.8	$2.3 \pm 0.4$
NA3	pi/Pt	16.8	$2.49 \pm 0.37$
		22.9	$2.22 \pm 0.33$
E326	pi/W	20.6	$2.70 \pm 0.08 \pm 0.40$
NA10	Pi/W	19.1	$2.8 \pm 0.1$
Goliath	pi/Be	16.8,18.1	2.5
Omega	pi/W	8.7	$2.6 \pm 0.5$

Table 6.2. K Factors for dilepton experiments (Ref. [6.15]).

As can be seen, the discrepancy is large, a factor of 2 or more. Calculations beyond the leading log at order  $\alpha_s$  were performed and the result was that the correction to the leading order was disturbingly large,  $K = 1 + 2\pi\alpha_s/3 \sim 1.6$  for  $\alpha_s \sim 0.3$ , appropriate for pair masses of a few GeV. Clearly, concerns about the convergence of the perturbation series were very real, until it was discovered that, for the dominant vertex corrections, the series exponentiates for all orders. The series is then expressible as  $K \rightarrow e^{2\pi\alpha_s/3} = 1.8$  [6.2] [6.4]. That the major part of the discrepancy is explained in this fashion is comforting, but the problem is not fully solved [6.3]. Other sources of the discrepancy have also been proposed. The contributions of very low  $x$

regions, below the accessible data used for the parameterizations, could be important since much of the cross section could still be “hidden” in that region. Also, corrections for Fermi motion in the heavy targets and the pion parton distribution shapes can be invoked. Most important, probably, is the uncertainty in the normalization of the data, which could be in the tens of percent.

### 6.3.2 W and Z Production

While one of the original motivations for using dilepton final states was a search for the intermediate vector boson (IVB) of the conventional weak interaction, it was many years before that was realized. Now, the production of both W and Z bosons forms an important part of the experimental program of all of the highest-energy colliders. The language used is that of the original Drell-Yan prescription, with only electroweak modifications.

The importance of W and Z production is many-faceted. Primarily, the precise determination the W mass is of utmost importance in the program of global electroweak parameter determination. The production of IVB plus hadronic jets serves as an important laboratory for QCD measurements. The analysis of the V-A asymmetry in W decays is a sensitive measure of parton density functions. Finally, the observation of W's is among the clues for the uncovering of the still elusive top quark.

*General experimental techniques.* The three major detectors which have or will have impact on the physics issues listed above are UA2 at CERN, CDF and D0 at Fermilab. The UA2 and D0 detectors feature precision calorimetry and no magnetic field measurement capability, save for muons. CDF, on the other hand, has a central superconducting solenoidal field which aids in electron identification (by comparing the calorimeter and momentum determination for the same presumed electrons) and allows for muon momentum analysis without iron, except as a filter.

In most cases, precision mass determination experiments are done in the electron channel. Only CDF, with its solenoidal field momentum determination for muons, is able to perform a precise mass measurement, using muons uncompromised by multiple scattering errors inherent in iron toroids. For

UA2 and D0, only precision electromagnetic calorimetry is available.

UA2 has completed its runs, while CDF and D0 are just starting a long period of experimentation at the Tevatron. The total data accumulated to date by UA2 are  $13\text{pb}^{-1}$  and CDF, about  $5\text{pb}^{-1}$ . The results from those two experiments are impressive, with the W mass being the centerpiece of their efforts in this context. While, clearly a major part of the initial IVB discovery, UA1 did not have a significant role in the precision mass determinations. D0 is, of course, just beginning and has no published data. However, at this writing (Fall, 1992), the Tevatron is running and both CDF and D0 have accumulated roughly  $100\text{nb}^{-1}$  with a hundred or so W's on tape. The Tevatron era is really just beginning, with  $100\text{pb}^{-1}$  expected in this first run during 1992-3.

The sizes of the existing data sets from CDF and UA2 are (in number of events)

CDF	$W \rightarrow e$	1130
	$W \rightarrow \mu$	592
	$Z \rightarrow ee$	65
	$Z \rightarrow \mu\mu$	123

UA2	$W \rightarrow e$	2065
	$Z \rightarrow ee$	156

Recent determinations from the two experiments yield [6.19] [6.20] [6.21] [6.22],

$$\begin{aligned} \text{CDF} \quad m_W(e) &= 79.91 \pm 0.35 \pm 0.24 \pm 0.19 \text{GeV} \\ m_W(\mu) &= 79.90 \pm 0.53 \pm 0.32 \pm 0.08 \text{GeV} \end{aligned}$$

$$\text{UA2} \quad m_W(e) = 80.35 \pm 0.33 \pm 0.17 \pm 0.81 \text{GeV}$$

Here, the first error is statistical, the second is systematic, and the third is the energy scale uncertainty. For UA2, the quantity measured is the ratio of the W mass to that of the Z mass, thereby cancelling the scale uncertainty. They find  $m(W)/m(Z) = 0.8813 \pm 0.00336 \pm 0.0019$ . They extract  $m(W)$  by scaling with the LEP value of  $m(Z) = 91.175 \pm 0.021$  GeV. The systematic

errors for both experiments are really *statistically* limited by the paucity of Z events.

*Running of  $\alpha_s$ .* The UA2 collaboration has expended considerable effort in a determination of the strong coupling,  $\alpha_s$ . They determine, in a comparison of  $W + 1$  jet to  $W + 2$  jet events,  $\alpha_s = 0.123 \pm 0.018 \pm 0.017$  ([6.23] [6.24]). Here, the first error is statistical, the second is experimental systematic (including parton distributions). This result is very dependent on Monte Carlo simulation and an independent determination of the parton densities required by the Monte Carlo. To date, CDF has not published a similar analysis. The relatively small value of  $\alpha_s$  observed at these high momentum scales is evidence that the coupling is indeed asymptotically free (Section 1.4.2).

## 6.4 Direct Photons: Theory

In this section an overview of some of the relevant theoretical issues for direct photon production will be presented. A more detailed review can be found in [6.25]. As noted previously, a calculation of direct photon production starts with the two  $O(\alpha\alpha_s)$  subprocesses  $gq \rightarrow \gamma q$  (Compton) and  $q\bar{q} \rightarrow \gamma g$  (annihilation). For large values of  $x_T$ , these two subprocesses provide the dominant contribution to direct photon production. The interplay between the two contributions can be studied by comparing cross sections obtained with particle and antiparticle beams. For example, the Compton subprocess dominates in  $p\bar{p}$  collisions for large  $x_T$ , since the antiquark distributions are small in this region. However, the annihilation term can be significant in  $p\bar{p}$  collisions, since the  $\bar{u}$  and  $\bar{d}$  distributions in the antiproton are the same as the  $u$  and  $d$  distributions in the proton. Both of these subprocesses result in final states which consist of a high- $p_T$  photon balanced approximately by a recoiling jet on the opposite side of the event. There will be very little hadronic activity in the immediate region of the photon.

For typical fixed target experiments  $x_T$  is in the range of 0.2 to 0.6 and the above two subprocesses provide the dominant mechanism for direct photon production. However, in colliding beam experiments it is possible to get to smaller values of  $x_T$ . For example, at  $\sqrt{s} = 1800$  GeV,  $p_T = 18$  GeV

corresponds to  $x_T = 0.02$ . Here one can encounter sizable contributions from bremsstrahlung processes. In this class of processes, a quark or gluon initiated jet in the final state radiates a photon in the process of hadronization. This gives rise to events with substantial hadronic activity in the general region of the produced photon. In the framework under discussion here, one can take this contribution into account by using photon fragmentation functions. These give the probability density for a quark or gluon to produce a photon which takes a fraction  $z$  of the parent parton's momentum. The simplest form for these functions follows from a simple QED calculation which yields

$$zD_{\gamma/q}(z, Q^2) = e_q^2 \frac{\alpha}{2\pi} [1 + (1 - z)^2] \ln(Q^2/\Lambda^2), \quad (6.15)$$

and

$$zD_{\gamma/g}(z, Q^2) = 0. \quad (6.16)$$

Here  $Q$  represents a scale which is characteristic of the transverse momentum of the photon with respect to the parent quark, which will typically be on the order of  $p_T$ . The quantity  $\Lambda$  serves as an infrared cutoff – in typical leading-logarithm calculations it is usually set equal to the value chosen for the QCD scale parameter  $\Lambda_{QCD}$  which appears in  $\alpha_s$  and in the scale violating distribution functions. It is possible to calculate QCD corrections to the fragmentation functions in Eqs. (6.15) and (6.16) that result from gluon radiation by quarks and gluons and from the production of  $q\bar{q}$  pairs from gluons. These may be calculated using modified forms of the evolution equations for the scale dependence of the parton distribution functions. A more detailed discussion of this procedure, together with parameterizations of the resulting functions, can be found in Ref. [6.25]. In addition to these calculable parts, there is also the possibility of nonperturbative contributions to the photon fragmentation functions. Generally, this type of term is thought to give rise to relatively soft photons, since their production would occur late in the parton shower and would represent a long distance effect. Vector meson dominance is often used to model this component.

The bremsstrahlung contribution can be calculated using the general factorized cross section Eq. (2.76) with all possible two-body quark-quark,

quark-gluon, and gluon-gluon subprocesses convoluted with the appropriate distribution and fragmentation functions. Notice that the fragmentation function in Eq. (6.15) increases logarithmically with the scale  $Q$ . This feature remains true also for the QCD corrected functions, as well. Thus, the fragmentation functions are formally of order  $\alpha/\alpha_s$ . When convoluted with subprocess cross sections which are of order  $\alpha_s^2$  (such as  $qq \rightarrow qq$ , etc.,) one obtains a result which is of order  $\alpha\alpha_s$ .

The bremsstrahlung contribution falls off more rapidly in  $x_T$  than do the other lowest order contributions. Part of this is due to the extra convolution in  $z$  and part is due to what is called the *trigger bias effect*. The distribution functions tend to fall off faster with increasing momentum fraction than do the fragmentation functions. Thus, the most efficient way of getting a high- $p_T$  photon is to shift towards lower  $x$  in the distribution functions and higher  $z$  in the fragmentation function. This tends to force the photon to have  $z$  near one where the fragmentation function is smaller relative to its value in the low- $z$  region. Hence, the bremsstrahlung contribution is largest in the region of small  $x_T$  values typically explored at colliders. Often this contribution is suppressed by the use of isolation cuts, which are required as part of the trigger in order to efficiently identify photons. The effects of such cuts can be modeled by modifying the fragmentation functions. When higher order effects are included in the calculation some care must be used to define the isolation cuts in a way which can be simulated in the theoretical calculation. These points are discussed, for example, in [6.26] and [6.27].

Two calculations of  $O(\alpha\alpha_s^2)$  have been presented in the literature and corresponding computer programs have been widely distributed. In [6.28] the inclusive invariant cross section was calculated and the integrations over the unobserved partons were done analytically. This results in a relatively fast program, but one which can only calculate a small number of observables. In [6.26] a Monte Carlo algorithm was used for the required integrations, resulting in a program which could be used for a greater number of observables, but at the cost of a larger amount of computer time.

One of the reasons for the high degree of interest in direct photon production is that the gluon distribution enters it in lowest order. In deeply

inelastic scattering the gluon distribution contributes to the structure functions only in the next-to-leading order and to the slope of the  $Q^2$  dependence in leading order. Accordingly, deeply inelastic data are sensitive to the gluon distribution only in the region of relatively small values of  $x$ , where the gluon contribution is comparable to that from the quarks. However, the direct photon data are sensitive to the gluon distribution at larger values of  $x$  and the inclusion of such data into global fits can provide complementary information [6.29]. Such fits have been done by a number of groups [6.30], [6.31], and [6.32]. The resulting gluon distributions are thus constrained both at low and high values of  $x$ .

A closely related process to single photon production is the production of photon pairs. This is a highly topical process since it forms a background to a possible Higgs boson signal in the intermediate mass range which covers masses from about 80 to 160 GeV. A next-to-leading order Monte Carlo based program has been presented in [6.33] and the program has been made available. The Monte Carlo nature of the program enables one to simulate the effects of various cuts. Thus, predictions can be compared to current data and one can also study strategies for Higgs searches and detector optimization. See [6.34] for an example and additional details. Additional discussion and references to earlier work are contained in [6.25] and [6.33].

## 6.5 Direct Photon Production: Experiment

Direct photon production provides an excellent arena both for precision tests of QCD and for measurements of gluon distribution functions. In this section, we concentrate on the backgrounds to direct photon production and the experimental techniques used to extract the signal. There are several reviews to which the reader is referred that examine these subjects in more detail [6.35].

The 4-vector of a photon can, in general, be reconstructed with greater precision than the 4-vector of a jet. The direct photon is one particle whose position and energy can be well measured in an electromagnetic calorimeter, while a jet consists of a number of particles spread out over a fairly wide area of phase space. Energy is deposited in both electromagnetic and hadronic

calorimeters. In addition, there is an ambiguity at some level as to which particles belong to the jet and which particles belong to the underlying event.

On the other hand, the rate for direct photon production is greatly reduced from that for jet production, because to lowest order direct photon production is proportional to  $\alpha\alpha_s$ , while jet production is proportional to  $\alpha_s^2$ . As a result, the  $\gamma/\text{jet}$  ratio is typically on the order of a few times  $10^{-4}$ .

Direct photon measurements suffer from potentially large backgrounds, primarily from those rare jets in which a large fraction of the momentum of the jet is carried by a single  $\pi^0$ , and one of the two photons of the  $\pi^0$  decay is not detected. Since the  $\gamma/\text{jet}$  ratio is on the order of  $10^{-4}$ , and the jet rate is suppressed by a factor of several hundred if the requirement is made that a  $\pi^0$  take 80% or more of the jet's momentum, the  $\gamma/\pi^0$  ratio is typically on the order of a few percent or a few tens of percent. The value of this ratio depends on the kinematic region and, as will be seen later, it also depends crucially on the imposition of an isolation cut. The  $\gamma/\pi^0$  ratio is the most critical number in a direct photon measurement. If this ratio is too small, then a measurement will not be possible, or at least will be very difficult. (Backgrounds can come from other sources such as  $\eta \rightarrow \gamma\gamma$ ,  $\omega \rightarrow \pi^0\gamma$ , etc. decays, but the bulk (typically  $>80\%$ ) of the background originates from  $\pi^0$ 's.)

There are a number of measurement strategies that are possible, each designed to minimize the backgrounds from these meson decays.

*Reconstruction.* This technique involves simply measuring the positions and energies of the two photons and requiring the resultant mass to be consistent with that of the  $\pi^0$  or  $\eta$  within experimental resolution. In practice, this technique is applicable mainly for fixed target experiments, due to the requirements of a large separation from the interaction point to the calorimeter and/or fine lateral sampling. Losses are inevitable, even if the reconstruction technique is possible. Consider the energy asymmetry distribution for the two photons from a  $\pi^0$  from Fermilab experiment E706 shown in Fig. 6.4 [6.36]. For perfect detection, this distribution would be flat from 0 to 1. ( $A = \beta |\cos\theta^*|$  where  $\theta^*$  is the decay angle in the  $\pi^0$  rest frame; since the  $\pi^0$  has spin 0, the decay distribution should be flat in  $\cos\theta^*$ .) Experi-

tal measurements show a “rolloff” of this distribution at high asymmetry, either because the soft photon is outside the acceptance of the calorimeter or because its energy is too soft to be measured. There can also be a similar “rolloff” at low asymmetry due to the coalescence of the two photons in the calorimeter, which is not present in this plot. These losses of  $\pi^0$ 's and  $\eta$ 's can cause a significant background to direct photons; however, this background can be reliably calculated, given the experimental knowledge of the  $\pi^0(\eta)$  cross sections and asymmetry distributions. In Fig. 6.5 is shown the  $\gamma/\pi^0$  ratio measured in Experiment E706 at Fermilab, along with the calculated background. The background-subtracted  $\gamma/\pi^0$  ratio is seen to be in excellent agreement with the leading log QCD prediction. Note the rise in the  $\gamma/\pi^0$  ratio as transverse momentum increases. This is due to the running of  $\alpha_s$  and the effect of the  $\pi^0$  fragmentation function.

*Conversion.* The percentage of electromagnetic showers (due to direct photon candidates) that convert in the material between the interaction point and the calorimeter (typically 1-2 radiation lengths) is measured. Showers originating from  $\pi^0$  or  $\eta$  decays will have a conversion fraction larger than that of showers from direct photons. A calculation of the amount of material traversed by the photons and the observed conversion percentage allows an extraction of the direct photon fraction in the data sample. This technique works best if the direct photon fraction of the sample is at least of the same order as the  $\pi^0$  background. Fig. 6.6 shows the measured conversion probability, in a preshower detector, for isolated direct photon candidates in UA2 [6.37]. Also shown are the expected conversion rates if the data sample consisted solely of  $\pi^0$ 's or solely of direct photons. Note that the data are closer to the photon expectation than to the  $\pi^0$  expectation, indicating that the  $\gamma/\pi^0$  ratio is larger than 1.

*Profiles.* Even if the two photons cannot be resolved, a measurement of the lateral and/or longitudinal profile of the electromagnetic shower may allow a discrimination between direct photons and  $\pi^0$ 's. Showers originating from  $\pi^0$ 's appear broader due to the opening angle of the two photons. This technique loses effectiveness as the  $\pi^0$  energy increases, since the opening angle decreases as  $1/E_\pi^0$ . The longitudinal development of direct photon and

$\pi^0$  showers will also differ as the average energy of a  $\pi^0$  photon is half that of the direct photon. Since the longitudinal development of an electromagnetic shower varies only logarithmically with the photon energy, the differences may be subtle. As for conversion, this technique works best if the  $\gamma/\pi^0$  ratio is fairly large.

*Isolation.* This technique requires that the photon candidate be “unaccompanied” inside a cone of a certain radius  $R(R = \sqrt{(\Delta\eta^2 + \Delta\phi^2)})$ ; typically  $R = 0.5 - 1.0$  centered on the photon direction, with  $\eta$  the pseudorapidity and  $\phi$  the azimuthal angle. Unaccompanied means that the amount of additional energy inside the cone is less than a certain fraction of the photon’s energy or less than some fixed scale. The application of isolation discriminates strongly against  $\pi^0$  events, since a  $\pi^0$  is usually accompanied by additional particles from the fragmentation of the jet. Direct photons from the leading order processes are unaffected, since the photon is isolated. Photons originating from bremsstrahlung processes are also strongly discriminated against, again because of the presence of a nearby jet. The effect of an isolation cut on the direct photon signal can be calculated in a nonleading order calculation, of the type described in Section 6.5 above. Isolation cuts are used for all collider direct photon measurements. Application of an isolation cut at the colliders can increase the  $\gamma/\pi^0$  ratio from the order of a few percent to on the order of 1 or greater. A leading log prediction for the  $\gamma/\pi^0$  ratio for the UA2 kinematic region is shown in Fig. 6.7 [6.38]. Note that the inclusive  $\gamma/\pi^0$  ratio is very small (a few percent at low transverse momentum) but the imposition of an isolation cut dramatically increases this ratio.

A large amount of data has been taken by many experiments using all of the techniques discussed above [6.35]. Good agreement is found with the predictions of perturbative QCD, with the possible exception of the low  $x_t (= p_t/\sqrt{s})$  data of CDF and UA2. Some of this direct photon data has been utilized in parton distribution fits [6.39] to measure, or at least constrain, the gluon distribution function in both protons and pions. The fixed target data are sensitive to gluon momenta fractions between 0.2 and 0.6, while the collider inclusive photon data probe the region from approximately 0.01-0.25.

More information about the direct photon event is possible if the jet opposite to the direct photon is also measured. The  $\cos\theta^*$  distribution for  $\gamma +$  jet events from CDF is shown in Fig. 6.8. The angular distribution is flatter than the distribution for two jet production, due to the absence of  $t$ -channel gluon exchange diagrams at leading order. Measurement of both the photon and the jet completely determines the kinematics of the events, in particular the momentum fractions of the incoming partons. This should be useful for parton distribution fits, especially for determining the gluon distribution at very small  $x \sim (10^{-3} - 10^{-4})$  at CDF and D0.

## References

- [6.1] J.C. Collins, D.E. Soper and G. Sterman, *Factorization of Hard Process in QCD* in Perturbative Quantum Chromodynamics, ed. A.H. Mueller, World Scientific p.1 (1990).
- [6.2] G. Altarelli, R. K. Ellis and G. Martinelli, Nucl. Phys. **B143**, 521 (1978), (E) **B146**, 544 (1978); ibid **B157**, 461 (1979); J. Kubar-Andre and F. E. Paige, Phys. Rev. **D19**, 221 (1979); K. Harada, T. Kaneko and N. Sakai, Nucl. Phys. **B155**, 169 (1979); (E) **B165**, 545 (1980); J. Abad and B. Humpert, Phys. Lett. **B80**, 286 (1979). B. Humpert and W.L. van Neerven, Nucl. Phys. **B184**, 225 (1981).
- [6.3] G. Sterman, Nucl. Phys. **B281**, 310 (1987); D. Appel, P. Mackenzie and G. Sterman, Nucl. Phys. **B309**, 259 (1988); S. Catani and L. Trentadue, Nucl. Phys. **B327**, 323 (1989); **B353**, 183 (1991); H. Contopanagos and G. Sterman, Stony Brook preprint, ITP-SB-92-61 (1992).
- [6.4] G. Parisi, Phys. Lett. **B90**, 295 (1980); G. Curci and M. Greco, Phys. Lett. **B92**, 175 (1980); L. Magnea and G. Sterman, Phys. Rev. **D42**, 4222 (1990).

- [6.5] E.B. Zijlstra and W.L. van Neerven, Nucl. Phys. **B383**, 525 (1992);  
W.L. van Neerven and E.B. Zijlstra, Phys. Letts. **B272**, 127 (1991);  
E.B. Zijlstra and W.L. van Neerven, *ibid* **B273**, 476 (1991).
- [6.6] W.L. van Neerven and E.B. Zijlstra, Nucl. Phys. **B382**, 11 (1992).
- [6.7] T. Matsuura, S.C. van der Marck and W.L. van Neerven, Phys. Lett. **B211**, 171 (1988); Nucl. Phys. **B319**, 570 (1989).
- [6.8] T. Matsuura, R. Hamberg and W.L. van Neerven, Nucl. Phys. **B345**, 331 (1990).
- [6.9] R. Hamberg, W.L. van Neerven and T. Matsuura, Nucl. Phys. **B359**, 343 (1991).
- [6.10] T. Matsuura, Higher Order Corrections to the Drell-Yan Process,  
Ph.D thesis submitted to the University of Leiden, (1989).
- [6.11] R.Hamberg, Second Order Contributions to Physical Quantities,  
Ph.D. thesis submitted to the University of Leiden, (1991).
- [6.12] J. H. Christenson *et al.*, Phys. Rev. Lett. **25**, 1523 (1970); Phys. Rev. **D8**, 2016 (1973).
- [6.13] L. Lederman and B. Pope, Phys. Rev. Lett. **27**, 765 (1971).
- [6.14] S.C.C. Ting, Rev. Mod. Phys. **47**, 235 (1977).
- [6.15] C. Gross-Pilcher and M.J. Schockhet, Ann. Rev. Nuc. and Part. Sci. **36**, 1 (1986).
- [6.16] J. Rutherford, Proceedings of the X International Symposium on  
Multiparticle Dynamics, Goa, India, 25-29 Sept., 1979, p. 789.
- [6.17] J. Alitti *et al.*, Phys. Lett. **B275**, 202 (1992).
- [6.18] F. Abe *et al.*, Phys. Rev. Lett. **67**, 2418 (1991).
- [6.19] F. Abe *et al.*, Phys. Rev. Lett. **65**, 2243 (1990).

- [6.20] F. Abe *et al.*, Phys. Rev. **D43**, 2070 (1991).
- [6.21] J. Alitti *et al.*, Phys. Lett. **B241**, 150 (1990).
- [6.22] J. Alitti *et al.*, Phys. Lett. **B276**, 354 (1992).
- [6.23] R. Ansari *et al.*, Phys. Lett. **B215**, 175 (1988).
- [6.24] J. Alitti *et al.*, Phys. Lett. **B263**, 563 (1991).
- [6.25] J. F. Owens, Rev. Mod. Phys. **59**, 465 (1987).
- [6.26] H. Baer, J. Ohnemus, and J. F. Owens, Phys. Rev. **D42**, 61 (1990).
- [6.27] E. L. Berger and Jianwei Qiu, Phys. Rev. **D44**, 2002 (1991).
- [6.28] P. Aurenche, A. Douiri, R. Baier, M. Fontannaz, and D. Schiff, Phys. Lett. **B140**, 87 (1984).
- [6.29] J.F. Owens and W.-K. Tung, Ann. Rev. Nucl. Part. Sci., **42**, 291 (1992).
- [6.30] P. Aurenche, R. Baier, M. Fontannaz, J.F. Owens, and M. Werlen, Phys. Rev. **D39**, 3275 (1989).
- [6.31] P. Harriman, A.D. Martin, R.G. Roberts, and W.J. Stirling, Phys. Rev. **D42**, 798 (1990).
- [6.32] Current global fits performed by the CTEQ parton distribution subgroup include direct photon data in the data set used for the fits.
- [6.33] B. Bailey, J. Ohnemus, and J.F. Owens, Phys. Rev. **D46**, 2018 (1992).
- [6.34] B. Bailey and J.F. Owens, FSUHEP report, in preparation.
- [6.35] Some reviews that discuss the experimental situation are: T. Ferbel, W.R. Molzon, Rev. Mod. Phys. **56**, 18 (1984); J.F. Owens, Rev. Mod. Phys. **59**, 465 (1987); J. Huston, Proceedings of the 1989 International Symposium on Lepton and Photon Interactions at High Energies (Stanford, 1989) ed. M. Riordan (World Scientific, Singapore),

p. 348; for an experimental compilation see also P. Aurenche and M. Whalley Rutherford-Appleton Laboratory Preprint RAL-89-106.

- [6.36] G. Alverson *et al.*, Phys. Rev. Lett. **27**, 2584 (1992); G. Alverson *et al.*, Phys. Rev. **D** (to be published).
- [6.37] J. Alitti *et al.*, CERN-PPE/91-68 (submitted to Physics Letters **B**).
- [6.38] J. Owens, leading log  $\pi^0$  and  $\gamma$  program.
- [6.39] D. Duke and J. Owens; P. Aurenche *et al.*, Phys. Rev. **D39**, 3275 (1989); P. Aurenche *et al.*, Phys. Lett. **B233**, 517 (1989); P.M. Harriman *et al.*, Phys. Rev. **D42**, 798 (1990); P. Sutton *et al.*, Rutherford-Appleton Laboratory Preprint RAL/91-058 (1991); W. Tung *et al.*, to be published in the Proceedings of the XXVIth International Conference in High Energy Physics, Dallas (1992).

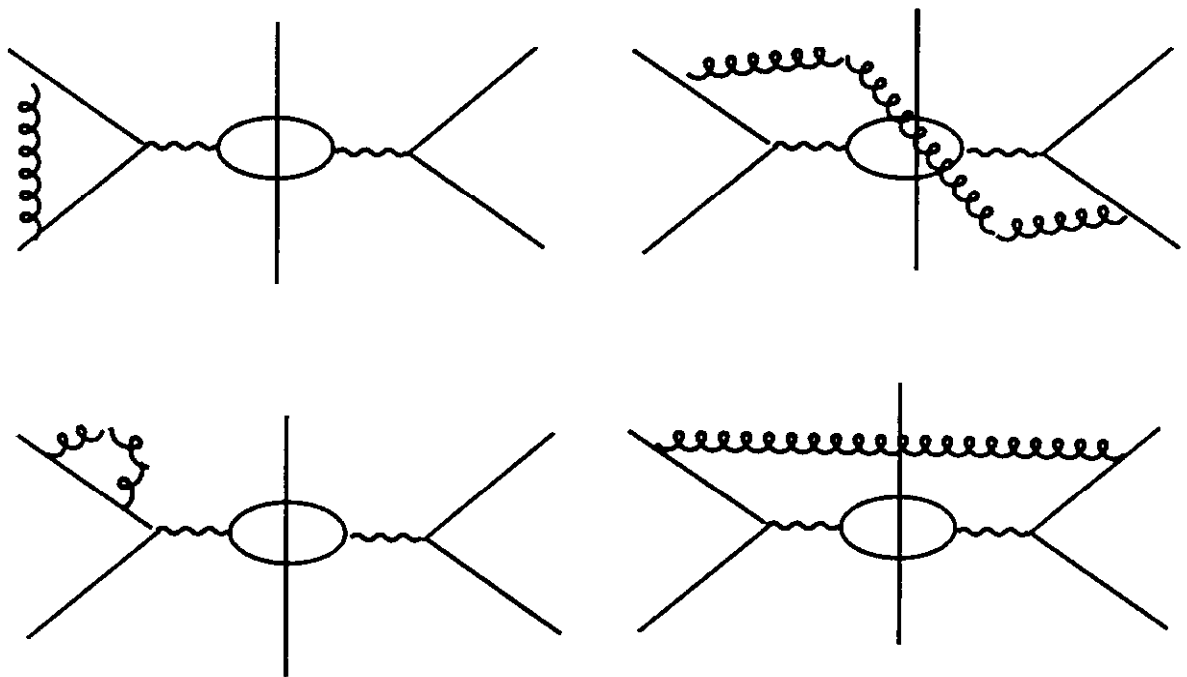


Figure 6.1. Cut diagrams for  $O(\alpha_s)$  corrections to the Drell-Yan cross section.

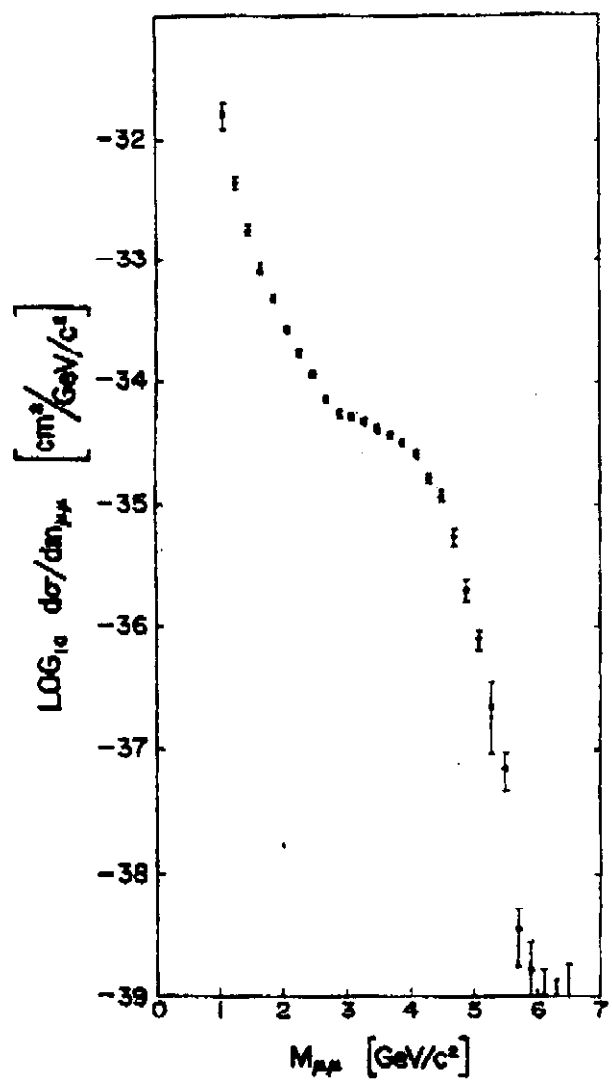


Figure 6.2. Dimuon spectra from early BNL experiment [6.13].

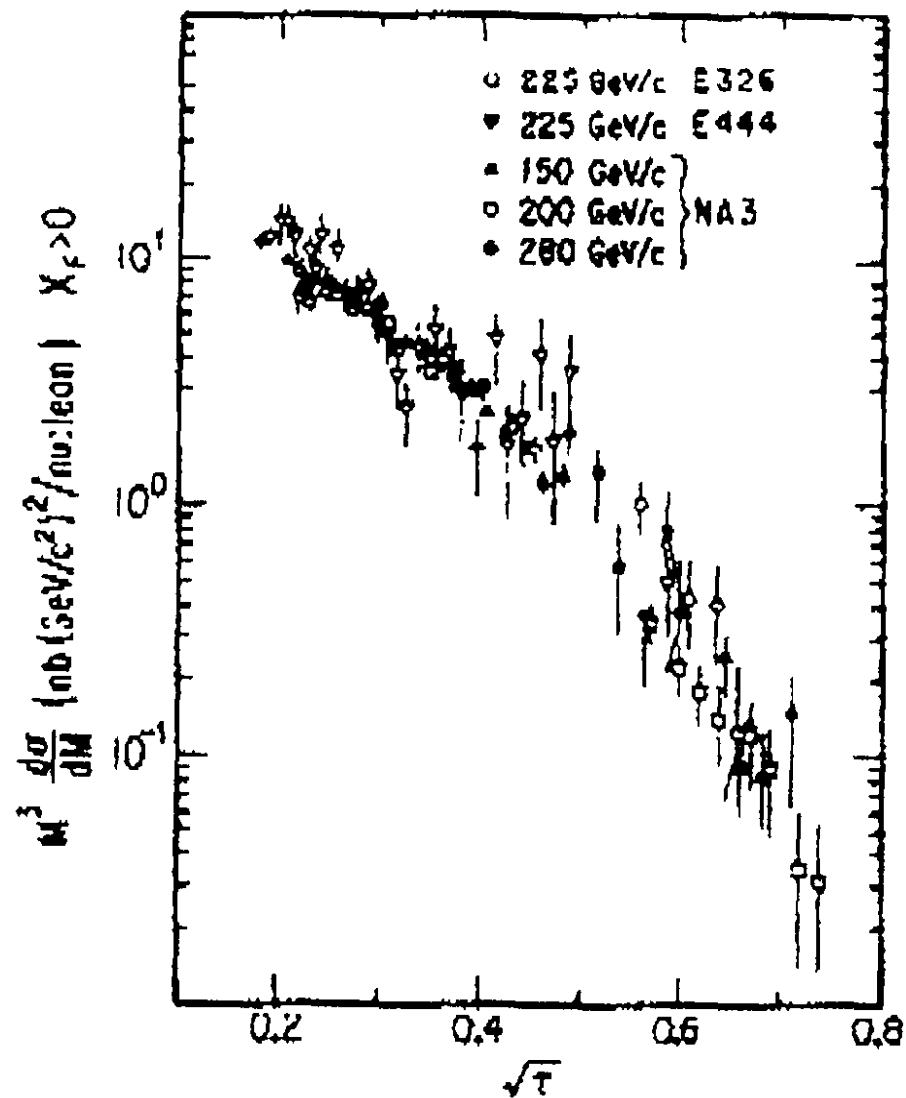


Figure 6.3. Scaling behavior of pion-nucleon Drell-Yan cross section.

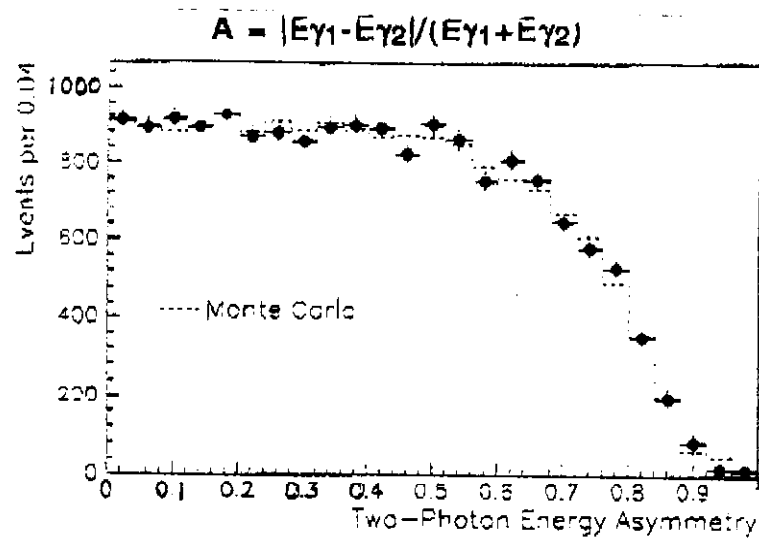


Figure 6.4. Photon energy asymmetry distribution in  $\pi^0$  decay [6.36].

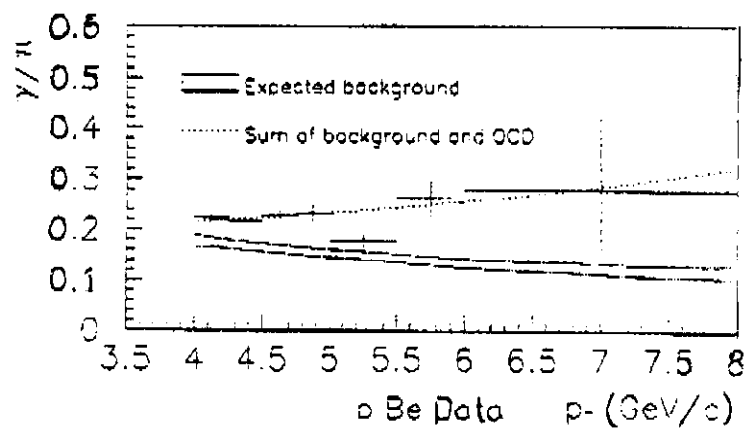


Figure 6.5.  $\gamma/\pi^0$  ratio in E706.

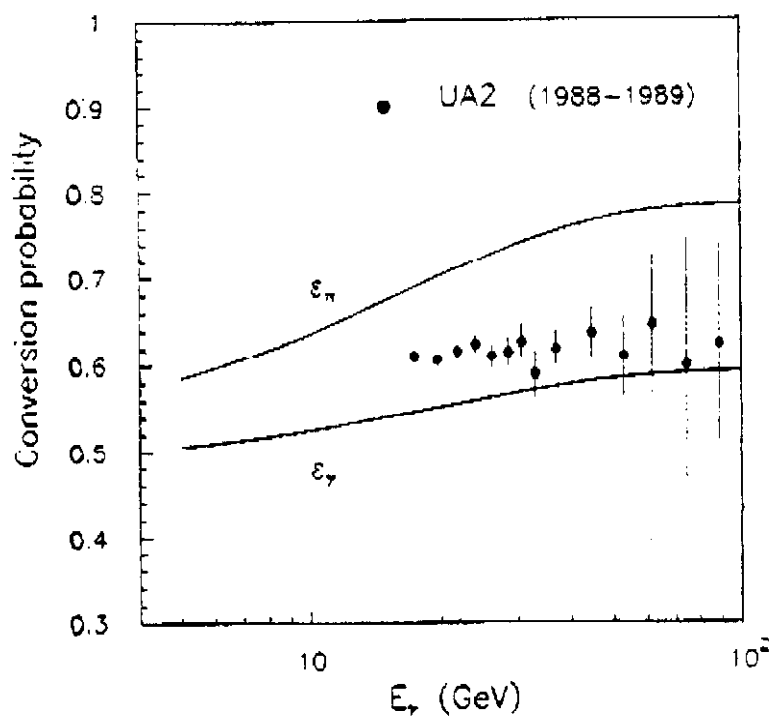


Figure 6.6. Measured preshower conversion probability [6.37]

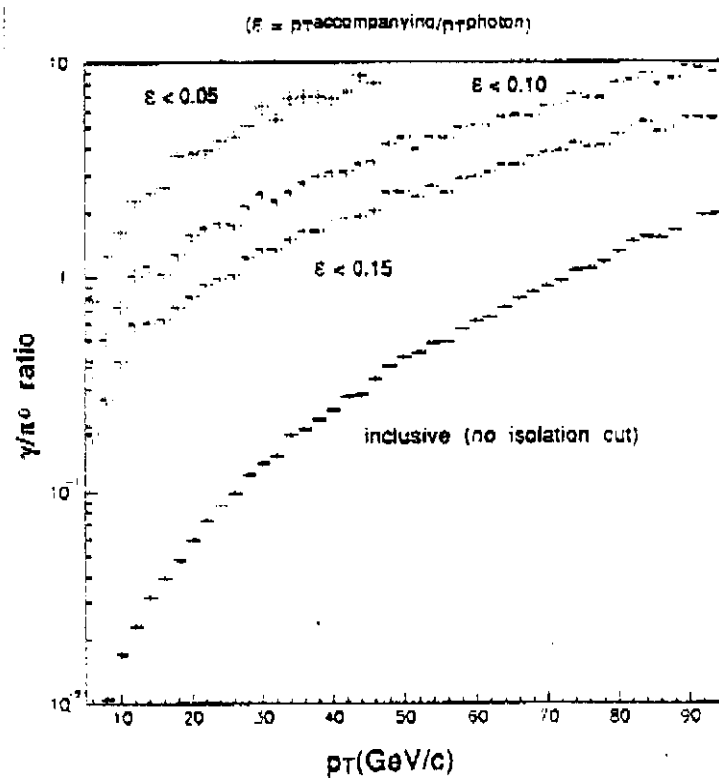


Figure 6.7. Leading log predictions for  $\gamma/\pi^0$  ratios with various isolation cuts.

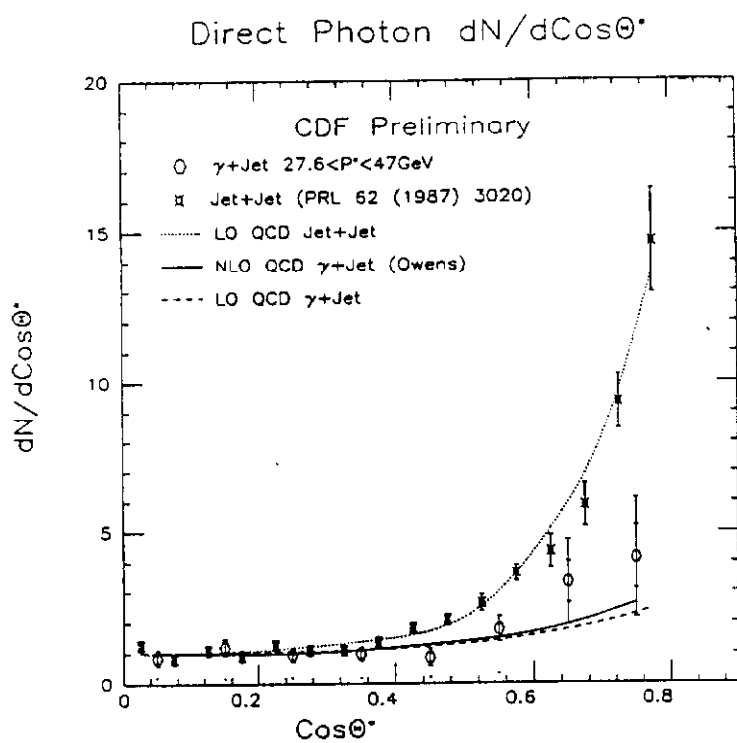


Figure 6.8. Angular distribution for  $\gamma + \text{jet}$  events at CDF.

## 7 QCD-induced Hard Hadron-Hadron Cross Sections

### 7.1 Jet Production in Hadron Collisions

In this section, we combine ideas developed in previous sections. First, in Section 6.1, we learned that the cross section to make muon pairs in hadron collisions is determined by both short-distance physics and long-distance physics, but that the long-distance effects can be isolated in factors that tell the probabilities to find partons in each of the two incoming hadrons. The remaining factor,  $H$  in Eq. (6.1), contains only short distance physics. One can interpret  $H$  as the cross section for the incoming partons to make a muon pair plus anything else. The “anything else” here is important: we sum over all final states of the hadronic system. Second, in Section 3.1, we saw that in electron-positron annihilation it is possible to define cross sections in which certain characteristics of the hadronic final state are specified without thereby introducing new sensitivity to long-distance physics. In particular, we could define infrared finite jet cross sections.

Combining these ideas, we expect that one can specify jet cross sections in hadron collisions such that the theoretical formula for the cross section is factored into parton distribution functions that contain long distance physics associated with the initial states and a hard scattering cross section that contains only short-distance physics. The general form of such a cross section, analogous to Eq. (3.7) for electron-positron annihilation, can be written in the style of [7.1] as

$$\mathcal{I} = \sum_{n=2}^{\infty} \int d\xi_A \int d\xi_B \sum_{a,b} f_{a/A}(\xi_A, \mu) f_{b/B}(\xi_B, \mu) \quad (7.1)$$

$$\times \int d\eta_1 dp_1 \cdots \int d\eta_n dp_n \frac{d\hat{\sigma}[n]}{d\eta_1 dp_1 \cdots d\eta_n dp_n} S_n(p_1^\mu, \dots, p_n^\mu). \quad (7.2)$$

Here  $\xi_A$ ,  $\xi_B$  are the momentum fractions of the incoming partons and  $\eta_i$  is the rapidity of outgoing parton  $i$ , while  $p_i$  is its transverse momentum. The

parton cross sections  $d\hat{\sigma}[n]/d\eta_1 d\mathbf{p}_1 \cdots d\eta_n d\mathbf{p}_n$  contain delta functions for overall four-momentum conservation. The effect of these delta functions is that the total transverse momentum of the outgoing partons vanishes, while  $\xi_A$  and  $\xi_B$  are determined by conservation of longitudinal momentum and energy. The “hat” on  $d\hat{\sigma}[n]$  indicates that infrared sensitivity arising from the initial state is factored into the parton distributions, as in the Drell-Yan cross section, Eq. (6.1).

The functions  $\mathcal{S}_n$  specify the measurement to be made on the hadronic final state. In order that this measurement not introduce any sensitivity to long-distance physics (in addition to the initial-state infrared sensitivity contained in the parton distribution functions), the measurement functions should be “infrared-safe.” That is, they should satisfy equations analogous to (3.10),

$$\mathcal{S}_{n+1}(p_1^\mu, \dots, (1-\lambda)p_n^\mu, \lambda p_n^\mu) = \mathcal{S}_n(p_1^\mu, \dots, p_n^\mu), \quad (7.3)$$

and

$$\mathcal{S}_{n+1}(p_1^\mu, \dots, p_n^\mu, \lambda p_A^\mu) = \mathcal{S}_{n+1}(p_1^\mu, \dots, p_n^\mu, \lambda p_B^\mu) = \mathcal{S}_n(p_1^\mu, \dots, p_n^\mu), \quad (7.4)$$

for  $0 \leq \lambda < 1$ . The first equation says that two collinear partons can be replaced by a single parton and that a zero-momentum parton can simply be eliminated without affecting the measurement. The second equation says that partons that are collinear with one of the beam momenta do not affect the measurement.

### 7.1.1 Cone definition

Measurements of jet cross sections in hadron collisions in recent years have concentrated on a cone definition of jets (following the spirit of the original jet paper [7.2] and of the early calculations of jet cross sections for hadron physics [7.3]). The main features of the algorithm are specified in an agreement reached at the 1990 Snowmass Workshop [7.4]. The idea was that this definition could provide a standard jet cross section for the purpose of comparing results between different experiments – without restricting the development of improved definitions in the future.

In the definition, one wants to maintain the invariance appropriate for hadron colliders under azimuthal rotations and longitudinal Lorentz boosts. Thus one describes the particles  $i$  using the absolute values  $p_{T,i}$  of their transverse momenta, their azimuthal angles  $\phi_i$ , and their rapidities  $\eta_i$ . (We treat all particles as being massless, so that the rapidities and the pseudo-rapidities are not distinguished).

The main feature of the cone definition is that a jet consists of particles whose momentum vectors lie in an  $\eta, \phi$ -cone. The cone consists of the interior of a circle of radius  $R$  in the  $(\eta, \phi)$  plane, centered on a cone axis  $(\eta_C, \phi_C)$ . Thus particle  $i$  is in the jet if

$$(\eta_i - \eta_C)^2 + (\phi_i - \phi_C)^2 < R^2. \quad (7.5)$$

A standard value for the cone radius is  $R = 0.7$ . Next, one defines the total transverse energy  $E_T$  of the jet and a jet axis  $(\eta_J, \phi_J)$  according to

$$\begin{aligned} E_T &= \sum_{i \in \text{cone}} p_{T,i}, \\ \eta_J &= \frac{1}{E_T} \sum_{i \in \text{cone}} p_{T,i} \eta_i, \\ \phi_J &= \frac{1}{E_T} \sum_{i \in \text{cone}} p_{T,i} \phi_i. \end{aligned} \quad (7.6)$$

Finally, the jet axis must coincide with the cone axis. If it does not on a first attempt, one simply iterates until stability is achieved.

This definition is quite simple and natural. However it can happen that two jet cones produced by the definition overlap. Thus a further specification (which is not contained in the Snowmass agreement) is needed. Typically, one merges jets with a very large overlap and splits particles between jets that have a smaller overlap. The reader is referred to the experimental papers for the details.

### 7.1.2 Calculations

As with electron-positron collisions, one can characterize an infrared safe cross section as “ $N$ -jet like” if the functions  $S_n$  are zero for  $n < N$  and non-zero for  $n \geq N$ . Cross sections that are 2-jet like in this sense can currently

be calculated at the one loop level using a computer program described in Refs. [7.5] and [7.1]. The program takes account of the cancellations of soft and collinear singularities between graphs with three parton final states and graphs with two parton final states but a virtual loop. The virtual loop graphs are taken from the calculation of R. K. Ellis and Sexton [7.6]. An independent program that can calculate some 2-jet like cross sections at one loop order is described in Ref. [7.7].

The extension of the above ideas to include  $W$  or  $Z$  plus  $n$  jets was initiated by [7.8]. At present the tree amplitudes for the reaction  $p + \bar{p} \rightarrow W, Z + n$  jets, where  $n \leq 4$  are available in the program VECBOS. However the jets are massless partons, which are not allowed to be soft or collinear. Using sophisticated techniques from string theory [7.9] the one-loop corrections to  $W$  or  $Z$  plus one jet production have recently been calculated [7.10]. This program is important because the present limit on the mass of the  $t$ -quark satisfies  $m_t > M_W$  so the top quark (hadron) probably decays into a  $W$  plus lighter mass quarks. The background for detecting the  $t$ -quark therefore involves knowledge of the reaction  $p + \bar{p} \rightarrow W, Z + n$  jets. Without a one-loop calculation, the scales in these cross sections are not well determined.

## 7.2 Jets in Hadron-hadron Collisions: Experiment

Experimental evidence for the existence of jets at hadron colliders was first observed by using a single high- $P_t$  particle to both trigger on and identify jets. This, however, results in a very biased experimental sample, and it was first realized at the ISR at  $\sqrt{s} = 62.3$  GeV [7.11] that one has to trigger in a more inclusive way, i.e. on the total amount of energy in a certain region of the detector. Cross sections were measured with an inclusive trigger, and two-jet back-to-back structure (in the transverse plane to the beam) was observed [7.12]. In addition, it was shown that the transverse momentum of particles relative to the jet axis is limited to about 500 MeV/c, independent of the momentum parallel to the jet axis. The first studies with a cone-based algorithm concluded that an opening angle of 40 degrees=0.7 rad includes nearly 100% of the jet energy, a value which is identical to currently used values at much higher energies. With the increase in the center of mass energy

at the CERN Sp $\bar{p}$ S collider to 540 GeV, the UA1 and UA2 experiments showed unambiguously the existence of jets in hadron-hadron collisions [7.13]. They also enabled the measurement of the jet cross section over a large region of transverse energy, out to 170 GeV [7.14]. Fig. 7.1 shows the UA1 and ISR jet cross section as measured initially in the central rapidity region ( $y < 1.0$ ).

In Fig. 7.1, the experimental points are compared to (at that time) known parton distributions. The rather good agreement between theory and experiment, in a quantity that varies over five orders of magnitude, was considered a major success for the predictive power of QCD. Note that the error on the experimental cross sections is of order 100% and that the experiments defined jets in different ways: at the ISR a cone size of 30 degrees was used, whereas UA1 was the first to propose and use a fixed cone size algorithm, with a cone size of  $R = 0.7$ . This value of the cone size has now become the default value, a specific example of a definition of jets as described in the “Snowmass agreement” [7.4]. Over the years, the accuracy of collider experiments has improved and now the most accurate cross sections are available from UA2 ( $\sqrt{s} = 630$  GeV) and CDF ( $\sqrt{s} = 1800$  GeV) at Fermilab. Both experiments use only calorimetric energy measurements to measure jets, use a fixed cone size algorithm to define jets, and compute  $E_t$  of the jet as the sum  $\sum_i E_{t,i}$  where  $i$  runs over all calorimeter cells inside the jet cone. We will discuss the experiments separately.

The final UA2 jet inclusive cross section [7.15], measured with an upgraded detector with extended rapidity coverage, is shown in Fig. 7.2. Here the jet was defined by using a fixed cone algorithm and a cone size  $R = 1.3$ . The basic assumption is that this cone size is large enough so that a final state parton, including all its radiation and fragmentation, is described and its energy contained within the cone.

Corrections for energy flowing out of the cone and entering the cone from the underlying event (= remnants due to the fragmentation of the incoming hadrons and to color conservation) are estimated using the simulation program HERWIG. The experimental errors obtained have several sources. The overall scale error on the cross section is 32%, in addition to the statistical accuracy of each data point. The overall scale error of 32% includes

the uncertainties due to absolute energy scale (11%), luminosity (5%), model dependence of acceptance corrections (25%), analysis parameters and jet algorithm (15%). The underlying event creates an uncertainty of 0.9 GeV on the  $E_t$  scale, resulting in an additional error of typically 10% at 60 GeV and 5% at 130 GeV in the cross section. The obtained experimental cross sections are compared to LO predictions based on EHLQ [7.16] parton distributions and both are shown in Fig. 7.3. The agreement between theory and experiment is very good in the central rapidity region. To illustrate this in Fig. 7.4 the ratio of experiment to theory is given for the central rapidity region, and indeed, for several different recent parton distributions the agreement is remarkable. The only discrepancy is in the  $y > 1.0$  region where the agreement becomes worse as rapidity increases. It should be noted that these are the only high precision, published data available to date in this rapidity region. This discrepancy should be investigated further. The UA2 collaboration also chose to do a LO comparison only and their results have not been compared to a NLO prediction. In fact, it would not be a trivial task to compare these experimental results to NLO predictions. In order to do so, one would want to reanalyze the data without the corrections for energy flowing into/out of the cone and use a smaller cone size.

The CDF experiment has measured the jet cross section at the Tevatron proton- antiproton collider at  $\sqrt{s} = 1800$  GeV. In contrast to UA2, the CDF cross section has been treated much more like a NLO quantity and has been measured as a function of the jet cone size. To define a jet, a fixed cone size algorithm ( $R = 0.7$ ) was used, along with other details of the “Snowmass agreement” [7.4], and Eq. (7.6) was used to derive the jet quantities  $E_t$ ,  $\eta_J$  and  $\phi_J$ . The only deviation from the prescriptions of Ref. [7.4] is that  $E_t$  was calculated by adding the energy of calorimeter cells in the cone and then converting to  $E_t$  by using the rapidity of the jet, instead of using the scalar sum of the  $E_t$  of each cell. The data include a correction for the energy inside the jet cone due to the underlying event, but no corrections for energy flowing in or out of the cone. The underlying event transverse energy correction is  $1.2 \pm 0.3$  GeV per unit area in  $\eta$ ,  $\phi$  space. Jets which are close in direction have to be merged and large transverse size jets have

to be split according to some algorithm. The algorithm used is similar to the one used at the parton level in the NLO calculation of the cross section. For a more detailed discussion of the criteria used we refer to [7.17]. The experimental data [7.18] are shown in Fig. 7.4, and they cover the rapidity region  $0.1 < \eta_J < 0.7$ . No published data for larger rapidities are available at this time. The overall systematic uncertainty in the measured cross section is: 60% (mainly due to energy resolution and unsmeared uncertainties) for  $E_t < 80$  GeV and 22% (dominated by knowledge of absolute energy scale) for  $E_t > 80$  GeV. Also shown in Fig. 7.4 is the absolute NLO theoretical prediction for the same cone size using HMRSB [7.19] parton distributions. The agreement between theory and experiment is remarkably good. Fig. 7.5 shows the ratio of the measured cross section and theory prediction (NLO) for different parton distributions. All parton distributions (HMRSB, MT-B and MT-S) agree very well with the data, except for HMRSE, which is inconsistent with the shape of the measured cross section. CDF has also measured the dependence of the cross section on the jet cone size used. This dependence is predicted in the NLO parton level calculation of the cross section and it is informative to compare the parton level prediction with the measured behavior at the calorimeter jet level. In Fig. 7.6 the experimental cross section at  $E_t=100$  GeV is determined for cone sizes 0.4, 0.7 and 1.0 and compared to the theoretical prediction for different choices of the scale used. Although there is some scale dependence in the theoretical prediction, the parton level prediction and calorimetric jet level measurement qualitatively show the same cone size dependence for the jet cross section.

The Future: (1) Given the disagreement of the measured UA2 jet cross section in the rapidity regions ( $> 1.$ ) with the theoretical prediction, it will be interesting to perform this measurement at the Tevatron collider. This can be done up to  $\eta = 3.0$  with both the CDF and D0 detectors. If disagreement persists, the discrepancy can be used as a measure of parton distributions in regions not accessible by other experiments. (2) The cone size dependence of the jet cross section should be extended to more transverse energy points and more cone sizes. Another interesting measurement along this line is the transverse energy flow within the jet as a function of the jet cone size used.

Early results along these lines have been presented by CDF [7.20] and again show rather good agreement between parton level and particle level for the jet. This should be extended to the calorimeter level and be done for different transverse energies. (3) Up to now only one definition of jets has been used in hadron-hadron collisions. Other experiments have used different jet algorithms (of the successive combination type; see Section 4.4) and these algorithms should be tried in hadron collider experiments, because they have different systematic errors. This would enable a comparison between jets produced in electron-positron collisions and jets produced in hadron collisions.

### 7.3 QCD Corrections: Heavy Quarks

Another important area of research in pQCD is the study of heavy-quark production. Precisely what is understood by the term heavy quark depends on the circumstances. However there is general agreement that  $u$ ,  $d$  and  $s$  are light-mass quarks while  $c$ ,  $b$  and the yet to be discovered  $t$  are heavy-mass quarks. The obvious evidence for heavy (confined) quarks is the existence of colorless spin-1 vector meson states such as the  $J/\psi$  and  $\Upsilon$ , which are produced copiously in electron-positron collisions. These physical particles contain charmed and bottom quarks and have well-defined masses and lifetimes. Within the context of pQCD there must be quantities which we can designate as heavy quark masses  $m_q$  with values approximately one-half those of the vector meson masses. Then  $m_c \approx 1.5 \text{ GeV}/c^2$  and  $m_b \approx 4.75 \text{ GeV}/c^2$  have a phenomenological significance even though they cannot be identified as on-mass-shell objects like electrons or hadrons. When mass effects are important, for example just above the “threshold” for pair production, we cannot ignore terms of order  $m/\sqrt{s}$  in a partonic reaction. Quark masses have already been discussed in Section 1.5.

The heavy quarks referred to above carry color and do not have the proper quantum numbers to make colorless hadrons. When they are produced in partonic collisions vacuum perturbations produce light quark-antiquark pairs over the time scale  $\Delta E \Delta t \approx h$ . The heavy quark then combines with a light quark to form a physical hadron with well defined mass, which subsequently

decays into a multitude of final states with well defined branching ratios. The production of the heavy quark is only the first stage of a complicated process, which involves both pQCD and confinement.

The theoretical description of heavy quark production and decay is usually split into several parts. One first calculates the heavy quark production cross section in the parton model at a scale set approximately by the heavy quark mass, including higher order corrections if possible. Then the heavy quark becomes an on-mass-shell meson or baryon by the non-perturbative process of finding the appropriate light quark in the sea of quark-antiquark pairs in the vacuum. There is a phenomenological description of this part (fragmentation function). The heavy hadron then decays into light-mass hadrons (on their mass shells) and the branching ratios can be measured experimentally. The final decay involves the transition of the heavy quark into a light quark according to weak or electromagnetic interactions. The strong corrections to the last process can again be calculated by pQCD providing there is a heavy scale to make the running coupling constant small. If we limit ourselves here to a discussion of the production of heavy quarks then there should be a kinematical region where the mass  $m$  and the other invariants, such as  $\sqrt{s}$ ,  $p_t$ , etc., are roughly of the same magnitude and significantly larger than  $\Lambda_{QCD}$ . Under such circumstances the scale parameter is the heavy quark mass, so we measure a cross section at a coupling constant whose scale is  $m$ , using light-mass partonic structure functions at a scale  $m$ . Differential distributions are calculable when  $p_t \approx m$  and scale  $M = (p_t^2 + m^2)^{1/2}$ . Outside these ranges there will be large logarithms in ratios of invariants which can be controlled by an analysis of the renormalization group equation. The real proof of these claims is the comparison between the theoretical predictions and the experimental results.

Here we assume that the heavy quarks are detected (via their decays). At higher values of  $\sqrt{s}$  where  $m/\sqrt{s} \ll 1$ , the heavy quarks become effectively massless, and must be incorporated into the parton distributions. The transition between these regions is still under investigation.

Heavy flavour production has been experimentally studied at electron-positron [7.23], hadron-hadron [7.24] and lepton-hadron [7.25] facilities. For

review articles we refer to [7.26], [7.27]. We have included an extensive list of references to original papers in the bibliography.

We will now write down some Born reactions and discuss the general properties of the heavy-quark cross sections. For this we need the lowest order matrix elements for heavy quark production in the reactions  $q + \bar{q} \rightarrow Q + \bar{Q}$ ,  $\gamma + g \rightarrow Q + \bar{Q}$ ,  $g + g \rightarrow Q + \bar{Q}$ . The differential and total cross sections for the reaction  $e^+ + e^- \rightarrow \mu^+ + \mu^-$ , when mediated by a single virtual photon, were given previously. One can use the QCD Lagrangian to show that the corresponding results for the reaction  $q + \bar{q} \rightarrow Q + \bar{Q}$  where  $q(\bar{q})$  are light (massless) quarks and  $Q(\bar{Q})$  are heavy quarks with mass  $m$  are

$$s^2 \frac{d^2\sigma}{dt_1 du_1} = \frac{4\pi\alpha_s^2}{3} \left[ \frac{t_1^2 + u_1^2}{s^2} + \frac{2m^2}{s} \right] \delta(s + t_1 + u_1), \quad (7.7)$$

and

$$\sigma(s, m^2) = \frac{8\pi\alpha_s^2}{27s^2} (s + 2m^2)\beta. \quad (7.8)$$

We use the notation  $t_1 = t - m^2$ ,  $u_1 = u - m^2$  where  $s, t$  and  $u$  are the standard invariants,  $\beta = (1 - 4m^2/s)^{1/2}$  and  $\alpha_s = g^2/(4\pi)$ . The results include a summation over final spins and colors and an average over initial spins and colors. Next consider the reaction  $\gamma + g \rightarrow Q + \bar{Q}$ , then the differential cross section is

$$s^2 \frac{d^2\sigma}{dt_1 du_1} = \pi\alpha_{em}\alpha_s e_H^2 B_{QED} \delta(s + t_1 + u_1), \quad (7.9)$$

where

$$B_{QED} = \frac{t_1}{u_1} + \frac{u_1}{t_1} + \frac{4m^2 s}{t_1 u_1} \left(1 - \frac{m^2 s}{t_1 u_1}\right), \quad (7.10)$$

is the same factor that appears in the QED result (i.e., in the square of the amplitude for the reaction  $\gamma + \gamma \rightarrow \mu^+ + \mu^-$ ). Note that we have summed over final spins and colors and averaged over initial polarizations and colors. The total cross section is

$$\sigma(s, m^2) = \frac{2\pi\alpha_{em}\alpha_s}{s} e_H^2 \left\{ \left(1 + \frac{4m^2}{s} - \frac{8m^4}{s^2}\right) \ln \left(\frac{1 + \beta}{1 - \beta}\right) - \left(1 + \frac{4m^2}{s}\right) \beta \right\}. \quad (7.11)$$

Now consider the reaction  $g + g \rightarrow Q + \bar{Q}$ . In this case the color structure is more complicated and the differential scattering amplitude takes the form

$$s^2 \frac{d^2\sigma}{dt_1 du_1} = \frac{\pi \alpha_s^2}{16} \left\{ 3 \left( 1 - \frac{2t_1 u_1}{s^2} \right) - \frac{1}{3} \right\} \left[ \frac{t_1}{u_1} + \frac{u_1}{t_1} + \frac{4m^2 s}{t_1 u_1} \left( 1 - \frac{m^2 s}{t_1 u_1} \right) \right] \delta(s + t_1 + u_1), \quad (7.12)$$

again summed and averaged over initial polarizations and colors. Finally the total cross section is

$$\sigma(s, m^2) = \frac{\pi \alpha_s^2}{3s} \left\{ \left( 1 + \frac{4m^2}{s} + \frac{m^4}{s^2} \right) \ln \left( \frac{1+\beta}{1-\beta} \right) - \left( 7 + \frac{31m^2}{s} \right) \frac{\beta}{4} \right\}. \quad (7.13)$$

The above results should be folded with the appropriate distribution functions to calculate physical cross sections and inclusive distributions in the Born approximation.

The evaluation of higher order corrections in pQCD is an involved issue which has been the subject of much theoretical investigation. All the theoretical inputs, such as the running coupling constant, the reduced cross section  $\hat{\sigma}_{ij}(s, m^2, Q^2)$  and the parton distribution functions  $F_i^p(x, Q^2)$  are scheme dependent.

First we have to choose the renormalization scheme. Since the cross section is a renormalization group invariant we can limit ourselves to mass and coupling constant renormalization. Usually mass renormalization is performed in the on-mass-shell renormalization scheme.

Let us discuss the influence of heavy quarks on the running coupling  $\alpha_s$ . For instance the running coupling constant should be continuous across heavy quark production thresholds, so it depends on  $n_f$ . If we define the two-loop corrected  $\alpha_s$  in the  $\overline{\text{MS}}$  scheme then

$$\alpha_s(Q^2, n_f) = \frac{1}{b_f \ln(Q^2/\Lambda^2)} \left[ 1 - \frac{b'_f \ln \ln(Q^2/\Lambda^2)}{b_f \ln(Q^2/\Lambda^2)} \right], \quad (7.14)$$

where  $b_f$  and  $b'_f$  are given by (see Eq. (1.48))

$$b_f = \frac{33 - 2n_f}{12\pi}, \quad b'_f = \frac{153 - 19n_f}{2\pi(33 - 2n_f)}. \quad (7.15)$$

is valid for top-quark production with  $\Lambda = \Lambda_5$  and  $n_f = 5$ . For bottom and charm production we need  $\alpha_s$  for four and three flavors respectively. So that there is continuity across the  $b$  and  $c$  thresholds we define

$$\begin{aligned}\alpha_{s,5}(Q^2) &= \alpha_s(Q^2, 5) \\ \alpha_{s,4}^{-1}(Q^2) &= \alpha_s^{-1}(Q^2, 4) + \alpha_s^{-1}(m_b^2, 5) - \alpha_s^{-1}(m_b^2, 4) \\ \alpha_{s,3}^{-1}(Q^2) &= \alpha_s^{-1}(Q^2, 3) + \alpha_s^{-1}(m_c^2, 4) + \alpha_s^{-1}(m_b^2, 5) \\ &\quad - \alpha_s^{-1}(m_b^2, 4) - \alpha_s^{-1}(m_c^2, 3)\end{aligned}\tag{7.16}$$

so that

$$\begin{aligned}\alpha_s(Q^2) &= \alpha_{s,5}(Q^2)\theta(Q^2 - m_b^2) + \alpha_{s,4}(Q^2)\theta(m_b^2 - Q^2)\theta(Q^2 - m_c^2) \\ &\quad + \alpha_{s,3}(Q^2)\theta(Q^2 - m_c^2)\end{aligned}\tag{7.17}$$

This result is also used in the calculation of the lowest order Born approximation even though it is not imperative to do so.

The best data for a test of pQCD heavy quark production are on  $b$ -production in  $p\bar{p}$  collisions.  $c$ -production is not so clean because its mass is not heavy enough and  $\alpha_s(m_c^2)$  is large. Data from the  $SppS$  and Fermilab Tevatron on inclusive  $b$ -quark production are shown in Fig. 7.7 together with the results of a pQCD calculation through order  $\alpha_s^3$ , (provided by R. Meng using the  $O(\alpha_s^3)$  exact calculations in [7.44]). The lower energy data are fit quite well. The higher energy data are above the theoretical predictions so we probably need to include some part of the  $O(\alpha_s^4)$  contribution.

## References

- [7.1] Z. Kunszt and D. E. Soper, Phys. Rev. **D46**, 192 (1992).
- [7.2] G. Sterman and S. Weinberg, Phys. Rev. Lett. **39**, 1436 (1977).
- [7.3] R. K. Ellis, M. A. Furman, H. E. Haber and I. Hinchliffe, Nucl. Phys. **B173**, 397 (1980); M. A. Furman, Nucl. Phys. **B197**, 413 (1982).

- [7.4] J. E. Huth *et al.*, in E. Berger, ed., Proc. Summer Study on High Energy Physics, Research Directions for the Decade, Snowmass, CO, Jun 25 - Jul 13, 1990.
- [7.5] S. D. Ellis, Z. Kunszt and D. E. Soper, Phys. Rev. **D40**, 2188 (1989); Phys. Rev. Lett. **64**, 2121 (1990); Phys. Rev. Lett. **69**, 1496 (1992).
- [7.6] R. K. Ellis and J. Sexton, Nucl. Phys. **B269**, 445 (1986).
- [7.7] F. Aversa, M. Greco, P. Chiappetta and J. Ph. Guillet, Phys. Rev. Lett. **65**, 401 (1990); Z. Phys. **C49**, 459 (1991).
- [7.8] F.A. Berends, W.T. Giele and H. Kuijf, Nucl. Phys. **B321**, 39 (1989); F.A. Berends, H. Kuijf, B. Tausk and W.T. Giele, Nucl. Phys. **B357**, 32 (1991).
- [7.9] Z. Bern and D.A. Kosower, Nucl. Phys. **B379**, 451 (1992); **B362** 389 (1991); Phys. Rev. Letts. **66**, 1669 (1991).
- [7.10] W.T. Giele, E.W.N. Glover and D.A. Kosower, FERMILAB-CONF-92-213-T; FERMILAB-CONF-91-243-T; FERMILAB-PUB-92-230-T.
- [7.11] S.D. Ellis and R. Stroynowski, Reviews of Modern Physics **49**, 753 (1977).
- [7.12] A. Angelis *et al.*, (CMOR collaboration) Nucl. Phys. **B244**, 1 (1984).
- [7.13] For review of these results see L. Dilella, Ann. Rev. Nucl. Part. Sci. **35**, 107 (1985) and references therein, M. Banner *et al.*, (UA2 collaboration) Phys. Lett. **B138**, 203 (1983).
- [7.14] A. Arnison *et al.*, (UA1 collaboration) Phys. Lett. **B123**, 115 (1983) and Phys. Lett. **B123**, 214 (1983); P. Bagnaia *et al.*, Phys. Lett. **B138**, 430 (1984).
- [7.15] J. Alitti *et al.*, (UA2 collaboration), Phys. Lett **B257**, 232 (1991).

- [7.16] E. Eichten *et al.*, Rev. Mod. Phys. **56**, 579 (1984); Rev. Mod. Phys. **58**, 1065 (1986) (E).
- [7.17] F. Abe *et al.*, (CDF collaboration) Fermilab preprint PUB-91/181-E (1991).
- [7.18] F. Abe *et al.*, (CDF collaboration) Phys. Rev. Lett. **68**, 1104 (1992); detailed numerical tables can be found in Fermilab preprint Pub-91/231-E (1991).
- [7.19] P. Harriman *et al.*, Rutherford Lab report RAL-90-007 (1990).
- [7.20] B. Flaughter (CDF collaboration), presented at the XXVI Int. Conf. on High Energy Physics 1992, Dallas TX.
- [7.21] R. Horgan and M. Jacob, Nucl. Phys. **B179**, 441 (1981).
- [7.22] A. Martin, R. Roberts and W. Stirling, Phys. Rev. **D37**, 1161 (1988).
- [7.23] A. Ali in *Physics at LEP*, CERN Report 8602, eds. J. Ellis and R. Peccei, vol.2,p.81.
- [7.24] J.P. Guillet, P. Nason and H. Plothow-Besch, in Proceedings of the European Committee for Future Accelerators "Large Hadron Collider Workshop", CERN 90-10, eds G.Jarlskog and D.Rein, vol.2,p.116.
- [7.25] G. Carboni *et al.*, in Proceedings of the European Committee for Future Accelerators "Large Hadron Collider Workshop" CERN 90-10, eds. G. Jarlskog and D. Rein, vol.2,p.199.
- [7.26] N. Ellis and A. Kernan, Phys. Rep. **C195**, 24 (1990).
- [7.27] R.K. Ellis and W. J. Stirling, FERMILAB-Conf-90/164-T.
- [7.28] E. Reya, P. Zerwas, W. Hollik, V. Khoze, R.J.N. Phillips, F. Berends, D. Rein and J. Zunft, *et al.*, in *Proceedings of the European Committee for Future Accelerators "Large Hadron Collider Workshop"* CERN 90-10, eds. G. Jarlskog and D. Rein, vol.2,p.295.

- [7.29] M.S. Witherall, in *Proceedings of the 1987 International Symposium on Lepton and Photon Interactions*, Hamburg FRG, eds. W. Bartel and R. Rückl, North Holland, Amsterdam, 1988.
- [7.30] A. Ali, G. Ingelman, G. A. Schuler, F. Barreiro, M. A. Garcia, J. F. de Trocóniz, R. A. Eichler and Z. Kunszt, " Heavy Quark Physics at HERA", in *Proceedings of the DESY Workshop on HERA Physics*, DESY, Hamburg (1988),DESY 88-119; G.A. Schuler, Nucl. Phys.**B299**, 21 (1988).
- [7.31] A. Ali, F. Barreiro, J.F. de Trocóniz, G.A. Schuler and J.J van der Bij, in *Proceedings of the European Committee for Future Accelerators "Large Hadron Collider Workshop"* CERN 90-10, eds. G. Jarlskog and D. Rein, vol.2,p.917.
- [7.32] F. Abe *et al.*, (CDF collaboration) Phys. Rev. Letts. **64**, 142, 147 (1990); P.K. Sinervo, Invited talk at the Rencontres de Physique de la Vallee d'Aoste, La Thuile, March (1990),UTPT-91-13; F. Abe *et al.*, (CDF collaboration) Fermi-Lab-91-352-E.
- [7.33] J.J. van der Bij and G.J. van Oldenborgh, Z. Phys. **C51**, 477 (1991); M.A.G. Aivazis, F.I. Olness and W-K. Tung, Phys. Rev. Letts. **65**, 2339 (1990).
- [7.34] E. Witten, Nucl. Phys. **B104**, 445 (1976); J. Babcock and D. Sivers, Phys. Rev. **D18**, 2301 (1978); M.A. Shifman, A.I. Vainstein and V.J. Zakharov, Nucl. Phys. **B136**, 157 (1978); M. Glück and E. Reya, Phys. Letts. **B83**, 98 (1979); J.V. Leveille and T. Weiler, Nucl. Phys. **B147**, 147 (1979).
- [7.35] M. Glück in *Proceedings of the HERA Workshop*, Hamburg. Oct. 1987 ed R.D Peccei, vol 1, p.119; M. Glück, R.M. Godbole and E.Reya, Z. Phys. **C38**, 441 (1988).
- [7.36] R. K. Ellis and Z. Kunszt, Nucl. Phys. **B303**, 653 (1988).
- [7.37] R. K. Ellis and P. Nason, Nucl. Phys. **B312**, 551 ( 1989).

- [7.38] J. Smith and W.L. van Neerven Nucl. Phys. **B374**, 36 (1992).
- [7.39] S. Riemersma, J. Smith and W.L. van Neerven, Phys. Letts. **B282**, 171 (1992).
- [7.40] F.I. Olness, R. Meng and D.E. Soper, Nucl. Phys. **B371**, 79 (1992).
- [7.41] E. Berger, R. Meng and Wu-Ki. Tung, Phys. Rev. **46**, 1895 (1992).
- [7.42] E. Berger and R. Meng, Phys. Rev. **46**, 169 (1992).
- [7.43] W. Beenakker, H. Kuijf, W.L. van Neerven and J. Smith, Phys. Rev. **D40**, 54 (1989);
- [7.44] W. Beenakker, W.L. van Neerven, R. Meng, G.A. Schuler and J. Smith, Nucl. Phys. **B351**, 507 (1991).
- [7.45] R. Meng, G. A. Schuler, J. Smith and W.L. van Neerven, Nucl. Phys. **B339**, 325 (1990);
- [7.46] S. Catani, M. Ciafaloni and F. Hautmann, CERN-TH.6398/92, to be published in the Proceedings of the Workshop on Physics at HERA, Oct. 1991. eds. W. Buchmüller and G. Ingelman.
- [7.47] G. Altarelli, M. Diemoz, G. Martinelli, and P. Nason, Nucl. Phys. **B308**, 724 (1988).
- [7.48] P. Nason, S. Dawson and R.K. Ellis, Nucl. Phys. **B303**, 607 (1988); **B327**, 49 (1989); (E).**B335**, 260 (1990).
- [7.49] M.L. Mangano, P. Nason and G. Ridolfi, Nucl. Phys. **B373**, 295 (1992).
- [7.50] M.L. Mangano and P. Nason, Phys. Letts. **B285**, 160 (1992).
- [7.51] UA1 Collaboration, C. Albajar *et al.*, Phys. Lett. **B213**, 4105 (1988); Z. Phys. **C48**, 1 (1990); Talk by S. McMahon (UA1 experiment) at the XXVth Rencontres de Moriond, Les Arcs, March 1990; UA1 Collaboration, C. Albajar *et al.*, Phys. Lett. **B256**, 121 (1991).

- [7.52] CDF collaboration (to be published).
- [7.53] CDF Collaboration, F. Abe *et al.*, Phys. Rev. Letts. **64**, 142, 147 (1990); talk at the XXVth Rencontres de Moriond, Les Arcs, March (1990).
- [7.54] M. Glück, J.F. Owens and E. Reya, Phys. Rev. **D17**,2324 (1978); B. L. Combridge, Nucl. Phys. **B151**,429 (1979); J. Babcock, D. Sivers and S. Wolfram, Phys. Rev.**D18**,162 (1978); K. Hagiwara and T. Yoshino, Phys. Lett. **B80**, 282 (1979); L.M. Jones, and H. Wyld, Phys. Rev. **D17**,782 (1978); H. Georgi *et al.*, Ann. Phys. **114**, 273 (1978).
- [7.55] G. Matthiae, Riv. Nuovo Cim. **4**, 1 (1981).
- [7.56] V. Fadin, V. Khoze and T. Sjöstrand, Z. Phys.**C48**, 467 (1990).
- [7.57] D. Kuebel, M. Pundurs, C-P. Yuan, E. Berger and F. Paige, Phys. Rev. **D43**, 767 (1991).
- [7.58] S. Catani, M. Ciafaloni and F. Hauptmann, Phys. Lett. **B242**, 97 (1990).
- [7.59] G. Marchesini and B.R. Webber, Nucl. Phys. **B330**, 261 (1990).
- [7.60] M.A. Shifman, A.I. Vainshtein and V.J. Zacharov, Nucl. Phys.**B136**, 157 (1988).
- [7.61] E. Laenen, S. Riemersma, J. Smith and W.L. van Neerven, Phys. Letts. **B291**; Nucl. Phys. **B392**, 162, 229 (1993).
- [7.62] E. Laenen, J. Smith and W.L. van Neerven, Nucl. Phys. **B369**,534 (1992).
- [7.63] R.K. Ellis and D.A. Ross, Nucl. Phys. **B345**, 79 (1990); J.C. Collins and R.K. Ellis, Nucl. Phys. **B360**, 3 (1991).
- [7.64] M.A.G. Aivazis, F.I. Olness and W-K. Tung, SMU-HEP/92-04.

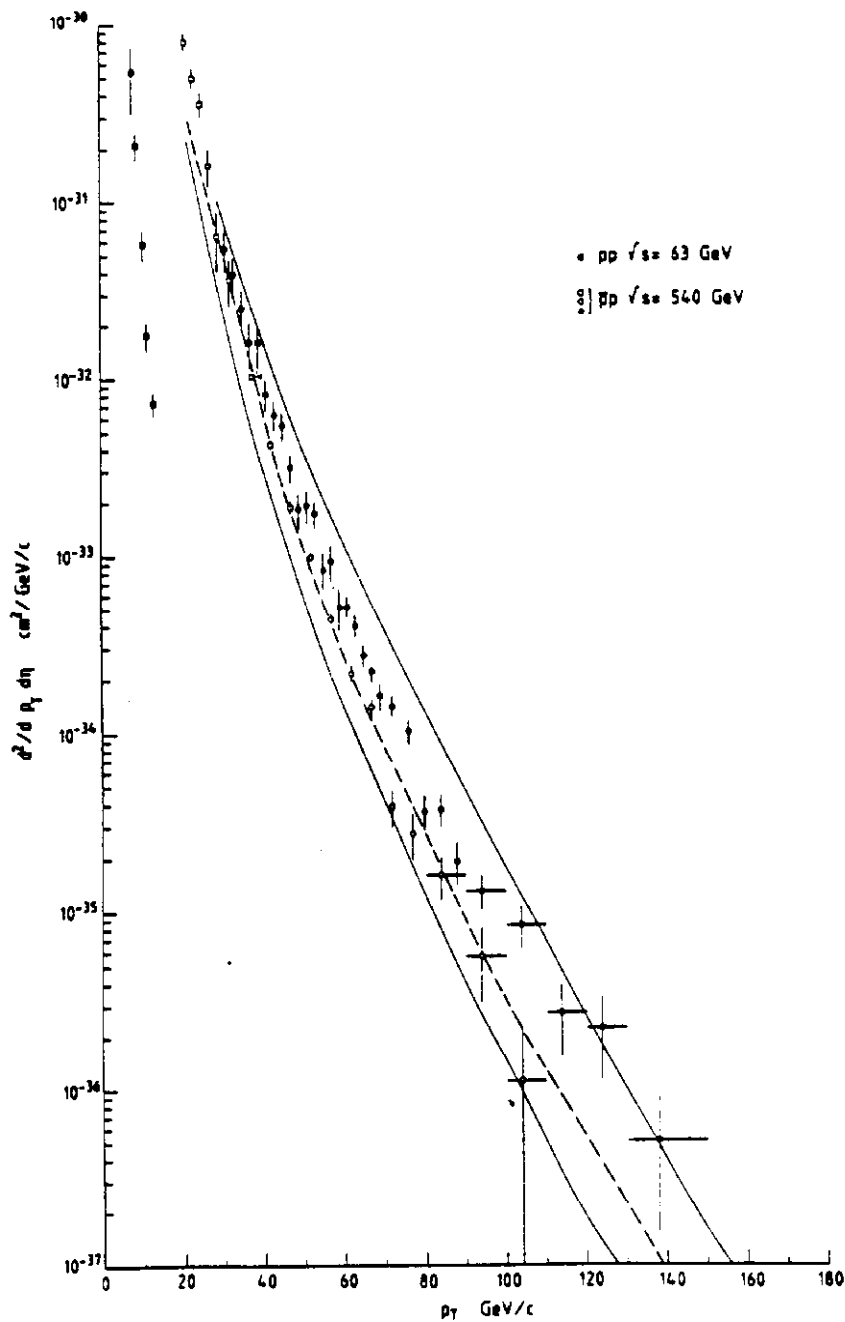


Figure 7.1. The jet cross section measured at the ISR and the CERN SPS by UA1 at rapidity = 0. The dashed curve represents the original prediction as given in [7.21] and the solid curves indicate the range of predictions.

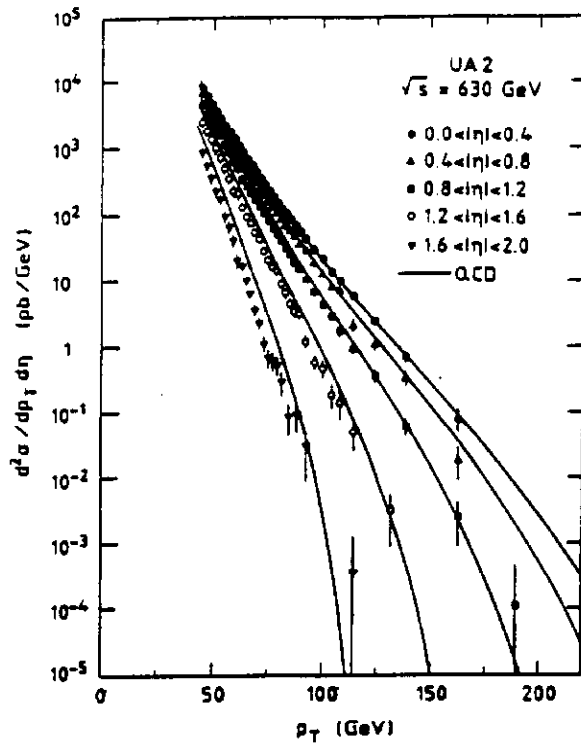


Figure 7.2. The inclusive jet cross section measured by the UA2 experiment for different pseudorapidities. The systematic error of 32% is not shown. The curves represent a LO QCD calculation with scale of  $E_t/2$ , using the EHLQ parton distributions.

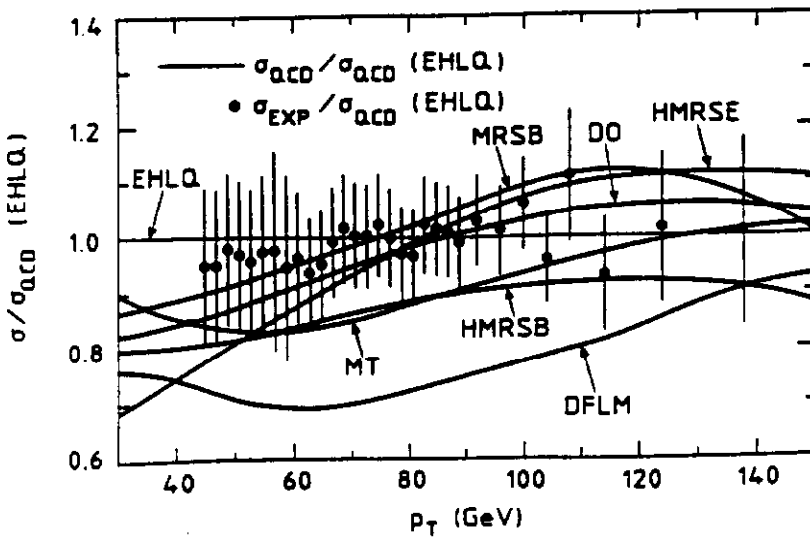


Figure 7.3. The ratio of experimental to theoretical (based on EHLQ) jet cross section at  $\eta < 0.85$  in the UA2 experiment (black dots). The curves represent calculations for different parton distributions, relative to the EHLQ distributions.

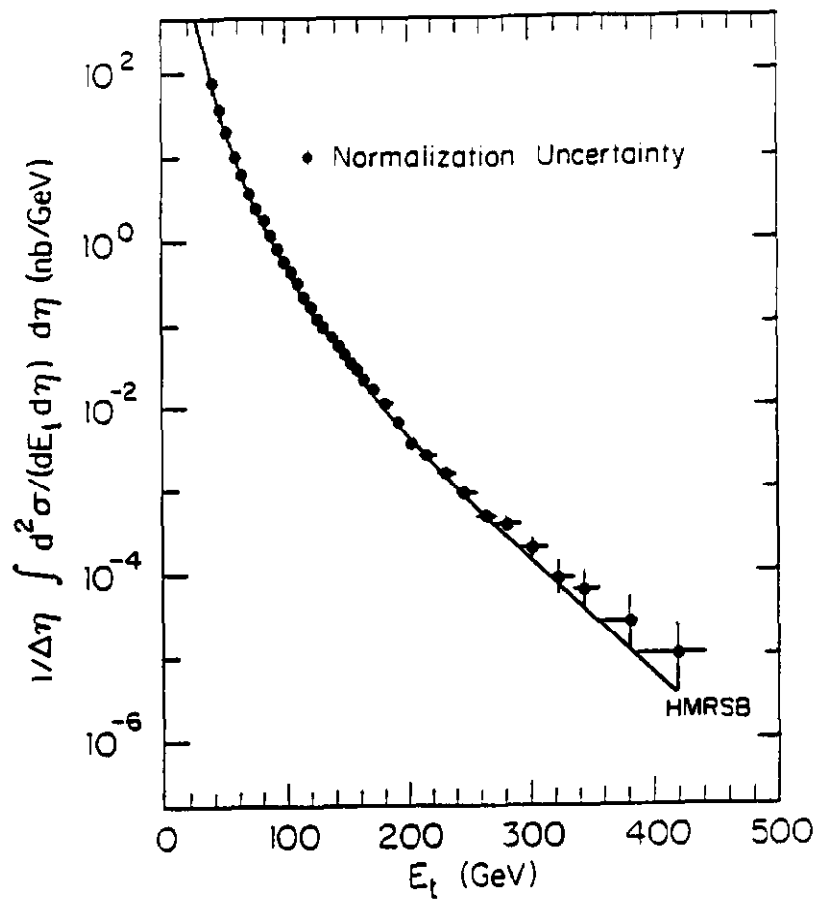


Figure 7.4. The inclusive jet cross section measured by CDF for a cone size  $R=0.7$  averaged over the pseudorapidity interval  $0.1 < \eta < 0.7$ . The curve represents the prediction of a NLO calculation using the HMRSB parton distributions. The errors shown represent the statistical and  $E_t$  dependent systematic errors. The overall normalization uncertainty is also indicated separately.

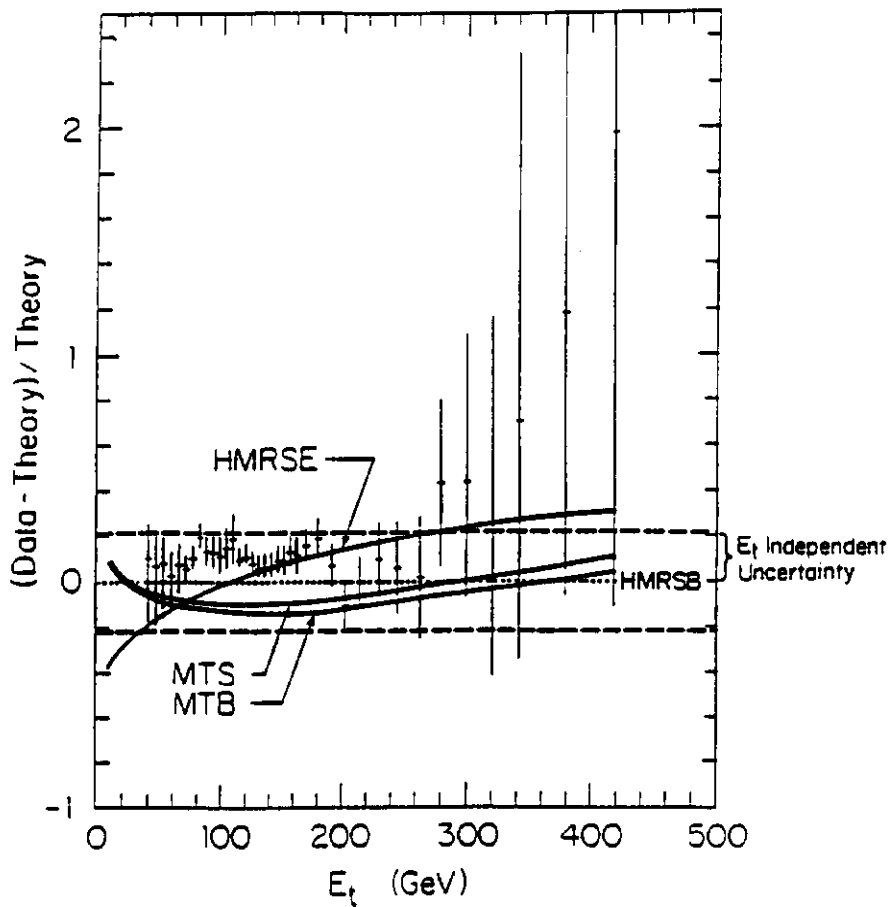


Figure 7.5. The CDF inclusive jet cross section compared to theory as the ratio  $(\text{data} - \text{theory}) / \text{theory}$ . The dashed lines indicate the systematic uncertainty in the data, while the error bars include  $E_t$  dependence. The reference parton distribution used is HMRSB and predictions using other sets are also shown.

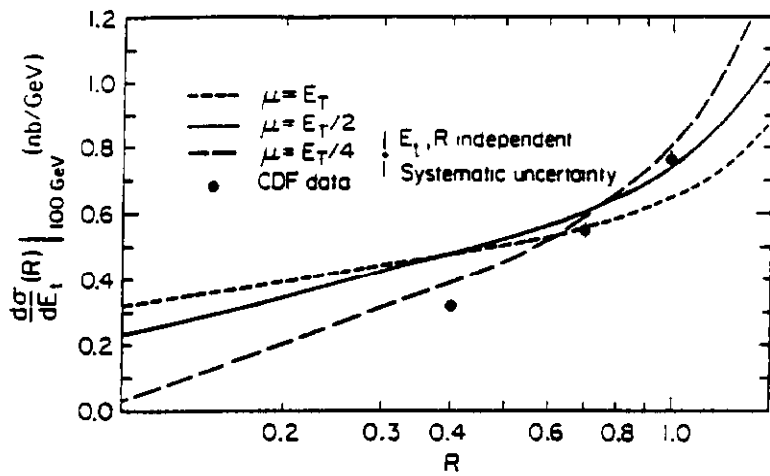


Figure 7.6. The cone size dependence of the jet cross section as measured by CDF (data points) at  $E_t = 100$  GeV. Statistical errors only are plotted on the data points. An overall systematic uncertainty is indicated separately. The curves represent NLO predictions based on the MRSB [7.22] parton distributions for different choices of the renormalization scale.

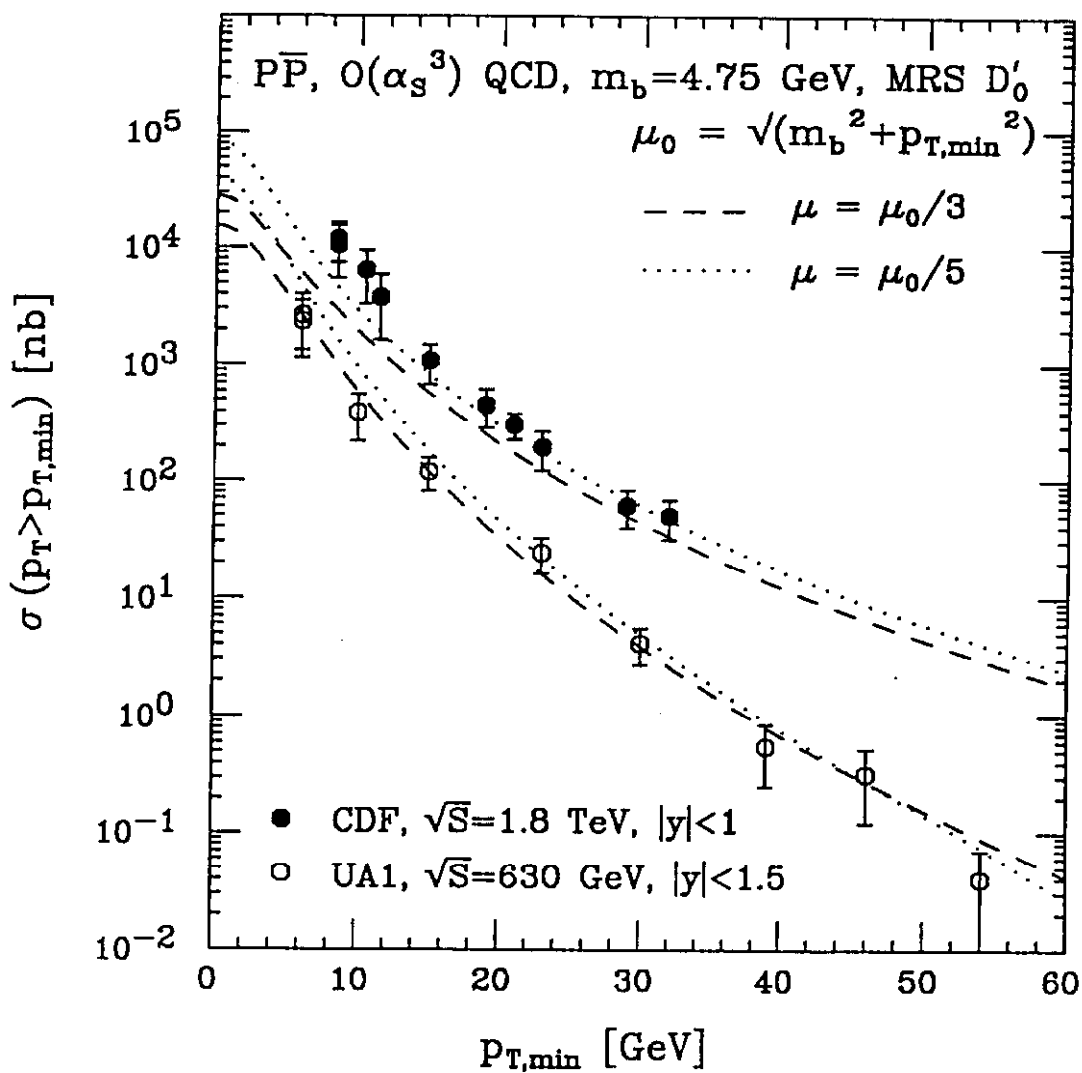


Figure 7.7. QCD fit to  $b$ -quark production data.

## 8 Global Analysis of Parton Distributions

Factorization theorems in perturbative QCD give a justification for and improvement of parton model predictions. In the “QCD improved” parton model, physically observed cross sections involving hadrons can be written as convolutions of perturbatively calculable partonic hard parts and parton distributions, which summarize uncalculable non-perturbative effects [8.1] (see Section 3 above).

### 8.1 Evolution of Parton Distributions

The parton distributions are often presented as functions of  $x$  and  $\mu_f$ ; and are customly interpreted as the probability densities to find a parton within a hadron with its momentum fraction between  $x$  and  $x + dx$ . Below we denote the factorization scale by  $\mu_f$ . Although perturbative QCD cannot predict the absolute normalization of these parton distributions, their evolution with the factorization scale can be calculated (Section 3.2.3). More precisely, the scale dependence is governed by a set of coupled integro-differential evolution equations, valid to all orders in  $\alpha_s$  [8.2]

$$\begin{aligned}\frac{d\phi_q(x, \mu_f)}{dt} &= \frac{\alpha_s(\mu_f)}{2\pi} \int_x^1 \frac{dy}{y} \left[ P_{qq}(y)\phi_q\left(\frac{x}{y}, \mu_f\right) + P_{qg}(y)\phi_g\left(\frac{x}{y}, \mu_f\right) \right] \quad (8.1) \\ \frac{d\phi_g(x, \mu_f)}{dt} &= \frac{\alpha_s(\mu_f)}{2\pi} \int_x^1 \frac{dy}{y} \left[ \sum_q P_{gq}(y)\phi_q\left(\frac{x}{y}, \mu_f\right) + P_{gg}(y)\phi_g\left(\frac{x}{y}, \mu_f\right) \right],\end{aligned}$$

where  $t = \ln(\mu_f^2/\Lambda^2)$ , and the subscript  $q$  denotes quark flavors. The kernels,  $P_{ij}(z)$ , have the physical interpretation as probability densities for obtaining a parton of type  $i$  from one of type  $j$  with a fraction  $z$  of the parent parton’s momentum. At the leading order (LO), the  $P_{ij}$  are given in Eq. (5.7) above. The Next-to-leading-order (NLO) (or 2-loop) expressions for  $P_{ij}(z)$  were calculated by several groups [8.3]. Up until recently, there had been an unresolved minor discrepancy for  $P_{gg}(z)$  between results obtained in different gauges. This has now been clarified [8.4].

This set of equations can be solved exactly in moment space [8.5], once a set of input distributions is specified at an initial value  $\mu_0$ . One can then

invert the moments to get the  $x$  and  $\mu_f$ -dependent parton distributions. However, this method requires the knowledge of initial parton distributions at all values of  $x$  from 0 to 1, and no experimental measurements at fixed  $\mu_f$  can reach all the way to  $x = 0$ . In current global analysis of parton distributions, one directly solves this set of equations numerically. Note that one needs input distributions only for  $x$  greater than or equal to the smallest momentum fraction at which parton distributions are desired.

## 8.2 Global Analysis

The global analysis of parton distributions involves making use of experimental data from many physical processes, and the use of the parton evolution equations to extract a set of universal parton distributions which best fit the existing data. These distributions can then be used in predicting all other physical observables at energy scales far beyond that presently achievable. Herein lies the wide-ranging usefulness of the QCD improved parton model.

A typical procedure for the global analysis involves following necessary steps:

1. Develop a program to numerically solve the evolution equations — a set of coupled integro-differential equations;
2. Make a choice on experimental data sets, such that the data can give the best constraints on the parton distributions;
3. Select the factorization scheme — the “DIS” or the “ $\overline{\text{MS}}$ ” scheme, and make a consistent set of choices on factorization scale for all the processes;
4. Choose the parametric form for the input parton distributions at  $\mu_0$ , and then evolve the distributions to any other values of  $\mu_f$ ;
5. Use the evolved distributions to calculate  $\chi^2$  between theory and data, and choose an algorithm to minimize the  $\chi^2$  by adjusting the parametrizations of the input distributions;

6. Parametrize the final parton distributions at discrete values of  $x$  and  $\mu_f$  by some analytical functions.

In all high energy data, deeply inelastic scattering of leptons on nucleon and nuclear targets remains the primary source of information on parton distributions, because of its high-statistics. Such data is known to be mostly sensitive to certain combinations of quark distributions. Drell-Yan lepton-pair production, and direct photons at large transverse momenta provide important complementary information on anti-quark and gluon distributions. Most data used in obtaining recent parton distributions are at fixed target energies. Collider results have not reached the accuracy necessary to be included into global fits. But, they will eventually offer a significant opportunity to probe the small- $x$  region (say  $x \leq 10^{-3}$ ).

Parton distributions defined in different factorization schemes are different. Commonly used factorization schemes in the literature are “DIS” and “ $\overline{\text{MS}}$ ” schemes. In principle, parton distributions obtained in one scheme can be directly transformed into the other scheme. However, the transformation is not reliable in certain kinematic regions where the perturbation series expansion has abnormal behavior [8.1]. It is preferable to perform independent analyses in these schemes.

The truncation of the perturbation series invariably leads to renormalization and factorization scale dependence for QCD predictions. Consequently, parton distributions obtained from the global analysis will depend on the choice of the scales. If significant scale dependence is found to exist in a particular kinematic region for some processes, then the usefulness of such data is limited, until new theoretical techniques are developed to reduce that dependence.

There is considerable freedom in choosing the parametric form of the input parton distributions at scale  $\mu_0$ . The parametrization must be general enough to accommodate all the possible  $x$  and quark-flavor dependence; but it should not contain so many parameters that the fitting procedure becomes very much under-determined. In practice, for each flavor it is common to use a functional form

$$\phi(x, \mu_0) = A_0 x^{A_1} (1 - x)^{A_2} P(x) \quad (8.2)$$

where  $P(x)$  is a smooth function. In above expression,  $x^{A_1}$  dominates the small  $x$  feature and  $(1-x)^{A_2}$  determines the large  $x$  behavior.

When calculating the  $\chi^2$ , both statistical and systematic errors should be taken into account. The most expedient, hence most often used, method is to combine these errors in quadrature [8.6]. However, real systematic errors are correlated; they must eventually be incorporated in that way when the analysis reaches a truly quantitative stage.

After minimizing the  $\chi^2$  (e.g., using the MINUIT package of CERN library), the resultant parton distributions can be presented in two ways. One way is just to give the relevant QCD parameters and the parametrization of input parton distributions at scale  $\mu_0$ . The user can then produce the parton distributions at another value of  $\mu_f$  by using this information as input to a reliable QCD evolution program. The other, the commonly used one, is to approximate the outcome of a global fit over  $(x, \mu_f)$  by a set of parametrized functions. Such parametrization varies widely between the available distributions sets, ranging from a simple interpolation formula over a large three-dimensional array ( $x, \mu_f$ , and flavor), to Chebeshev polynomial expansions, to simple  $\mu_f$ -dependent parametrizations of the form of the above equation with an appropriately chosen smooth function  $P(x)$ . It was found that a logarithmic factor of the form  $\log^{A_3}(1/x)$  is particularly effective in rendering the  $\mu_f$ -dependence of the coefficient functions  $A_i$  smooth for the QCD evolved distributions.

Although, in principle, the form of the parametrization is arbitrary so long as the approximated distributions still fit the data, extrapolation of the distributions out of the fitting region (e.g., into the small  $x$  region) will give very different predictions. It has been demonstrated that good fits to data can be obtained with the coefficient  $A_1$  (which controls the small  $x$  behavior) varying, say, from -0.5 to 0.2. Such uncertainty should be regarded as evidence of our lack of knowledge of the uncharted region. It is not meaningful to take the extrapolation of any particular set of parton distributions as "predictions". This uncertainty can be reduced either by new experimental measurements or by theoretical advances which allow true predictions extending to small  $x$  along the same way the usual evolution equation does for

the  $\mu_f$  variable.

### 8.3 Survey of Recent Parton Distributions

The first generation parton distribution sets, based on leading order evolution and data of the early 1980's, have been widely used in calculations of high energy processes [8.7]. However, since then experimental data have been drastically improved (and substantially changed, in some cases), and these distributions are no longer able to fit the new data.

The second generation global analyses, based on next-to-leading order evolution and more recent data, have been carried out by several groups in recent years. Some of the groups perform specialized analyses focusing on some specific issue or process (such as the gluon distributions and direct photon production [8.8], neutrino scattering [8.9] etc.,); and others study a wide range of processes [8.6] [8.10]. These analyses differ considerably on various issues, such as the range of data used, the way experimental errors are treated, the choice of schemes, assumptions on the input distributions, and so on.

A compilation of currently available parton distribution sets, both old and new, have been made at CERN and it has been distributed as a program package PDFLIB [8.11]. Because most of the older distributions are seriously inconsistent with current data, and because of the differences mentioned above, indiscriminant use of all the distributions in this collection can lead to rather meaningless results.

For example, it is important to only compare correct corresponding objects. Thus, the LO, NLO-DIS, and NLO- $\overline{\text{MS}}$  distributions are different objects, and should not be compared or mixed. When calculating physical quantities (such as cross sections or structure functions), LO, NLO-DIS, and NLO- $\overline{\text{MS}}$  distributions must be convoluted with the corresponding LO, NLO-DIS, and NLO- $\overline{\text{MS}}$  hard scattering parts in order to yield meaningful predictions.

We are about to enter yet another era of precision in QCD global analysis. Recently released NMC data[8.12] on  $F_2^n/F_2^p$ ,  $F_2^p - F_2^n$ , and  $F_2^{p,d}$  using a

muon beam and CCFR data[8.13] on  $F_{2,3}^{Fe}$  using (anti-) neutrinos should have a significant impact on QCD global analyses because of their extended kinematic coverage (particularly at small  $x$ ), their high statistics and minimal systematic errors. The precision of the current generation of DIS experiments (including the previously published SLAC, BCDMS, and CDHSW data) now far exceeds the size of next-to-leading order QCD contributions to these processes; thus they probe the full complexity of QCD mixing effects between quarks and gluons in a properly conducted QCD analysis. At the same time, data being accumulated at the Fermilab Tevatron on many hadron collider processes (such as W-, Z-production, lepton pair production, direct-photon production, jet production, and heavy flavor production) are beginning to be quantitative enough to provide complementary information and constraints on parton distributions. Finally, the HERA electron-proton collider will soon provide direct measurements of structure functions at very small  $x$ .

The new DIS data have been incorporated in two recent global analysis efforts [8.14], [8.15]. The most notable result from each of the new global analyses is the apparent extraordinary quantitative agreement of the NLO-QCD parton framework with the very high statistics DIS experiments over the entire kinematic range covered and the consistency of this framework with all available experiments on lepton pair and direct photon production as well. The parton distributions are determined with much more precision than before.

On the other hand, these analyses also are calling into question, for the first time, the ultimate consistency of the existing theoretical framework with all existing experimental measurements! (This can be regarded as testimony to the progress made in both theory and experiment – considering the fact that contradictions come with precision, and they are a necessary condition for discovering overlooked shortcomings and/or harbingers of new physics.) When all available total inclusive DIS data and their associated errors are taken seriously in the latest analysis, the CTEQ Collaboration [8.15] found a good global fit only if the strange quark has a much softer distribution than the non-strange ones and rises above the latter in the small  $x$  region below  $x = 0.1$ . This result is unexpected, and it also appears to be in conflict with

the dedicated measurement of  $s(x)$  done with dimuon final states in neutrino scattering [8.16]. (The latter is not included in any of the existing global analyses.) Thus, either there are unknown theoretical flaws in the next-to-leading order QCD analysis or some of the experimental data sets need to be re-examined both in their measured values and in the assessed systematic errors. In the MRS analysis [8.14], the strange quark content of the nucleon is assumed to be consistent with the dimuon result; reasonable fits are obtained only by letting the normalization of the data sets vary freely, unconstrained by the stated experimental errors plus some other added uncertainties.

The emergence of the apparent contradictions has already spurred vigorous efforts by both theorists and experimentalists to rigorously examine the existing assumptions and to institute new improvements in their respective analyses. These efforts, added by anticipated data from the hadron collider experiments and from HERA, will undoubtedly contribute significantly to further progress – in directions not necessarily clear at present. That is, of course, the fun of physics!

## References

- [8.1] J.F. Owens and W.-K. Tung, Annu. Rev. Nucl. Par. Sci. **42** (1992) 291.
- [8.2] L.V. Gribov and L.N. Lipatov, Sov. J. Nucl. Phys. **15**, 78 and 1218 (1972); G. Altarelli and G. Parisi, Nucl. Phys. **B126**, 298 (1977).
- [8.3] E.G. Floratos *et al.*, Nucl. Phys. **B129**, 66 (1977); and erratum, Nucl. Phys. **B139**, 545 (1978); E.G. Floratos *et al.*, Phys. Lett. **98B**, 89, 285, (1981); A. Gonzalez-Arroyo *et al.*, Nucl. Phys. **B153**, 161 (1979); **B166**, 429 (1980); G. Curci *et al.*, Nucl. Phys. **B175**, 27 (1980); W. Furmanski and R. Petronzio, Phys. Lett. **97B**, 438 (1980); R.T. Herrod and S. Wada, Phys. Lett. **96B**, 195 (1980); R.T. Herrod *et al.*, Z. Phys. **C9**, 351 (1981).
- [8.4] R. Hamberg and W.L. van Neerven, Nucl. Phys. **B379**, 143 (1992).

- [8.5] E. Reya, Phys. Rept. **69**, 195 (1981); G. Altarelli, Phys. Rept. **81**, 1 (1982).
- [8.6] J.G. Morfín and W.K. Tung, Z. Phys. **C52**, 13 (1991).
- [8.7] D.W. Duke and J.F. Owens, Phys. Rev. **D30**, 49 (1984); E. Eichten *et al.*, Rev. Mod. Phys. **56**, 579 (1984) and erratum **58**, 1065 (1986); M. Glück, E. Reya and E. Hoffmann, Z. Phys. **C13**, 119 (1982).
- [8.8] P. Aurenche *et al.*, Phys. Rev. **D39**, 3275 (1989).
- [8.9] M. Diemoz *et al.*, Z. Phys. **C39**, 21 (1988).
- [8.10] A. Martin *et al.*, Phys. Rev. **D37**, 1161 (1988); Mod. Phys. Lett. **A4**, 1135 (1989); P.N. Harriman, *et al.*, Phys. Rev. **D42**, 798 (1990); J. Kwiecinski *et al.*, Phys. Rev. **D42**, 3645 (1990).
- [8.11] H. Plothow-Besch, “PDFLIB: Structure Functions and  $\alpha_s$  Calculation User’s Manual” CERN-PPE, 1991.03.21. W5051 PDFLIB.
- [8.12] NMC Collaboration, P. Amaudruz *et al.*, Preprint CERN-PPE/92-124.
- [8.13] CCFR Collaboration, Nevis Preprints, S.R. Mishra *et al.*, #1459; W.C. Leung *et al.*, #1460; and P.Z. Quintas *et al.*, #1461.
- [8.14] A. Martin, R. Roberts, and J. Stirling, Phys. Rev. (to be published, 1993).
- [8.15] J. Botts, J.G. Morfín, J.F. Owens, J.W. Qiu, W.K. Tung, and H. Weerts, Phys. Lett. (to be published, 1993).
- [8.16] CCFR Collaboration, S.A. Rabinowitz *et al.*, Phys. Rev. Lett. **70**, 134 (1993).

## A Color Matrix Identities and Invariants

Only a few identities are necessary for the calculations described in the text. In general, for representation  $R$ ,  $SU(N)$  generators can be picked to satisfy

$$\text{Tr} [T_a^{(R)} T_b^{(R)}] = T(R) \delta_{ab}, \quad (\text{A.1})$$

with  $T(R)$  a number characteristic of the representation. Also of special interest is the representation-dependent invariant,  $C_2(R)$ , defined by

$$\sum_{a=1}^{N^2-1} (T_a^{(R)})^2 = C_2(R) I, \quad (\text{A.2})$$

with  $I$  the identity matrix.

We encounter only two representations here, the  $N$ -dimensional “defining” representation,  $F$ , and the  $N^2 - 1$ -dimensional adjoint representation,  $A$ . The generators  $T_a^{(F)}$  are a complete set of  $N \times N$  traceless hermitian matrices, while the generators  $T_a^{(A)}$  are defined by the  $SU(N)$  structure constants  $C_{abc}$  (Eq. (1.5)) as

$$(T_a^{(A)})_{bc} = -i C_{abc}. \quad (\text{A.3})$$

For these two representations, the relevant constants are

$$\begin{aligned} T(F) &= \frac{1}{2} & C_2(F) &= \frac{N^2 - 1}{2N} \\ T(A) &= N & C_2(A) &= N. \end{aligned} \quad (\text{A.4})$$

Another useful identity, special to the defining representation, enables us to work with simple products of the generators,

$$T_a^{(F)} T_b^{(F)} = \frac{1}{2} [i C_{abc} T_c^{(F)} + d_{abc}] T_c^{(F)} + \frac{1}{6} \delta_{ab} I, \quad (\text{A.5})$$

with  $I$  the  $3 \times 3$  identity, and the  $d_{abc}$  real. Unlike the previous equations, this and the following equation apply only to  $SU(3)$ . A numerical value that occurs in the three-loop correction to the total  $e^+ e^-$  annihilation cross section is

$$D = \sum_{abc} d_{abc}^2 = 40/3. \quad (\text{A.6})$$

## B Cut Diagram Notation

A convenient technique for organizing calculations of  $|\mathcal{M}|^2$  in cross sections is through *cut diagrams*, which combine contributions to  $\mathcal{M}$  and  $\mathcal{M}^*$  into a single diagram for  $|\mathcal{M}|^2$  with slightly modified Feynman rules.

The form of cut diagrams is derived in Fig. B.1, for the annihilation of a fermion pair of momenta  $k_1$  and  $k_2$  into a set of  $n$  final state lines, of which only a fermion with momentum  $p_1$  and an antifermion of momentum  $p_n$  are exhibited.

The underlying identity for these manipulations is

$$\begin{aligned} & [\bar{w}(\gamma^{\mu_1}\gamma^{\mu_2}\cdots\sigma^{\alpha\beta}\cdots\gamma^\nu\gamma_5\cdots)w']^* \\ &= \bar{w}'(\cdots\gamma^\nu\gamma_5\cdots\sigma^{\alpha\beta}\cdots\gamma^{\mu_2}\gamma^{\mu_1})w, \end{aligned} \quad (\text{B.1})$$

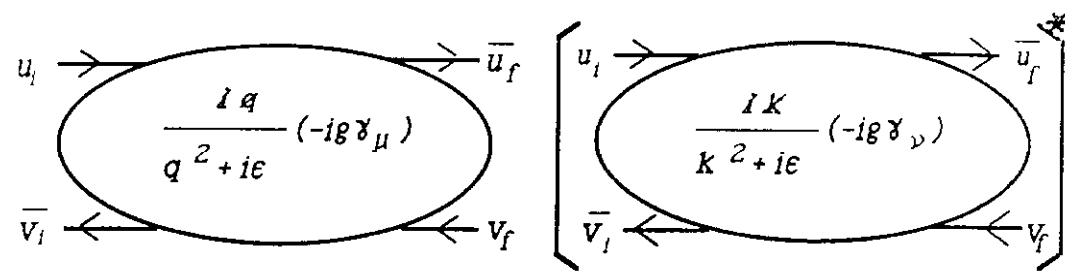
where  $w$  and  $w'$  are any two Dirac spinors.

Fig. B.1a shows a typical fermion propagator and vertex in  $\mathcal{M}$  and  $\mathcal{M}^*$ . Fig. B.1b shows the application of Eq. (B.1) to Fig. B.1a. The diagram in  $\mathcal{M}^*$  has been flipped over, all arrows on fermion lines have been reversed, and all momenta have been reversed in sign. This leaves the sign of momenta in fermion propagators the same, as shown. Color sums can be reversed in the same manner as spinor sums, because the color generators are hermitian.

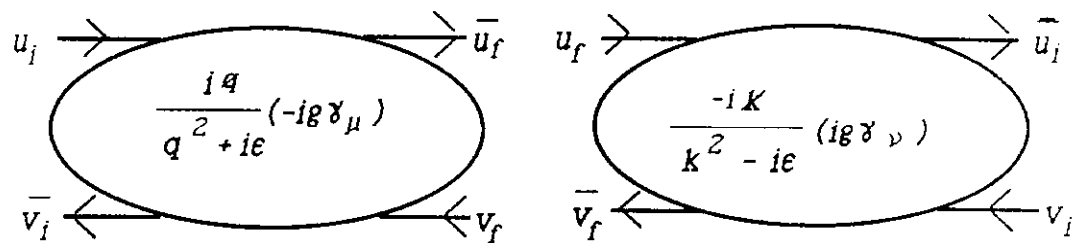
Fig. B.1c exhibits the cut diagram notation, in which the contribution of any final state is a modified forward scattering diagram. The final-state lines are indicated by a vertical line (the “cut”). Cut lines are represented in the integral corresponding to the cut diagram by factors

$$(\not{p}_i + m_i)(2\pi)\delta_+(p_i^2 - m_i^2), \quad (\text{B.2})$$

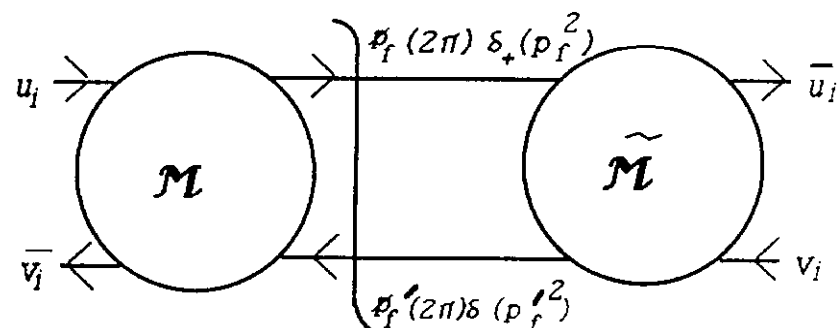
for fermions or antifermions, after a spin sum. For polarized fermions or for vectors, the usual spin projections replace  $(\not{p}_i + m_i)$ . The Feynman rules for  $\mathcal{M}$  are the normal ones, and those for  $\widetilde{\mathcal{M}}$  differ only in the sign of *explicit* factors of  $i$  at vertices and in propagators. The three-gluon vertex also changes sign in  $\widetilde{\mathcal{M}}$ , because of the reversal of momenta.



(a)



(b)



(c)

Figure B.1. Cut diagram identities.

## C Dimensional Regularization

In Section 1, our description of renormalization was a bit abstract, depending as it does on the substitution, Eq. (1.25). For many purposes, it is useful to introduce an intermediate step in this replacement, in which the divergent integral is *regulated*, that is, modified to become a finite integral. This will involve the introduction of a new, unphysical, parameter. The replacement in Eq. (1.25) will then appear as a “subtraction”, in which the regulated integral is combined with a term that cancels its dependence on the regularization parameter. At present, far and away the most popular regularization scheme is *dimensional regularization*, primarily because of its calculational simplicity. It is difficult to follow much of the theoretical literature of pQCD without at least a passing acquaintance with dimensional regularization.

Most of the essential features are contained in the scalar one-loop self-energy, Fig. 1.2,

$$G^{(2)}(p, n) = i\mu^{2-n/2} \int \frac{d^n k}{(2\pi)^n} \frac{1}{(k^2 - m^2 + i\epsilon)((p - k)^2 - m^2 + i\epsilon)}, \quad (\text{C.1})$$

where  $n$  is the number of dimensions, initially taken as an integer,  $n = 1, 2, \dots$ . For  $n \geq 4$ , the integral is UV divergent as  $k \rightarrow \infty$ . The factor  $\mu^{4-n}$ , with  $\mu$  an arbitrary mass is included to give  $G^{(2)}$  dimensionless for all  $n$ . To simplify further, let us do the integral in “Euclidean” space, where  $k^2 = k_0^2 + \mathbf{k}^2$ . The process of relating Euclidean to Minkowski integrals (Wick rotation) is independent of the regularization process, and for our purposes consists of multiplying by a factor  $i$ .

For  $n \geq 4$ ,  $G^{(2)}(p, n)$  is ill-defined, but for  $n < 4$  it is finite. The idea of dimensional regularization is to extend  $G$  to an *analytic function* of  $n$  for all  $\text{Re}(n) < 4$ , and then to use analytic continuation to extend it to the rest of the complex  $n$  plane. When we recall that analytic continuation is a unique process, we begin to see the power of the method.

So, how are we to extend  $G$  to noninteger, let alone complex, values of  $n$ ? Actually, it is quite a simple process: more general integrals require more care, but the basic steps are the same for every Feynman diagram.

- (i) First comes a technical step, called *Feynman parameterization*, which is a trick to rewrite the product of denominators as a single denominator,

$$G^{(2)}(p, n) = i\mu^{4-n} \int \frac{d^n k}{(2\pi)^n} \int_0^1 dx [k^2 - 2xp \cdot k + xp^2 - m^2]^{-2}. \quad (\text{C.2})$$

- (ii) Next, we complete the square in the single denominator,  $\ell = k - xp$ , to get

$$G^{(2)}(p, n) = i\mu^{4-n} \int \frac{d^n \ell}{(2\pi)^n} \int_0^1 dx [\ell^2 + x(1-x)p^2 - m^2]^{-2}. \quad (\text{C.3})$$

Notice that the shift of integration variable is perfectly permissible for  $n < 4$ , where the integral is convergent.

- (iii) In this form, we can trivially change variables to polar coordinates, and do the (trivial) angular integrals

$$G^{(2)}(p, n) = i\mu^{4-n} \frac{\Omega(n)}{(2\pi)^n} \int_0^1 dx \int_0^\infty \frac{d\ell \ell^{n-1}}{[\ell^2 + x(1-x)p^2 - m^2]^2}. \quad (\text{C.4})$$

- (iv) At this stage, the  $n$ -dependence is segregated into the angular volume,  $\Omega(n)$ , while the divergence at  $n = 4$  is entirely in the radial  $\ell$  integral. These two quantities are quite easy to promote from integer to complex  $n$ .

So, we are left with two integrals to extend to the complex “ $n$ -plane”. Consider first the angular integral. We are already familiar with one- and two-dimensional angular integrals,

$$\begin{aligned} \Omega(2) &= \int_0^{2\pi} d\theta_1 \\ &= 2\pi, \end{aligned} \quad (\text{C.5})$$

$$\begin{aligned} \Omega(3) &= \int_0^\pi d\theta_2 \sin(\theta_2) \Omega(2). \\ &= 4\pi. \end{aligned} \quad (\text{C.6})$$

For integer  $n$  dimensions we easily find the following recursion relation:

$$\begin{aligned}\Omega(m) &= \int_0^\pi d\theta \sin^{m-2}(\theta_m) \Omega(m-1), \\ &= \frac{\Gamma(1/2)\Gamma((n-1)/2)}{\Gamma(n/2)} \Omega(m-1),\end{aligned}\quad (\text{C.7})$$

where  $\Gamma(z)$  is the Euler *Gamma function* defined by the integral representation

$$\Gamma(z) \equiv \int_0^\infty dx x^{z-1} e^{-x}, \quad (\text{C.8})$$

for  $\text{Re } z > 0$ .

The recursion relation Eq. (C.7) is trivially solved by use of Eq. (C.5) as an initial condition. We find

$$\Omega(n) = \frac{2\pi^{n/2}}{\Gamma(n/2)}. \quad (\text{C.9})$$

We can use this result to give a meaning to the integral Eq. (C.4) for all values of  $n$ , and not just positive integers. But let us first list a few basic properties of the Gamma function, which appears in the results of typical integrals like Eq. (C.4). It is defined by Eq. (C.8) for  $\text{Re } z > 0$ , and by analytic continuation for all other values of  $z$ . A little algebra shows that for integer  $z \geq 1$

$$\Gamma(z) = (z-1)! \quad (\text{C.10})$$

The Gamma function obeys the recursion relation

$$\Gamma(z-1) = \frac{\Gamma(z)}{(z-1)}. \quad (\text{C.11})$$

Since  $\Gamma(z)$  is analytic for all  $z$  with positive real parts, it is easy to deduce that it is analytic for all  $z$ , except at negative integers, where it has simple poles. It is precisely this last property that makes dimensional regularization such a convenient technique.

Now let us return to our basic one-loop integral, Eq. (C.3). The remaining, radial integral in Eq. (C.4) can be analytically continued from a finite

integral for  $n$  real and less than 4, to a complex integral by using yet another integral representation involving gamma functions,

$$\int_0^\infty dy y^{w-1} (y+1)^{-w-z} = \frac{\Gamma(w)\Gamma(z)}{\Gamma(w+z)}. \quad (\text{C.12})$$

(This combination of Gamma functions is often called a “beta function”, not be confused with the beta function introduced in connection with renormalization.) Combining these results, we find

$$\begin{aligned} G^{(2)}(p, n) &= \frac{i\mu^{4-n}}{(4\pi)^{n/2}} \Gamma(2 - n/2) (p^2)^{n/2-2} \\ &= \frac{i}{(4\pi)^2} \left[ \frac{1}{2 - n/2} + \ln(p^2/\mu^2) + \dots \right]. \end{aligned} \quad (\text{C.13})$$

In this way, the superficially divergent integral becomes the sum of a momentum-independent pole term, plus momentum-dependent finite parts. Minimal subtraction (MS) schemes consist of subtracting the pole terms only in dimensional regularization. The renormalization scale enters automatically by modifying the Lagrange density, as described below.

*Dimensionally continued field theory.* Let us now discuss how dimensional regularization is introduced in QCD. As its name implies, dimensional regularization involves treating the number of spacetime dimensions as a parameter,  $n$ . The unregulated theory, of course, is defined at  $n = 4$ . It is often convenient to parameterize the regularization in terms of the “small” quantity

$$\epsilon = 2 - n/2. \quad (\text{C.14})$$

The rules that we will need to implement dimensional regularization may be summarized as

- (i) For QCD, the regulated theory is defined by a Lagrangian of the form Eq. (1.2), but with all couplings,  $g$ , replaced as

$$g \rightarrow g\mu^\epsilon, \quad (\text{C.15})$$

with  $\epsilon$  given by Eq. (2.15), and with  $\mu$  an arbitrary mass scale, which we will refer to as the *renormalization scale*.

(ii) Vector indices run from  $1, \dots, n$  and we make the replacements

$$\frac{d^4 k}{(2\pi)^4} \rightarrow \frac{d^n k}{(2\pi)^n}, \quad 4 = \sum_{\mu=1}^4 \rightarrow n = \sum_{\mu=1}^n g_\mu^\mu, \quad (\text{C.16})$$

in all momentum integrals (loop *and* phase space). We will see below what we mean explicitly by  $d^n k$ .

(iii) There are  $n$  Dirac matrices  $\gamma^\mu, \mu = 1, \dots, n$ , and the standard anticommutation relations

$$\{\gamma^\mu, \gamma^\nu\}_+ = 2g^{\mu\nu}, \quad \mu = 1, \dots, n, \quad (\text{C.17})$$

are satisfied by all  $n$  of them. Fortunately, however, it is *not* necessary to make the number of spinor components  $n$ -dependent. Thus we may retain Dirac trace identities such as

$$\text{Tr}[\not{p}_1 \not{p}_2 \not{p}_3 \not{p}_4] = 4[(p_1 \cdot p_2)(p_3 \cdot p_4) + (p_1 \cdot p_4)(p_2 \cdot p_3) - (p_1 \cdot p_3)(p_2 \cdot p_4)], \quad (\text{C.18})$$

which depend on the  $\gamma^\mu$  being  $4 \times 4$  matrices. We should emphasize that Eq. (C.18) may be taken as a rule, because the true  $\epsilon$ -dependence due to the trace will not affect physical answers at  $n = 4$ , *not* because Eq. (C.18) is really correct in  $n$  dimensions. On the other hand, the anticommutation relations, along with  $g^\mu_\mu = n$  lead to the following easy-to-prove,  $n$ -dependent identities for Dirac matrices,

$$\begin{aligned} \gamma_\mu \not{p} \gamma^\mu &= (2-n) \not{p} \\ \gamma_\mu \not{p}_1 \not{p}_2 \gamma^\mu &= 4p_1 \cdot p_2 - 2\epsilon \not{p}_1 \not{p}_2 \\ \gamma_\mu \not{p}_1 \not{p}_2 \not{p}_3 \gamma^\mu &= -2 \not{p}_3 \not{p}_2 \not{p}_1 + 2\epsilon \not{p}_1 \not{p}_2 \not{p}_3. \end{aligned} \quad (\text{C.19})$$

The basic one-loop integrals may now be evaluated in terms of Eqs. (C.9) and (C.12) straightforwardly. For instance, consider the Minkowski space integral

$$I_s(n) = \int \frac{d^n \ell}{[\ell^2 - M^2 + i\epsilon]^s}, \quad (\text{C.20})$$

where  $\ell^2 = \ell_0^2 - \vec{\ell}^2$ . Wick rotation,  $\ell_0 \rightarrow i\ell_0$ , gives

$$\begin{aligned} I_s(n) &= (-1)^s i \int \frac{d\ell_n d^{n-1}\ell}{[\ell_E^2 + M^2 - i\epsilon]^s}, \\ &= (-1)^s i \frac{\Omega_{n-1}}{2} \int_0^\infty \frac{d\ell_E^2 (\ell_E^2)^{n/2-1}}{[\ell_E^2 + M^2 - i\epsilon]^s} \\ &= (-1)^s i \pi^{n/2} (M^2 - i\epsilon)^{n/2-s} \frac{\Gamma(s - n/2)}{\Gamma(s)}, \end{aligned} \quad (\text{C.21})$$

where we have used Eqs. (C.9) and (C.12). Similarly, we have

$$\begin{aligned} \tilde{I}_s^{\mu\nu}(n) &= \int d^n \ell \frac{\ell^\mu \ell^\nu}{[\ell^2 - M^2 + i\epsilon]^s} \\ &= \frac{1}{2} (-1)^{s-1} i \pi^{n/2} \frac{\Gamma(s - \frac{n}{2} - 1)}{\Gamma(s)} g^{\mu\nu} (M^2 - i\epsilon)^{\frac{n}{2} - s + 1}. \end{aligned} \quad (\text{C.22})$$

These forms are all that is necessary to derive the results of in Eqs. (4.19) and (4.20).

## D Kinematics and Cross Sections

In this appendix<sup>3</sup> we discuss the kinematics and formulas in frequently-encountered cross sections. In this discussion upper case letters will be used to designate incoming and outgoing hadrons,  $h$ , as  $A + B \rightarrow C + X$ , etc. Lower case letters will be used when referring to the hadron constituents which are undergoing the hard scattering.

The cross sections below are described for the most part in the language of the parton model, Section 2, with hard scattering functions  $H_{ab}$  (see Eq. (3.38)) approximated by Born cross sections. They serve as well, however, for leading-power pQCD, when factorization scale dependence is introduced into the distributions and fragmentation functions. At lowest order (LO), the hard scattering function reduces to the Born cross section, using  $\alpha_s(Q^2)$ , with  $Q^2$  an appropriate momentum transfer squared.

Let A and B be initial state hadrons and C an observed final state hadron, with four vectors  $p_A$ ,  $p_B$ , and  $p_C$ , respectively. For these momenta, Mandelstam variables are defined as

$$s = (p_A + p_B)^2, \quad t = (p_A - p_C)^2, \quad \text{and} \quad u = (p_B - p_C)^2. \quad (\text{D.1})$$

With this definition,

$$s + t + u = p_A^2 + p_B^2 + p_C^2 + (p_A + p_B - p_C)^2. \quad (\text{D.2})$$

The variable  $s$  is the squared center-of-mass energy while  $t$  and  $u$  are the squares of the four-momentum transfers from particles A and B to particle C. A similar set of variables describes the partonic scattering,  $a + b \rightarrow c + d$ , identified by ‘hats’, as  $\hat{s}$ . Thus, by Eq. (D.2), the Mandelstam variables for massless two-body elastic scattering satisfy the constraint  $\hat{s} + \hat{t} + \hat{u} = 0$ .

A number of additional variables will be encountered in discussions of large transverse momentum processes. These describe momentum components which are transverse or longitudinal with respect to the beam direction. These are denoted by  $p_T$  and  $p_\ell$ , respectively. Reference will be made

---

<sup>3</sup>This appendix closely follows a similar discussion in [D.1]

to the their scaled counterparts

$$x_T = 2p_T/\sqrt{s}, \quad x_F = 2p_\ell/\sqrt{s}. \quad (\text{D.3})$$

With these definitions the kinematically allowed ranges of  $x_T$  and  $x_F$  are (0,1) and (-1,1), respectively, if the masses of the hadrons are neglected. Another useful variable which is often used is the rapidity,  $y$ , which is defined as

$$y = \frac{1}{2} \ln \left( \frac{E + p_\ell}{E - p_\ell} \right). \quad (\text{D.4})$$

This expression, when evaluated for a massless particle, has a much simpler form. In this case,

$$y = \ln \cot \frac{\theta}{2}, \quad (\text{D.5})$$

where  $\theta$  is the center-of-mass scattering angle. This form, called the *pseudorapidity* when applied to physical particles, is convenient experimentally, since one needs to know only  $\theta$ . For many high energy processes the dependence on the particle masses is negligible and therefore the rapidity and pseudorapidity become equivalent.

In the derivations which follow it will often be necessary to work directly with the four-vectors of the interacting partons. Suppose that parton a carries a fraction  $x_a$  of hadron A's longitudinal momentum and that a similar definition for  $x_b$  exists for parton b. Then in the overall hadron-hadron center-of-mass system the four-vectors for a and b can, assuming massless partons and neglecting any parton transverse momenta, be written as

$$p_a^\mu = \frac{x_a \sqrt{s}}{2} (1, 0, 0, 1) \quad \text{and} \quad p_b^\mu = \frac{x_b \sqrt{s}}{2} (1, 0, 0, -1), \quad (\text{D.6})$$

where the positive  $z$  axis is taken to be along the direction of the incident hadron A. If the scattered parton c has transverse momentum  $p_T$  and rapidity  $y_1$ , then its four-vector is just

$$p_c^\mu = p_T (\cosh y_1, 1, 0, \sinh y_1). \quad (\text{D.7})$$

With these results it is easy to evaluate the Mandelstam variables at the parton level:

$$\hat{s} = x_a x_b s, \quad \hat{t} = -x_a p_T \sqrt{s} e^{-y_1}, \quad \text{and} \quad \hat{u} = -x_b p_T \sqrt{s} e^{y_1}. \quad (\text{D.8})$$

For the case of two-body scattering, the partonic Mandelstam variables can also be written in terms of the four-vector of the recoiling parton  $d$ , in the event that correlations are being studied. Let

$$p_d^\mu = p_T(\cosh y_2, -1, 0, \sinh y_2). \quad (\text{D.9})$$

Then  $\hat{t}$  and  $\hat{u}$  may also be written as

$$\hat{t} = -x_b p_T \sqrt{s} e^{y_2} \text{ and } \hat{u} = -x_a p_T \sqrt{s} e^{-y_2}. \quad (\text{D.10})$$

Starting with two-body scattering at the parton level the partial cross section for the inclusive production of two partons can be written as (Section 2.1),

$$\begin{aligned} d\sigma(AB \rightarrow cd) &= \frac{1}{2\hat{s}} \sum_{ab} \phi_{a/A}(x_a) dx_a \phi_{b/B}(x_b) dx_b \sum |M(ab \rightarrow cd)|^2 \\ &\quad (2\pi)^4 \delta^4(p_a + p_b - p_c - p_d) \frac{d^3 p_c}{(2\pi)^3 2E_c} \frac{d^3 p_d}{(2\pi)^3 2E_d}. \end{aligned} \quad (\text{D.11})$$

Note that unpolarized parton distributions, as defined in Section 3.4, say, include a sum over colors and spins. These quantum numbers are therefore *averaged* in the initial state of the partonic cross section, and these averages are implicit in  $\sum_{ab}$  in Eq. (D.11). At the level of two-body scattering one associates a jet with each of the outgoing partons (Section 2.3.3). However, when more complicated final states are taken into account, e.g.,  $2 \rightarrow 3$  processes, the jet must be carefully defined using energy and angular size resolutions, or a 'Jade' algorithm, etc. (Sections 4.4 and 7.2).

In order to convert Eq. (D.11) into the invariant cross section for inclusive single jet production it is easiest to use

$$\frac{d^3 p_d}{2E_d} = d^4 p_d \delta(p_d^2), \quad (\text{D.12})$$

to integrate over  $p_d$  using the four-dimensional delta function. In addition, with massless partons it is convenient to make the replacement

$$\delta(p_d^2) \rightarrow \delta(\hat{s} + \hat{t} + \hat{u}) \quad (\text{massless partons}). \quad (\text{D.13})$$

This results in

$$E \frac{d^3\sigma}{d^3p}(AB \rightarrow jet + X) = \sum_{abcd} \int dx_a dx_b \phi_{a/A}(x_a) \phi_{b/B}(x_b) \times \frac{\hat{s}}{\pi} \frac{d\sigma}{dt}(ab \rightarrow cd) \delta(\hat{s} + \hat{t} + \hat{u}), \quad (\text{D.14})$$

where the differential cross section for the two-body parton scattering subprocesses is denoted by

$$\frac{d\sigma}{dt}(ab \rightarrow cd) = \frac{1}{16\pi\hat{s}^2} \sum |M(ab \rightarrow cd)|^2. \quad (\text{D.15})$$

The argument of the delta function in Eq. (D.14) can be expressed in terms of  $x_a$  and  $x_b$  using the results given above. The  $x_b$  integration may then be done, giving the final result

$$E \frac{d^3\sigma}{d^3p}(AB \rightarrow jet + X) = \sum_{abcd} \int_{x_a^{min}}^1 dx_a \phi_{a/A}(x_a) \phi_{b/B}(x_b) \times \frac{2}{\pi} \frac{x_a x_b}{2x_a - x_T e^y} \frac{d\sigma}{dt}(ab \rightarrow cd), \quad (\text{D.16})$$

where

$$x_b = \frac{x_a x_T e^{-y}}{2x_a - x_T e^y}, \quad (\text{D.17})$$

and

$$x_a^{min} = \frac{x_T e^y}{2 - x_T e^{-y}}. \quad (\text{D.18})$$

Eq. (D.16) is also applicable for the calculation of the direct photon inclusive invariant cross section resulting from the subprocesses  $q\bar{q} \rightarrow \gamma g$  and  $gq \rightarrow \gamma q$ .

Next, in order to calculate single particle inclusive invariant cross sections, the fragmentation function  $D_{C/c}(z_c)$  (Section 2.3.2) must be included. This function, when multiplied by  $dz_c$  gives the probability for obtaining a hadron C from parton c with the hadron carrying a fraction  $z_c$  of the parton's momentum. Using  $d^3p/E = z_c^2(d^3p_c/E_c)$  the resulting expression is

$$E \frac{d^3\sigma}{d^3p}(AB \rightarrow C + X) = \sum_{abcd} \int dx_a dx_b dz_c \phi_{a/A}(x_a) \phi_{b/B}(x_b) D_{C/c}(z_c)$$

$$\times \frac{\hat{s}}{\pi z_c^2} \frac{d\sigma}{dt} (ab \rightarrow cd) \delta(\hat{s} + \hat{t} + \hat{u}). \quad (\text{D.19})$$

As in the previous case, the argument of the delta function may be expressed in terms of the parton kinematic variables and the  $z_c$  integration may then be done. The final form for the cross section is

$$E \frac{d^3\sigma}{d^3p} (AB \rightarrow h + X) = \sum_{abcd} \int_{x_a^{min}}^1 dx_a \int_{x_b^{min}}^1 dx_b \phi_{a/A}(x_a) \phi_{b/B}(x_b) D_{h/c}(z_c) \times \frac{1}{\pi z_c} \frac{d\sigma}{dt} (ab \rightarrow cd), \quad (\text{D.20})$$

where now

$$\begin{aligned} z_c &= \frac{x_T}{2x_b} e^{-y} + \frac{x_T}{2x_a} e^y, \\ x_b^{min} &= \frac{x_a x_T e^{-y}}{2x_a - x_T e^y}, \\ x_a^{min} &= \frac{x_T e^y}{2 - x_T e^{-y}}. \end{aligned} \quad (\text{D.21})$$

Eq. (D.20) is also applicable for the calculation of the single photon inclusive invariant cross section (Sections 2.5 and 6.4), when the photon results from the fragmentation from one of the scattered partons. In this case one must replace  $D_{h/c}$  by  $D_{\gamma/c}$ .

The above equations for the invariant cross sections include a summation over all of the possible two-body parton scattering subprocesses. In addition, the summation implies a symmetrization under  $\hat{t}$  and  $\hat{u}$  interchange, i.e., interchange of the beam and target. Note that for the case of three quark flavors there are 127 terms contributing to the inclusive single particle cross section.

The partial cross section in Eq. (D.11) can also be used as a starting point for a two-jet inclusive cross section. At lowest order, the transverse momentum components of the delta function insure that the jets are produced with equal and opposite transverse momenta. The dijet cross section can then be written in terms of the rapidities of the two jets and the transverse momen-

tum,  $p_T$ , possessed by each:

$$\begin{aligned}
& \frac{d\sigma}{dy_1 dy_2 dp_T^2} (AB \rightarrow jet_1 + jet_2 + X) \\
&= \sum_{ab} \int dx_a dx_b \phi_{a/A}(x_a) \phi_{b/B}(x_b) \frac{\hat{s}}{2} \frac{d\sigma}{dt} (ab \rightarrow 12) \\
&\quad \times \delta(x_a \frac{\sqrt{s}}{2} + x_b \frac{\sqrt{s}}{2} - p_T \cosh y_1 - p_T \cosh y_2) \\
&\quad \times \delta(x_a \frac{\sqrt{s}}{2} - x_b \frac{\sqrt{s}}{2} - p_T \sinh y_1 - p_T \sinh y_2) \quad (D.22)
\end{aligned}$$

The two delta functions in this expression are the energy and longitudinal parts of the original four-dimensional delta function appearing in Eq. (D.11). Together, they allow the integrations on both  $x_a$  and  $x_b$  to be carried out. The resulting two jet cross section is

$$\frac{d\sigma}{dy_1 dy_2 dp_T^2} (AB \rightarrow jet_1 + jet_2 + X) = \sum_{ab} x_a \phi_{a/A}(x_a) x_b \phi_{b/B}(x_b) \frac{d\sigma}{dt} (ab \rightarrow 12), \quad (D.23)$$

where

$$x_a = \frac{p_T}{\sqrt{s}} (e^{y_1} + e^{y_2}), \quad x_b = \frac{p_T}{\sqrt{s}} (e^{-y_1} + e^{-y_2}). \quad (D.24)$$

Another variable which is often used in studies of jet production is the dijet invariant mass,  $M_{jj}^2$ . This is easily shown to be given by

$$M_{jj}^2 = 2p_T^2 [1 + \cosh(y_1 - y_2)], \quad (D.25)$$

if the masses of the individual jets are neglected. The mass distribution is then given by

$$\frac{d\sigma}{dy_1 dy_2 dM_{jj}} = \frac{M_{jj}}{1 + \cosh(y_1 - y_2)} \frac{d\sigma}{dy_1 dy_2 dp_T^2}. \quad (D.26)$$

The dijet cross section in Eq. (D.23) has no integrations remaining to be done. That is, knowledge of the four-vectors of the two jets has completely determined the kinematics of the parton scattering process. Thus, it is possible to use Eq. (D.23), or an equivalent expression, to determine the

parton-parton scattering angular distribution, averaged over all of the participating subprocesses. Let  $\theta^*$  be the parton-parton center-of-mass scattering angle. Then, Eq. (D.23) can be rewritten as

$$\frac{d\sigma}{dx_a dx_b d \cos \theta^*} = \frac{x_a x_b s}{2} \sum_{ab} \phi_{a/A}(x_a) \phi_{b/B}(x_b) \frac{d\sigma}{dt} (ab \rightarrow 12), \quad (\text{D.27})$$

where  $x_a$  and  $x_b$  have the values given in Eq. (D.26).

## References

- [D.1] J. Owens, Rev. Mod. Phys. **59**, 465 (1987).